THE UNIVERSITY OF TEXAS AT AUSTIN
CENTER FOR TRANSPORTATION RESEARCH

TECHNICAL REPORT 0-7117-1
TxDOT PROJECT NUMBER 0-7117

Strut-and-Tie Method for Reinforced Concrete Members with Cold Joints

Brandon Li
Andrea Campos Sanchez
Simon Arzadon
Jarrod Zaborac
Zachary D. Webb
Hansol Jang
Yongjae Yu
Hwa-Ching Wang
Elias I. Saqan
Anca C. Ferche
Oguzhan Bayrak

June 2025

Published April 2025

https://library.ctr.utexas.edu/ctr-publications/0-7117-1.pdf

PRELIMINARY REVIEW COPY

Technical Report Documentation Page

1. Report No. FHWA/TX-25 0-7117-1	2. Government Accession No.	3. Recipient's Catalog No.
4. Title and Subtitle Strut-and-Tie Method for Reinforced Concrete Members with Cold Joints		5. Report Date Submitted: June 2025 6. Performing Organization Code
7. Author(s) Brandon Li https://orcid.org/0009-0006-1554-8425 Andrea Campos Sanchez Simon Arzadon Jarrod Zaborac, Ph.D. https://orcid.org/0000-0003-2573-5102 Zachary D. Webb Hansol Jang, Ph.D. Yongjae Yu, Ph.D. https://orcid.org/0000-0002-7621-9733 Hwa-Ching Wang, Ph.D. Elias I. Saqan, Ph.D. https://orcid.org/0000-0002-2718-6816 Anca C. Ferche, Ph.D. https://orcid.org/0000-0003-4380-5194 Oguzhan Bayrak, Ph.D.		8. Performing Organization Report No. 0-7117-1
9. Performing Organization Name and Address Center for Transportation Research The University of Texas at Austin 3925 W. Braker Lane, 4th Floor Austin, TX 78759		10. Work Unit No. (TRAIS) 11. Contract or Grant No. 0-7117
12. Sponsoring Agency Name and Address Texas Department of Transportation Research and Technology Implementation Division 125 E. 11th Street Austin, TX 78701		13. Type of Report and Period Covered Technical Report September 2021 – June 2025 14. Sponsoring Agency Code
15. Supplementary Notes Project performed in cooperation with the Texas Department of Transportation and the Federal Highway Administration.		
16. Abstract Cold joints are a frequent and often unavoidable occurrence in reinforced concrete construction; however, current design provisions offer limited guidance for assessing their effect on load transfer and failure mechanisms, particularly when cold joints intersect critical load paths in disturbed regions. This research proposes a mechanically-based analytical approach that integrates shear-friction behavior into the strut-and-tie method (STM) framework. The analytical model was informed by a comprehensive literature review, a survey of US transportation agencies, and an extensive experimental program consisting of slant shear, deep beam, and a drilled-shaft footing cap test. The study investigated both two- and three-dimensional structural behavior and evaluated the effects of joint orientation, surface roughness, and reinforcement configuration on cold joint performance. Experimental results revealed distinct shear transfer mechanisms in cold joints intersected by compression struts. These findings guided the development of an analytical framework that captures interface behavior and supports a rational design procedure. The proposed analytical approach is compatible with existing design specifications, addressing both interface shear resistance and strut effectiveness within the STM framework. This research delivers validated practical design guidelines for reinforced concrete structures with cold joints, advancing the reliability, safety, and consistency of structural design.		
17. Key Words Cold Joints, Deep Beams, Drilled-Shaft Footing, Strut-and-Tie Modeling, Interface Shear Resistance	18. Distribution Statement No restrictions. This document is available to the public through the National Technical Information Service, Alexandria, Virginia 22312; www.ntis.gov.	

19. Security Classif. (of report)	20. Security Classif. (of this page)	21. No. of pages	22. Price
Unclassified	Unclassified	278	

Form DOT F 1700.7 (8-72) Reproduction of completed page authorized

THE UNIVERSITY OF TEXAS AT AUSTIN
CENTER FOR TRANSPORTATION RESEARCH

Strut-and Tie Method for Reinforced Concrete Members with Cold Joints

Brandon Li
Andrea Campos Sanchez
Simon Arzadon
Jarrod Zaborac
Zachary D. Webb
Hansol Jang
Yongjae Yu
Hwa-Ching Wang
Elias I. Saqan
Anca C. Ferche
Oguzhan Bayrak

CTR Technical Report:	0-7117-1
Report Date:	Submitted: June 2025
Project:	0-7117
Project Title:	Investigate the Strength of Struts Crossing Cold Joints
Sponsoring Agency:	Texas Department of Transportation
Performing Agency:	Center for Transportation Research at The University of Texas at Austin

Project performed in cooperation with the Texas Department of Transportation and the Federal Highway Administration.

Center for Transportation Research
The University of Texas at Austin
3925 W. Braker Lane, 4th floor
Austin, TX 78759

http://ctr.utexas.edu/

Disclaimers

Author's Disclaimer: The contents of this report reflect the views of the authors, who are responsible for the facts and the accuracy of the data presented herein. The contents do not necessarily reflect the official view or policies of the Federal Highway Administration or the Texas Department of Transportation (TxDOT). This report does not constitute a standard, specification, or regulation.

Patent Disclaimer: There was no invention or discovery conceived or first actually reduced to practice in the course of or under this contract, including any art, method, process, machine manufacture, design or composition of matter, or any new useful improvement thereof, or any variety of plant, which is or may be patentable under the patent laws of the United States of America or any foreign country.

Engineering Disclaimer

NOT INTENDED FOR CONSTRUCTION, BIDDING, OR PERMIT PURPOSES.

Project Engineer: Oguzhan Bayrak
Professional Engineer License State and Number: Texas No. 106598
P.E. Designation: Research Supervisor

Acknowledgments

The authors express sincere appreciation to the Texas Department of Transportation (TxDOT) for providing the funds and supports to conduct this research study. The contributions of the project manager Jadé Adediwura (RTI Division) and other members of TxDOT, including Courtney Holle, Victoria McCammon, Zoran Umicevic, Jesus Alvarez (Bridge Division), facilitated great improvements to the outcomes of this project.

Table of Contents

List of Tables

List of Figures

Chapter 1. Introduction

1.1. Overview

Cold joints are formed at the interfaces between layers of concrete placed at different times. Whether introduced deliberately (through staged concrete placement, retrofit actions, or roadway expansion project), as shown in Figure 1-1, or arising unintentionally (due to unforeseen delays in concrete placement), cold joints represent structural discontinuities characterized by complex stress-transfer mechanism, potentially serving as planes of weakness within reinforced concrete (RC) members. Frequently, cold joints occur within the disturbed regions (D-region) of structures, where the structural behavior is dominated by the nonlinear stress field, invalidating traditional sectional design and analysis methods. Instead, the strut-and-tie method (STM) is commonly employed, as it effectively accounts for the intricate stress-transfer mechanisms in D-regions.

Prior to the 2016 edition of AASHTO LRFD Bridge Design Specifications, no explicit indication was provided for specific consideration of struts crossing cold joints. However, the 2016 interim revisions of AASHTO LRFD introduced a requirement to verify the shear-friction capacity of cold joints when intersected by a strut. Despite this advancement, current design expressions for shear-friction capacity of cold joints remains limited to the application of sectional analysis, offering no guidelines directly addressing the approach for evaluating the strength of cold joints intersected by struts and the performance of cold joints in D-regions of structures. Project 0-7117 seeks to address this gap by investigating the strength of struts crossing cold joints through an extensive analytical and experimental program, aiming to develop design guidelines for the AASHTO LRFD Bridge Design Specifications and TxDOT Bridge Design Manual.

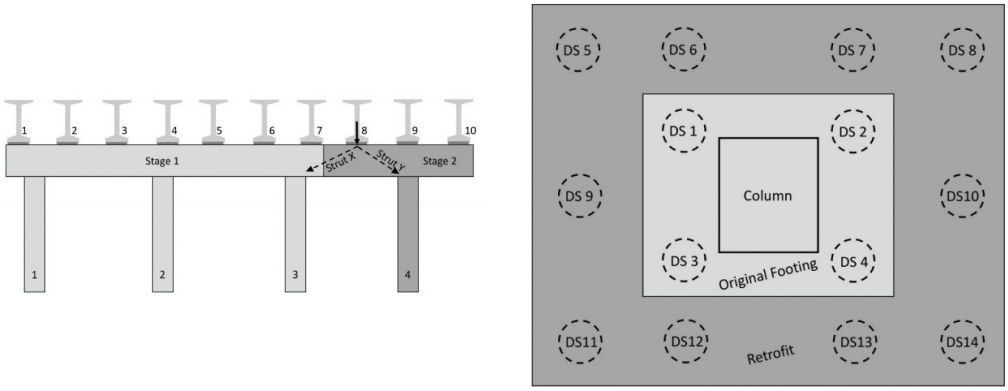

(a) Multi-column bent cap *(b) Retrofitted pier cap*

Figure 1-1 Examples of cold joints in D-regions (Bayrak, 2020)

1.2. Project Objective

The objective of this research project focuses on integrating shear-friction behavior of cold joints into the strut-and-tie framework, providing a mechanically-based numerical approach to evaluate the strength of reinforced concrete structures with cold joints. To assess the influence of common cold joint characteristics, a comprehensive literature review and industrial survey were included in this research project. Based on the information gathered from previous research and common design practice, three comprehensive experimental programs were developed, ranging from small to large scale specimens and encompassing both two and three-dimensional structural behavior. The experiments were designed to provide valuable insight into the overall structural behavior and the response of cold joints for the establishment of a mechanical model that reflects the shear transfer mechanism of cold joints in the D-regions of structures. The mechanical model is structured to support a design procedure that aligns with current design specifications, addressing both interface shear design for cold joints and the strut-and-tie method for D-regions. The overarching objective of this research is to develop a reliable and practically applicable analytical approach, along with corresponding design guidelines, for cold joints located within the D-regions of reinforced concrete structures.

1.3. Project Scope

To fulfill the objective of the project, the following seven tasks were undertaken:

1. Investigate the shear resisting mechanism of cold joints and available model integrating cold joints in the strut-and-tie framework by conducting state-of-the-art literature review.

2. Evaluate common design practices and parameters for cold joints by distributing surveys to certified engineering parties.

3. Identify the key variables influencing the interface shear resistance of cold joints through slant shear experiments and evaluate the accuracy of current interface shear expressions.

4. Investigate the effect of cold joints on the structural behavior and shear performance of deep beams designed with two-dimensional STM.

5. Investigate the effect of cold joints on the structural behavior and shear performance of drilled-shaft footings designed with three-dimensional STM.

6. Propose analytical approaches and design recommendations, compatible with current strut-and-tie provisions, to assess and design the structures in D-regions intersected by cold joints.

The findings from Tasks 1 and 2 were used to identify key design variables for the subsequent experimental program. Based on the results of the slant shear tests, variables found to significantly influence cold joint behavior were incorporated into the design of the large-scale experiments, which included ten deep beams and one drilled-shaft footing cap. Data from these experiments were analyzed to develop a reliable analytical model and corresponding design procedures for the D-regions of structures containing cold joints.

1.4. Organization

Chapter 2 provides background information and a review of design provisions related to interface shear resistance of cold joints and the principles of strut-and-tie modeling. Existing specifications and models concerning struts intersected by cold joints are also reviewed. The chapter concludes with practical applications involving struts crossing cold joints, highlighting the urgent need for formal design guidelines on this topic.

Chapter 3 presents the industrial survey, including the questions posed and the responses received, offering valuable insight into current practices for cold joint design.

Chapter 4 details the slant shear experimental program, covering specimens design and fabrication, testing protocols, instrumentation, experimental results, and data-based analysis.

Chapter 5 focuses on the deep beam experimental program. It begins with the application of the strut-and-tie method in preliminary specimen design and proceeds to describe the selected design variables, specimen configurations, fabrication process, and material properties. The chapter also outlines the instrumentation used to monitor structural behavior, the test setup, and the testing procedure. Experimental results are discussed across several dimensions, including load–deflection response, shear capacity, crack patterns, failure modes, reinforcement strain behavior, serviceability, and strain/displacement fields captured using a non-contact optical tracking system.

Chapter 6 presents the design and results of the drilled-shaft footing cap experiment, following a structure similar to the deep beam program.

Chapter 7 offers an in-depth discussion of cold joint behavior within the strut-and-tie system, based on experimental findings. This chapter also details the methodology, assumptions, and development of the proposed analytical approaches and design recommendations.

Finally, Chapter 8 summarizes the key findings and conclusions of the research, concluding with reflections on its practical implications and potential directions for future work.

Chapter 2. Literature Review

2.1. Shear Behavior of Cold Joints - Shear Friction

This section provides background information and theoretical foundations for the shear behavior of cold joints based on the shear-friction hypothesis, reviews relevant design code provisions, and summarizes key experimental findings from previous research.

2.1.1. Background and Theory

Advancements in precast concrete connections throughout the late 1950s and into the 1960s resulted in a need for a simple connection design method (Mast, 1968). Birkeland and Birkeland (1966) noted that damage was commonly concentrated at shear interfaces within precast connections. As a result, the shear friction hypothesis was developed (Birkeland & Birkeland, 1966; Mast, 1968). The shear friction concept is shown schematically in Figure 2-1. For a cracked concrete element (Figure 2-1(a)) subjected to external shear, V, and a compression force, P, the slip due to the shear force is resisted by the friction force, μP. If the interface is sufficiently rough, the slip will tend to produce a vertical movement, δ (i.e., crack width opening—see Figure 2-1(b)). In an interface with sufficiently anchored and appropriately oriented reinforcement, this vertical displacement causes tension in the reinforcement. As a result, compressive stresses develop across the interface to equilibrate the tensile stresses from the reinforcement. Thus, the basic equation for shear friction theory is:

$$V_n = \mu A_{vf} f_y \tag{2-1}$$

where V_n is the nominal shear force resistance, μ is the coefficient of friction, A_{vf} is the area of interface shear reinforcement, and f_y is the yield strength of the interface shear reinforcement. Based on the shear friction equation, Mast (1968) proposed that for a crack in monolithic concrete and a roughened interface between precast and cast-in-place concrete, the friction coefficient, μ, should be taken as 1.4. The upper limit of tensile stresses introduced by the elongation of reinforcement across the interface were recommended to be conservatively taken as the lesser of $0.15f_c'$ and 600 psi.

Equation (2-1) can also be expressed as a function of the compression and friction forces acting on the interface. Note that the friction coefficient, μ, in Equation (2-1) has replaced the tangent of the internal friction angle, ϕ, from Figure 2-1(b). This substitution is based on the definition of the internal friction angle. The internal-friction angle is defined as the angle between the normal force acting on a plane and the resultant of the normal and shear force acting on the same plane. Thus, the tangent of the internal-friction angle is identical to the coefficient of friction by inspection of Figure 2-1. Also, the internal-friction angle is the slope of the straight-line envelope associated with the Mohr-Coulomb failure criterion for concrete,

$$|\tau| = c - \sigma \tan \phi \tag{2-2}$$

where τ is the failure shear stress, c is the concrete cohesion stress, σ is the normal stress acting on the same plane as the failure shear stress, and ϕ is the internal friction angle.

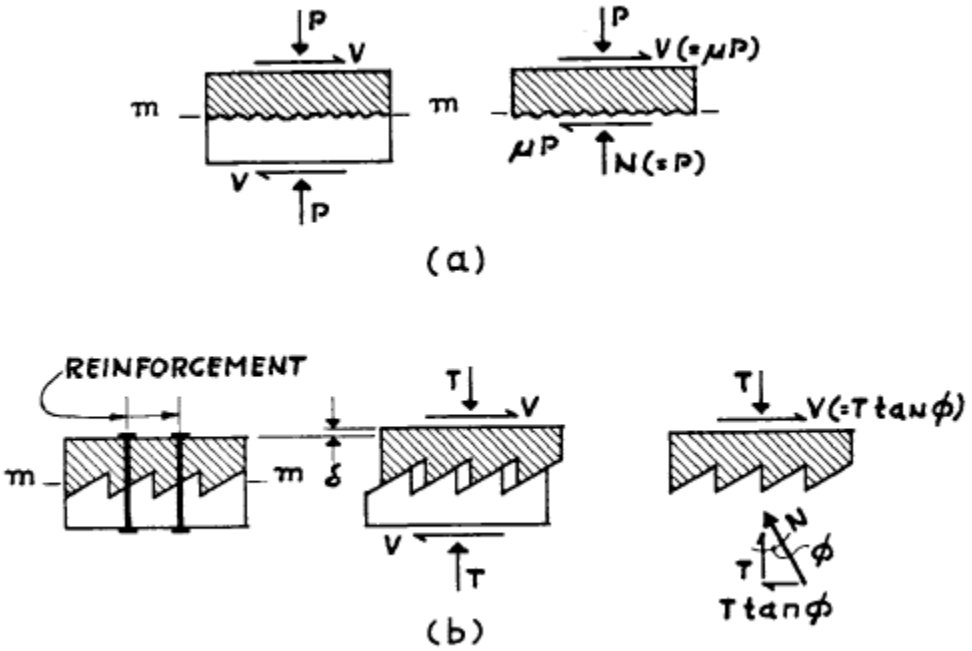

Figure 2-1 Shear friction hypothesis (Reprinted from Birkeland & Birkeland, 1966)

In addition to Equation (2-1), Mast (1968) and Birkeland and Birkeland (1966) also discussed practical upper limits for design, based on the specified compressive strength of concrete, f'_c, and the interface shear stress magnitude, v_n. Other researchers (Hofbeck et al., 1969; Mattock & Hawkins, 1972) also demonstrated that concrete strength played a role in interface shear strength. Notably, Hofbeck et al. (1969) hypothesized that the behavior of initially cracked and initially uncracked shear interfaces would be nearly identical for certain combinations of relative reinforcement strength (the product of the reinforcement ratio, ρ, and reinforcement yield stress, f_y) and concrete compressive strength (e.g., ρf_y = 1.4 ksi and f'_c = 4 ksi). That is, for interface with relative reinforcement strength exceeding these certain combinations, the shear resistance is governed by the concrete compressive strength.

Doweling action of the reinforcement and concrete cohesion were neglected in the original shear friction theory. Hofbeck et al. (1969) tested 38 push-off specimens, as shown in Figure 2-2. More specifically, they tested four specimens (two initially uncracked and two initially cracked) with rubber sleeves around the reinforcement where the bars crossed the interface (to reduce doweling action) to compare with similar specimen without rubber sleeves. In the initially uncracked specimens, the measured slip along the interface was similar to the specimens without the rubber sleeves. Conversely, increased slips were observed in the initially cracked specimens with rubber sleeves, and there was an approximately 29% reduction in interface shear strength.

Hofbeck et al. (1969) concluded that the difference was related to shape of the crack patterns. Typically, several short, diagonal cracks occurred over the length of the shear interface in the initially uncracked specimen. This resulted in unfavorable kinematics to develop appreciable dowel action. Conversely, the reinforcement was orthogonally oriented to the crack interface for the pre-cracked specimens, which allowed for a significant dowel action contribution to shear resistance to develop.

Hofbeck et al. (1969) also noted that there was a concrete contribution to the interface shear strength for specimens with a large enough relative reinforcement strength (approximately 0.20 ksi). Hermansen and Cowan (1974) dubbed this contribution the "apparent cohesive stress." Furthermore, they proposed the modified shear-friction theory, which is given in general by Equation (2-3).

$$V_n = cbd + \mu A_{vf} f_y \tag{2-3}$$

where b is the width of the shear plane, and d is the depth of the shear plane, and other terms are as previously defined within Section 2.1.1. Hermansen and Cowan (1974) took c equal to 0.58 ksi for initially uncracked specimens in their proposal for the modified shear-friction theory for bracket design. Note that, around this same time, Mattock and Hawkins (1972) proposed a similar expression that included an apparent cohesion contribution and the influence of stresses perpendicular to the shear interface (i.e., a super position of the mechanisms in Figure 2-1(a) and (b)).

Hofbeck et al. (1969) conducted a series of statistical analysis on the push-off experimental results to propose appropriate coefficients and shear strength upper limits for the original and the modified shear-friction theory. The experimental results indicated that the upper limit of reinforcement tensile stresses proposed by previous research (Mast, 1968) is reasonably conservative for specimens with relative reinforcement strength less than $0.15f_c'$ and 600 psi. For heavily reinforced specimens with larger relative reinforcement strength, it was observed that the experimental shear strength considerably exceeded the upper limit. Hofbeck et al. (1969) suggested taking 1.0 as the friction coefficient and the lesser of $0.30f_c'$ and 1500 psi as the upper limit of relative reinforcement strength. This recommendation prevented unconservative estimates by decreasing the friction coefficient and leveraged the additional contribution of excessive reinforcement by increasing the upper limit of relative reinforcement strength. For the modified shear-friction theory, the cohesion contribution was derived from the Zia failure envelope. The distribution of experimental results suggested that the friction coefficient is approximately 0.8 when the cohesion contribution is substantial. It was also noted that when the interface shear strength reaches the upper limit, $0.3\,f_c'$, the effect of the relative reinforcement strength is insignificant to the shear strength.

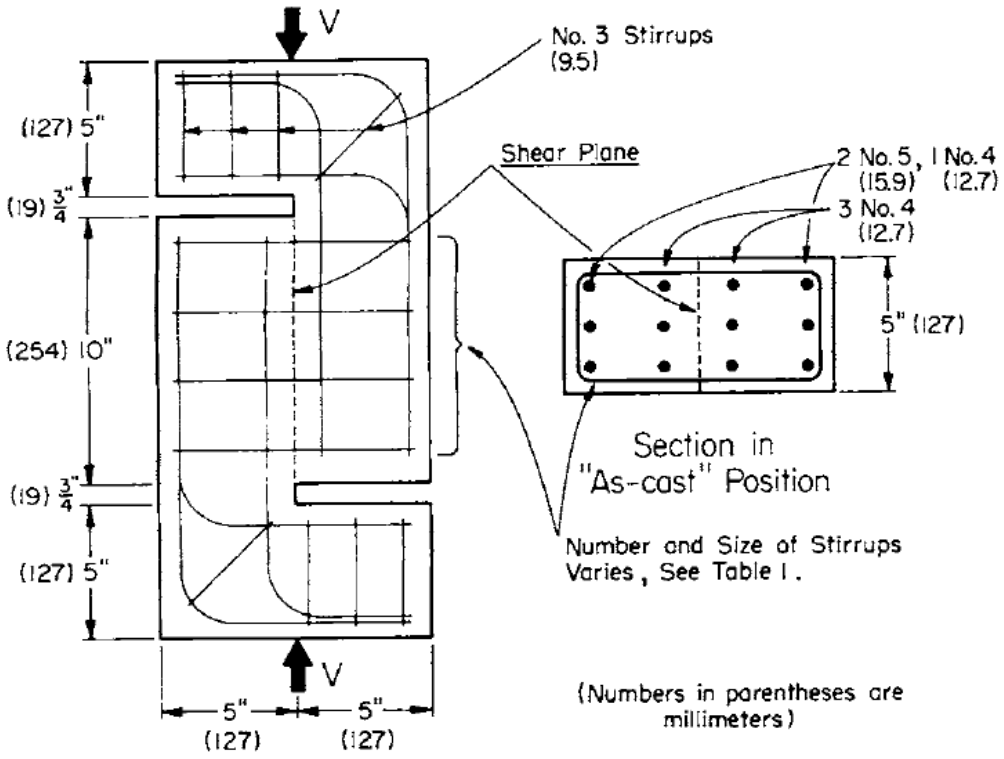

Figure 2-2 Details of push-off specimen (Reprinted from Hofbeck et al., 1969)

Mattock (1974) tested 23 push-off specimens with reinforcement that was oriented at angles, α (see Figure 2-3), ranging from 116.5–180° relative to the shear plane. The goal of this study was to extend the hypotheses proposed by Mattock and Hawkins (1972), which were limited to cases where reinforcement was oriented orthogonally to the shear plane. Ultimately, Mattock (1974) showed that it was possible to generalize the theories; however, the author also noted the importance of checking the angle of reinforcement relative to the crack/shear-plane orientation. Mattock (1974) categorized the orientation between the shear plane to the reinforcement into three groups. Different considerations and assumptions were made to determine the stress in the reinforcement of each category. For layers of reinforcement with inclinations between 0-90° relative to the shear plane, the reinforcement was subjected to tension from the applied shear. Thus, it was assumed that reinforcement would yield prior to the failure of concrete, and the reinforcement stress was taken as the yielding stress. For angle between 90–129°, the reinforcement is subjected to compression. The yielding assumption is not valid in this case, and a different formulation is proposed to estimate the stress of reinforcement. For layers of reinforcement with inclinations between 129–180° relative to the shear plane, negligible amounts of compression will develop in the reinforcement. Thus, Mattock (1974) conservatively recommended taking the reinforcement stress equal to zero.

A generalized form of the modified shear-friction theory, assuming the shear interface reinforcement can develop its full yield strength, is given in Equation (2-4).

$$V_n = cA_{cv} + A_{vf} f_y \cos\alpha + \mu(A_{vf} f_y \sin\alpha + P) \quad (2\text{-}4)$$

where A_{cv} is the area of concrete considered to be engaged in shear transfer, $0° \leq \alpha \leq 90°$, and other terms are as previously defined.

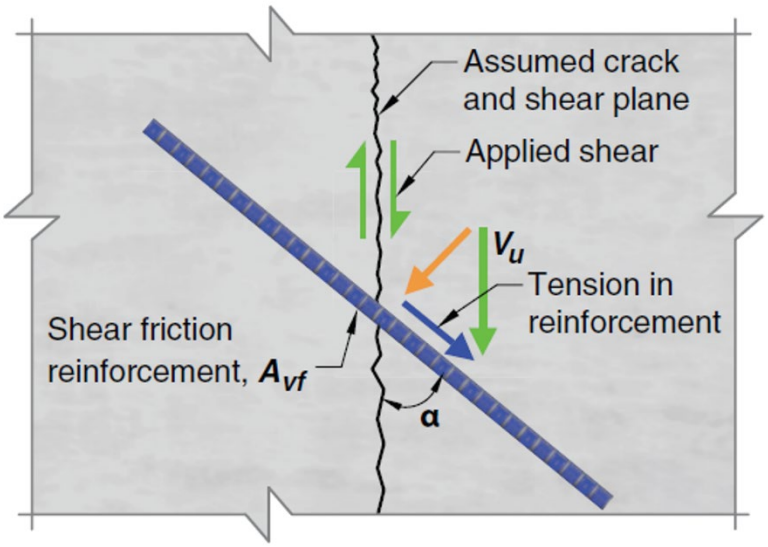

Figure 2-3 Definition of shear friction reinforcement angle, α (Adapted from ACI Committee 318, 2025)

Mattock et al. (1975) conducted 12 corbel push-off experiments to investigate the effect of moment and tensile forces on interface shear behavior, as shown in Figure 2-4. The specimens were subjected to eccentric loading, creating moments and shear simultaneously across the shear plane. Mattock (1975) concluded that the effect of moment is negligible to the interface shear resistance when the applied moment is less than the interface flexural strength. Mattock (1975) also noted that both compressive and tensile forces acting normal to the interface should be considered in the shear calculation. As shown in Equation (2-4), the permanent normal force is positive when compression and negative when tension. Additionally, some specimens exhibited flexural failure prior to interface shear failure. This observation emphasized the need to effectively transfer both moment and shear across the interface. In the design prospective, the total area of reinforcement across the interface should satisfy the sum of the reinforcement area necessary to resist tension force and shear.

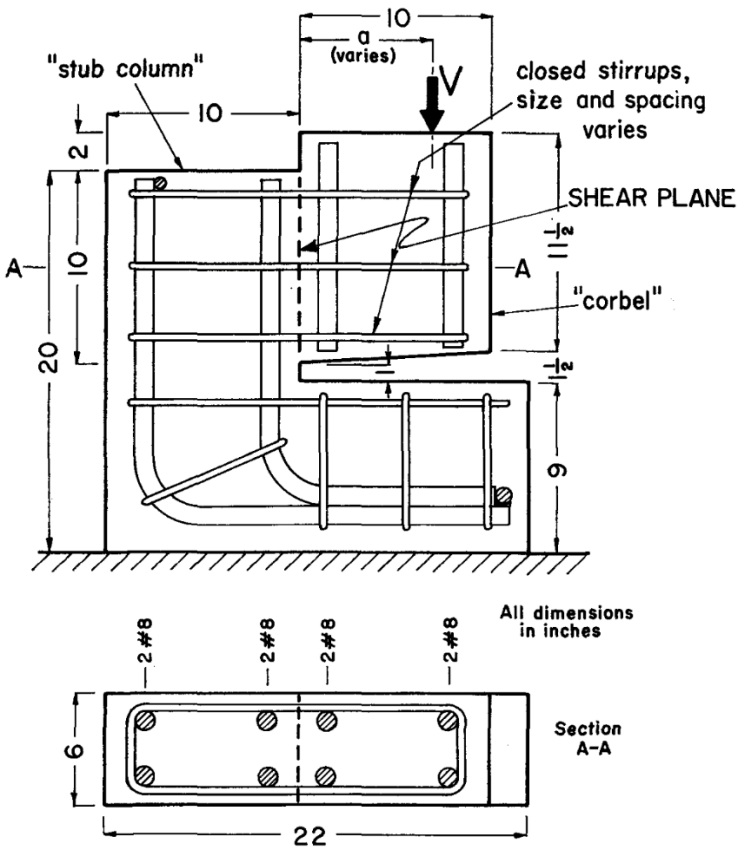

Figure 2-4 Details of corbel push-off specimen (Reprinted from Mattock et al., 1975)

Mattock (1976) synthesized the results of push-off experiments conducted throughout the 1970s to propose a formulation for calculating shear transfer across concrete interfaces. In this formulation, different friction coefficients for were proposed based on the interface conditions. The friction coefficient was taken as 1.4 for deliberately roughened interfaces, and 0.6 for smooth interfaces. For deliberately roughened interface, this research also recommended using the modified shear-friction theory to calculate shear transfer. The upper limit of modified shear-friction theory was taken as 0.2 f_c' when calculating the shear strength of the interface between precast and cast-in-place concrete. These recommendations serve as the foundation for the coefficients and upper limits implemented in current design specifications.

The shear friction and modified shear-friction models discussed so far are solutions based on the lower-bound theorem of limit analysis, which may be stated as,

> [If a statically admissible] stress field which (a) satisfies the equations of equilibrium, (b) satisfies the stress boundary conditions, and (c) nowhere violates the yield criterion…can be found, uncontained plastic flow will not occur at a lower load. (Chen & Han, 1988, p. 413)

More specifically, Equation (2-4) represents a statically admissible stress field subjected to the Mohr-Coulomb yield criterion in Equation (2-2) (Chen, 1982). Recall that Equation (2-2) is the linear portion of the Mohr-Coulomb failure criterion. Chen (1982) also presented two lower-bound solutions for the tension and compression cutoffs, given by Equations (2-5) and (2-6), respectively. Note that the shear interface reinforcement is assumed to be orthogonal to the shear plane and the influence of normal force, *P*, was neglected for simplicity in these two equations.

$$\frac{\tau}{f_c'} = \left(\frac{A_{vf}f_y}{A_{cv}f_c'} + f_t'\right)\sqrt{\frac{1-\sin\phi-2\left(\frac{f_t'}{f_c'}\right)\sin\phi}{\left(\frac{A_{vf}f_y}{A_{cv}f_c'}+\frac{f_t'}{f_c'}\right)(1-\sin\phi)}} \tag{2-5}$$

$$\frac{\tau}{f_c'} = \sqrt{\left(\frac{A_{vf}f_y}{A_{cv}f_c'}\right)\left(1-\frac{A_{vf}f_y}{A_{cv}f_c'}\right)} \leq 0.5 \tag{2-6}$$

with

$$f_c' = \frac{2c\cos\phi}{1-\sin\phi} \tag{2-7}$$

$$f_t' = \frac{2c\cos\phi}{1+\sin\phi} \tag{2-8}$$

where f'_t is the tensile strength of concrete, and other terms are as previously defined within Section 2.1. The compressive and tensile strengths of concrete could also be taken from tests, in lieu of using Equations (2-7) and (2-8).

2.1.2. Design Codes

This section summarizes four relevant design code provisions related to shear friction: the AASHTO *LRFD Bridge Design Specifications* (AASHTO, 2024), the *Building Code Requirements for Structural Concrete* (ACI Committee 318, 2025), the Canadian Standard Association's *Design of Concrete Structures* (CSA Standard A23.3-19, 2019), and the *fib Model Code for Concrete Structures 2020* (fib International, 2024).

2.1.2.1. AASHTO LRFD Bridge Design Specifications

Article 5.7.4 of the AASHTO LRFD outlines design guidelines for interface shear transfer / shear friction. The basic equations are as follows:

$$V_n = cA_{cv} + \mu\left(A_{vf}f_y + P\right) \tag{2-9}$$

$$V_n \leq K_1 f_c' A_{cv} \tag{2-10}$$

$$V_n \leq K_2 A_{cv} \tag{2-11}$$

where V_n is the nominal interface shear force resistance, c is the cohesion factor, A_{cv} is the area of concrete considered to be engaged in shear transfer, μ is the friction factor, A_{vf} is the area of interface shear reinforcement within interface area A_{cv}, f_y is the yield strength of the interface shear reinforcement, P is the permanent net compressive force normal to the shear plane (taken as a positive value or zero if it is tensile), K_1 is the fraction of concrete strength available to resist interface shear, f'_c is the specified compressive strength of concrete, and K_2 is the upper limit for interface shear resistance. The material constants c, μ, K_1, and K_2 are defined in Table 2-1 for various surface roughness conditions. Equation (2-9) is a specific form of Equation (2-4) with α, the reinforcement angle relative to the shear interface (see Figure 2-3), equal to zero (i.e., reinforcement is orthogonal to the shear transfer area), neglecting the contribution of reinforcement parallel to the orientation of the shear interface. The shear resistance is subjected to a concrete-strength-based limit and a shear stress limit.

Table 2-1 AASHTO LRFD cohesion stress and coefficient of friction values for various surface conditions (AASHTO, 2024)

Surface condition	c (ksi)	μ	K_1	K_2 (ksi)
Clean, intentionally roughened to an amplitude of 0.25 in. (concrete slab on concrete girder)	0.28	1.0	0.30	1.8 (normal weight) 1.3 (lightweight)
Normal weight, monolithically placed	0.40	1.4	0.25	1.5
Lightweight concrete, monolithically placed or clean, intentionally roughened to an amplitude of 0.25 in.	0.24	1.0	0.25	1.0
Clean, intentionally roughened to an amplitude of 0.25 in.	0.24	1.0	0.25	1.5
Clean, not intentionally roughened	0.075	0.6	0.20	0.8
Concrete anchored to steel	0.025	0.7	0.20	0.8

The values presented in Table 2-1 are based on lower-bound values that have been empirically validated (Hofbeck et al., 1969; Kahn & Mitchell, 2002; Kahn & Slapkus, 2004; Loov & Patnaik, 1994; Mattock, 2001; Mattock et al., 1976; Patnaik, 1999). Additionally, the AASHTO LRFD provides a minimum area of interface shear reinforcement, as shown in Equation (2-12). Also, if P in Equation (2-9) is tensile then additional reinforcement, A_{vp}, must be added to the required interface shear reinforcement per Equation (2-13).

$$A_{vf} \geq \frac{0.05 A_{cv}}{f_y} \tag{2-12}$$

$$A_{vp} = \frac{P}{f_y} \tag{2-13}$$

2.1.2.2. ACI Building Code Requirements for Structural Concrete

Section 22.9 of ACI 318-25 provides design requirements for shear friction. Equation (2-14) and Table 2-2 summarize the general requirements. ACI 318-25 follows the original shear-

friction theory, neglecting the contribution of concrete cohesion to the shear interface resistance from Equation (2-4). Note that inclined reinforcement may only be used in the Equation (2-14) if the shear force results in a tension force in the reinforcement, as shown in Figure 2-3 ($0° \leq \alpha \leq 90°$). ACI 318-25 has similar requirements to Equation (2-13) if P is tensile. These provisions have been empirically validated with available test results (Kahn & Mitchell, 2002; Mattock, 1977; Mattock & Hawkins, 1972).

$$V_n = A_{vf} f_y \cos\alpha + \mu(A_{vf} f_y \sin\alpha + P) \tag{2-14}$$

where λ is the lightweight concrete factor, and other terms are as previously defined within Section 2.2. Upper limits for V_n are given in Table 2-3.

Table 2-2 ACI 318-25 coefficient of friction values for various surface conditions (ACI Committee 318, 2025)

Concrete surface condition	μ
Placed monolithically	1.4λ
Clean, intentionally roughened to an amplitude of 0.25 in.	1.0λ
Clean, not intentionally roughened	0.6
Concrete anchored to steel	0.7λ

Table 2-3 ACI 318-19 maximum V_n across the assumed shear plan (ACI Committee 318, 2025)

Condition	Maximum V_n (kips)		
Normal weight concrete placed monolithically or placed against hardened concrete intentionally roughened to an amplitude of 0.25 in.	Lesser of (a), (b), and (c)	$0.002f'_cA_{cv}$	(a)
		$(0.48+0.08f'_c)\,A_{cv}$	(b)
		$1.6A_{cv}$	(c)
Other cases	Lesser of (d) and (e)	$0.002f'_cA_{cv}$	(d)
		$0.8A_{cv}$	(e)

2.1.2.3. Design of Concrete Structures (CSA A23.3:19)

Interface shear transfer design guidance is detailed in Clause 11.5 of CSA A23.3:19. Once again, the basic form mirrors Equation (2-4). The factored shear stress resistance in CSA A23.3:19 is

$$v_r = \lambda(c + \mu\sigma) + \rho f_y \cos\alpha \tag{2-15}$$

subjected to the limit of

$$\lambda(c + \mu\sigma) \leq 0.25 f'_c \tag{2-16}$$

where v_r is the factored interface shear stress resistance, σ is the effective normal stress (calculated with Equation (2-17)), ρ is the ratio of shear friction reinforcement (equal to A_{vf}/A_{cv}, the ratio of shear reinforcement to concrete interface area), and other terms are as previously defined within Section 2.2. Table 2-4 summarizes the cohesion stress and coefficient of friction values for various surface conditions. Note that, like ACI 318-25, inclined reinforcement may only be included if the shear force induces tension ($0° \leq \alpha \leq 90°$, refer to Figure 2-3).

$$\sigma = \rho f_y \sin\alpha + \frac{N}{A_g} \tag{2-17}$$

where N is the unfactored permanent load perpendicular to the shear plane (taken as positive for compression and negative for tension), A_g is the gross area of the section, and other terms are as previously defined within Section 2.2.

Clause 11.5.3 also provides Equation (2-18) as an alternate method for monolithically placed concrete or for concrete cast against a clean, intentionally roughened concrete surface with an amplitude greater-than-or-equal-to 0.20 in.

$$v_r = \lambda k \sqrt{\sigma f_c'} + \rho f_y \cos\alpha \tag{2-18}$$

where k is equal to 0.5 for concrete placed against hardened concrete and 0.6 for monolithically placed concrete and other terms are as previously defined within Section 2.2. While CSA A23.3:19 does not explicitly give references to which studies were used to validate the values presented in Table 2-4, a quick comparison with Table 2-1 reveals that the values for c and μ in CSA A23.3:19 are typically less-than-or-equal-to the values used in AASHTO LRFD.

Table 2-4 CSA A23.3:19 cohesion stress and coefficient of friction values for various surface conditions (CSA Standard A23.3-19, 2019)

Surface condition	c (ksi)	μ
Clean, not intentionally roughened	0.036	0.60
Clean, intentionally roughened to an amplitude of not less than 0.20 in.	0.073	1.00
Monolithically placed	0.15	1.40
Concrete anchored to steel	0.00	0.60

2.1.2.4. *fib* Model Code for Concrete Structures 2020

Subsection 30.1.3.8 of MC2020 (fib International, 2024) contains design guidelines for shear at the interface between concrete cast at different times. Unlike the other codes discussed so far, MC2020 (fib International, 2024) considers interfaces with and without reinforcement. An interface without reinforcement is assumed to behave with rigid bond-slip behavior. The interface shear stress design limit, τ_{Rdi}, is calculated using Equation (2-19). While Equation (2-19) obviously does not contain the influence of reinforcement, note that it is still based on Equation (2-4).

$$\tau_{Rdi} = c_a f_{ctd} + \mu\sigma_n \leq 0.5\nu f_{cd} \tag{2-19}$$

where c_a is the coefficient for adhesive bond (refer to Table 2-5), f_{ctd} is the design value for the axial tension strength of concrete, σ_n is the lowest expected permanent compressive stress on the shear plane, ν is the effectiveness factor of concrete (calculated with Equation (2-20) using ksi units), f_{cd} is the design value for the cylinder compression strength of concrete, and other terms are as previously defined within Section 2.2.

$$\nu = 0.55\left(\frac{4.35}{f_{cd}}\right)^{1/3} < 0.55 \tag{2-20}$$

Equation (2-21) provides the interface shear stress design limit for a reinforced interface. Note that it was converted from input units of N/mm to ksi.

$$\tau_{Rdi} = \frac{c_r}{3.6} f_{ck}^{1/3} + \mu\sigma_n + \kappa_1 \rho f_{yd}(\mu \sin\alpha + \cos\alpha) + \kappa_2 \rho \sqrt{f_{yd} f_{cd}} \leq \beta_c \nu f_{cd} \tag{2-21}$$

where c_r is the coefficient for aggregate interlock effects, f_{ck} is the characteristic compressive strength of concrete, κ_1 is the interaction coefficient for tension force in the reinforcement, κ_2 is the interaction coefficient for flexural resistance, f_{yd} is the design yield strength of reinforcement in tension, β_c is the coefficient for the strength of the compressive strut, and other terms are as previously defined within Section 2.2.

Equation (2-21) presents the most distinct expression discussed thus far, however it retains the fundamental components of the modified shear-friction theory (e.g., concrete, clamping stress, and reinforcement contributions with an upper limit defined by the concrete compression strength). The most significant difference is the explicit inclusion of dowel action. The interaction coefficients, κ_1 and κ_2, account for the relationship between the clamping stress and the dowel action provided by the reinforcement. The dowel action introduces coupling compressive and tensile stresses in the reinforcing bars. These coupling stresses provide flexural and shear resistance when transverse displacement occur in the reinforcing bars. When the reinforcing bars are simultaneously elongated, the tensile forces developed in the bars are limited by the existing coupling stresses. To represent this interaction, the *fib* MC 2020 (fib International, 2024) introduce the interaction factor in the design expressions. The interaction factors are determined according to the slipping and opening tendency of the interface. For rough interfaces, the opening introduced by the slip is more significant than smooth interfaces. In this case, the clamping force capacity is reduced by half to account for the presence of dowel action. For increasingly smooth surfaces, the dowel action will eventually govern the entire reinforcement contribution, resulting in negligible clamping forces. Accordingly, the interaction coefficients represent the increase in clamping forces and the reduction in dowel action as the interface roughness increases. Randl (2013) described the technical background, development, and validation of Equations (2-20) and (2-21), also called the "extended shear-friction theory," in the design recommendations for interface shear transfer in MC2020 (fib International, 2024).

Table 2-5 MC2020 coefficients for adhesive bond for various surface conditions (fib International, 2024)

Surface condition*		c_a
Very rough (including shear keys)	$R_t \geq 0.12$ in.	0.50
Rough (strongly roughened interface)	$R_t \geq 0.06$ in.	0.40
Smooth (concrete with little-to-no treatment)		0.20
Very smooth (steel, plastic, timber formwork)		0.025

*R_t is the peak-to-mean line height determined with the sand patch method

Table 2-6 MC2020 coefficients for adhesive bond for various surface conditions (fib International, 2024)

Surface condition	c_r	κ_1	κ_2	β_c	μ	
					$f_{ck} \geq 2.9$ ksi	$f_{ck} \geq 5.1$ ksi
Very rough $R_t \geq 0.12$ in.	0.22	0.5	0.9	0.5	0.8	1.0
Rough $R_t \geq 0.06$ in	0.11	0.5	0.9	0.5	0.7	
Smooth	0	0.5	1.1	0.4	0.6	
Very smooth	0	0	1.5	0.3	0.5	

2.1.3. Summary

In summary, most modern design codes strongly resemble the basic form of the modified shear-friction theory; however, there are several notable differences among the codes. For example, the AASHTO LRFD (2024) specification only accounts for the contribution of shear interface reinforcement oriented orthogonally to the shear plane, while the other three specifications consider the contribution of inclined reinforcement. The friction coefficients are similar across all design codes for interfaces between normal weight concrete layers, but the influence of lightweight concrete is accounted for differently. The AASHTO LRFD simply specifies different values for lightweight concrete interfaces, while ACI 318-25 (2025) and CSA A23.3:19 (2019) use the concrete density modification factor. MC2020 (2024), on the other hand, addresses the influence of lightweight concrete through the concrete tension strength estimate. The AASHTO LRFD (2024) is the only specification of the four that stipulates a minimum amount of shear reinforcement; conversely, MC2020 (2024) is the only code that allows for the design of unreinforced interfaces. MC2020 (2024) is also the only code that determines the cohesion/interlock contribution based on concrete strength. This dependence is also demonstrated in the definition of the concrete compression strength in Equation (2-7), which is based on the Mohr-Coulomb failure criterion. The other codes simply take lower-bound values, irrespective of the concrete compression strength. That stated, all codes provide some upper limit for interface resistance based on the concrete compression strength, where AASHTO LRFD (2024) and ACI 318-25 (2025) provide additional shear stress limits. Despite these differences, all the expressions presented in Section 2.2 have been shown to be sufficiently conservative for design. A brief survey of existing experimental data is provided in the next section.

2.1.4. Relevant Experimental Data

Several methods are commonly used for evaluating shear interface resistance experimentally, including the following: splitting, corbel with moment, pull-off, push-off, slant-shear, and composite beam tests. The six methods are graphically summarized in Figure 2-5. Soltani and Ross (2017) noted that splitting, corbels, and pull-off tests are not ideal for evaluating code expressions for estimating interface shear resistance due to unrepresentative or imperfect stress transfer mechanisms and boundary conditions.

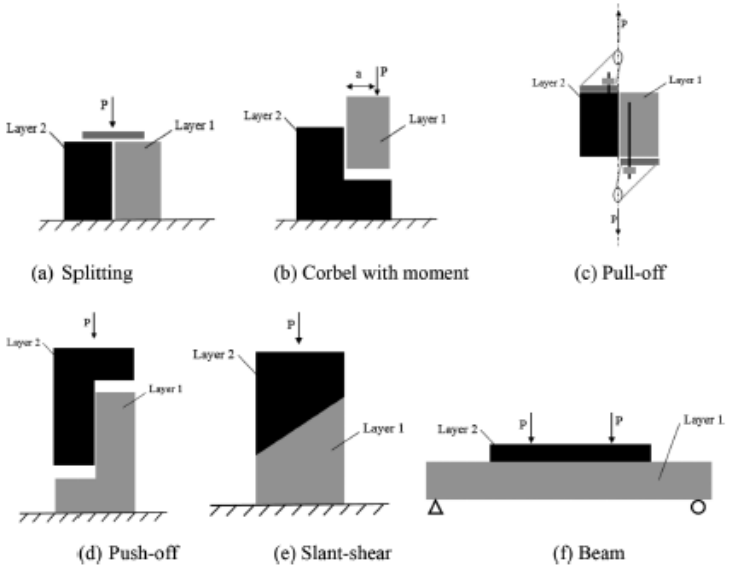

Figure 2-5 Interface shear test methods (Reprinted from Soltani & Ross, 2017)

There have been several database analyses completed in the last two decades. In 2001, Mattock compiled a database of 185 push-off specimens from 10 studies to evaluate the performance of the ACI 318-99 (ACI Committee 318, 1999) shear friction provisions. The database was classified into seven groups:

- Initially cracked, normal-weight concrete subjected to monotonic loading
- Initially cracked, normal weight concrete subjected to cyclic loading prior to static loading until failure
- Initially cracked, normal weight concrete subject to sustained loading prior to static loading until failure
- Initially cracked, sand-lightweight concrete
- Initially cracked all lightweight concrete
- Initially cracked normal weight concrete with a deliberately roughened interface according to Section 11.7.9 of ACI 318-99
- Initially cracked normal weight concrete with a smooth interface

Ultimately, Mattock (2001) made recommendations for establishing upper-limits based on concrete strength that were later adopted by ACI and are still in the current edition (ACI Committee 318, 2025).

Lang (2011) conducted another large database analysis that targeted the AASHTO LRFD (2010) provisions. Lang focused on five major variables: interface condition, concrete density,

concrete compression strength, shear reinforcement ratio, and applied clamping stress. Lang's database contained results from 537 tests from 16 test programs, including results from push-off specimens and composite beams. Lang analyzed the specimens with the 2010 AASHTO LRFD provisions. It was found that the shear friction provisions were typically conservative, but the reliability index was below 3.5, which is the value recommended by MacGregor (1976). As a result, Lang recommended a replacement for Equation (2-9), but it was not adopted.

Sneed and Shaw (2014) created a similar database focused on the lightweight concrete. Their database contained 300 test results from 8 research programs, and it included results from push-off, pull-off, and corbel with moment tests. Sneed and Shaw concluded that the shear friction resistance was not influenced by the concrete density. This is at odds with earlier observations made by Mattock et al. (1976). As discussed in the preceding section, all modern design codes still reduce the interface strength of lightweight concrete.

Soltani and Ross (2017) expanded the database compiled by Lang (2011) (537 tests to 774 tests); however, Soltani and Ross (2017) focused exclusively on the initially uncracked specimens (497 out 774 tests). Furthermore, they filtered out an additional 69 tests due to unrepresentative test conditions, undesirable failure modes (e.g., flexure), and grout injected interfacesThe goal was to evaluate the AASHTO LRFD (AASHTO, 2014), Eurocode 2 (European Committee for Standardization, 2005), and CSA A23.3-14 (CSA Standard A23.3-14, 2014) shear friction provisions. They also filtered out specimen for each code evaluation (e.g., the minimum reinforcement requirement from AASHTO (2014) [Equation (2-12)] was considered as a filtering criterion) resulting in three code-specific databases. Ultimately, Soltani and Ross (2017) concluded that all three codes were acceptably conservative, on average. However, both the Eurocode2 (2005) and CSA A23.3-14 (2014) were more likely to be unconservative for highly reinforced interfaces. A notable trend in the AASHTO LRFD (2014) evaluation was an increase in conservatism for high-strength concrete. 11% of specimens with concrete strengths ranging from 3–6-ksi were unconservative prior to the application of resistance factors, while no unconservative predictions were observed for specimens with concrete strengths higher than 7.3 ksi.

It must be noted that a minority (less than 10%) of tests in Soltani and Ross's (2017) filtered database were slant-shear tests. However, slant-shear tests are the closest of the typical shear friction test methods to an idealized, uniaxially loaded, prismatic strut. Such test data is of relevance to this project and the goals of Tasks 4–7, which culminate in the development of design guidelines for the strength of compression struts crossing cold joints. The following paragraphs relate specifically to various slant-shear test results in the literature.

Santos and Júlio (2011) performed an extensive series of slant-shear tests to investigate various methods of interface roughening, curing conditions, and temporal effects (i.e., concretes cast at different times). The results of their test program showed that larger time gaps between casting of the first and second layers typically resulted in increased bond strength. The authors hypothesized that the bond strength increased due to the shrinkage difference between two

concrete layers. This difference in shrinkage acted as pre-strain on the interface, neutralizing strain introduced by the applied shear forces. Thus, design recommendations for shear friction capacity should account for the possible differences in performance between staged construction (where ages may be similar) and retrofitting efforts (where casting times may be decades apart).

Diab et al. (2017) tested cylindrical and prism specimens in slant shear to investigate the interface behavior between self-compacting concrete (SCC) and old concrete. They found that results from 6 x 12 in. cylinders had the lowest coefficient of variation (2.74%) compared to 3 x 6 in. cylinders (7.82%), 8 x 8 x 20 in. prisms (4.26%), and 4 x 4 x 16 in. prisms (20.18%). Conversely, they concluded that prism tests resulted in more reliable strengths, on average. Diab et al. based this conclusion on comparison with a theoretical failure envelope. Diab et al. also noted that the stiffness of substrates significantly influences the interface shear strength, highlighting the importance of matching stiffnesses between the substrates of specimens for reliable comparative analyses. Furthermore, they noted that the interface shear strength was dependent on the ratio of the two concrete strengths when the ratio ranged from 1.0 to 1.4. The effect of concrete strengths ratio was negligible when exceeding 1.4.

Piancastelli et al. (2017) compared test results between slant-shear tests and double-sleeve tests (see Figure 2-6). The double-sleeve test was designed specifically to investigate the bond strength of concrete jacketing—a strengthening/repair method. Ultimately, their results showed that the double-sleeve test method was more appropriate for evaluating the behavior of retrofitted concrete columns. Piancastelli et al. (2017) noted that monolithic behavior of the two concretes could not be achieved in the slant-shear specimens; furthermore, the average cohesion stress was higher in the slant-shear tests than in the double-sleeve tests.

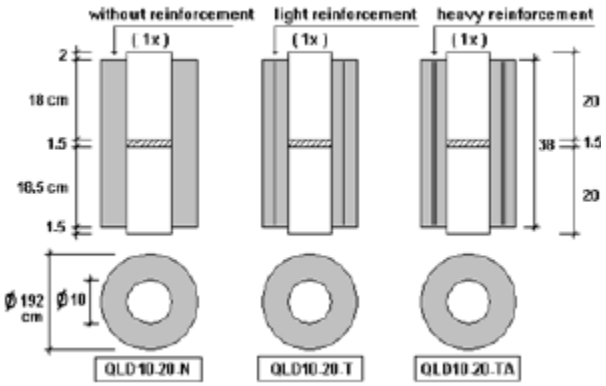

Figure 2-6 Double-sleeve tests (Reprinted from Piancastelli et al., 2017)

Farzad et al. (2019) studied the bond strength between conventional and ultra-high-performance concretes (UHPC). They performed 45 tests on three types of specimens: third-point flexural, direct-shear, and slant-shear. Ultimately, their focus was on developing a nonlinear finite element analysis method for defining the contact between the conventional and ultra-high-performance concretes. Farzad et al. (2019) found that using a very thin (approximately 0.004 in.) layer of concrete interface material performed significantly better than tying the conventional and

ultra-high-performance layers together directly (maximum prediction error of 18% compared to 150%).

Hu et al. (2020) performed dynamic load tests on slant-shear cylinders. They used a series of small shear keys (average depths of 0.05 or 0.10 in.) along the interface to provide the effective surface roughness. Hu et al. (2020) determined that there was little-to-no difference in performance between these two conditions. Furthermore, Hu et al. concluded that the strain rate impacted all important aspects of bond (e.g., interface shear resistance) and dynamic behavior (e.g., energy dissipation). Finally, the authors determined that the influence of concrete age can be neglected for cases where the layers were cast more than 28 days apart.

Figueiredo et al. (2022) investigated the bond performance between normal weight and sand-lightweight concrete using 75 slant-shear, 24 push-off, and 24 pull-off tests. They modified the slant-shear tests, as shown in Figure 2-7. This modification resulted in higher interfacial stresses for a given applied load based on nonlinear finite element analysis results (Figueiredo et al., 2022). Figueiredo et al. (2022) also noted a dependence on the ratio of the substrate compressive strengths, similar to Diab et al. (2017).

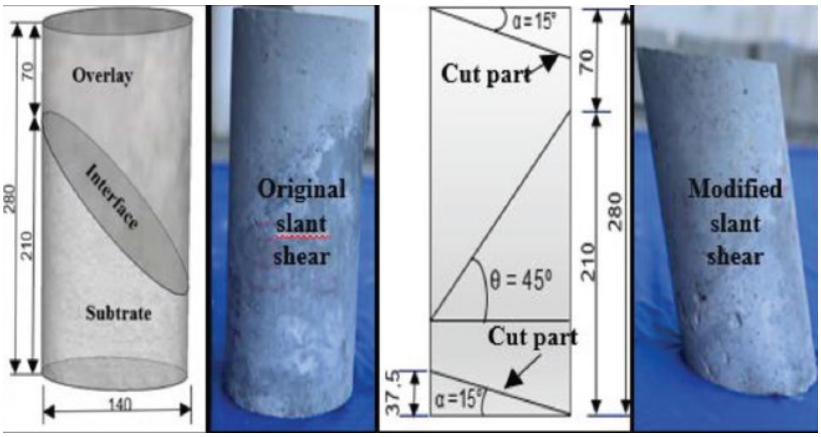

Figure 2-7 Modified slant-shear test (Adapted from Figueiredo et al., 2022b)

All the experimental programs introduced in this subsection implemented various interface roughening approaches with different roughness amplitudes. These studies universally concluded that the interface shear resistance increase significantly with the interface roughness. However, many of the roughness amplitudes applied to the specimens in these experiments are less than the amplitude thresholds required by the specifications. Therefore, it is necessary to validate the amplitudes used by current design codes for classifying the interface conditions and determining the interface shear coefficients.

In conclusion, interface roughness, casting age difference, and compressive strength of concrete were found to influence the interface shear behavior. The concrete material properties of the substrate and the overlay were also observed to affect the interface shear resistance in some cases, including concrete stiffness, strength difference between layers, and shrinkage rate.

However, many of these material effects were concluded from research using unconventional concrete materials, such as, UHPC, SCC, and crushed limestone aggregate. The effect of material properties on conventional concrete-to-concrete interface requires further validations.

2.2. Strut-and-Tie Method

This section presents the background and theory behind the strut-and-tie method and modern strut-and-tie design code provisions.

2.2.1. Background and Theory

The truss analogy for the analysis of shear in reinforced concrete structures dates back over a century to the Hennebique Construction Method (Hennebique, 1898) and the truss models developed by Ritter (1899) and Mörsch (1902) The analogy is based on the strategic placement of reinforcing bars to act as tension chords that equilibrate the concrete compression fields, which is commonly visualized as discrete compression strut resultants, as shown in Figure 2-8. The method has undergone numerous refinements since its inception (Collins et al., 1996; Collins & Mitchell, 1980; Drucker, 1961; Kupfer, 1964; Leondardt, 1965; Marti, 1985; Rüsch, 1965; Schlaich et al., 1987), and it forms the basis for many modern sectional shear provisions (AASHTO, 2024; ACI Committee 318, 2025; fib International, 2024). Schlaich et al. (1987) published a unified design approach based on the strut-and-tie method, which is a generalization of the traditional truss analogy. The authors proposed subdividing a structure into B- (beam or Bernoulli) and D- (discontinuity, disturbance, or detail) regions primarily based on the linear-elastic stress trajectories, as shown in Figure 2-9 (Schlaich et al., 1987). Typically, Saint-Venant's principle is used to delineate B- and D-regions. For example, a beam's depth is commonly used as the distance at which vertical stresses from a point load become negligible (e.g., Figure 2-9). Similarly, the width of a column may be used to approximate the distance at which the axial stresses in a column are uniform (e.g., Figure 2-10). To summarize, a B-region refers to an area of a structure where the internal state of stress is adequately represented by the sectional forces (e.g., axial, shear, and moment); thus, sectional methods apply for analysis and design. Conversely, D-regions are regions where the stress-strain field is disturbed (i.e., nonlinear). As a result, sectional forces can no longer represent the internal stresses flow, and sectional methods do not typically apply for the analysis and design of D-regions. Thus, the more general strut-and-tie method is usually recommended for D-region analysis and design (AASHTO, 2024; ACI Committee 318, 2025; fib International, 2024).

The strut-and-tie method is based on the lower-bound theorem of limit analysis, which derives from the theory of plasticity (refer to Section 2.2.1). In the case of the strut-and-tie method, the actual stress field is simplified into an analogous set of axial elements. As implied by the name "strut-and-tie," the axial elements are divided into two categories: i) compression struts; and ii) tension ties. The struts and ties are connected at nodal zones. In an appropriately selected strut-and-tie model, the concrete struts only carry compression and reinforcement ties carry all the

tension. However, this deliberately idealized model does not completely align with the actual load distribution in structure. To account for this, as well as to generally account for brittle failure modes in concrete, concrete efficiency factors are typically used to limit the compressive stresses acting on nodal zone faces.

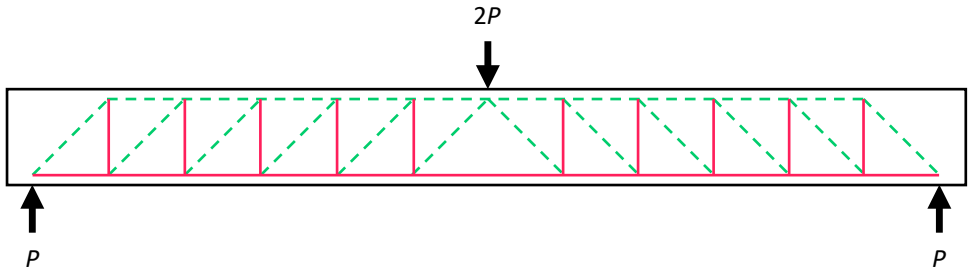

Figure 2-8 Truss analogy for the shear design of reinforced concrete

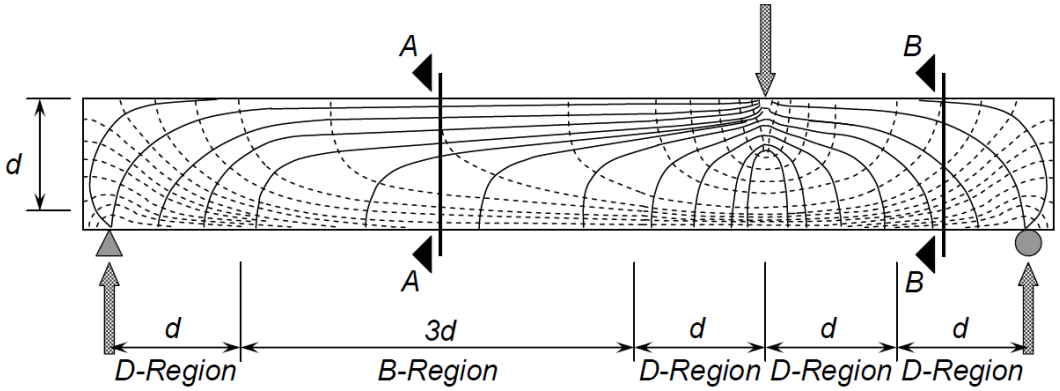

Figure 2-9 Stress trajectories in B- and D-regions (Reprinted from Birrcher et al., 2009)

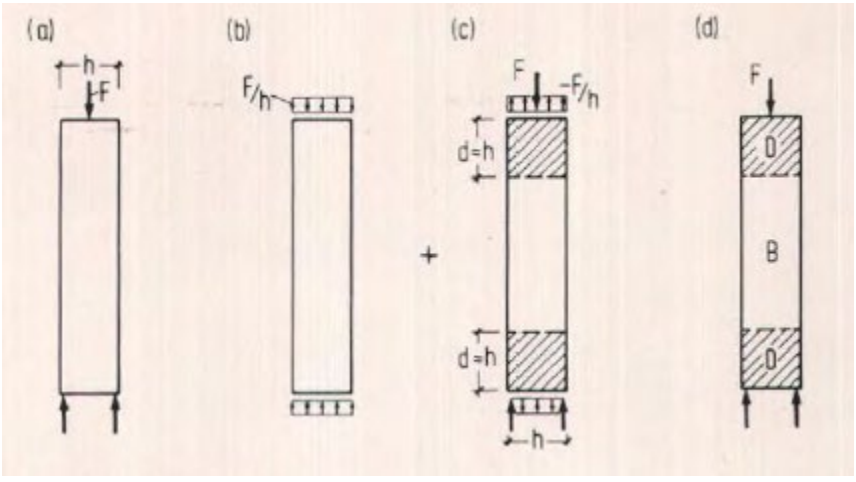

Figure 2-10 Separation of B- and D-regions in a column (Reprinted from Schlaich et al., 1987)

There are two primary strategies for developing a strut-and-tie model: i) the aforementioned linear-elastic stress trajectory method; and ii) the load path method (Schlaich et al., 1987). Figure 2-11 shows an example of the elastic stress trajectory method. Commonly, this

is recommended for highly stressed regions of a structure where an elastic solution can be developed easily (Schlaich et al., 1987). For other cases, particularly those in which elastic solutions are unavailable, the load path method is recommended (Schlaich et al., 1987). The load path method assumes that external forces find their counteracting reaction on the opposite side of the structure, as shown in Figure 2-12. Note that the assumed load paths do not cross. Regardless of the development method, the model can typically be optimized. For example, alternative load paths may be considered to ensure that tension ties are orthogonal to the structure's primary axes to avoid inclined reinforcement (Schlaich et al., 1987). Schlaich et al. (1987) also recommended minimizing the total number of ties and strain energy in the ties to ensure a more optimal model. This tends to ensure more optimum load paths that limit deformations, thereby preventing violations to the underlying limit analysis theory (e.g., wide cracks). Additionally, limitations on the compression field (i.e., strut) angle are commonly prescribed for this reason. Lampert and Thürlimann (1971) proposed the following limitation based on testing by Lampert (1970).

$$0.5 \leq \tan\theta \leq 2.0 \tag{2-22}$$

Thürlimann (1979) provided additional explanation for the limits based on a comparison between the mean crack strain and the strains in an orthogonal reinforcement layout (i.e., longitudinal reinforcement oriented at 0° and stirrups oriented at 90°). Both the lower and upper limit correspond to a mean-crack-to-reinforcement-yield-strain ratio of 5 for the onset of yielding in the longitudinal and shear reinforcement, respectively. Ramirez and Breen (1991)simplified the limit to the following:

$$25° \leq \theta \leq 65° \tag{2-23}$$

Many modern design codes have adopted this simplification—the angle between a compression strut and an adjacent tie must be greater-than-or-equal-to 25° (AASHTO, 2024; ACI Committee 318, 2025). Examination of cracking behavior may also be used to supplement model optimization; that is, if the cracking behavior of a similar structure is known, then the approximate location of struts and tie may be inferred based on the crack pattern (MacGregor, n.d.). This is essentially a special case of the load path method.

In any case, once the model has been developed then the equivalent axial forces can be calculated from equilibrium. Once the equivalent internal forces have been calculated, the struts, ties, and nodal zones can be proportioned. Various design codes with specific guidance on this process are discussed in Section 2.2.2.

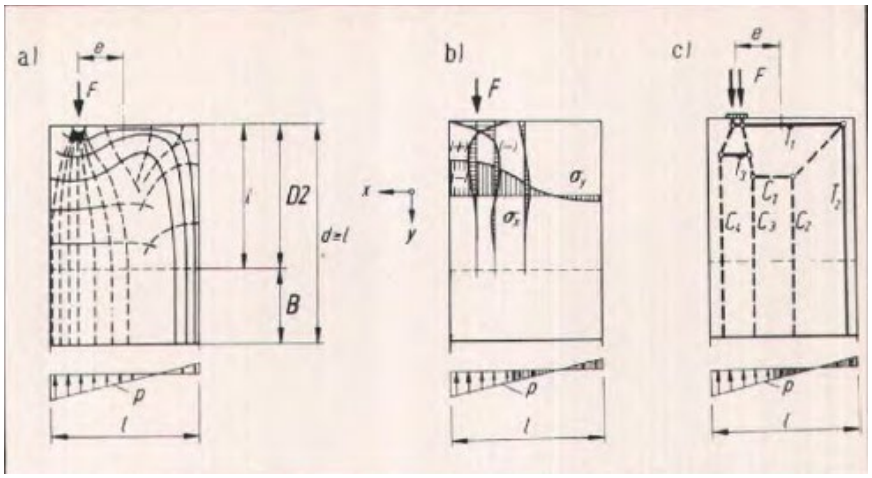

Figure 2-11 Development of strut-and-tie model from elastic stress trajectories (Reprinted from Schlaich et al., 1987)

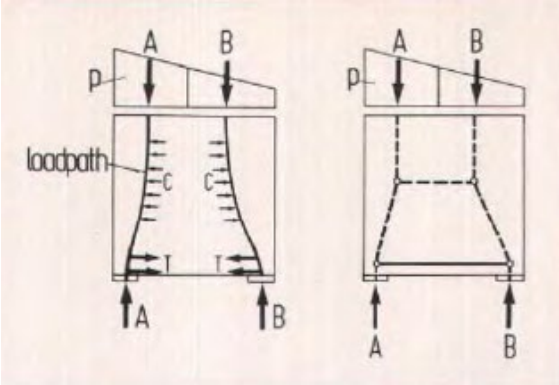

Figure 2-12 Development of strut-and-tie model with the load path method (Reprinted from Schlaich et al., 1987)

2.2.2. Design Codes

This subsection summarizes four relevant design code provisions for the strut-and-tie method: the AASHTO *LRFD Bridge Design Specifications* (AASHTO, 2024), the *Building Code Requirements for Structural Concrete* (ACI Committee 318, 2025), the Canadian Standard Association's *Design of Concrete Structures* (CSA Standard A23.3-19, 2019), and the *fib Model Code for Concrete Structures 2020* (fib International, 2024).

2.2.2.1. AASHTO LRFD Bridge Design Specifications

In the AASHTO LRFD Article 5.8, the nominal resistance of a tie is given by Equation (2-24) and the nominal resistance of a node face is given by Equation (2-25).

$$P_n = f_y A_s + A_{ps}(f_{pe} + f_y) \tag{2-24}$$

$$P_n = mvf_c' A_{cn} + A_s' f_s' \tag{2-25}$$

where P_n is the nominal resistance of a tie or node face, f_y is the yield strength of non-prestressed reinforcement, A_s is the area of non-prestressed reinforcement, A_{ps} is the area of prestressed reinforcement, f_{pe} is the effective stress in the prestressed reinforcement (after losses), m is the confinement modification factor (Equation (2-26)), v is the concrete efficiency factor, f'_c is the specified compression strength of concrete, A_{cn} is the area of the node face, A'_s is the area of non-prestressed, compression reinforcement, and f'_y is the yield strength of the non-prestressed, compression reinforcement.

$$m = \sqrt{\frac{A_2}{A_1}} \leq 2.0 \tag{2-26}$$

where A_1 is the area of the bearing device and A_2 is the notional area due to compression spreading.

Nodal region behavior is grouped into three categories based on the number of connected ties: compression-compression-compression (CCC—no ties), compression-compression-tension (CCT—ties in one direction), and compression-tension-tension (CTT—ties in two directions). Figure 2-13 shows a graphic depiction of the three node types and the associated concrete efficiency factors. Note that the values presented in Figure 2-13 are only valid if 0.3% crack control reinforcement is provided in the vertical and horizontal directions. Otherwise, the concrete efficiency factor is taken as 0.45. Furthermore, note the following limitation for the strut-to-node interface efficiency factor:

$$0.45 \leq 0.85 - \frac{f'_c}{20 \text{ ksi}} \leq 0.65 \tag{2-27}$$

Finally, note that the AASHO LRFD strut-and-tie method approves the use of non-hydrostatic nodes. That is, shear stresses are allowed to exist in the node. Conversely, a hydrostatic node must be proportioned such that all nodal faces have the same stress. A schematic comparison is shown in Figure 2-14. Researchers have observed that the use of non-hydrostatic nodes is typically much less restrictive for design and more representative for the stress distribution of certain structures than hydrostatic nodes (Birrcher et al., 2009).

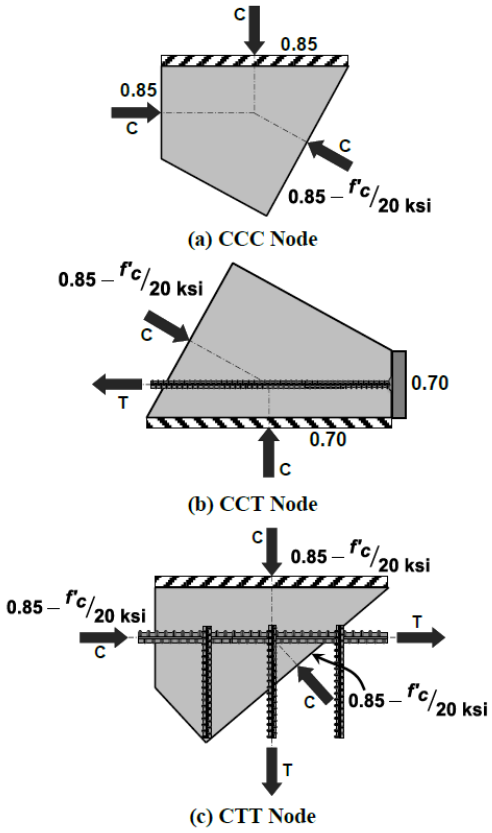

Figure 2-13 Depiction of efficiency factors (Reprinted from AASHTO, 2024)

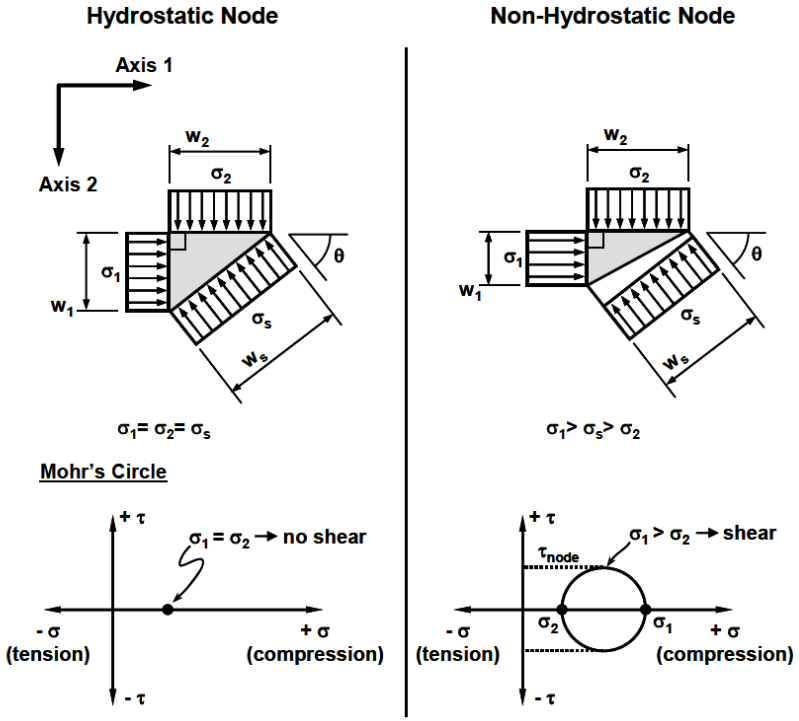

Figure 2-14 Hydrostatic and non-hydrostatic nodes (Reprinted from Brown et al., 2006)

2.2.2.2. Building Code Requirements for Structural Concrete (ACI 318-25)

Chapter 23 of ACI 318-25 outlines the ACI strut-and-tie method. The nominal resistance of a tie is given by Equation (2-28) and the nominal resistance of a node face is given by Equation (2-29).

$$P_n = f_y A_s + A_{ps} \Delta f_p \tag{2-28}$$

$$P_n = 0.85 \nu m f_c' A_{cn} + A_s' f_s' \tag{2-29}$$

where Δf_p is the increase in prestressed reinforcement stress due to factored loads, and other terms are as previously defined within Section 3.2. Like AASHTO LRFD, non-hydrostatic nodes are recommended. The concrete efficiency factors are given by Table 2-7 and Table 2-8 and for strut-to-node interfaces and nodal zones, respectively. The minimum distributed reinforcement requirements are summarized in Table 2-9. Struts are considered laterally restrained if the D-region is continuous in the out-of-plane direction (e.g., continuous corbel supporting a slab), there is a sufficient volume of concrete surrounding the strut, or if the strut is in a sufficiently detailed joint (ACI Committee 318, 2025). The fourth criterion in Table 2-7 applies to D-regions that do not satisfy Table 2-9 or occur in beam-column joints. It is a sectional shear check intended to preclude diagonal tension failure and is given by Equation (2-30) with input units of kips and inches.

$$V_u \leq 0.158 \tan \theta_s \, \lambda \lambda_s \sqrt{f_c'} b_w d \tag{2-30}$$

where V_u is the ultimate shear force, θ_s is the strut inclination, λ is the concrete density modification factor, λ_s is the size effect modification factor for structures without minimum distributed reinforcement (see Equation (2-31)), b_w is the width of the web, d is the effective flexural depth, and other terms are as previously defined within Section 3.2.

$$\lambda_s = \sqrt{\frac{2}{1 + \frac{d}{10}}} \leq 1 \tag{2-31}$$

where input units are in inches, and all terms are as previously defined within Section 3.2.

Table 2-7 Strut-to-node coefficient (ACI Committee 318, 2025)

Strut location	Strut type	Criteria	v
Tension members or tension zones of members	Any	All cases	0.4
All other cases	Boundary struts	All cases	1.0
	Interior struts	Minimum distributed reinforcement	0.75
		Located in regions satisfying 23.4.4	0.75
		Beam-column joints	0.75
		All other cases	0.4

Table 2-8 Nodal zone coefficient (ACI Committee 318, 2025)

Configuration of nodal zone	v
CCC	1.0
CCT	0.80
CTT	0.60

Table 2-9 Minimum distributed reinforcement (ACI Committee 318, 2025)

Lateral restraint of strut	Reinforcement configuration	Minimum distributed reinforcement ratio
Not restrained	Orthogonal grid	0.0025 in each direction
	Reinforcement in one direction cross strut at angle α_1	$0.0025/\sin^2 \alpha_1$
Restrained	Distributed reinforcement not required	

2.2.2.3. Design of Concrete Structures (CSA A23.3:19)

Strut-and-tie method design guidance is detailed in Clause 11.4 of CSA A23.3:19. The nominal resistance of a tie is given by Equation (2-32) and the nominal resistance of a node face is given by Equation (2-33).

$$P_n = f_y A_s + \left(f_{po} + 58 \text{ ksi}\right) A_{ps} \tag{2-32}$$

$$P_n = v m f_c' A_{cn} + A_s' f_s' \tag{2-33}$$

where f_{po} is the stress in prestressed reinforcement for no strain in the concrete, v is the concrete efficiency given by Equation (2-34) and Table 2-10, and other terms are as previously defined within Section 2.2.2. For a strut-to-node interface, CSA A23.3:19 assumes the concrete efficiency, v in Equation (2-34), to be dependent on the principal strain, ε_1 in Equation (2-35).

$$v = \frac{1}{0.8 + 170\varepsilon_1} \leq 0.85 \tag{2-34}$$

$$\varepsilon_1 = \varepsilon_s + (\varepsilon_s + 0.0002) \cot^2 \theta_s \tag{2-35}$$

where ε_s is the tie tensile strain passing through the strut at angle θ_s, as shown in Figure 2-15.

Like AASHTO LRFD and ACI 318-25, CSA A23.3:19 contains stipulations for minimum distributed reinforcement. The minimum required reinforcement ratio is 0.2% in orthogonal directions.

Table 2-10 Nodal zone coefficient (CSA, 2019)

Configuration of nodal zone	ν
CCC	0.85
CCT	0.75
CTT	0.65

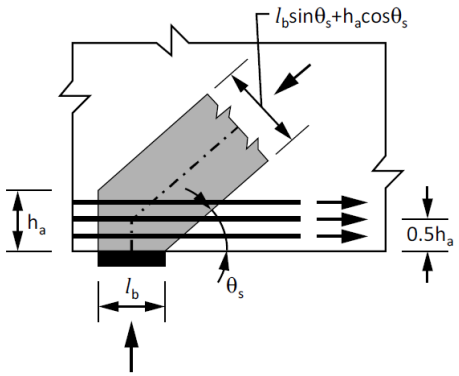

Figure 2-15 Strut anchored by bearing plate and reinforcement (Adapted from CSA, 2019)

2.2.2.4. *fib* Model Code for Concrete Structures 2020

Finally, Subsection 7.3.6 describes the methodology for design with stress fields and strut-and-tie models for MC2020. The tensile fields or ties are proportioned to satisfy the following reinforcement stress limits (neglecting material safety factors):

$$f_s \leq f_y \tag{2-36}$$

$$f_{ps} \leq f_{p0.1k} \tag{2-37}$$

where f_s and f_{ps} are the stresses in non-prestressed and prestressed reinforcement, $f_{p0.1k}$ is the 0.1% proof strength of prestressed reinforcement, and other terms are as previously defined within Section 2.2.2.

Concrete stresses are limited to (neglecting material safety factors):

$$f_c \leq \nu\left(\frac{4.35}{f_{ck}}\right)^{\frac{1}{3}} f_{ck} \leq \nu f_{ck} \tag{2-38}$$

where f_c is the stress in the concrete, f_{ck} is the characteristic compressive strength of concrete, and ν is the concrete efficiency factor given by Table 2-11.

Table 2-11 Concrete efficiency factor (fib International, 2024)

Stress condition	ν
Undisturbed uniaxial compression	1.0
Cracks parallel to the direction of compression	0.75
Reinforcement skewed from the direction of compression	0.55
Significant biaxial compression	1.1

2.2.3. Design of Struts Crossing Cold Joints

Interim revisions to AASHTO LRFD (2016) added requirements that struts crossing cold joints should be investigated; however, this was only done in the commentary to the code, and no explicit guidance is given on how to combine shear friction with the strut-and-tie method (AASHTO, 2024). ACI 318-25 is more explicit in its requirements: the ACI 318-25 shear-friction requirements apply when shear transfer is expected to occur across a cold joint or existing/potential crack. However, the shear-friction theory is frequently formulated based on sectional forces. As discussed in Section 2.2.1, this may not be consistent with the actual stress distribution in a D-region. As such, there is a clear need to express shear-friction behavior in a manner consistent with the concept of effective strut strength within the STM framework. The Fédération Internationale de la Précontrainte (FIP) published recommendations for the *Practical Design of Structural Concrete* (Fédération Internationale de la Précontrainte (FIP), 1999). An equation for the effective strength of a prismatic strut across a cold joint was proposed, calculated as follows:

$$f_{cd,eff} = \beta f_{ctd} \frac{1 + \tan^2 \alpha_f}{\tan \alpha_f - \mu} \leq f_{1cd} \tag{2-39}$$

where $f_{cd,eff}$ is the effective concrete strength of the strut, β is the cohesion factor, f_{ctd} is the tensile strength of concrete, α_f is the inclination of the cold joint relative to the strut direction, μ is the friction coefficient, and f_{1cd} is the compressive strength of concrete. Figure 2-16 shows a sketch of this idealized case.

The FIP formulation in Equation (2-39) is based on modified shear-friction theory. The stresses are calculated with similar cohesion and friction factors to the methods described earlier; however, Equation (2-39) does not include the influence of interface reinforcement in its formulation. Furthermore, it relies on simple, easily defined geometry, which is not typical of the struts that are assumed to form in structural elements. Thus, there is a need to adapt these guidelines so that they are: i) consistent with standard AASHTO LRFD assumptions; and ii) able to predict the capacity of more complex, realistic geometric conditions safely and accurately.

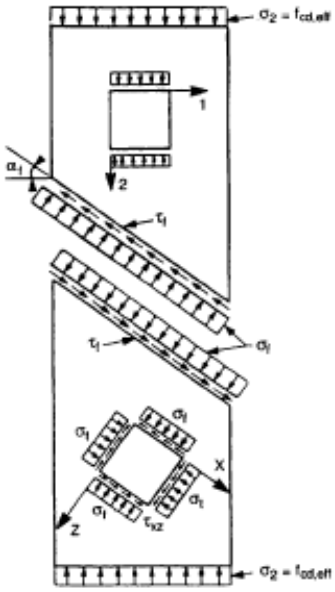

Figure 2-16 Prismatic strut crossing a cold joint (Reprinted from (Fédération Internationale de la Précontrainte (FIP), 1999)

2.3. In-Service Applications of Cold Joints

The Performing Agency has preliminarily identified the following scenarios that may benefit from recommendations made over the course of TxDOT Project 0-7117:

- Staged construction (e.g., Figure 2-17)
- Spliced girder bridges (e.g., Figure 2-18)
- Accelerated bridge construction
- Pier cap retrofit (e.g., Figure 2-19)
- Roadway expansion (e.g., Figure 2-17)

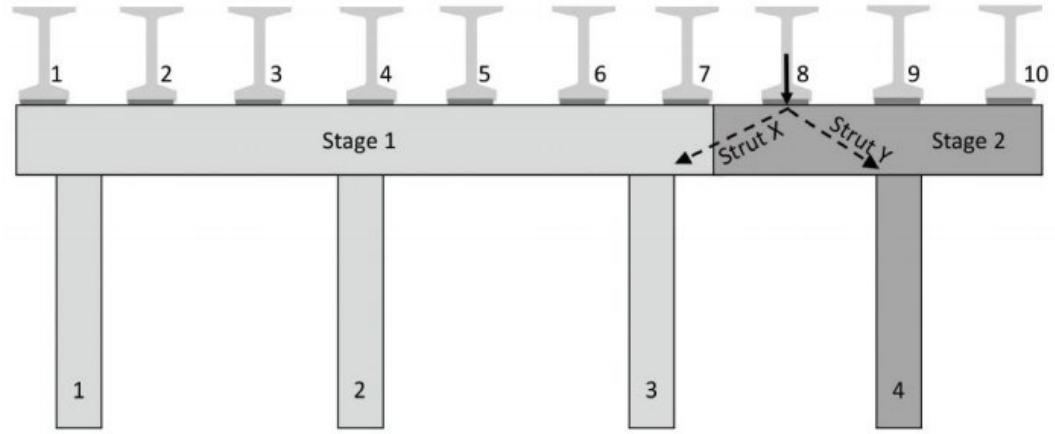

Figure 2-17 Cold joint in multi-column bent cap (Bayrak, 2020)

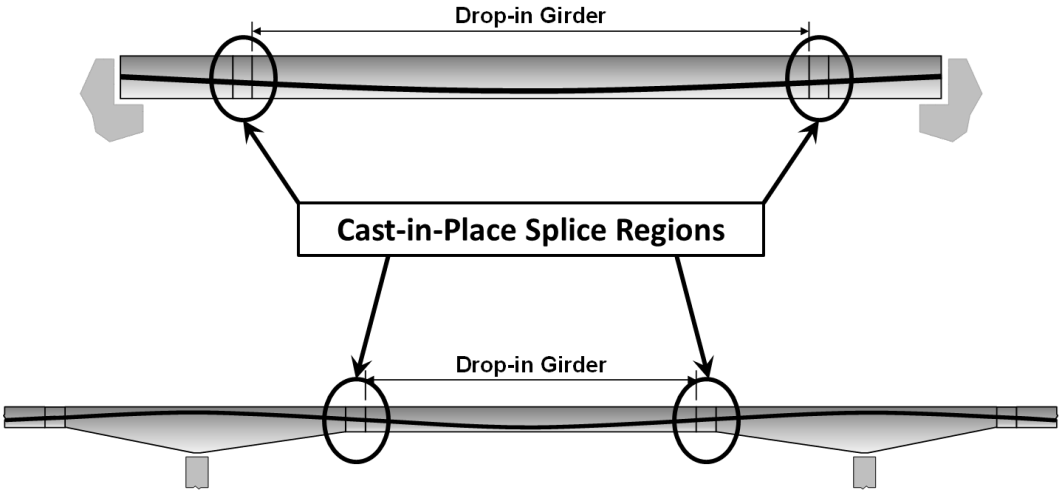

Figure 2-18 Cold joint in spliced girder (Williams et al., 2012)

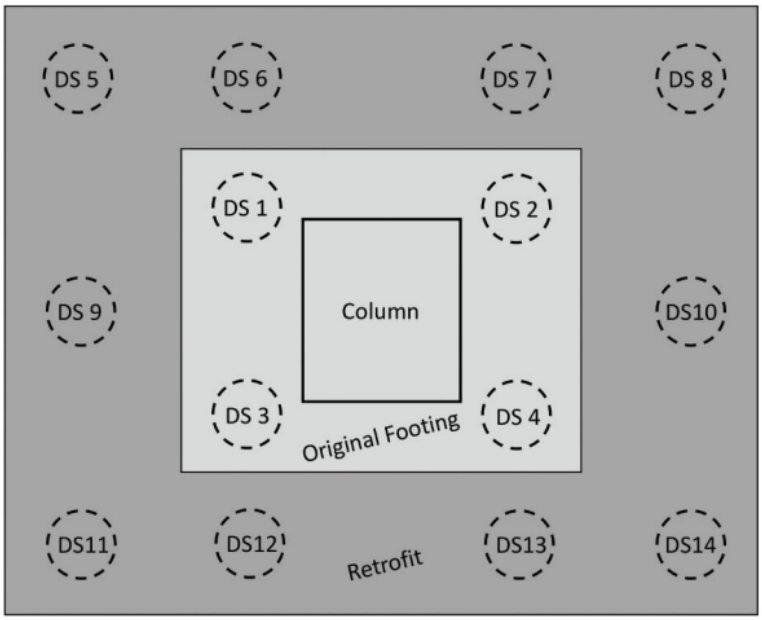

Figure 2-19 Cold joint in retrofitted pier cap (Bayrak, 2020)

2.4. Summary and Key Findings

The key findings from this literature review are summarized below:

- Existing code provisions based on the modified shear-friction theory have been extensively validated. While code-based expressions are generally conservative on average, concerns remain regarding their reliability under certain conditions (Lang, 2011; Soltani & Ross, 2017)

- Slant-shear and push-off tests are widely regarded as the most effective general methods for determining interface shear strength. Alternative methods, such as double-sleeve or composite-beam tests, may provide advantages in specific scenarios and should be considered when developing design recommendations for struts intersecting cold joints.

- Design provisions for struts crossing cold joints are inconsistently addressed in current standards. Both ACI 318-25 (2025) and AASHTO LRFD (2024) require that shear friction checks for struts crossing cold joints, however, only ACI 318-25 (2025) provides explicit guidance. This guidance is based on a sectional approach, which may not fully account for the complex stress state that occurs in a D-region. Alternatively, the FIP (1999) provides uniaxial strength recommendations for prismatic struts crossing a cold joint. These various methods require validation and adaptation, particularly with reference to AASHTO LRFD (2024) to support the development of a holistic update to the AASHTO *LRFD Bridge Design Specifications* and TxDOT *Bridge Design Manual*.

Chapter 3. Industrial Survey

A survey was distributed to Departments of Transportation (DOTs) across the United States to gather information on current practices related to cold joint design. This section presents the results and key conclusions of the distributed survey. The detailed responses are provided in Appendix A.

3.1. Experience with Cold Joints

3.1.1. General Responses

The survey contained a total of 22 responses spanning across the United States, as shown in Figure 3-1 and Table 3-1. In general, most respondents held design engineering positions. More specifically, their experience was on new construction rather than on existing structures (retrofitting). Yet, when asked about their individual involvement with the design of struts crossing cold joints, there was little to no knowledge and sectional analysis or other "good practices" were still the most popular methods for such situations. Notably, there was indication that the implementation of the STM was a recent addition in design practice, therefore; there were minimal occurrences of the use of STM in cold joint scenarios.

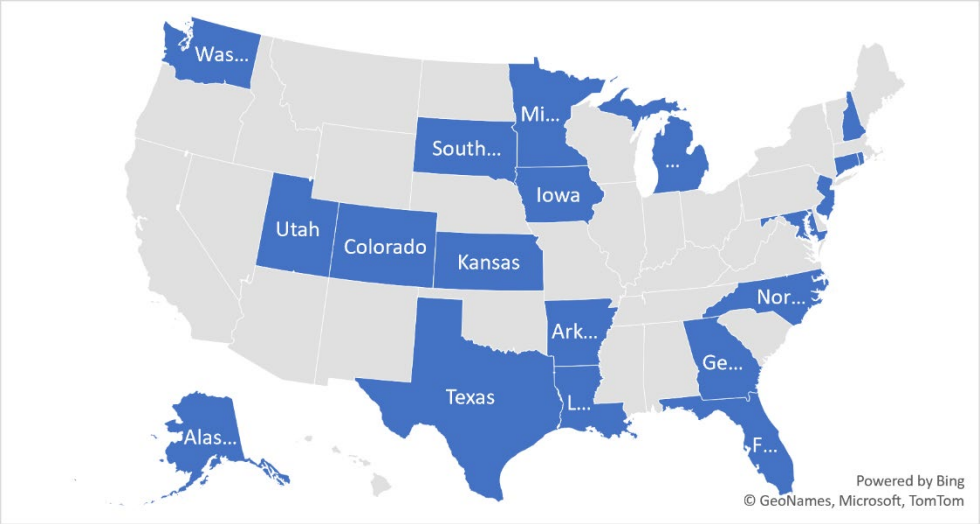

Figure 3-1 Demographic distribution of respondents

Table 3-1 Respondent expertise level

Organization/Unit	Position/Title
Alaska Department of Transportation & Public Facilities/ Bridge	Engineer Technician II
Arkansas Department of Transportation	Staff Engineer
Colorado Department of Transportation/ Bridge Staff	PE II
Connecticut Department of Transportation	Transportation Principal Engineer
Florida Department of Transportation/ Structures Design Office	Structures Design Engineer
Georgia Department of Transportation	State Bridge Engineer
Iowa Department of Transportation/ Bridges and Structures Bureau	Bridge Project Development Engineer
Kansas Department of Transportation	State Bridge Engineer
Louisiana Department of Transportation and Development/ Bridge & Structural Design Section	Assistant Bridge Design Administrator
Maryland State Highway Administration	Transportation Design Engineer
Michigan Department of Transportation	Bridge Design Policy Specialist
Minnesota Department of Transportation	Assistant Bridge Design Manual Engineer
New Hampshire Department of Transportation	Project Engineer
New Jersey Department of Transportation	Supervising Engineer
North Carolina Department of Transportation/ Structures Management Unit	Project Engineer - Policy Development
Rhode Island Department of Transportation/ Bridge Engineering	Chief Civil Engineer
South Dakota Department of Transportation	Bridge Design Engineer
Texas Department of Transportation/ Bridge Division	Transportation Engineer
Utah Department of Transportation/ Structures	Senior Design Engineer
Virginia Department of Transportation	Program Manager Complex Structures and ABC Support
Washington State Department of Transportation	Bridge Design Engineer
West Virginia Department of Transportation	State Bridge Engineer

3.1.2. Responses B- vs. D-Region

To understand the application of the STM in the industry, participants were asked to identify whether cold joints occur more frequently in B- or D-regions. Most agreed that D-regions are the most common location of cold joints. Respondents noted that their respective state DOTs have only adopted the use of STM for a relatively short period of time. At the same time, respondents expressed their avoidance of placing cold joints at highly stressed locations.

3.1.3. Interface Treatment

To accurately replicate the interface condition at the cold joint in the experimental research, respondents were asked to identify all, if any, typical construction practices for interface roughness, as shown in Figure 3-2. Based on the results presented in Figure 3-3, intentional roughening and shear key were the most common methods for interface roughness at a cold joint. However, approximately half of the respondents indicated that the interface was left untreated.

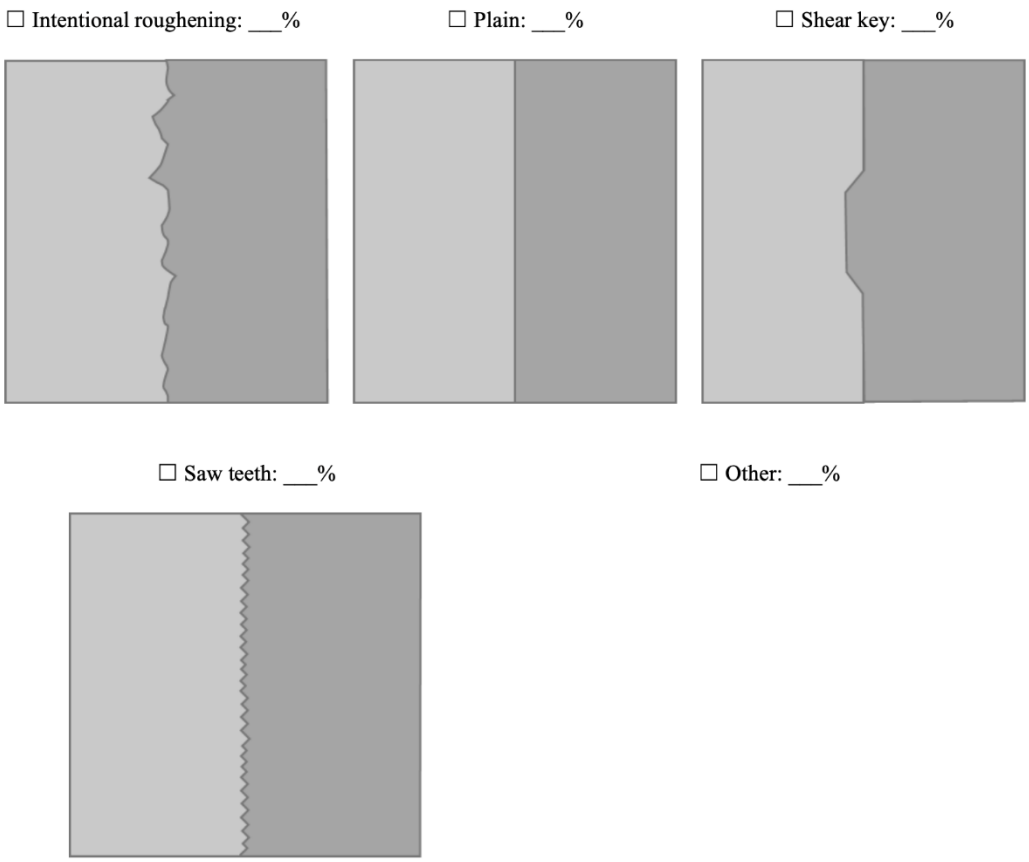

Figure 3-2 Interface roughness methods included in survey

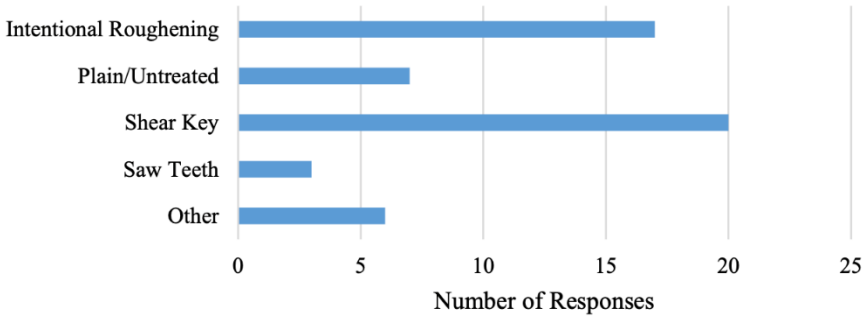

Figure 3-3 Responses on interface roughness at cold joint

Furthermore, those who selected intentional roughening were asked to further elaborate on what specific method was used, such as sandblasting, hydro-blasting, etc. Responses indicated that bush hammering was the most common method for roughening the surface; however, numerous responses associated intentional roughening with shear key applications. Thus, the shear key was the most widely used alternative.

3.1.4. Roughness Inspection

Many standardized practices exist for interface roughness inspection during construction. For the final inspection phase, respondents were asked to select all out of 6 standardized approaches which they have experience implementing for evaluating interface roughness prior to the second cast. Based on the results in Figure 3-4, two-thirds of the responses specified other and described visual inspection, while only a few used standardized practices.

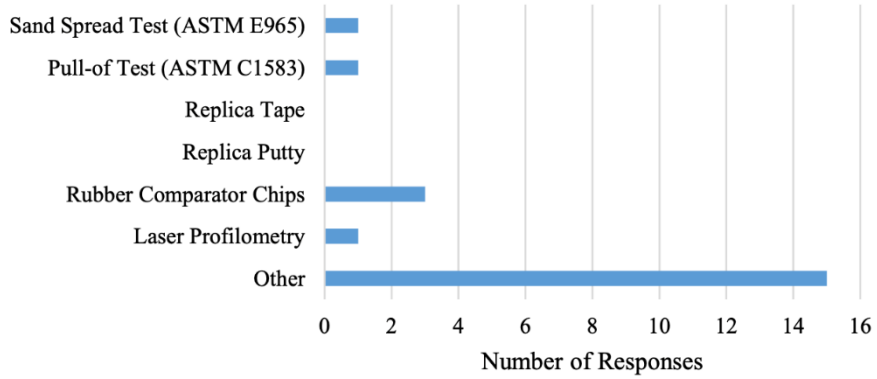

Figure 3-4 Responses on inspection of interface roughness

3.1.5. Interface Reinforcement

One of the objectives of this survey was to identify common design and detailing practices for cold joints. Survey participants were asked to select how reinforcement across the cold joint interface is typically detailed in their respective state, including different detailing illustrated in Figure 3-5. It was found that straight bars, 90-degree hooks, and post-installed anchors are the most common detailing, as shown in Figure 3-6.

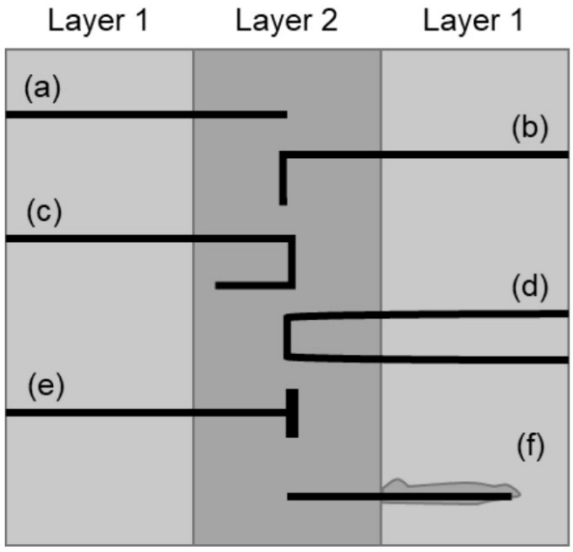

Figure 3-5 Interface shear reinforcement detailing included in survey

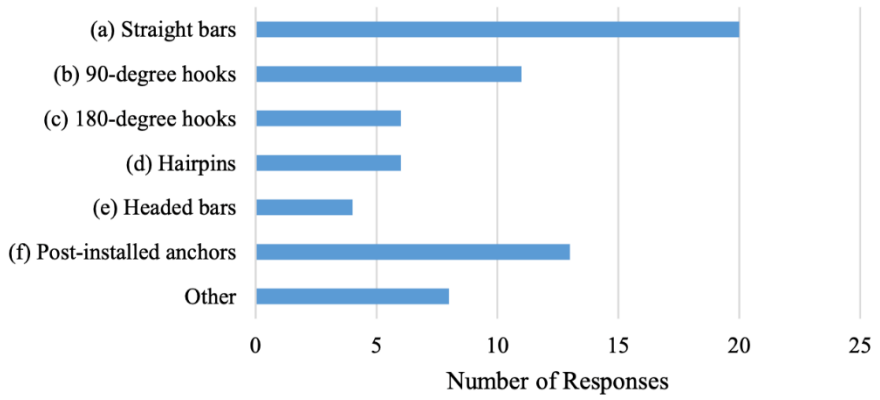

Figure 3-6 Responses on interface shear reinforcement detailing

3.2. Summary and Key Findings

A survey was conducted to identify common design and detailing practices for cold joints. The results of the survey provided beneficial information on interface treatment and its inspection, reinforcement configurations, and constructability. The following presents the key findings of this survey:

1. 95% of respondents had no experience with the design of struts crossing cold joints. However, respondents did express that the STM is a recent addition to design practice, and cold joints are usually evaluated using sectional analysis. The lack of experience in practice warranted investigation and development of method to designing struts across cold joints.

2. Shear key and intentional roughening are typical interface treatments in practice. For the roughening approaches, bush hammering was found to be the most common method for creating interface roughness. More so, standardized methods for roughness inspection are rarely used. Nevertheless, more consistent methods for roughening interfaces should be considered to ensure consistent interface properties.

3. Common reinforcement details for development and the use of post-installed anchors were the most popular among participants. However, these methods do not account for the complex stress distribution in D-regions which may hinder the direct use of the STM in cold joint scenarios.

Chapter 4. Experimental Program: Slant Shear Testing of Cold Joints

This chapter presents the slant shear experimental program designed to investigate the interface shear behavior of cold joints under combined shear and compression. The objective of these tests is to evaluate the influence of key construction variables on the shear strength and failure mechanisms of cold joints. The experimental setup, specimen design, testing protocol, and results are described in detail, providing foundational data to inform the development of subsequent large-scale structural experimental programs and the analytical model introduced in later chapters.

4.1. Test Matrix and Specimen Design

The experimental program consists of 54 small-scale (6×12 in.) and 4 large-scale (12×24 in.) slant shear cylinder specimens, structured into seven distinct series. Each series focused on one of the seven key design parameters: cold joint inclination, interface roughness, variation in concrete compressive strength between layers, casting age difference, aggregate size, interface reinforcement ratio, and interface area. Within each series, slant shear cylinders were further divided into groups varying the variable under investigation. For the small-scale slant shear cylinders, each group contained three specimens of identical design. For the large-scale slant shear cylinders, no duplicate specimens were fabricated for each group. The test matrix is summarized in Table 4-1.

Table 4-1 Slant shear test matrix

Size (in.)	Series	Groups	α (°)	Interface Roughness	Concrete Strength	Casting Age	Agg. Size
6×12	I-Angle	I-40	40	R1	N-N	3 days	A1-A1
		I-45	45	R1	N-N	3 days	A1-A1
		I-50	50	R1	N-N	3 days	A1-A1
		I-60	60	R1	N-N	3 days	A1-A1
	II-Interface Roughness	II-M	-	M	N-N	3 days	A1-A1
		II-NR	40	NR	N-N	3 days	A1-A1
		II-R1	40	R1	N-N	3 days	A1-A1
		II-R2	40	R2	N-N	3 days	A1-A1
	III-Concrete Strength	III-H1	40	R1	N-H1	3 days	A1-A1
		III-H2	40	R1	N-H2	3 days	A1-A1
	IV-Casting Age	IV-1/6	40	R1	N-N	4 hours	A1-A1
		IV-28	40	R1	N-N	28 days	A1-A1
		IV-56	40	R1	N-N	56 days	A1-A1
	V-Aggregate Size	V-A2	40	R1	N-N	3 days	A1-A2
		V-A3	40	R1	N-N	3 days	A1-A3
	VI- Min. Interface Shear Reinforcement	VI-40	40	R1	N-N	3 days	A1-A1
		VI-45	45	R1	N-N	3 days	A1-A1
		VI-60	60	R1	N-N	3 days	A1-A1
12×24	VII- Min. Interface Shear Reinforcement	VII-30-NR	30	NR	N-N	3 days	A1-A1
		VII-30	30	R1	N-N	3 days	A1-A1
		VII-45	45	R1	N-N	3 days	A1-A1
		VII-60	60	R1	N-N	3 days	A1-A1

Note: α = target interface angle measured from the vertical
M = casted monolithically
NR = not intentionally roughened
R1 = intentionally roughened with stripes
R2 = intentionally roughened with gridlines
N = normal strength concrete (f_c'= 2.50 ksi)
H1 = higher strength concrete (f_c'= 3.75 ksi)
H2 = higher strength concrete (f_c'= 2.95 ksi)
A1 = 5/8" river gravel used in mixture
A2 = only fine aggregate used in mixture
A3 = 3/8" crushed concrete used in mixture

4.1.1. Small-Scale Slant Shear Specimen

A total of 54 small-scale slant shear specimens were designed, constructed, and tested in this experimental program. Six intrinsic variables were investigated through six series of 6×12 slant shear cylinders:

1. *Series I* focused on the impact of the cold joint inclination by investigating four different angles measured from the vertical: 40°, 45°, 50°, 60°. The interface angle is proportional to the normal forces transferring across the interface, as shown in Figure 4-1. As per design code expressions (AASHTO, 2024), the normal force acting on the cold joint contribute directly to the frictional force developing along the interface. Accordingly, increase in the normal force is expected to enhance the interface shear resistance of the cold joints.

(a) 40° *(b) 45°* *(c) 50°* *(d) 60°*

Figure 4-1 Cold joint inclination of specimens in Series I

2. *Series II* examined the effect of the interface condition at the cold joint through different interface roughness. One group of specimens had no intentional roughening applied to the substrate (NR), while two other groups were designed to feature different interface conditions to achieve varying roughness levels. The first treatment, denoted as R1, involved the application of unidirectional stripes spaced at 0.5 in. with a depth of 0.125 in. onto the substrate. A more intensive interface roughening, referred to as R2, was accomplished by applying orthogonal gridlines to the substrate with the same spacing and depth as R1. Since intentional roughening of cold joints is encouraged in practice to enhance the interface shear resistance, the R1 treatment was applied to all slant shear specimens in *Series I, III, IV,* and *V* to investigate the effect of each test variable on the behavior of slant shear specimens with intentionally roughened interfaces. The different levels of interface treatment are demonstrated in Figure 4-2. Additionally, to compare the behavior of slant shear specimens to cylinders without cold joints, specimens in Group *M* were cast monolithically to serve as the control specimen in *Series II*.

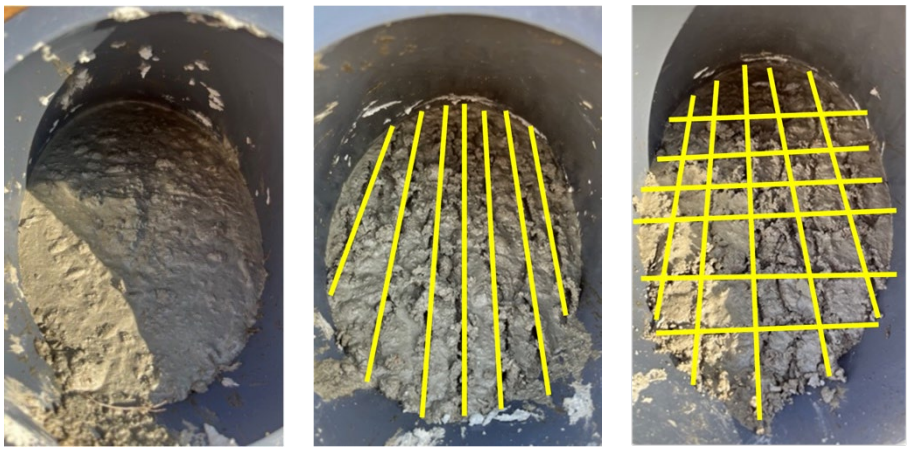

(a) NR *(b) R1* *(c) R2°*

Figure 4-2 Levels of interface roughness

3. The variation in concrete compressive strength between layers was introduced in *Series III*. The control mixture (N) used in this research maintained a water-to-cement ratio of 0.45. The average compressive strength of the control mixture was 2.7 ksi. For the overlay of each group in *Series III*, the water-to-cement ratios were reduced to 0.42 and 0.37, increasing the average compressive strength of the overlays to 3.0 and 3.8 ksi, respectively. The concrete mix designs are shown in Table 4-2 in the following section.

4. Unlike *Series I, II, III,* and *V*, for which the overlay was cast 3 days after the placement of the substrate, *Series IV* consisted of specimens with distinct casting age differences. For specimens in groups *IV-1/6, IV-28* and *IV-56*, the overlay was cast 4 hours, 28 days, and 56 days after the substrate, respectively, to investigate the influence of casting age difference. With 4 hours of casting age difference, *IV-1/6* simulated an unintentional delay during construction phase. This short time difference between the casting of substrate and overlay also allowed the investigation into the minimum time difference required to form a cold joint. The 28 days and 56 days casting age differences were chosen to simulate scenarios representative for various sequences of construction, retrofit, repair or expansion.

5. In *Series V,* two different maximum aggregate sizes were adopted for the concrete mixtures of the overlay (A2 and A3). The general mixture, *N*, used for the substrates contained river gravel with a maximum aggregate size of 5/8 in., denoted as A1. For the overlay, A2 substituted all coarse aggregate with fine aggregate, while A3 incorporated crushed concrete with a maximum diameter of 3/8 in.

6. *Series VI* investigated the influence of interface shear reinforcement across the cold joints, as stipulated in AASHTO LRFD (2024) design code expression. The interface shear reinforcement was designed for three different interface angles (40°, 45°, 60°) according to the minimum reinforcement requirement per AASHTO LRFD (2024), as shown in

Equation (4-1). The specimens were reinforced with #1 threaded bars anchored with threaded fasteners. The reinforcement ratios of Specimens *VI-40, VI-45* and *VI-60* were 0.112%, 0.092% and 0.075% respectively, which were intended to be closely aligned with the minimum reinforcement ratio (0.083%) required for Grade 60 reinforcing bars calculated from Equation (4-1). The design of *Series VI* specimens is illustrated in Figure 4-3.

$$A_{vf} \geq \frac{0.05A_{cv}}{f_y} \tag{4-1}$$

where A_{vf} is the minimum required area of interface shear reinforcement, A_{cv} is the area of concrete interface, and f_y is the nominal yielding strength of the reinforcement.

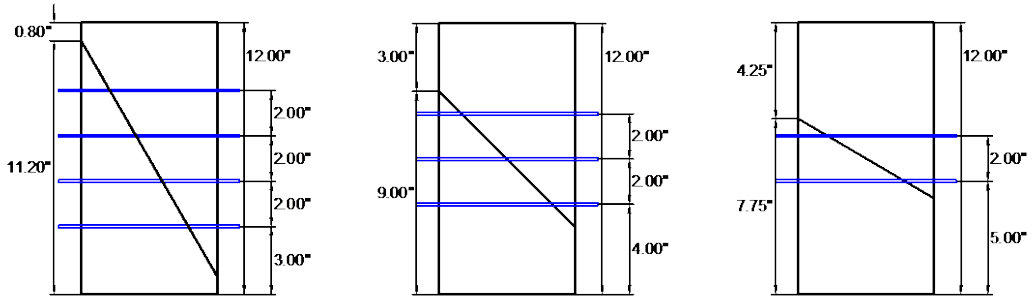

(a) VI-40 (b) VI-45 (c) VI-60

Figure 4-3 Design slant shear specimens in Series VI

4.1.2. Large-Scale Slant Shear Specimen

Series VII investigated the size effect and the influence of reinforcement across the cold joints. Four slant shear specimens, measuring 24 in. in height and 12 in. in diameter, were designed and fabricated in *Series VII.* Specimens *VII-30, VII-45,* and *VII-60* were fabricated with different inclinations of cold joint (30°, 45°, 60°). The cold joints of these three specimens were subjected to *R1* interface roughness, as described in Section 4.1.1. The cold joint of Specimen *VII-30-NR* was designed with an inclination of 30°, and the interface was left untreated prior to the cast of the overlay. All four specimens in *Series VII* were reinforced with #2 threaded bars to satisfy the minimum required area of interface shear reinforcement per AASHTO LRFD (2024) (i.e., Equation (4-1)). The interface reinforcing bars were anchored on the side of the specimens with threaded fasteners. As a result, the reinforcement ratios across the cold joints of Specimens *VII-30, VII-30-NR, VII-45* and *VII-60* were 0.087%, 0.087%, 0.092%, and 0.075%, respectively. The details of specimens in *Series VII* is illustrated in Figure 4-4.

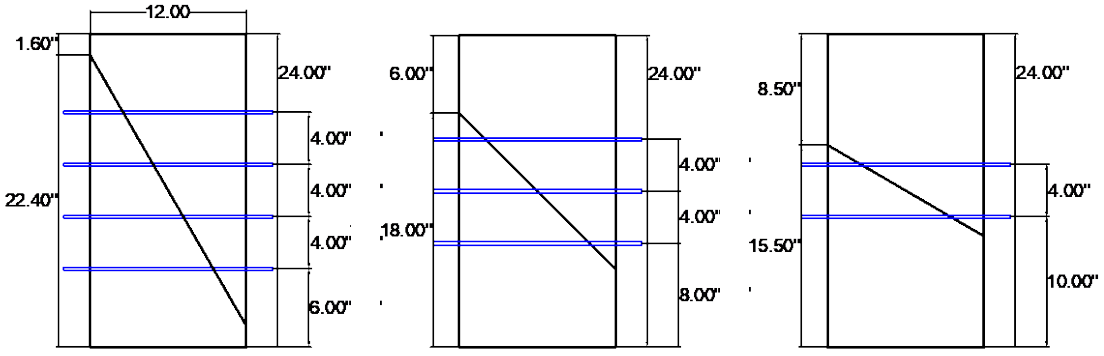

(a) VII-30 & VII-30-NR (b) VII-45 (c) VII-60

Figure 4-4 Design slant shear specimens in Series VII

4.2. Materials

The general mixture, *N*, with a water-to-cement ratio of, was a typical concrete mix design used in TxDOT construction projects, detailed in Table 4-2. To achieve higher strength concrete mixtures (*H1* and *H2*), the water-to-cement ratio was reduced to 0.37 and 0.42 respectively. Due to the low water-to-cement ratio of mixtures *H1* and *H2*, plasticizer was added to improve the workability of concrete during placement.

Table 4-2 Concrete mix designs

Mixture	Cement (lb/yd^3)	Water (lb/yd^3)	Coarse agg. (lb/yd^3)	Fine agg. (lb/yd^3)	w/c
N	611	275	1720	1196	0.45
H1	635	235	1720	1196	0.37
H2	620	260	1720	1196	0.42

Three 6×12-in. (150×300-mm) cylinders and three dog-bone specimens with a 4×4 in. (100×100-mm) cross-sectional area and a total length of 20 in. were fabricated to obtain the material properties of both the substrate and the overlay for each batch of concrete. The compression cylinders were cast using 6×12-in. plastic concrete cylinder molds. The dog-bone specimens were constructed using 4×4×20-in. metal forms with attached anchorages, as shown in Figure 4-5. Standard compression tests were performed on the compression cylinders following ASTM C39/C39M14. The dog-bone specimens were used for direct tensile tests following CRD C16415 procedures. The experimentally determined material properties are summarized in Table 4-3.

Figure 4-5 Metal molds for dog-bone specimens

Table 4-3 Material Properties

Series	Groups	f'_{c_sub} (ksi)	f'_{c_ovr} (ksi)	f'_{t_sub} (psi)	f'_{t_ovr} (psi)
I-Angle	I-40	2.48	2.55	334	332
	I-45				
	I-50				
	I-60				
II-Interface Roughness	II-M	2.58	2.56	325	323
	II-NR				
	II-R1				
	II-R2				
III-Concrete Strength	III-H1	2.50	3.75	325	335
	III-H2		2.95		290
IV-Casting Age	IV-1/6	3.10	3.42	332	267
	IV-28	3.17	4.04		323
	IV-56	2.98	5.08		277
V-Aggregate Size	V-A2	2.24	2.95	277	235
	V-A3	4.36	3.05		-

Note: 1 ksi = 6.8948 MPa, 1psi = 0.0068948 MPa

f'_{c_sub} = concrete compressive strength of substrate

f'_{c_ovr} = concrete compressive strength of overlay

f'_{t_sub} = concrete tensile strength of substrate

f'_{t_ovr} = concrete tensile strength of overlay

4.3. Fabrication Procedure

4.3.1. Small-Scale Slant Shear Specimen

To achieve the specified interface angle for the slant shear specimens, wood stands were designed and constructed to ensure the fabrication accuracy. The wood stands for the small-scale

and the large-scale slant shear specimens at interface angles of 40° and 30° are respectively presented in Figure 4-6(a) and Figure 4-6(b). The schematics of the wood stands are referenced in Appendix B. Also shown in Figure 4-6, 6×12-in. plastic concrete cylinder molds were used to cast the small-scale slant shear specimens, and the large-scale slant shear specimens were cast using 12×24-in. concrete forming Sonotubes.

(a) Wood stand for 6×12-in. cylinders

(b) Wood stand for 12×24-in. cylinder

Figure 4-6 As-built wood stand for slant shear specimens

For the small-scale slant shear specimens, a custom wood gauge was fabricated for each inclination angle to ensure the consistency of the interfacial level, as shown in Figure 4-7. The gauge measures the level of the substrate relative to the top of the cylindrical mold. The cast of the substrate was terminated when the surface of the substrate matched the inclined geometry of the wood gauge. This measurement ensures equal volumes of substrate and overlay, aligning the center of the cold joints to the mid-height of the specimens.

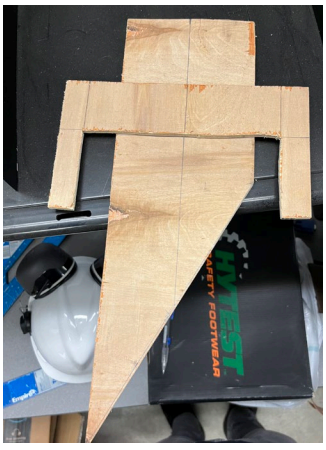

Figure 4-7 Wood gauge for 6×12-in. cylinders (40°)

The casting procedure remained consistent across all six series in the experimental program, as depicted in Figure 4-8. The concrete was mixed using a 9-ft^3 concrete mixer, as shown

in Figure 4-8(a). The uniformly mixed concrete was placed in the cylindrical molds when the molds were attached to the wood stands during the cast for the substrates. The substrates were poured in two separate lifts, each lift was rodded 25 times and tapped 3 times on each side of the cylinders. Once rodded and tamped, the interfacial level and inclination were checked using the wood gauge, as presented in Figure 4-8(b). The surfaces of the substrates were intentionally roughened after initial setting, as shown in Figure 4-8(c). After the cast, a small piece of water-saturated burlap was placed on the surface of the substrate in each cylinder to maintain the curing condition for the substrate before casting the overlay. These pieces of burlap were removed seven days after the cast of the substrates for specimens with casting interval longer than seven days. For the rest of the specimens, the burlap was removed right before the cast of the overlays. All compression cylinders and dog-bone specimens cast along with the substrates were demolded a day after the cast, and cured for seven days by covering the water-saturated burlap over the specimens.

After the designated time intervals, the cylindrical molds were detached from the wood stands and placed vertically for the cast of the overlays. The overlays were also cast in two lifts, each lift was rodded 25 times and tapped 3 times on each side of the cylinders. All specimens, including the slant shear specimens and the material samples, were demolded a day after the cast. These specimens were covered with water-saturated burlaps for seven days to maintain proper curing condition, as shown in Figure 4-8(d).

(a) (b) (c) (d)

Figure 4-8 Casting procedure for small-scale slant shear specimens (a) Concrete mixing (b) Wood gauge fabricating (c) Interface roughening (d) Curing with burlap

Sulfur caps were applied to the top and bottom contact surfaces of the slant shear and the compression specimens according to ASTM C617/C617M (*ASTM International*, 2016). With a nominal strength of 9.0 ksi (62 MPa), the sulfur caps performed adequately during testing without fracture, ensuring a uniform loading condition at the load applying surfaces. The specimens with completed, leveled sulfur caps are shown in Figure 4-9.

(a) (b)

Figure 4-9 Testing preparation for small-scale slant shear specimens (a) Sulfur capping (b) Finished product

4.3.2. Large-Scale Slant Shear Specimens

The casting procedure for the large-scale slant shear specimens followed the same sequence as the small-scale slant shear specimens. The interface roughening was performed after the cast of the substrates without removing the cylinder molds from the wood stands, as shown in Figure 4-10(a). However, slight changes were implemented to improve the construction quality. The concrete was vibrated using an electric concrete vibrator for the substrate and the overlay, as shown in Figure 4-10(b). The wood stands were disassembled so that the overlays of the specimens can be cast vertically, also presented in Figure 4-10(b). The photograph of fabricated specimens in *Series VII* is presented in Figure 4-10(c).

(a) (b) (c)

Figure 4-10 Casting procedure for large-scale slant shear specimens (a) Intentional roughening (b) Concrete vibrating (c) Finished product

12×12-in. steel plates were attached to the top loading surfaces of the specimens with hydro-stone prior to the experiments. Hydro-stone powder was mixed with water until a highly viscous consistency was achieved. The hydro-stone with ideal consistency was immediately applied to the top contact surface of the slant shear specimen, as shown in Figure 4-11(a). The

steel plate was placed and leveled on top of the hydro-stone, creating a flat loading surface with proper orientation, as shown in Figure 4-11(b). After leveling the steel plate, the as-built interface angle was measured using a digital angle gauge, as shown in Figure 4-11(c).

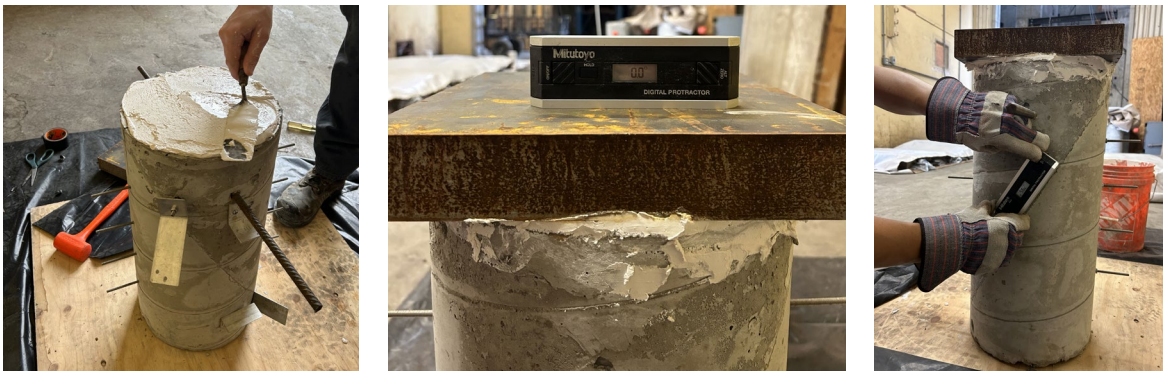

(a) (b) (c)

Figure 4-11 Testing preparation of large-scale specimens (a) Hydro-stone application (b) Leveled steel plate (c)Interface angle measurement

4.4. Test Setup and Instrumentation

4.4.1. Small-Scale Slant Shear Specimen

The small-scale slant shear specimens were tested in the 440-kip MTS load frame, as shown in Figure 4-12(a). A tilt saddle and roller were used at the top and bottom of the slant shear specimen, respectively, to allow for rotation and lateral displacement. The small-scale slant shear test setup is depicted in Figure 4-13(a). The slant shear tests were performed by applying a uniaxial compression load at a constant displacement rate of 0.05 in./min., according to ASTM C882/C882M standards (*ASTM C882/C882M*, 2020). The specimens were tested until 50% decrease in the applied load was observed after reaching peak load. During the experiment, the applied load and the slip along the interface were simultaneously recorded using the MTS and NDI Optical Tracking System (Optotrak), respectively. The Optotrak featured a set of cameras that captured the spatial coordinates of targets, as shown in Figure 4-12(b). To quantify the slip at the interface, six pairs of targets were placed along the cold joint at 1-in. spacing, as illustrated in Figure 4-13(b). For the material tests, the compression cylinders were tested in the Forney High Capacity Compression Machine per ASTM C39/C39M-21 standards (ASTM C39/C39M, 2021)Direct tensile tests were performed on the dog-bone specimen using the 220-kip MTS load frame in accordance with CRD C16415 specifications (*CRD-C164-15*, 1992).

(a) 440-kip MTS *(b) Optotrak*

Figure 4-12 Testing machines for small-scale slant shear test

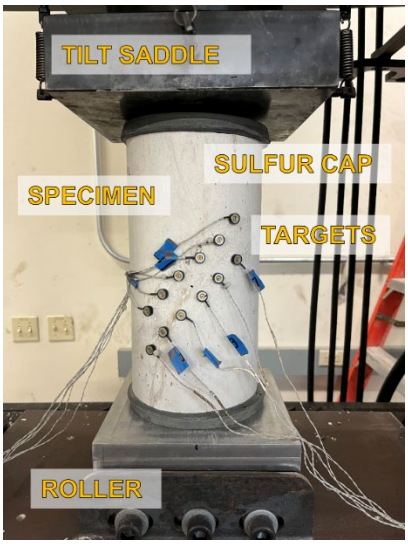

(a) Test setup

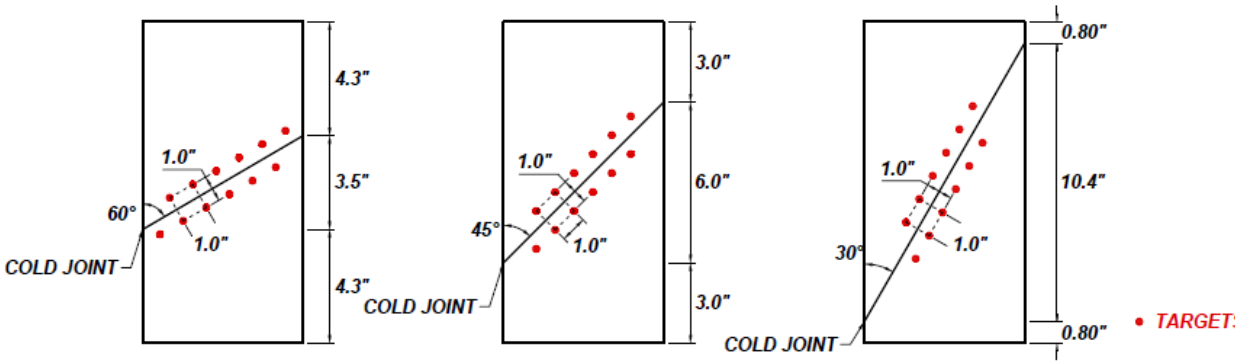

(b) Target arrangement

Figure 4-13 Small-scale slant shear test setup

4.4.2. Large-Scale Slant Shear Specimen

The large-scale slant shear specimens were tested in the 550-kip MTS load frame. The boundary conditions of the large-scale slant shear experiments were identical to that of the small-scale slant shear tests. The large-scale slant shear test setup is shown in Figure 4-14 and Figure 4-15. Similar to the small-scale slant shear test, a compressive load was applied at a displacement-controlled rate of 0.05 in./min until the load reached 50% of the maximum load (*ASTM C882/C882M*, 2020). This protocol enabled the recording of the full load-deflection response of the specimen. The applied load and slip along the interface were simultaneously monitored throughout the test. The arrangement of the LVDTs is presented in Figure 4-15. The LVDTs were attached along the loading direction and installed parallel to the reinforcement bar. In addition, two LVDTs were placed diagonally, in-plane with the cold joint interface to independently monitor the displacement of the substrate and the overlay. The LVDT data was recorded using the High-Precision Keysight data acquisition system (DAQ) at a frequency of 1 Hz. To obtain the entire

strain profile of the specimens and the slip along the interface during the experiments, digital image correlation (DIC) system was instrumented in the experimental program, as shown in Figure 4-14(a). The DIC obtained the strain of the specimen surface by monitoring the displacement of the imprinted speckled patterns in the testing region with two high-speed cameras. A specific set of targets was used to calibrate the DIC system and correlate the coordinates of two cameras. The calibration allows the system to process the images taken during the experiments based on the orientation and the dimension of specimens.

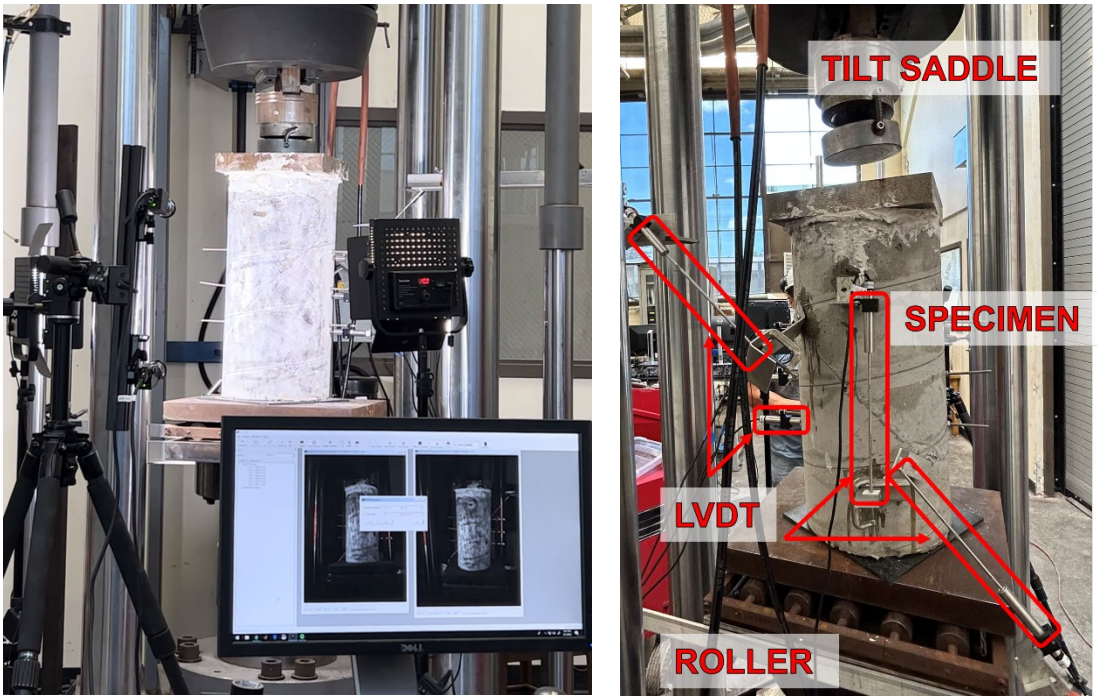

(a) DIC setup (Front View) *(b) LVDT setup (Back View)*

Figure 4-14 Large-scale slant shear test setup

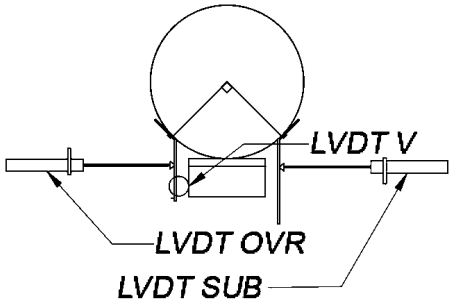

(a) LVDT layout (top view)

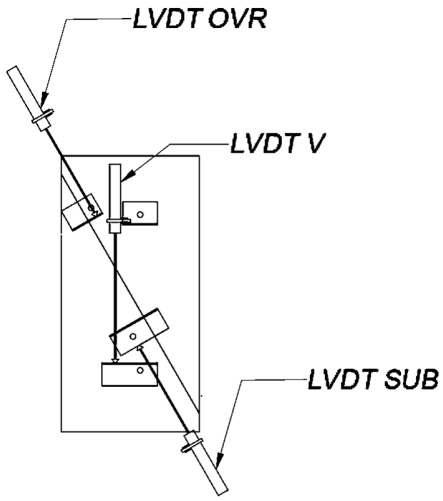

(b) LVDT layout (back view)

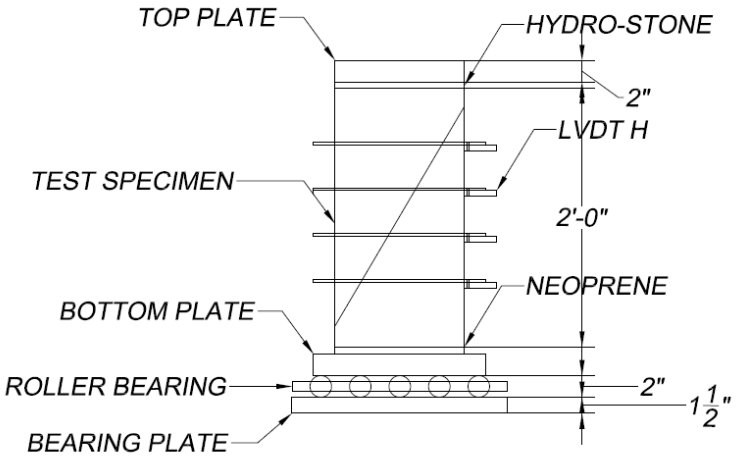

(c) Test setup (front view)

Figure 4-15 LVDT layout

4.5. Experimental Results

4.5.1. Failure Modes

Based on the observed crack pattern and characteristics of fracture, the failure modes of the slant shear specimens were classified into three typical modes:

1. Slant shear failure (SS) – the specimen experienced failure along the cold joint interface, as shown in Figure 4-16(a);
2. Crushing of concrete (CC) – the specimen experienced vertical cracks throughout the cylinder, as shown in Figure 4-16(b);
3. Combination of SS and CC (SC) – the specimen experienced failure at the cold joint with propagated vertical cracks, as shown in Figure 4-16(c).

Table 4-4 lists the number of small-scale slant shear specimens that experienced SS for each group of each series, denoted as n_{SSF}. The failure mode of each large-scale specimen is listed in Table 4-8. Failure mode photos of all the slant shear specimens are referenced in Appendix C.

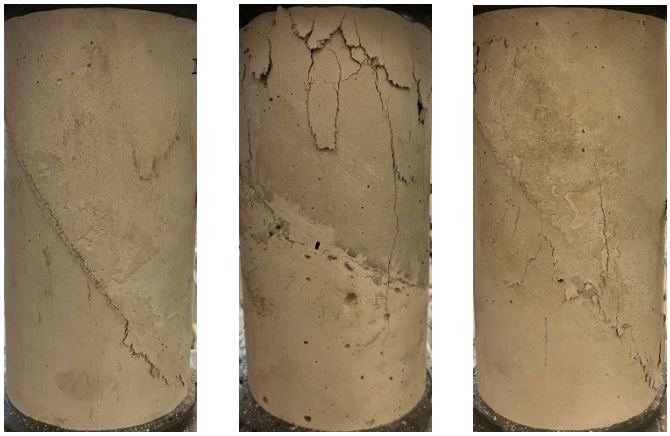

(a) SS (b) CC (c) SC

Figure 4-16 Failure modes for slant shear tests

4.5.2. Data Processing Methodology

The data processing methodology used to characterize the experimentally observed response of the specimens that failed through slant shear is summarized in this section. The shear force-slip plots are provided in Appendix D.

The as-built interface angle was determined by linear regression (least square method) of the target's coordinates for both the substrate and overlay. The average of the two interface angles

was taken as the as-built angle of the cold joint measured from the vertical, denoted as θ_{cj} in Figure 4-17 and presented in Table 4-4. The calculated as-built interface angle was further validated by measuring the interface of specimens that failed through slant shear.

During the slant shear test, the coordinate system of the recorded spatial data of the targets was established with the x-axis (i.e., global x-axis) aligned to the direction of the applied force, P, as illustrated in Figure 4-17. To calculate the slip at the cold joint interface, δ_s, the target coordinates were projected from the global axis to the local axis (i.e., x'-axis parallel to the cold joint interface). For a given target at point (u,v) shown in Figure 4-17(d), the u-value is projected onto the x'- and y'-axes. The same procedure was done for the v-value of the target coordinate. By adding the u- and v-values, a concise matrix (i.e., transformation matrix) can be formulated to project a target coordinate from the global axis to the local axis. The complied transformation matrix is expressed as:

$$\begin{bmatrix} u' \\ v' \end{bmatrix} = \begin{bmatrix} \cos\theta_{cj} & -\sin\theta_{cj} \\ \sin\theta_{cj} & \cos\theta_{cj} \end{bmatrix} \begin{bmatrix} u \\ v \end{bmatrix} \quad (4\text{-}2)$$

where u' and v' are the local coordinate values for a given target. The projection method was performed for each target coordinate of all slant shear specimens.

Based on the target arrangement illustrated in Figure 4-17(a), the five pairs of targets (excluding the outermost target of the overlay and the substrate) were used to capture the slip along the cold joint. More specifically, each pair of targets consisted of one target on the substrate and the other on the overlay, as shown in Figure 4-17(a). Since the cold joint interface is aligned with the x'-axis, the slip can be determined by the displacement of a target relative to its pair in the x'-direction at each time step.

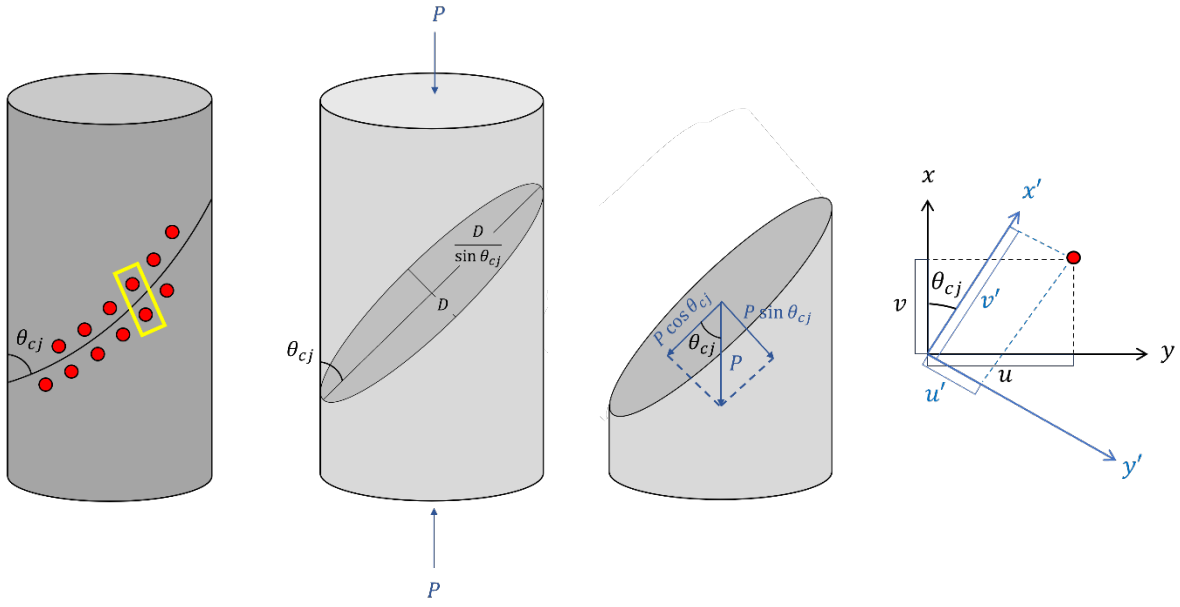

Figure 4-17 Global and local coordinate system

The shear force, V, along the interface is expressed as a function of the applied load, P, and the as-built interface angle, θ_{cj}, as shown in Figure 4-17(c) and (4-3). The average shear capacity, V_{avg}, of specimens governed by slant shear failure for each group is presented in Table 4-4. The shear stress, τ_{test}, at each time step was calculated by dividing the shear force by the area of the elliptical interface, as described in (4-4). Table 4-4 lists the shear stress for slant shear specimens governed by slant shear failure.

$$V = P\cos\theta_{cj} \tag{4-3}$$

$$\tau_{test} = \frac{4Vsin\theta_{cj}}{\pi D^2} \tag{4-4}$$

where D is the diameter of the specimen.

4.5.3. Test Results and Discussion

4.5.3.1. Small-Scale Slant Shear Tests

4.5.3.1.1. Capacity and Failure Modes

Table 4-4 Experimental results for small-scale slant shear tests

Series	Groups	P_{avg} (kips)	θ_{cj} (°)	ρ_{cj} (%)	f'_{c_sub} (ksi)	f'_{c_ovr} (ksi)	n_{SSF}	V_{avg} (kips)	δ_{s_peak} (in. × 10^{-3})	τ_{avg} (ksi)
I-Angle	I-40	78	44	-	2.48	2.55	2	56	1.34	1.35
	I-45	82	48	-			2	53	3.55	1.43
	I-50	76	48	-			0	-	-	-
	I-60	84	67	-			0	-	-	-
II-Interface Roughness	II-M	73	-	-	2.58	2.56	0	-	-	-
	II-NR	51	40	-			3	39	3.27	0.89
	II-R1	71	43	-			3	52	4.33	1.25
	II-R2	72	43	-			2	53	1.71	1.23
III-Concrete Strength	III-H1	86	44	-	2.50	3.75	0	-	-	-
	III-H2	83	43	-		2.95	1	59	0.17	1.41
IV-Casting Age	IV-1/6	110	39	-	3.10	3.42	0	-	-	-
	IV-28	92	40	-	3.17	4.04	3	70	1.09	1.60
	IV-56	129	39	-	2.98	5.08	2	105	3.20	2.37
V-Aggregate Size	V-A2	44	39	-	2.24	2.95	3	32	3.93	1.23
	V-A3	71	43	-	4.36	3.05	2	55	1.75	0.78
VI- Min. Interface Shear Reinforcement	VI-40	98	38	0.11	2.62	4.04	2	71	2.55	1.68
	VI-45	104	46	0.09			0	-	-	-
	VI-60	94	59	0.07	4.36	3.34	3	65	7.27	1.65

Note: P_{avg} = average capacity of three slant shear specimens in the same group
θ_{cj} = as-built angle of the cold joint measured from the vertical
ρ_{cj} = as-built reinforcement ratio of the cold joint
f'_{c_sub} = concrete compressive strength of substrate
f'_{c_ovr} = concrete compressive strength of overlay
n_{SSF} = number of specimens that experienced SS out of three slant shear tests
V_{avg} = average shear capacity of specimens governed by SS
$\delta_{s_{peak}}$ = average slip of cold joints corresponding to peak strength for specimens governed by SS
τ_{avg} = average shear stress of specimen governed by SS

The experimental results for the small-scale slant shear tests are summarized in Table 4-4. The interface shear resistance is determined only for specimens governed by slant shear failure. A comprehensive analysis of the test results is given for each series:

1. In *Series I*, the specimens displayed similar maximum applied loads, P_{avg}, across all interface angles. The test results reveal that the variation of interface angle (with *R1* interface roughness) has negligible effect on the maximum applied compression load. However, a shift in failure mode from slant shear failure to concrete crushing was noticeable with the increase of the interface angles.

2. In *Series II*, the maximum applied loads of the control specimen (*II-M*) and those with roughened interfaces (*II-R1* and *II-R2*) are similar. However, *II-NR* exhibited a 28% reduction in capacity. The test results indicate that interface roughness significantly influences the maximum applied load and the interface shear resistance. It is worth noting that, despite the additional grid treatment applied to *II-R2*, the capacity remained similar to *II-R1* (i.e., the roughness pattern did not influence the specimen's strength). As a result, it is concluded that the influence of interface amplitude is more significant than interface texture. These conclusions are consistent with findings from previous research (Figueiredo et al., 2022; Saldanha et al., 2013; Santos & Júlio, 2011).

3. The variation in concrete compressive strength between layers was found to have a negligible influence on the response of the slant shear specimens. Despite the 10% and 40% increase of compressive strength of the substrate, *III-H1* and *III-H2* had similar ultimate capacities. The failure mode observed in *Series III* specimens was a combination of slant shear failure and crushing of concrete. This outcome resulted from the sufficient shear resistance provided by cold joints with appropriate interface roughening, leading to the crushing of weaker layers prior to the slant shear failure of cold joints. These conclusions are consistent with findings from previous research (Figueiredo et al., 2022; Hofbeck et al., 1969; Patnaik, 1999).

4. In *Series IV*, the test results indicate that the casting age difference influences both the maximum applied load and the failure mode of the specimens. The interface shear resistance of specimens with longer casting age difference (*IV-56*) was 15% greater than that of *IV-28*. This phenomenon was also observed in previous experimental and analytical studies (Santos & Júlio, 2011). The specimens with a casting age difference of four hours (*IV-1/6*) exhibited crushing of concrete, closely resembling the behavior of monolithically cast cylinders (*II-M*) rather than typical slant shear specimens. This conclusion highlight the minimum casting age difference necessary to classify the interface between layers as a cold joint.

5. The test results from *Series V* demonstrate a significant effect of aggregate size on shear resistance. As the aggregate size decreased, the interface shear resistance decreased, accordingly. Even with intentional interface roughening, specimens without coarse aggregate in *V-A2* exhibited a 44% decrease in maximum applied load compared to specimens in *I-40*, while the maximum applied load of specimens with smaller maximum aggregate size in *V-A3* remained similar.

6. In *Series VI*, the presence of interface shear reinforcement was observed to increase the interface shear capacity. More than 15% increase in capacity was observed for specimens in *Series VI* compared to those without reinforcement in *Series I*. This indicates that the interface shear reinforcement effectively contributes to the cold joint resistance when the cold joint is subject to a combination of shear and compression force.

4.5.3.1.2. Interface Shear Resistance

The interface shear resistance was determined for the specimens that experienced slant shear failure, as defined in (4-4). The test results were compared to the nominal interface shear resistance of five current design code expressions: AASHTO LRFD *Bridge Design Specifications* (AASHTO, 2024), ACI 318-25 *Building Code Requirements for Structural Concrete* (ACI Committee 318, 2025), the Canadian Standard Association's *Design of Concrete Structures* (CSA Standard A23.3-19, 2019), *fib Model Code for Concrete Structures* (fib International, 2024), and the *Design of Concrete Structures – Part 1-1: General Rules for Buildings* (European Committee for Standardization, 2005), as expressed in Table 4-5. The experimental results and design code estimations are listed and plotted in Table 4-6 and Figure 4-18, respectively.

Table 4-5 Design code provisions for shear friction

Design code	Surface roughness	c (ksi)	μ	Design Expression
AASHTO LRFD 2024	not roughened	0.075	0.6	$\tau_n = c + \mu(\rho f_y + \sigma_n)$
	roughened	0.24	1.0	
ACI 318-25	not roughened	N/A	0.6λ	$\tau_n = \mu(\rho f_y sin\alpha + \sigma_n) + \rho f_y cos\alpha$
	roughened	N/A	1.0λ	
CSA A23.3:19	not roughened	0.036	0.6	$\tau_n = \lambda[c + \mu(\rho f_y sin\alpha + \sigma_n)] + \rho f_y cos\alpha$
	roughened	0.073	1.0	

Design code	Surface roughness	c_a	μ	Design Expression
fib MC2020	smooth	0.35	0.6	$\tau_n = c_a f_{ctd} + \mu(\rho f_y sin\alpha + \sigma_n) + \rho f_y cos\alpha$
	rough	0.45	0.7	
	very rough	0.5	0.9	
Eurocode 2	smooth	0.2	0.6	$\tau_n = c_a f_{ctd} + \mu(\rho f_y sin\alpha + \sigma_n) + \rho f_y cos\alpha$
	rough	0.4	0.7	

Note: 1 ksi = 6.8948 MPa

τ_n = nominal interface shear resistance (ksi)
c = cohesion factor of concrete-to-concrete interface (ksi)
μ = coefficient of friction
c_a = unitless cohesion factor of concrete-to-concrete interface
ρ = reinforcement ratio of the reinforcing steel crossing the interface
f_y = yielding strength of reinforcing steel (ksi)
σ_n = normal stress acting on the interface (ksi)
α = inclination of the reinforcement crossing the interface
λ = concrete density modification factor
f_{ctd} = design axial tensile strength of concrete of the weaker layer (ksi)

According to AASHTO LRFD (2024), ACI 318-25 (2025), and CSA A23.3:19 (2019), the slant shear specimens with roughening amplitude of (0.125 in.) in this experimental program is classified as untreated smooth interfaces. Thus, the coefficients for not roughened interface listed in Table 4-5 were used to calculate the interface shear resistances for roughened cold joints in this research. The calculated shear resistances are on average, 40% lower compared to the experimental results, as shown in Figure 4-18(a), (b), and (c). The root mean squared error (RMSE), and coefficient of determination (R^2) listed in Table 4-6 were used as statistical parameters to determine the accuracy of the calculated interface shear resistance, computed as shown in Equation (4-5) and (4-6). The R-square value of interface shear resistance calculated from AASHTO LRFD (2024), ACI 318-25 (2025), and CSA A23.3:19 (2019) is 0.84, 0.80, and 0.82, respectively.

$$\text{RMSE} = \sqrt{\frac{\sum_{i=1}^{n}(Y_{pred} - Y_{ref})^2}{n}} \tag{4-5}$$

$$R^2 = 1 - \frac{\sum_{i=1}^{n}(Y_{pred} - Y_{ref})^2}{\sum_{i=1}^{n}(Y_{ref})^2} \tag{4-6}$$

In contrast, *fib* MC2020 (2024) and Eurocode 2 (2005) require a smaller amplitude of interface roughness to consider the influence of intentional roughening. Eurocode 2 (2005) classifies *R1* and *R2* interface conditions as roughened interfaces. The *fib* MC2020 (2024) considers *R1* and *R2* a rough and very rough interface, respectively., based on the roughening patterns achieved. As such, the calculated interface shear resistances using Eurocode 2 (2005) and *fib* MC2020 (2024), shown in Figure 4-18(d) and (e), demonstrated a better alignment with the experimental results, specifically with an R-square value of 0.90 and 0.91, respectively.

Overly conservative results are obtained when the intentionally roughened interface is considered an untreated interface due to insufficient amplitude according to the code expressions in AAHTO LRFD (2024), ACI 318-25 (2025), and CSA A23.3:19 (2019). Therefore, the interface shear resistance of the specimens was recalculated by assuming the cold joints as roughened interfaces, referred to as RI (Rough Interface Assumption) approach. This approach directly utilized the coefficients for roughened interface in Table 4-5 to calculated the capacities of intentionally roughened specimens in this research. The calculated shear resistance using the RI approach are summarized in Table 4-6 and shown in Figure 4-18(a), (b), and (c). Although the R-square value was improved to 0.96, 0.96 and 0.97, respectively, by the intentionally roughened interface factors in AAHTO LRFD (2024), ACI 318-25 (2025), and CSA A23.3:19 (2019), the number of unconservative cases observed in RI approach indicated a need for refinement.

Since the shear resistance of the cold joints is underestimated by current design expressions and overestimated by the previously introduced RI approach in AASHTO LRFD (2024), ACI 318-25 (2025), and CSA A23.3:19 (2019), a modified approach is proposed to obtain the coefficients of cohesion and friction. To better represent the shear resistance of cold joints with intermediary

levels of interface roughness, linear interpolation was employed to derive the cohesion and friction coefficient based on the amplitude of the interface roughness, denoted as LIF (Linearly Interpolated Factors). Coefficients of cohesion and friction obtained from current specifications and the LIF approach are demonstrated in Figure 4-19. The calculated results are listed and plotted in Table 4-6 and Figure 4-18(a), (b), and (c), respectively.

The interface shear resistance of the specimens is better predicted with the LIF method compared to current design expressions. The R-square value of interface shear resistance calculated from applying LIF to AASHTO LRFD (2024), ACI 318-25 (2025), and CSA A23.3:19 (2019) was improved to 0.96, 0.92 and 0.93, respectively. This indicates that intentional interface roughening should be considered even if the amplitude is smaller than the required height specified in these three design specifications to accurately calculate the shear resistance of cold joints. Also, the total unconservative counts observed using the LIF approach decreased from 24 cases to 3 cases compared to the RI approach.

Table 4-6 Experimental results and design code estimations for interface shear resistance of small-scale slant shear specimens

Specimen	τ_{test}	Current Code Expression					RI			LIF		
		τ_{AASHTO}	τ_{ACI}	τ_{CSA}	τ_{Euro}	τ_{fib}	τ_{AASHTO}	τ_{ACI}	τ_{CSA}	τ_{AASHTO}	τ_{ACI}	τ_{CSA}
I-40-1	1.27	1.38	1.14	1.21	0.88	0.87	0.76	0.68	0.72	1.07	0.91	0.96
I-40-3	1.43	1.66	1.42	1.50	1.08	1.07	0.93	0.85	0.89	1.30	1.14	1.19
I-45-1	1.43	2.03	1.79	1.87	1.34	1.33	1.15	1.08	1.11	1.59	1.43	1.49
I-45-2	1.43	1.78	1.54	1.61	1.16	1.15	1.00	0.92	0.96	1.39	1.23	1.29
II-R1-1	1.23	1.33	1.09	1.16	0.85	0.84	0.73	0.65	0.69	1.03	0.87	0.92
II-R1-2	1.22	1.38	1.14	1.21	0.89	0.88	0.76	0.68	0.72	1.07	0.91	0.97
II-R1-3	1.31	1.46	1.22	1.29	0.94	0.93	0.81	0.73	0.77	1.13	0.97	1.03
II-R2-1	1.29	1.26	1.02	1.09	1.01	0.79	0.69	0.61	0.65	0.97	0.81	0.87
II-R2-3	1.17	1.43	1.19	1.27	1.17	0.91	0.79	0.72	0.75	1.11	0.95	1.01
II-NR-1	0.95	0.58	0.51	0.54	0.58	0.55	0.58	0.51	0.54	0.58	0.51	0.54
II-NR-2	0.78	0.47	0.39	0.43	0.46	0.43	0.47	0.39	0.43	0.47	0.39	0.43
II-NR-3	0.94	0.52	0.45	0.48	0.51	0.48	0.52	0.45	0.48	0.52	0.45	0.48
III-H2-3	1.41	1.52	1.28	1.36	0.98	0.98	0.85	0.77	0.81	1.18	1.03	1.08
IV-28-1	1.62	1.63	1.39	1.46	1.08	1.07	0.91	0.83	0.87	1.27	1.11	1.16
IV-28-2	1.70	1.73	1.49	1.57	1.16	1.15	0.97	0.90	0.93	1.35	1.20	1.25
IV-28-3	1.47	1.41	1.17	1.24	0.93	0.92	0.78	0.70	0.74	1.09	0.93	0.99
IV-56-1	2.34	2.14	1.90	1.98	1.44	1.43	1.22	1.14	1.18	1.68	1.52	1.58
IV-56-2	2.40	2.24	2.00	2.07	1.50	1.49	1.27	1.20	1.23	1.76	1.60	1.65
V-A2-1	1.23	1.15	0.91	0.98	0.71	0.70	0.62	0.54	0.58	0.88	0.72	0.78
V-A2-2	1.21	1.29	1.05	1.12	0.81	0.80	0.70	0.63	0.67	1.00	0.84	0.89
V-A2-3	1.24	1.28	1.04	1.12	0.81	0.80	0.70	0.63	0.66	0.99	0.83	0.89
V-A3-2	0.70	0.89	0.65	0.61	0.56	0.55	0.46	0.29	0.36	0.67	0.39	0.49
V-A3-3	0.85	1.04	0.80	0.74	0.67	0.66	0.55	0.36	0.44	0.80	0.48	0.59
VI-40-1	1.68	1.51	1.29	1.36	1.00	0.99	0.84	0.78	0.82	1.17	1.04	1.09
VI-40-2	1.68	2.44	2.22	2.30	1.66	1.65	1.40	1.35	1.39	1.92	1.79	1.84
VI-45-1	1.66	2.11	1.89	1.96	1.43	1.42	1.19	1.15	1.19	1.65	1.52	1.57
VI-45-2	1.59	1.80	1.58	1.65	1.21	1.20	1.01	0.96	1.00	1.40	1.27	1.32
VI-45-3	1.71	2.20	1.98	2.05	1.49	1.48	1.25	1.20	1.24	1.72	1.59	1.65
RMSE	-	0.58	0.64	0.61	0.45	0.43	0.29	0.28	0.26	0.30	0.42	0.37
R^2	-	0.84	0.80	0.82	0.90	0.91	0.96	0.96	0.97	0.96	0.92	0.93

Note: τ_{test} = interface shear resistance obtained from the slant shear test (ksi)
τ_{AASHTO} = nominal interface shear resistance calculated from AASHTO LRFD 2024 (ksi)
τ_{ACI} = nominal interface shear resistance calculated from ACI 318-25 (ksi)
τ_{CSA} = nominal interface shear resistance calculated form CSA A23.3:19 (ksi)
τ_{Euro} = nominal interface shear resistance calculated from Eurocode 2 (ksi)
τ_{fib} = nominal interface shear resistance calculated from *fib* MC2020 (ksi)

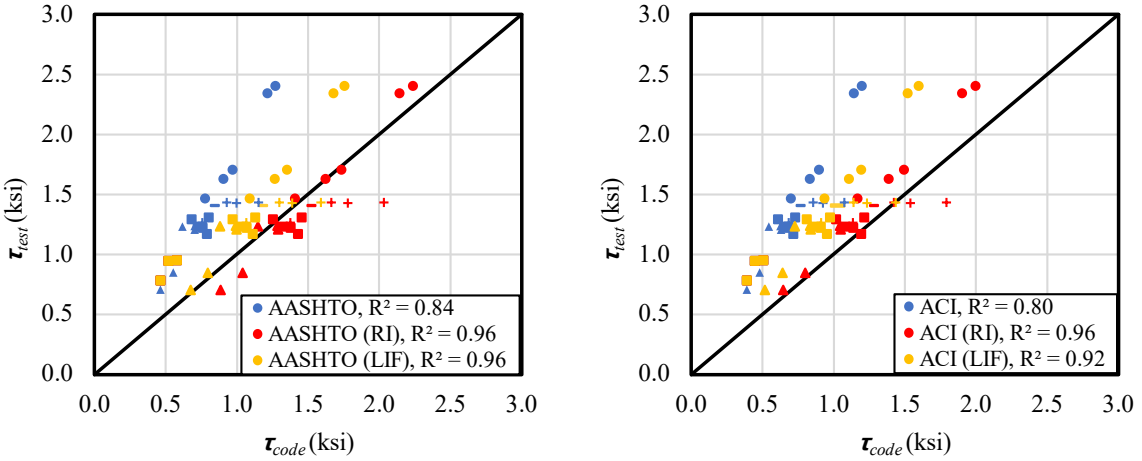

(a) AASHTO LRFD 2024

(b) ACI 318-25

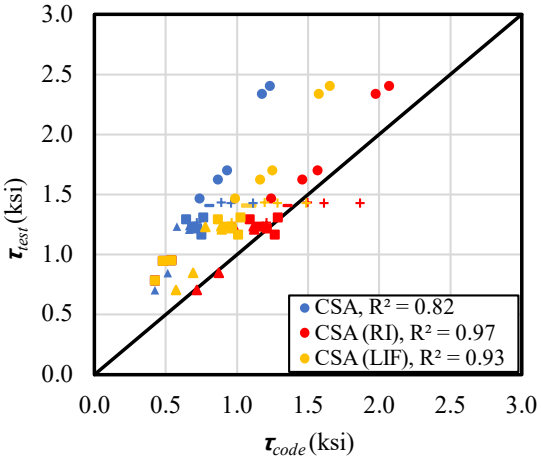

(c) CSA A23.3:19

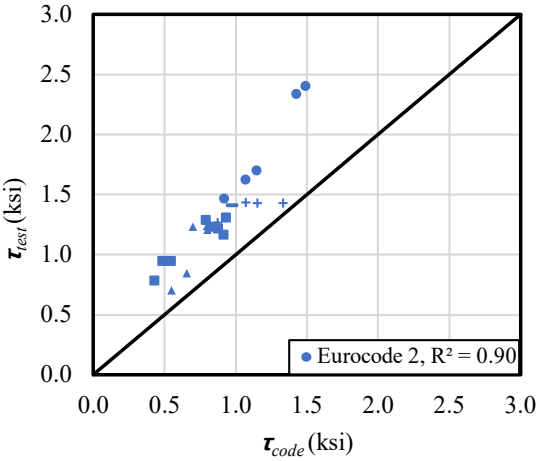

(d) Eurocode 2

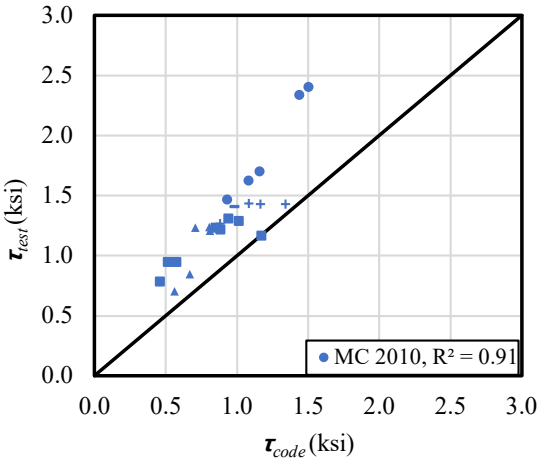

(e) *fib* MC 2020

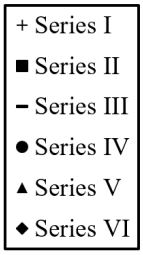

Figure 4-18 Experimental results versus calculated interface shear resistance

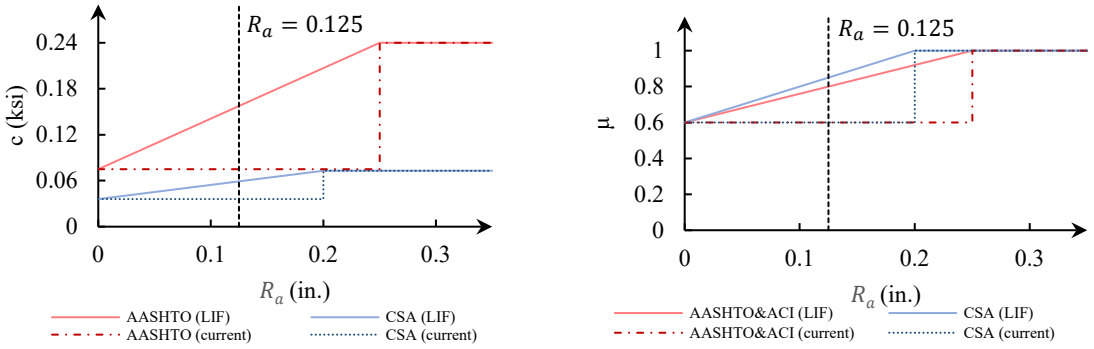

Figure 4-19 Linear interpolation of (a) Cohesion and (b) Friction factors

4.5.3.1.3. Database Analysis

To further validate the proposed LIF method, a database was constructed to include relevant studies that used slant shear tests and reported the following experimental data: roughness amplitude, cold joint inclination, and failure mode. The database covered common roughening methods and amplitudes; therefore, the applicability of the LIF approach could be well-justified in common scenarios. The range of variables and properties of specimens are listed in Table 4-7, while Appendix E includes the experimental results of the database. The normal stress and shear stress acting on the interface at peak load were computed according to the reported variables and test measurements.

Figueiredo et al. (2022) conducted 75 slant shear tests to study the bond performance between normal-weight and sand-lightweight concrete. Five types of interface roughening were applied to the specimens: smooth, vibrated, and three intentionally roughened methods. A laser-based displacement sensor was used to accurately measure the amplitude of roughness.

Santos & Julio (2011) performed 150 prismatic slant shear tests to investigate interface roughness and casting age difference. The interface shear stress for prismatic specimens was computed by considering the area of the cold joint as rectangular instead of elliptical. Different methods of interface preparation were applied to the substrate which include wire-brushing, sandblasting, shotblasting, and hand-scrubbing. The roughness profile of the substrate was quantified using a laser roughness analyzer.

Diab et al. (2017) tested cylindrical and prismatic slant shear specimens to investigate the interface behavior between self-compacting concrete and old conventional concrete. Four types of interface roughness were applied to the specimens: hand brush, mechanical roughness, 0.12 in. depth × 0.12 in. width groves, and 0.24 in. depth × 0.24 in. width groves.

Saldanha et al. (2013) proposed a modified slant shear test approach on prismatic, reinforced concrete specimens. Traditional slant shear tests were conducted to validate the proposed method. Two interface roughening approaches were applied to both types of slant shear

specimens, including hand-scrubbed interface and wavy interface. The test results of 12 slant shear experiments and the roughness profile measured by laser sensor were reported by this research.

Hu et al. (2020) conducted 24 traditional slant shear tests along with 72 dynamic slant shear tests. Rectangular indentions with two different depths were applied to the interface to quantify the surface roughness. The amplitude of interface roughening was 0.12 and 0.24 in. Additionally, the specimens were designed with two cold joint inclinations, 30° and 40°, measured from vertical to investigate the interfacial behavior.

Force components used to determine shear and normal stress acting on the cold joint could be clearly identified only when specimens were governed by the slant shear failure. Since the validation was conducted by comparing the shear capacity estimated by the LIF approach and the experimental results, only experiments governed by slant shear failure are included in the validation study. As a result, a total of 124 slant shear test results were included to validate the LIF approach.

Table 4-7 Database investigation of slant shear tests

Source	**N**	**D** (in.)	Geometry	$\boldsymbol{\theta_{cj}}$ (°)	$\boldsymbol{R_a}$ (in.)	Roughening Approach
Figueiredo et al.	75	5.51	cylindrical	30	0.034 – 0.22	hand-scrubbing; vibrating
Santos & Júlio	150	5.91	prismatic	30	0.01 – 0.048	wire-brushing; sandblasting; shotblasting; hand-scrubbing
Diab et al.	150	5.91	cylindrical, prismatic	30	0.12, 0.24	patterned groves
Saldanha et al.	12	5.91	prismatic	30	0.197, 0.59	hand-scrubbing; patterned groves
Hu et al.	96	2.77	cylindrical	30, 40	0.12, 024	patterned groves

Note: 1 in. = 25.4 mm

N = number of slant shear tests

D = diameter of the cylindrical specimen, or side length of the prismatic specimen

θ_{cj} = inclination of the cold joint measured from the vertical

R_a = amplitude of roughness

Test results from the database investigation are used to validate the LIF approach based on shear friction expressions in AASHTO LRFD (2024), ACI 318-25 (2025), and CSA A23.3:19 (2019). The validation was performed by comparing cold joint shear resistance from the database and interface shear resistance calculated using the LIF approach. The validation exclusively focuses on roughened interfaces with intermediary levels of amplitude to which the LIF approach is applicable. The test results of the slant shear database and experimental program in this research

presented in Figure 4-20, along with the calculations from current design specifications and the LIF approach.

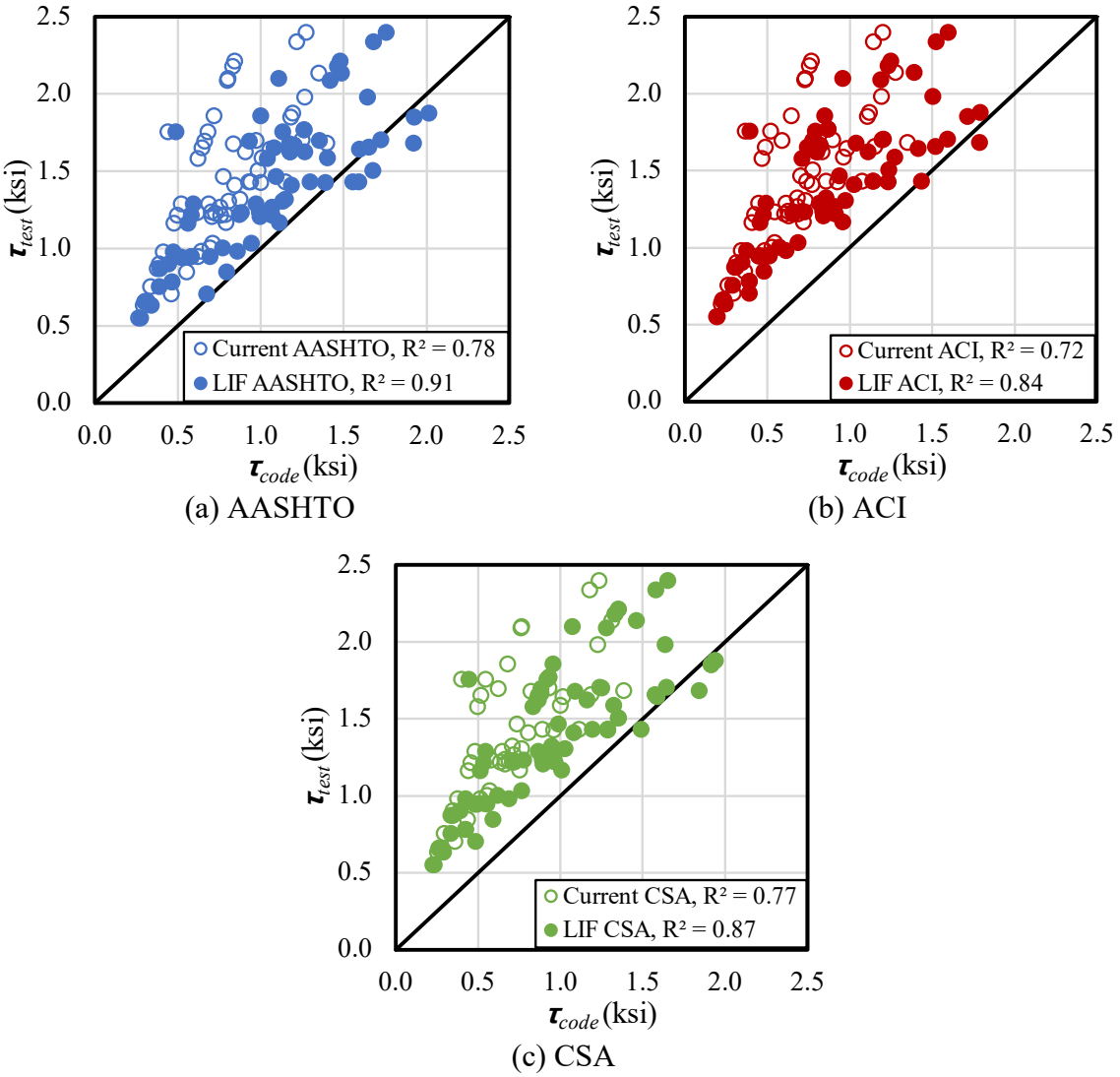

Figure 4-20 Experimental versus calculated interface shear resistance using the current code expressions and the proposed LIF approach

Based on the validation results, it is evident that the LIF approach improves the accuracy of shear friction expressions. The R-square value of interface shear resistance calculated from applying LIF to AASHTO LRFD (2024), ACI 318-25 (2025), and CSA A23.3:19 (2019) was improved from 0.78, 0.72 and 0.77 to 0.91, 0.84 and 0.87, respectively.

The LIF approach appears to be more impactful under higher normal and shear stress. According to the conclusion from the experimental program, the shear resistance of cold joints with intentional roughening is expected to be higher than non-roughened interface. The shear

resistance for cases reaching high peak normal and shear stress is proven to be sensitive to the contribution of interface roughness, even when the amplitude of roughness is lower than the requirement of specifications. The LIF approach improves the accuracy of calculation by directly reflecting the effect of roughening amplitude, while current design expressions fail to address the contribution of intermediary interface roughness. This implies that the LIF approach can lead to substantial improvements in calculating the shear resistance of cold joint with a roughened interface.

4.5.3.2. Large-Scale Slant Shear Tests

4.5.3.2.1. Capacity and Failure Modes

The experimental results for the large-scale slant shear specimens are presented in Table 4-8. Specimen *VII-30* exhibited 58% increase in interface shear resistance compared to Specimen *VII-30-NR*. Similar to *Series II*, the interface roughness was found to significantly increase the capacity and interface shear resistance. The slant shear specimens with an interface angle greater than 45° experienced crushing of concrete. Identical conclusion was drawn from the failure patterns observed in *Series I*, where the governing failure switched from shear failure of cold joint to crushing of concrete as the inclination increase.

Table 4-8 Experimental results for large-scale slant shear tests

Series	Specimen	P	θ_{cj}	ρ_{cj}	f'_{c_sub}	f'_{c_ovr}	Failure Mode	V	δ_{s_peak}	τ_{test}
VII- Min. Interface Shear Reinforcement	VII-30	380	31	0.089	3.56	4.92	SS	326	1.40	1.48
	VII-30-NR	242	31	0.089			SS	207	5.18	0.94
	VII-45	407	44	0.090			CC	-		
	VII-60	426	59	0.074			CC	-		

Note: P = capacity of slant shear specimen (kips)
θ_{cj} = as-built angle of the cold joint measured from the vertical (º)
ρ_{cj} = as-built reinforcement ratio of the cold joint (%)
f'_{c_sub} = concrete compressive strength of substrate (ksi)
f'_{c_ovr} = concrete compressive strength of overlay (ksi)
V = shear capacity of specimen governed by SS (kips)
$\delta_{s_{peak}}$ = average slip of cold joints corresponding to peak strength for specimens governed by SS (in. $\times 10^{-3}$)
τ_{test} = shear stress of specimen governed by SS (ksi)

4.5.3.2.2. Interface Shear Resistance

Similar to the small-scale slant shear specimens, the interface shear resistance was determined only for specimens governed by slant shear failure (*VII-30* and *VII-30-NR*). The shear stress of *VII-30* calculated at peak load was 12% lower than the corresponding small-scale specimen (*VI-40*). Additionally, specimen with 30° inclination governed by slant shear failure (*VII-30*) exhibited 10% decrease in capacity comparing to specimen with 60° inclination governed by concrete crushing (*VII-60*). This decrease in capacity due to the variation of inclination was not

observed in the small-scale slant shear specimens with the same governing failure mode, reinforcement ratio and interface roughness. Accordingly, these two observations indicate a potential size effect of interface area on the shear capacity.

The experimental results are compared with the calculated interface shear resistance based on current design codes and proposed LIF method as shown in Table 4-9. Note, *fib* MC2020 (2024) and Eurocode 2 (2005) are excluded from Table 4-9 to focus the investigation on the proposed LIF method. The interface shear resistances calculated using the LIF method based on the three design codes (AASHTO, 2024; ACI Committee 318, 2025; CSA Standard A23.3-19, 2019) demonstrate better alignment with the experimental results for the large-scale slant shear specimens.

Table 4-9 Experimental results and design code estimations for interface shear resistance of large-scale slant shear specimens

Specimen	τ_{test} (ksi)	Current Code Expression			RI			LIF		
		τ_{AASHTO} (ksi)	τ_{ACI} (ksi)	τ_{CSA} (ksi)	τ_{AASHTO} (ksi)	τ_{ACI} (ksi)	τ_{CSA} (ksi)	τ_{AASHTO} (ksi)	τ_{ACI} (ksi)	τ_{CSA} (ksi)
VII-30	1.48	0.64	0.59	0.63	1.18	0.96	1.04	0.91	0.78	0.83
VII-30-NR	0.94	0.45	0.40	0.43	0.45	0.40	0.43	0.45	0.40	0.43

4.5.3.2.3. Strain Contour and Interface Slip

The images captured by DIC during the experiment were analyzed to obtain the strain and displacement response of the specimens. The geometry of specimens calculated from the DIC data, shown in Figure 4-21, is consistent with the actual geometry of the testing region. This geometry comparison validated the accuracy of the measurement, enabling the use of DIC data in the following discussion. The principal compression strain profiles of each test at peak load are presented in Figure 4-22. The principal compressive strain was observed to concentrate significantly along the cold joint prior to failure, regardless of the governing failure modes.

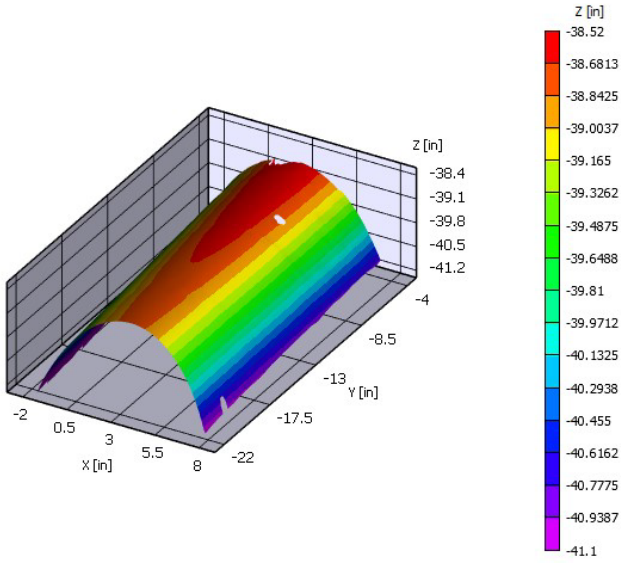

Figure 4-21 Topographic map of monitoring surface from DIC

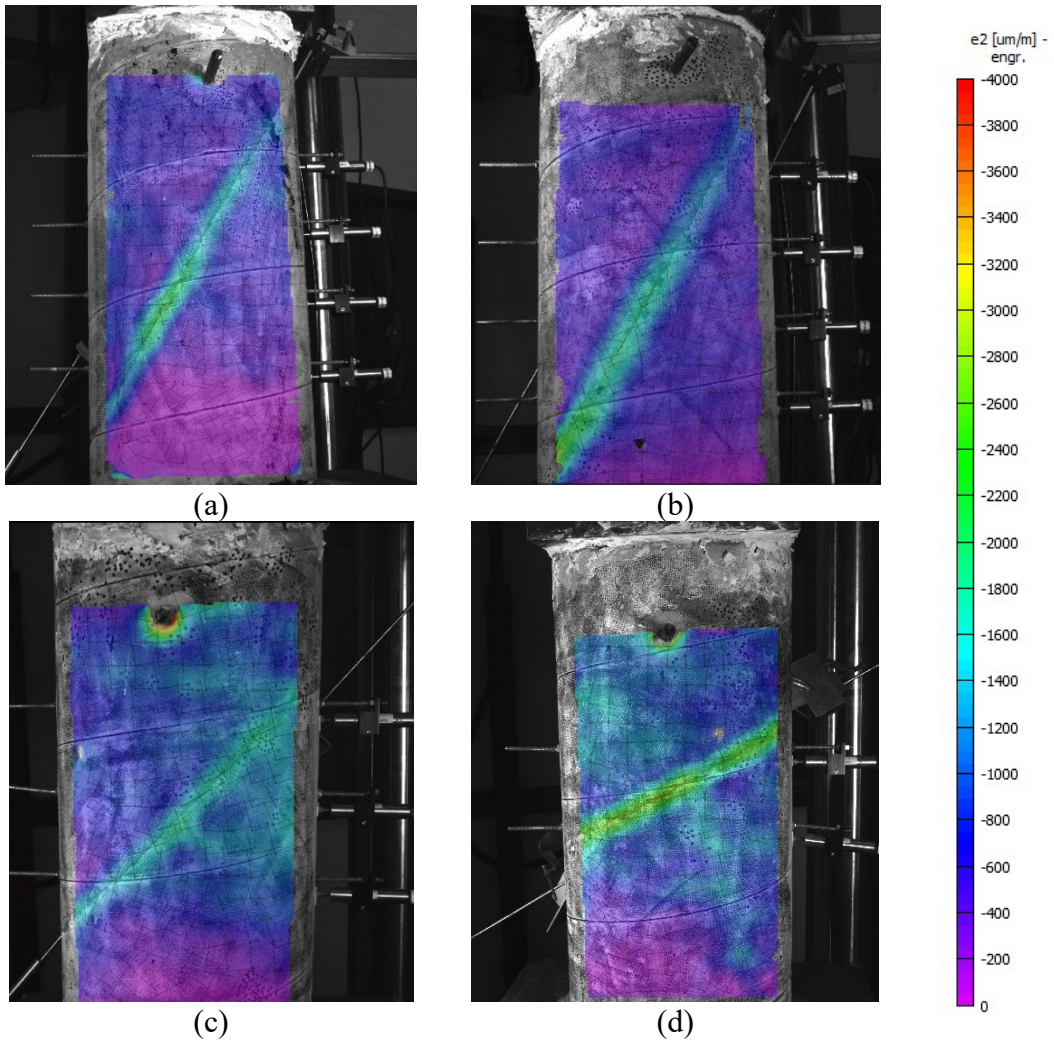

Figure 4-22 Strain contour at peak load (a) VII-30 (b) VII-30-NR (c) VII-45 (d) VII-60

The interface shear-slip relationships of both specimens governed by slant shear failure are shown and compared in Figure 4-23. The slip along the interface of Specimen *VII-30-NR* is significantly greater than that of Specimen *VII-30* under the same applied shear force. The difference in interface slip indicates that the interface roughening increases both the shear capacity and the interface stiffness of cold joint, reducing the slip between the interface.

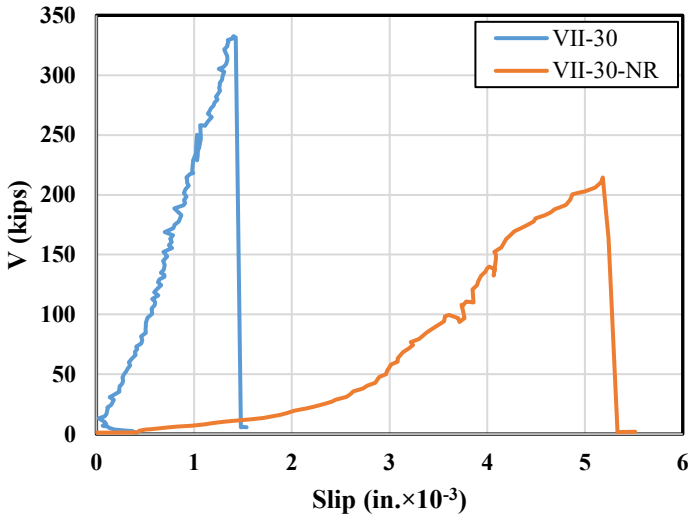

Figure 4-23 Shear force-slip diagram

4.6. Summary

This chapter summarizes the results of an experimental study on the interface shear resistance through slant shear tests across six intrinsic variables: interface angle, interface roughness, concrete strength, casting age, aggregate size, and minimum amount of interface shear reinforcement. A multifaceted set of data was obtained to contribute to the interface shear transfer database. To that end, a total of 54 small-scale and four large-scale slant shear specimens were designed, fabricated, and tested. A comprehensive analysis of the experimental results and comparison to current design code estimations was conducted. The conclusions drawn from this experimental program is listed as follows:

- The application of interface roughening and the used of concrete with a larger maximum aggregate size significantly enhanced the shear resistance of cold joints. However, current design specifications only address the effect of interface roughness with no modification directly accounting for aggregate size;

- The increase in casting age difference was found to enhance the interface shear resistance. However, when the casting interval was shortened to 4 hours, all specimens experienced concrete crushing failure. This indicates the presence of lower bound in casting age different for the formation of cold joints;

- A shift in failure mode from slant shear failure to crushing of concrete was observed for specimens with interface angles greater than 48°, measured from the vertical (i.e., the direction of compression being applied);

- The variation in concrete compressive strength between layers had negligible effect on the ultimate capacity and failure mode. The capacity of the interface was governed by the weaker concrete layer;

- The interface shear resistance calculated according to *fib* MC2020 (2024) and Eurocode 2 (2005) closely aligned with the experimental results;

- A modified method is proposed (a method that employs Linearly Interpolated Factors, LIF) to address the evident contribution of intermediary amplitudes of interface roughness when calculating interface shear resistance per AASHTO LRFD (2024), ACI 318-25 (2025), and CSA A23.3:19 (2019). The LIF method improves the calculated values for the interface shear resistance;

- The database analysis validates the impact of LIF approach by improving the accuracy of interface shear resistance calculation. Meanwhile, the unconservative counts remain below 25% of the total number of calculations with no predictions higher than 20% of the experimentally measured shear resistance;

- Significant impact of interface roughness on the shear capacity of the interface and the influence of inclination on the failure mode were substantiated through the experimental results of *Series VII.* From the shear-slip diagram of specimens in *Series VII*, it was further concluded that the interface stiffness increases with the interface roughness;

- Size effect was observed by comparing the shear stress at peak of VII-30 to the shear stress of VI-40. The reduction in interface shear resistance supports the existence of size effect; and

- The DIC results indicated that the strain concentration occurred throughout the interface regardless of the failure mode of specimens.

Chapter 5. Experimental Program: Deep Beams with Cold Joints

This section presents the deep beam experimental program designed to investigate the effect of cold joints on the shear behavior of reinforced concrete (RC) members in disturbed regions (D-regions). The specimen design, experimental setup, instrumentations and testing protocols are described in detail. The experimental data facilitated a comprehensive analysis of shear capacity, load-deflection response, failure mode, crack propagation, strain distribution, and displacement fields for all 10 specimens. The experimental findings were subsequently used to develop analytical methods for evaluating deep beams with cold joints using strut-and-tie model in the following chapter.

5.1. Overview of Experimental Program

The objective of phase II testing is to investigate the effect of cold joints on the strength of struts in reinforced concrete members with a predominately two-dimensional behavior. Phase II experimental program consists of 10 deep beam specimens. Each beam specimen, measuring 332 inches in length with a 21×42-inch cross-section, accommodated one test on each end, totaling two tests in a specimen. Each test focused on the shear behavior of the deep beam specimen within the shear span between the loading point to the near-end support, referred to as the testing region. These testing regions were deliberately designed to study the effect of independent experimental variables. The conventional reinforced concrete beam design relies on sectional analysis by assuming *plane sections remain plane*. However, this assumption is invalid in the D-regions of a structure, characterized by nonlinear strain fields. The behavior of deep beams, defined as beam with shear-span-to-depth ratio (*a/d* ratio) below 2.5, is primarily influenced by nonlinear strain and stress fields induced from the vicinity of the applied load and the reaction force. The strut-and-tie method (STM) was therefore used for both the design and evaluation of the deep beam specimens.

The strut-and-tie method conceptualizes the load transfer mechanism of a simply-supported reinforced concrete deep beam through single or multiple panels of a triangular truss system. This truss system consists of concrete struts carrying the compression forces and reinforced ties carrying the tension forces, as illustrated in Figure 5-1. The intersections between struts and ties are defined as the nodes.

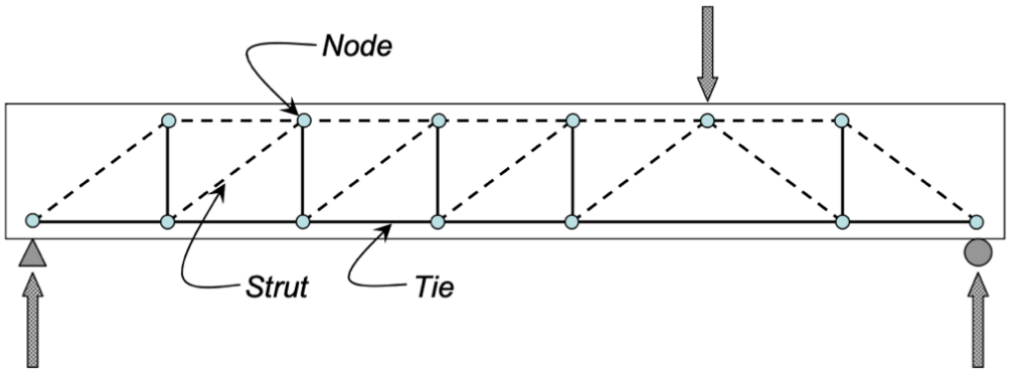

Figure 5-1 STM implemented in simply supported beam (Reprinted from Birrcher et al., 2009)

The specimens consist of cold joints intersecting the strut-and-tie panels with various design details. These details were systematically introduced in the experimental program to evaluate variables deemed influential to interface shear behavior from phase I testing. To focus the investigation on the strength of struts intersecting by the cold joints, the specimens were deliberately designed to be governed by crushing of struts. The crushing of struts was determined from the strut-and-tie model by evaluating the capacity strut-to-node interfaces. The strut-and-tie design and analysis procedure is detailed in the following subsection.

5.2. Overview of Strut-and-Tie Modeling

The strut-and-tie method (STM) idealizes the stress distribution in members with a representative truss system comprising compression resisting elements (*struts*) and tension resisting elements (*ties*). The intersections of struts and ties are referred to as *nodes*. The dimensions of elements and the angles between struts and ties were specifically considered to develop representative truss models for structures. The truss models were used to determine the load demand of each element from the applied load based on equilibrium.

The initial phase in developing a strut-and-tie model involves establishing the relationship between the applied load and the reaction forces. This entails calculating the proportion of the applied load to the reaction force for each support, which varies depending on the boundary conditions. Nodes are designated corresponding to the locations of the applied load and the reaction forces. It is important to note that two nodes are specifically allocated for the loading point to effectively transfer the applied load to both supports while satisfying the equilibrium.

While maintaining equilibrium, various truss configurations can be developed within the STM framework. It was observed that the load tends to follow the path of least resistance and deformation. Hence, the model with least ties often offers a more accurate simulation, as ties exhibit greater deformation capacity compared to concrete struts. Moreover, to prevent interference between the development of tensile stress in the reinforced ties and compression stress

in the concrete struts, it is imperative to ensure that the angle, θ, between struts and ties exceeds 25 degrees. The distribution of applied load and the idealized strut-and-tie model of deep beam in this experimental program are illustrated in Figure 5-2.

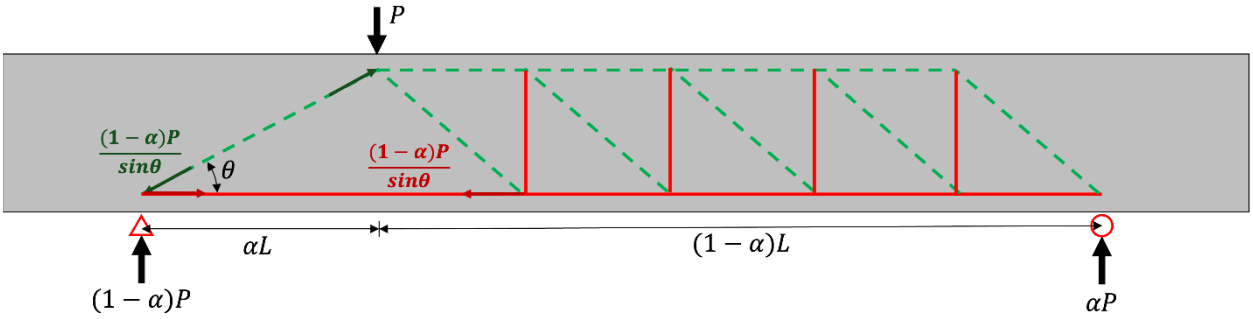

Figure 5-2 Example of load transfer through truss elements in STM

5.2.1. Proportioning STM elements

Given that all struts and ties are connected through multiple nodes, it is essential to establish the dimensions of these nodes to calculate the forces transferred within the nodal regions. Nodes are categorized into three distinct types based on the elements intersecting them: *CCC*, *CCT*, and *CTT* nodes. *CCC* nodes correspond to nodes where only struts intersect, *CCT* nodes are nodes intersected by one tie in only one direction, and *CTT* nodes refer to nodes where ties intersect in multiple directions.

In the testing regions of specimens in Task 5, one node is classified as a *CCC* node at the location of the applied load, while another node is classified as a *CCT* node at the support. Accordingly, the following paragraph focus on elucidating the proportioning of *CCC* and *CCT* nodes.

5.2.1.1. Proportioning the CCC node

A comprehensive diagram of the *CCC* node is presented in Figure 5-3(a). The length of the bearing face, l_b, is determined by both the dimension of the loading plate and the proportion of the applied load, α, transferred to the near-end support. For example, in the case of a specimen with an a/d ratio of 1.85, 71% of the applied load is transferred to the near-end support in the testing region. Therefore, 71% of the loading plate length is deemed to be the length of the bearing face for the *CCC* node positioned at the loading point.

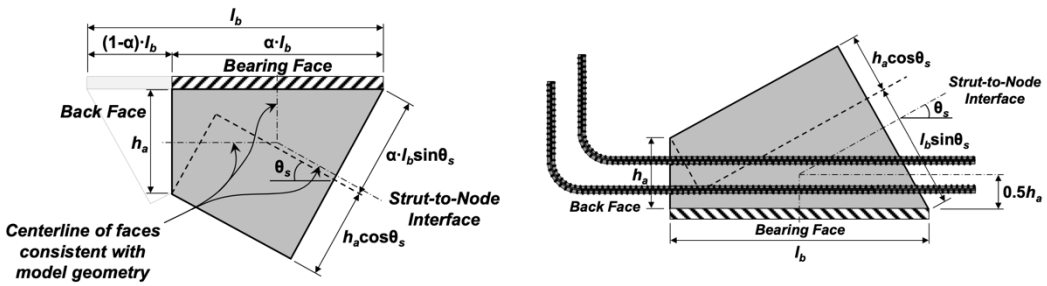

(a) CCC Node *(b) CCT Node*

Figure 5-3 Nodal geometries (AASHTO LRFD, 2024)

The height of the back face, h_a, can be approximated with the depth of equivalent stress block obtained from flexural analysis. For specimens featuring rectangular cross-section in Task 5, the height of the back face can be calculated according to Equation 2.1. Subsequently, the width of the strut-to-node interface, w_s, can be derived from the length of the bearing face, l_b, the height of the back face, h_a, and the angle of strut adjoining the node, θ. Since the strut-to-node interface must be perpendicular to the direction of strut to calculate the compression load transmitted to the interface, the width of the strut-to-node interface is determined per Equation 2.2.

$$h_a = \frac{(A_s \cdot f_s - A_s' \cdot f_s')}{0.85 f_c' \cdot b_w} \quad (2.1)$$

$$w_s = \alpha \cdot l_b \cdot sin\theta + h_a \cdot cos\theta \quad (2.2)$$

where, A_s = area of tension reinforcement, in^2
A_s' = area of compression reinforcement, in^2
b_w = web width, in.
f_c' = specified concrete compressive strength, psi
f_s = stress in tension reinforcement, psi
f_s' = stress in compression reinforcement, psi

5.2.1.2. Proportioning the CCT node

A *CCT* node is depicted in Figure 5-3(b). The length of the bearing face, l_b, shares identical dimension with the loading plate. The width of the back face, h_a, is calculated as twice the distance from the near face of the member to the centroid of tensile reinforcement. Similar to a *CCC* node, the width of the strut-to-node interface can be determined using Equation 2.3 based on the dimensions previously obtained for the node.

$$w_s = l_b \cdot sin\theta + h_a \cdot cos\theta \quad (2.3)$$

5.2.2. Calculating the Capacity of STM elements

5.2.2.1. Calculating the Nominal Strength of Node Faces

The specimens in Task 5 were designed in accordance with AASHTO LRFD 2024. The nominal resistance of the node faces should be calculated as Equation 2.4. The compressive stress at the node face, $\boldsymbol{f_{cu}}$, is limited by Equation 2.5, where $\boldsymbol{m}$ represents the confinement modification factor, $\boldsymbol{v}$ is the concrete efficiency factor and $\boldsymbol{f'_c}$ indicates the compressive strength of concrete. As per AASHTO LRFD 2024, $\boldsymbol{m}$ is set to unity when the width of the bearing area is greater or equal to the width of the reinforced concrete member. The concrete efficiency factors are influenced by the presence of crack control reinforcement and the bearing condition of the node face. To satisfy the requirement for crack control reinforcement, both the horizontal and vertical reinforcement ratios, $\boldsymbol{\rho_h}$ and $\boldsymbol{\rho_v}$, defined in the following annotation, must exceed 0.3%. For specimens failing to meet the requirement for crack control reinforcement ratio, $\boldsymbol{v}$ is limited to 0.45. Conversely, for specimens with adequate crack control reinforcement, the permissible efficiency factors for various types of interfaces across different categories of nodes are detailed in Table 5-1 and depicted in Figure 5-4.

$$P_n = f_{cu} \cdot A_{cn} \tag{2.4}$$

$$f_{cu} = m \cdot v \cdot f_c' \tag{2.5}$$

where, A_{cn} = effective cross-sectional area of the node face, in^2

A_v = total area of vertical crack control reinforcement within spacing s_v, in^2

A_h = total area of horizontal crack control reinforcement within spacing s_h, in^2

b_w = web width, in.

P_n = nominal resistance of a node face, in^2

s_v = spacing of vertical crack control reinforcement, in.

s_h = spacing of horizontal crack control reinforcement, in.

$\rho_v = \dfrac{A_v}{b_w s_v}$

$\rho_h = \dfrac{A_v}{b_w s_v}$

Table 5-1 Efficiency factors for nodes with crack control reinforcement

	Node Type		
Face	***CCC***	***CCT***	***CTT***
Bearing Face	0.85	0.70	$0.85 - \frac{f'_c}{20\ ksi}$ $0.45 \leq v \leq 0.65$
Back Face			
Strut-to-Node Interface	$0.85 - \frac{f'_c}{20\ ksi}$ $0.45 \leq v \leq 0.65$	$0.85 - \frac{f'_c}{20\ ksi}$ $0.45 \leq v \leq 0.65$	

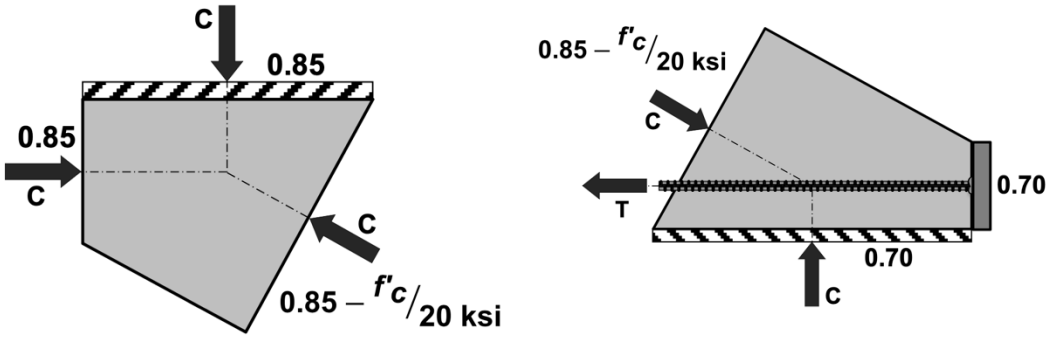

(a) CCC node *(b) CCT node*

Figure 5-4 Efficiency factors (AASHTO 2024)

5.2.2.2. Calculating the Nominal Strength of Tie

The nominal resistance of a reinforced tie is determined as per Equation 2.6. The reinforcement in the ties must be adequately anchored with sufficient development length. The development length of a tie intersecting a CCT node is identified as the end of the reinforcing bars to the edge of the extended nodal zone. The edge of the extended nodal is determined from the intersection of the reinforcement centroid and the edge of the diagonal prismatic strut, as depicted in Figure 5-5. This configuration ensures that the reinforcement in ties outside of the nodal region and the strut can be fully developed until its yielding stress.

$$P_n = f_y A_{st} + A_{ps}\left[f_{pe} + f_y\right] \tag{2.6}$$

Where, A_{st} = total area of longitudinal non-prestressed reinforcement, in^2

A_{ps} = area of prestressing steel, in^2

f_y = yield strength of non-prestressed longitudinal reinforcement, ksi

f_{pe} = effective stress in prestressing steel after losses, ksi

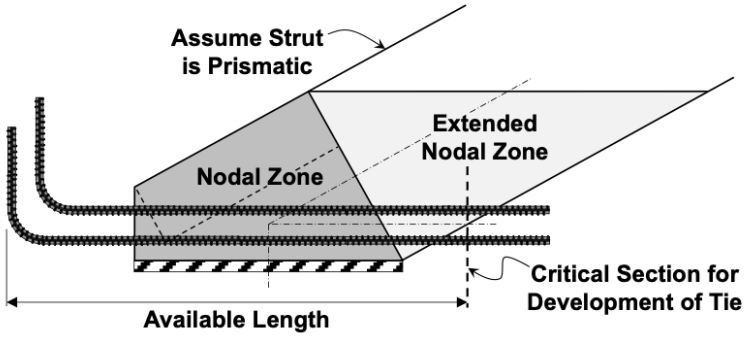

Figure 5-5 Available development length for ties (AASHTO 2024)

5.3. Specimen Design and Test Matrix

The objective of this experimental program is to investigate the effect of cold joints on the shear behavior of reinforced concrete deep beam designed using the strut-and-tie method. As previously introduced, the capacity of the ties is determined solely from the yielding stress of the reinforcement, neglecting the concrete tensile strength. Accordingly, with sufficient continuous reinforcement, the effect of cold joint is expected to be insignificant to the tie capacity.

The strut capacity is determined from the capacity of the strut-to-node interface, indicating that the capacity throughout the strut-axis is not directly evaluated. When the strut is intersected by a cold joint, the strut capacity may be limited by the shear resistance of the cold joint before the compressive strength of concrete at the strut-to-node interface is fully developed. Therefore, the experiments focus on investigating the effect of cold joints on the strength of the strut in the strut-and-tie model.

To investigate the strength of struts crossing cold joints, the failure of specimens was intentionally designed to be governed by compressive failure of the strut-to-node interface. The preliminary design of specimens was conducted by gradually increasing the applied load in the strut-and-tie model for deep beam specimens. Based on the applied load, the demands of the nodal faces and the ties was determined. The capacity of each nodal face and tie was calculated to evaluate its demand. If the capacity of a nodal face or a tie was exceeded by the its demand, the nodal face or the tie was considered as the failure governing component and the corresponding applied load was determined as the maximum design applied load. The preliminary design of all specimens in this research were governed by the capacity of the strut-to-node interface, interpreted as strut governing failure. Although there are currently no specific design guidelines indicating the methodology for calculating the strength of struts crossing cold joints, it was anticipated that the strength would decrease compared to the strength of a monolithic strut. Therefore, the preliminary design of strut-governing specimens was conducted by neglecting the influence of cold joints.

All specimens were fabricated in the Ferguson Structural Engineering Laboratory at The University of Texas at Austin. The experimental program consists of ten tests conducted on five

reinforced concrete beams, each with cross-sectional dimensions of 21×42 in. (533×1067 mm) and a total length of 332 in. (8433 mm). A customized test setup allowed each beam to accommodate two experiments by adjusting the location of the applied load. The variables of interest were independently implemented in each testing region between the loading plate and the supporting plate. Each testing region is considered as an individual specimen in this study. The details of specimens are provided in Table 5-2, and the definitions of design variables corresponding to the orientations of the cold joints are illustrated in Figure 5-6 and calculated according to Equation (5-1) to (5-3). The design objectives and the target variables of each specimen will be elaborated in the subsequent paragraphs.

Table 5-2 Test matrix for task 5 – deep beam experiments

Beam ID	b (in.)	d (in.)	a (in.)	a/d	ρ_v&ρ_h (%)	ρ_{cj} (%)	θ (°)	Size and spacing s_v & s_h	Cold Joint Orientation
I-1.85-03-H	21	38.3	71	1.85	0.3	0.3	26.7	No. 5 at 9.5 in.	Horizontal
I-1.4-03-H	21	38.3	54	1.4	0.3	0.3	33.7	No. 5 at 9.5 in.	Horizontal
I-1.0-03-H	21	38.3	38	1.0	0.3	0.3	43.0	No. 5 at 9.5 in.	Horizontal
II-1.85-00-H	21	38.3	71	1.85	0	0	26.7	-	Horizontal
III-1.85-00-V	21	38.3	71	1.85	0.3	0	63.3	No. 5 at 9.5 in.	Vertical
III-1.85-00-V^R	21	38.3	71	1.85	0.3	0	63.3	No. 5 at 9.5 in.	Vertical
IV-1.85-03-V	21	38.3	71	1.85	0.3	0.3	63.3	No. 5 at 9.5 in.	Vertical
IV-1.2-03-V	21	38.3	46	1.2	0.3	0.3	52.2	No. 5 at 9.5 in.	Vertical
V-1.85-00-V^D	21	38.3	71	1.85	0.3	0	63.3	No. 5 at 9.5 in	Vertical
V-1.85-03-V^D	21	38.3	71	1.85	0.3	0.3	63.3	No. 5 at 9.5 in	Vertical

Note: b = the width of deep beam specimen
d = the effective depth of the deep beam specimen
a = the shear span of the deep beam specimen
ρ_v = the vertical web reinforcement ratio
ρ_h = the horizontal web reinforcement ratio
ρ_{cj} = the ratio of reinforcement crossing cold joints
θ = the inclination of cold joints measured from the idealized strut line
s_v = the spacing between vertical web reinforcing bars
s_h = the spacing between horizontal web reinforcing bars
^{R} = specimen with intentionally roughened cold joint
^{D} = specimen with cold joint intersected by dowel reinforcement

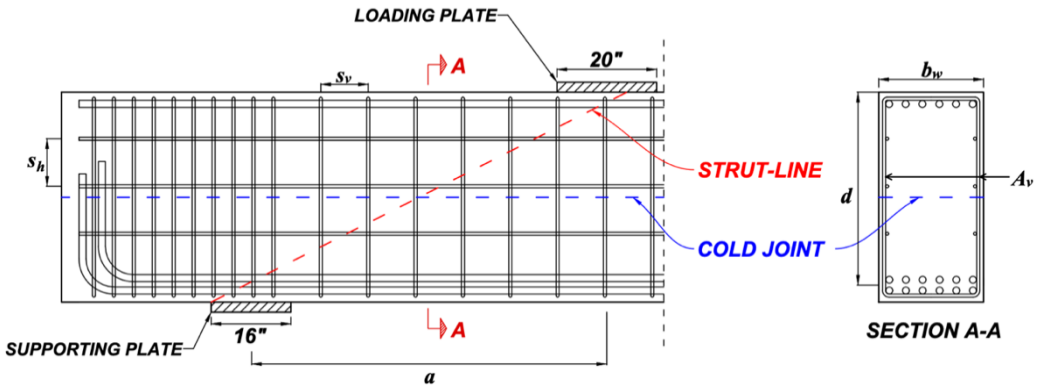

(a) Specimens with horizontal cold joint

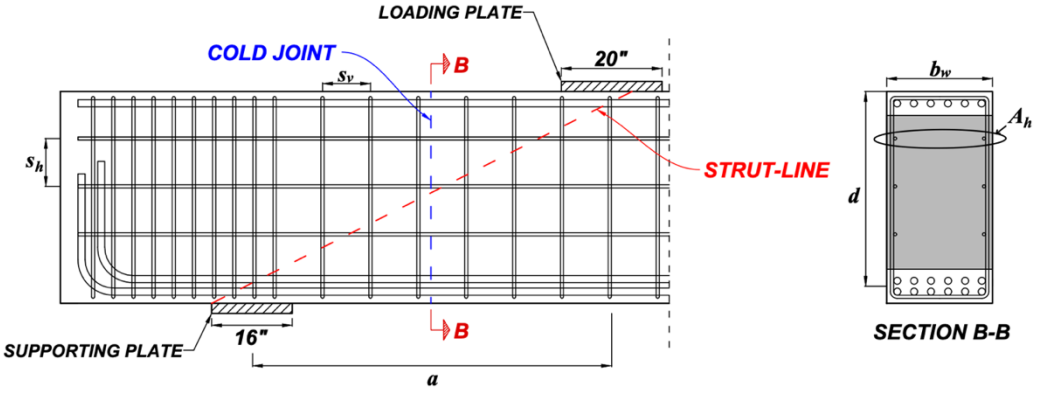

(b) Specimens with vertical cold joint

Figure 5-6 Details of specimens and definitions of design variables

$$\rho_v = \frac{A_v}{b_w s_v} \tag{5-1}$$

$$\rho_h = \frac{A_v}{b_w s_h} \tag{5-2}$$

$$\rho_{cj} = \begin{cases} \rho_v, & \text{for horizontal cold joint} \\ \rho_h, & \text{for vertical cold joint} \end{cases} \tag{5-3}$$

Cold joints were introduced horizontally in four specimens to simulate the delay in concrete placement and implemented vertically in the remaining six specimens to represent the expansion or retrofit of structures. Key parameters deemed influential to the behavior of cold joints, including the inclinations of the cold joint, the reinforcement ratio, the interface roughness, and the implementation of dowel reinforcement were deliberately incorporated and tailored to accommodate the orientation of cold joints in this experimental program.

To investigate the influence of shear span-to-effective depth ($\boldsymbol{a/d}$) ratio on deep beams with adequate crack control reinforcement crossing cold joints, specimens in Series I and Series

IV were designed with various $\boldsymbol{a/d}$ ratio, ranging from 1.0 to 1.85. The $\boldsymbol{a/d}$ ratio influences the orientation of the idealized compressive strut in the strut-and-tie model. Therefore, adjustments in the $\boldsymbol{a/d}$ ratio result in varying the inclination angles between the strut-lines and the cold joints. Since the strut-lines represent the idealized compressive load paths in deep beams, specimens in these series essentially focus on studying the influence of inclination between the compression load path and the cold joint. Based on the geometry of the specimens and the orientation of the cold joints, a reduction in the $\boldsymbol{a/d}$ ratio increases the inclination between the strut-line and the horizontal cold joints in Specimen I-1.85-03-H, I-1.4-03-H and I-1.0-03-H. Conversely, for Specimen IV-1.85-03-V and IV-1.2-03-V, the reduction of the $\boldsymbol{a/d}$ ratio decreases the inclination between the strut line and vertical cold joints. These specimens were all designed with 0.3% of vertical and horizontal web reinforcement. Accordingly, for the preliminary design of these specimens using STM, the efficiency factors listed in

Table 5-1 were applied to calculate the nodal face capacities.

Based on the shear friction theory, interface shear resistance is enhanced by the reinforcement ratio. In this study, cold joints were deliberately designed without reinforcement to evaluate the interface shear resistance of unreinforced cold joints in deep beams. To isolate the effect of unreinforced horizontal cold joint, Specimen II-1.85-00-H was strategically designed without web reinforcement in the entire testing region. Since Specimen II-1.85-00-H was designed with web reinforcement ratio less than 0.3%, the nodal face capacities of Specimen II-1.85-00-H were calculated using an efficiency factor of 0.45. The experimental results of Specimen II-1.85-00-H were later compared to the results of Specimen I-1.85-03-H to investigate the effect of web control reinforcement and reinforcement crossing horizontal cold joints on deep beams behavior. The design drawing of specimens in Series I and Series II are presented in Figure 5-7, in which the blue dash line represents the location of the cold joint.

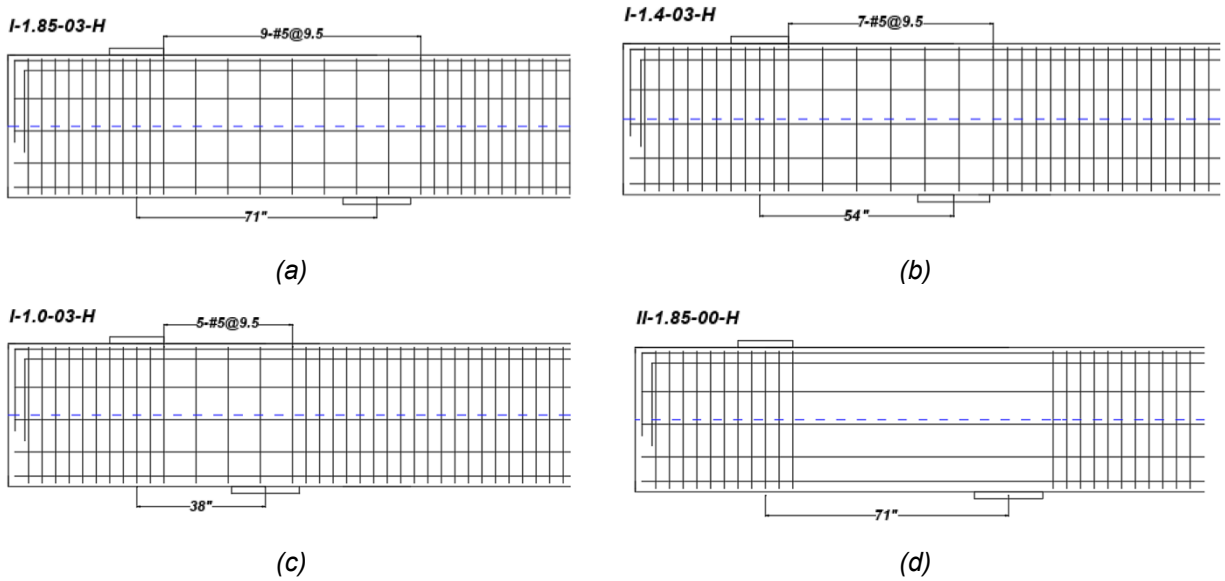

Figure 5-7 Details of specimens in Series I and Series II

The effect of interface roughness was investigated in Series III. The cold joint in Specimen III-1.85-00-V was left as a form-finished surface to compare the interface behavior to the intentionally roughened cold joint in Specimen III-1.85-00-V^R. The cold joint in Specimen III-1.85-00-V^R was roughened using an electric-powered bush hammer prior to the second concrete placement. The bush hammer resulted in an interface with an approximate roughening amplitude of 0.25 in., corresponding to the requirement for a roughened interface according to AASHTO LRFD (2024). To isolate the effect of interface roughness, no web reinforcement was designed to intersect the vertical cold joints. Aside from the cold joints, these two specimens were designed with 0.3% of vertical and horizontal web reinforcement in the testing region, allowing for the utilization of optimal concrete efficiency factors in design practice as prescribed by the AASHTO LRFD (2024), as listed in

Table 5-1. The design of specimens in Series III aims to study the behavior of deep beams with unreinforced vertical cold joints and validate the applicability of efficiency factors in strut-and-tie method. The design drawing of specimens in Series III are presented in Figure 5-8. The photographs demonstrating a form-finished cold joint and an intentionally roughened cold joint are presented in Figure 5-9.

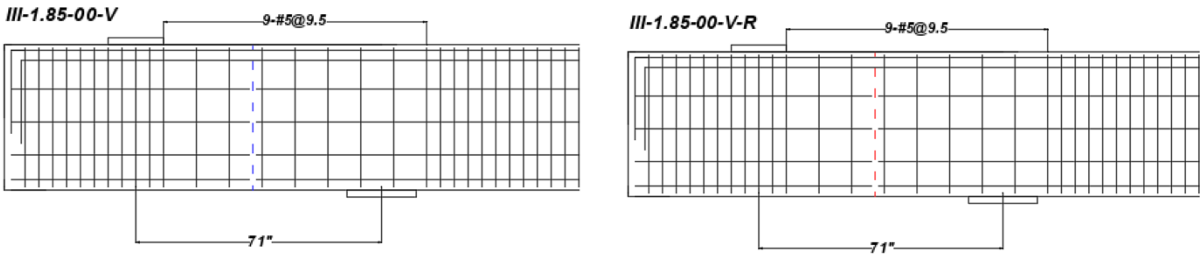

(a) *(b)*

Figure 5-8 Drawing of specimens in Series III

(a) Roughened interface *(b) Non-roughened interface*

Figure 5-9 Photos of interface roughness

To investigate the influence of reinforcement crossing vertical cold joints, Specimen IV-1.85-03-V was designed with 0.3% of horizontal reinforcement intersecting the vertical cold joint. As previously mentioned, Specimen IV-1.85-03-V and IV-1.2-03-V were designed with two distinct

a/d ratios, facilitating the investigation of the a/d ratio effect on vertical cold joints. The design diagrams of specimens in Series IV are presented in Figure 5-10.

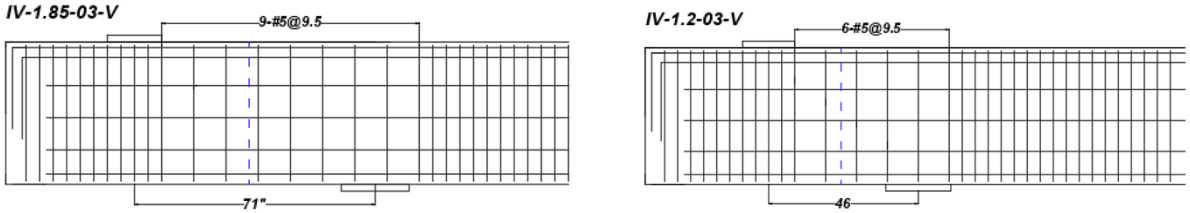

(a) (b)

Figure 5-10 Drawing of specimens in Series IV

The post-installed reinforcement was implemented in two specimens with vertical cold joints, representing practical cases where no continuous reinforcement protruding from the pre-existing structures is provided for the cold joint. Specimen V-1.85-00-VD was designed with 12 post-installed #8 reinforcing bars in the tie region according to the strut-and-tie model, aiming to transfer tension load across the cold joint. Each post-installed tension reinforcing bars was designed with a doweling length of 18 in. The spacing between dowel bars was carefully designed to avoid damaging the concrete between holes while aiming to locate the dowel bars as close as possible to the centroid of the existing tension reinforcement. This positioning approach was essential to optimized the transfer of tension load across the section without expanding the dimension of structure. The sectional design of specimens with post-installed reinforcement was illustrated in Figure 5-11, which satisfies the spacing requirements for post-reinforcement while maintaining an adequate distance between existing and post-installed reinforcement.

In addition to the post-installed tension reinforcement, 6-#6 post-installed reinforcing bars were design in the strut region of Specimen V-1.85-03-VD to assess the contribution and anchorage efficiency of shear resisting dowel bars. The anchorage details of the shear resisting dowel reinforcement was designed according to TxDOT design examples for bridge girder expansion connection (12 in. dowel for #6 bars). The design drawings of specimens in Series V are presented in Figure 5-12, where the post-installed reinforcement is represented by green solid lines.

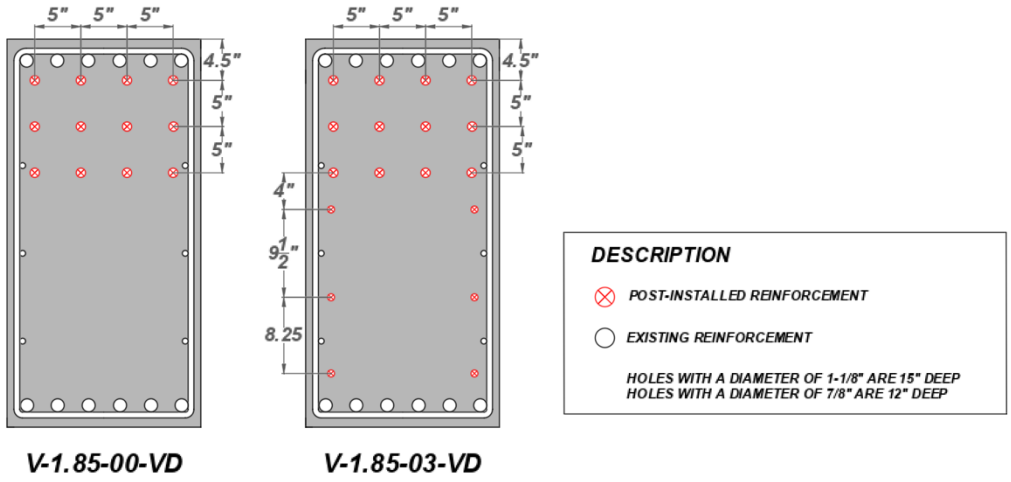

Figure 5-11 Design for post-installed reinforcement

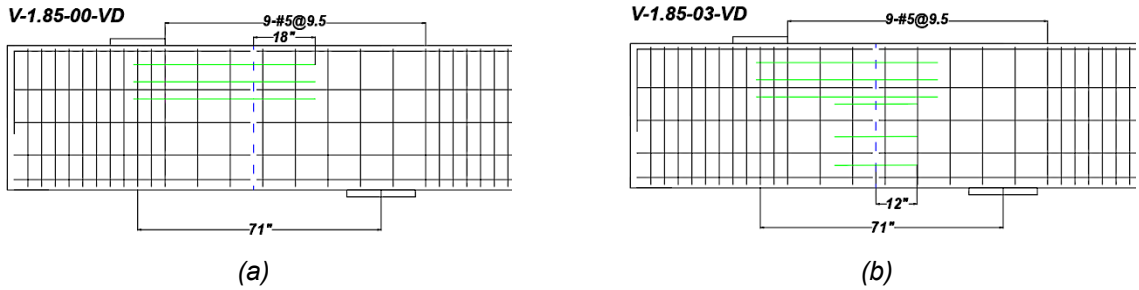

Figure 5-12 Drawing of specimens in Series V

5.4. Materials

Grade 60 deformed steel reinforcement complying with the specifications of ASTM A615/A615M was used throughout the experimental program. To determine the mechanical properties of the reinforcing bar, tensile tests were conducted on three coupons for each bar size within every steel batch in accordance with ASTM A370.

The ready-mix concrete used in this study was designed to achieve a nominal compressive strength of 4000 psi (28 MPa) at 28 days. The mixture design and the nominal properties are detailed in Table 5-3. The compressive strength and the modulus of elasticity were experimentally determined using 4×8 in. cylinders, following ASTM C39/C39M and ASTM C469/C469M, respectively. A total of 15 cylinders were cast for each batch of concrete and cured under the same environmental conditions as the deep beam specimens to evaluate the concrete properties at 7 days, 28 days, and the day of experiment. The measured tensile strength of longitudinal and transverse reinforcement and the compressive strength and modulus of elasticity of each concrete layer are summarized in Table 5-4.

Table 5-3 Concrete mixture design

Materials/Properties	Quantity
Type I portland cement, lb/yd3 (kg/m3)	451 (268)
Class F fly ash, lb/yd3 (kg/m3)	113 (67)
Coarse aggregate: 3/8 in. washed rock, lb/yd3 (kg/m3)	1700 (1009)
Fine aggregate: sand, lb/yd3 (kg/m3)	1369 (812)
Water, gal./yd3 (L/m3)	32 (158)
Hydration controlling admixture, fl oz/100 lb CM (mL/100 kg CM)	1 to 8 (65 to 520)
High range water reducing admixture, fl oz/100 lb CM (mL/100 kg CM)	1 to 6 (65 to 390)
Water-cement ratio (w/c)	0.47
Slump, in. (mm)	7 to 9 (180 to 230)

Table 5-4 Material properties

Beam ID	$f'_{c,sub}$ (ksi)	$f'_{c,ovr}$ (ksi)	$E_{c,sub}$ (ksi)	$E_{c,ovr}$ (ksi)	f_{yl} (ksi)	f_{yt} (ksi)
I-1.85-03-H	3.10	3.82	2371	3983	66	66
I-1.4-03-H	3.10	3.82	2371	3983	66	66
I-1.0-03-H	2.85	2.07	3259	3070	64	61
II-1.85-00-H	2.93	2.17	3112	2587	64	61
III-1.85-00-V	4.60	5.09	4352	4300	71	69
III-1.85-00-V^R	4.73	5.56	4131	4733	71	69
IV-1.85-03-V	4.67	4.19	4637	4225	64	61
IV-1.2-03-V	4.70	4.07	4265	4167	64	61
V-1.85-00-V^D	3.08	4.08	3337	3680	65	61
V-1.85-03-V^D	3.46	4.01	3707	4208	65	61

Note: $f'_{c,sub}$ = concrete compressive strength of substrate
$f'_{c,ovr}$ = concrete compressive strength of overlay
$E_{c,sub}$ = modulus of elasticity for concrete of substrate
$E_{c,ovr}$ = modulus of elasticity for concrete of overlay
f_{yl} = yielding strength of longitudinal reinforcement
f_{yt} = yielding strength of web reinforcement

To provide bonding between post-installed reinforcement and concrete, epoxy-based chemical adhesive was applied to holes drilled into the existing concrete before embedding dowel reinforcement. The material properties of the chemical adhesive corresponding to #5 and #8 reinforcing bars used in the experimental program is summarized in Table 5-5.

Table 5-5 Properties of chemical adhesive for different diameters of reinforcement

Properties	#5	#8
d_0 (in.)	5/8	1
$\tau_{k,cr}$ (psi)	1070	820
$\tau_{k,uncr}$ (psi)	1520	1520
$h_{ef,min}$ (in.)	3-1/8	4
$h_{ef,max}$ (in.)	12-1/2	20
h_{min} (in.)	$h_{ef} + 2d_0$	
c_{min} (in.)	3-1/8	5
s_{min} (in.)	3-1/8	5

Note: d_0 = diameter of post-installed reinforcing bars
$\tau_{k,cr}$ = nominal bonding strength in cracked concrete
$\tau_{k,uncr}$ = nominal bonding strength in uncracked concrete
$h_{ef,min}$ = minimum embedment length
$h_{ef,max}$ = maximum embedment length
h_{ef} = design embedment length
h_{min} = minimum concrete member thickness
c_{min} = minimum edge distance
s_{min} = minimum anchor spacing

5.5. Fabrication Procedure

5.5.1. Fabrication of Steel Cage

This section outlines the general fabrication procedure employed for the steel cages across all 10 specimens, along with specific methodologies tailored to achieve distinct control variables. The fabrication process commenced with the attachment of strain gauges at designated locations. A standard strain gauge fabrication protocol was meticulously followed during construction to ensuring the fidelity of strain data obtained from the experiments. The procedure began with implementing a sequence of three grinding levels, progressing from coarse to fine, at the designated strain gauge locations on the rebars. Acetone was applied to these ground areas to establish a pristine interface for strain gauge attachment. Subsequently, strain gauges were mounted onto the reinforcement using the CN glue, and were later coated with three layers of M-coat to provide insulation against water ingress during casting. SB tape and VM tape were then applied over the strain gauges to shield the wiring while mitigating heat transmission to the gauges. Finally, electrical tape was employed to encase the entire region as a protective layer, and epoxy

was applied on the electrical tape to forestall potential collisions and frictions among rebars during construction. The strain gauge installation procedure is presented in Figure 5-13.

(a) Rebar surface after grinding *(b) Strain gauge with 3 layers of M-coat*

(c) SB tape for wire protection *(d) VM tape for heat insulation*

(e) Electrical tape wrapping *(f) Epoxy coating*

Figure 5-13 Strain gauge installation

After installing strain gauges on the rebars, the steel cages were assembled incorporating specific equipment and techniques to create cold joints. The fabrication process initiated with arranging all longitudinal reinforcement at appropriate spacings on two construction supports. Subsequently, stirrups were securely tied to the longitudinal reinforcement according to the specified design spacing. Finally, compression reinforcement at the bottom and skin reinforcement were fastened to the stirrups, with auxiliary bars added to maintain the clear cover on all sides and

ensure the structural integrity of the steel cage during concrete placement. The steel cage of I-1.85-03-H and I-1.4-03-H is shown in Figure 5-14.

Figure 5-14 Steel cage of I-1.85-03-H and I-1.4-03-H

The specimens with vertical cold joints utilized wooden stoppers of matching cross-sectional dimensions to the beams for the first cast. The stoppers were constructed in two segments and affixed to the steel cages within the interior section. The top segment comprised two layers of plywood with grooves aligned to the longitudinal bar configuration. The bottom segment was positioned beneath the top segment and penetrated by the rebars, facilitating continuous reinforcement crossing the interface. The steel cage and wooden stoppers of specimen III-1.85-00-V and III-1.85-00-V-R for the first concrete placement is presented in Figure 5-15. The wooden stoppers were removed after the first cast, and the remaining stirrups and skin reinforcement were subsequently tied to the exterior sections.

Figure 5-15 Steel cage of III-1.85-00-V and III-1.85-00-V-R with wooden stopper in between the interior and the exterior section

5.5.2. Concrete Placement

A customized steel formwork was employed for the concrete placement of all 10 specimens across 5 beams. This steel formwork comprised three components: the bottom soffit, a pair of side forms, and a pair of end forms. To integrate the steel cage with the formwork, the fabricated steel cage was positioned on the soffit, with the side forms subsequently placed adjacent to each side of the soffit. The section width along the length of the beam was maintained using 9 top ties and 7 bottom ties. Finally, the end forms were affixed to the formwork using structural hex-bolts to withstand the pressure exerted by the concrete during placement.

The concrete placement for each specimen was conducted in two stages to create a cold joint within each specimen. For specimens with horizontal cold joints designed to simulate unexpected delays during concrete placement, the overlay was cast three days after the substrate placement. Alternatively, the overlay of specimens with vertical cold joints was cast 28 days after the placement of substrate to simulate the expansion of a bridge girder after the concrete of existing structures has been fully cured.

Specific methodologies were employed to create a horizontal cold joint along the mid-height of the beam. Reflective plastic zip ties were fastened to the stirrups at the designated elevation of the cold joint during the fabrication of steel cages. This approach clearly visualized the desired cold joint location during casting, allowing for the concrete placement to be halted upon reaching the predetermined elevation.

For specimens featuring vertical cold joints, external bracings and supports were constructed to ensure the stability of the wooden stoppers. Diagonal bracings were attached from the top ties to the bottom of the stoppers to prevent overturning during casting. Additional top ties were directly positioned above the stoppers to counteract any potential uplifting force induced by the concrete pressure. Supports connecting to the steel end form were installed at each end to prevent the displacement of the wooden stoppers and secure the position of the cold joint. Additionally, four ½-inch holes were drilled on each side of the steel form to accommodate continuous threaded rods running through both side forms, effectively restraining the displacement of the wooden stoppers. The concrete placement procedure for III-1.85-00-V and III-1.85-00-V-R are presented in Figure 5-16.

(a) Steel cage fabricated for the interior section

(b) Concrete cast in the interior section

(c) Steel cage fabricated for the exterior section

(d) Concrete cast in the exterior section

Figure 5-16 Concrete placement procedure for specimens with vertical cold joints

5.5.3. Post-Installed Reinforcement

For specimens designed with post-installed reinforcement, dowel bars were installed in the interior section of specimen V-1.85-00-VD and V-1.85-03-VD before the concrete was placed in the exterior section. The post-installing procedure strictly followed the guidelines provided by the epoxy distributor. According to the guidelines, holes were drilled into the vertical surface of the cold joints prior to the placement of the exterior section using an electric hammer drill with a concrete drill bit. To ensure the drilling accuracy, measuring and stabilizing tools were used in the beginning of the drilling process to maintain the correct positions and angles. After the holes were drilled, steel wire brushes and compressed air were used to remove debris and dust from the holes. Each hole was brushed and blown three times with compressed air before injecting the chemical

adhesive. The epoxy-based chemical adhesive was applied using a customized epoxy dispenser equipped with extension plastic hose and injection piston. The injection piston fit perfectly with the plastic hose and the dispenser, preventing air bubble formation within the doweling section. Before the hardening of chemical adhesive, the reinforcing bars were inserted into the drilled holes to ensure effective bonding between the reinforcing bars, the chemical adhesive, and the existing concrete. The doweling procedure is presented in Figure 5-17. and the interior section after the installation of dowel bars is shown in Figure 5-18.

(a) Hole drilling

(b) Steel wire brush

(c) compressed air

(d) Epoxy dispensing

(e) Rebar installation

Figure 5-17 Installation procedure for dowel bars

Figure 5-18 Interior section after the installation of dowel bars

5.6. Test Setup and Procedure

5.6.1. Test Setup

The specimens were tested under an idealized simply-supported setup with a set of adjustable loading applying rams. The setup consisted of two supporting frames anchored to a 96,000-pound strong floor, along with two 2000-kip capacity rams operated by pneumatic pumps. Prior to the experiments, the self-weight of the specimen and transfer girders was temporarily supported using two cylindrical concrete blocks and four hollow steel shafts.

The load was applied in a direction opposite to gravity, ensuring that cracks on the tension side would appear on the top of the specimen for easier visual inspection during the test. The primary hydraulic ram located on top of the strong floor beneath the testing region was used to apply load until failure. A secondary ram was positioned on the opposite side of the specimen to elevate the specimens evenly and prevent drastic rigid body motion before engagement with the supporting frames. The capacity of the strong floor, 6000 kips, exceeded the combined capacity of the hydraulic rams, ensuring adequate support throughout the experiments.

Two supporting frames consisted of two transfer girders were anchored to the strong floor using six 3-inch diameter steel rods, providing reaction forces from the top to the bottom. A pin and a roller were placed between the specimen and the transfer girders to establish the simply supported boundary condition. The photograph of the test setup with label for each component is shown in Figure 5-19. This configuration allowed for controlled loading and observation condition for the behavior of specimens under applied forces.

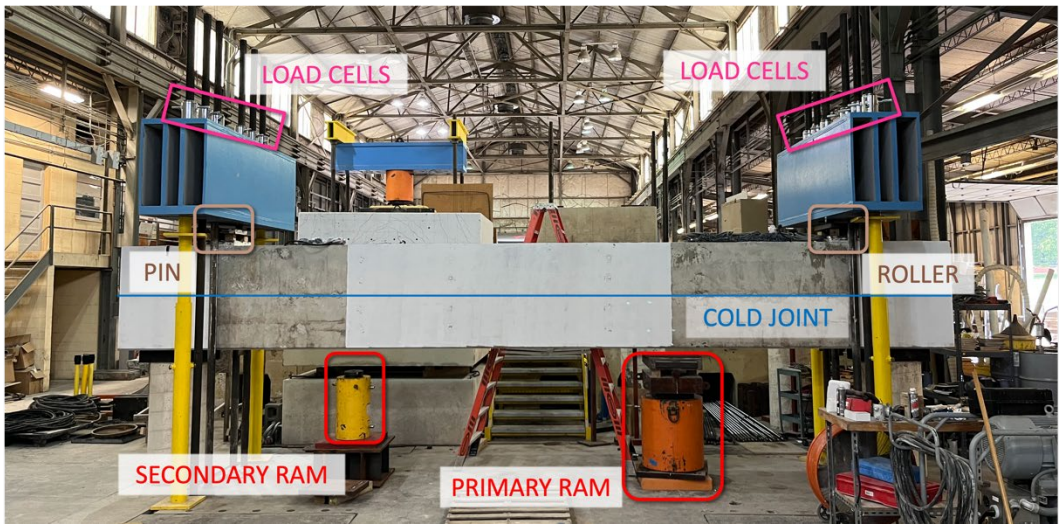

Figure 5-19 Test setup for deep beam specimens

5.6.2. Instrumentation

5.6.2.1. Load and Displacement Measurements

A 500-kip capacity load cell was mounted on top of each supporting rod using threaded fasteners. During the experiment, the uplifting applied load was transferred from the specimens to the transfer girders. The transfer girders were anchored to the strong floor via the threaded rods, restraining the upward displacement of the girders due to the uplifting load. The total reaction force provided by the reaction frame was determined by summing the forces in individual threaded rod recorded by the load cells. Differences in load cell readings across each transfer girder were analyzed to evaluate the presence of torsional effects during testing. This approach allowed for the identification of any uneven load distribution or unintended twisting of the system. The configuration of the supporting frame is illustrated in Figure 5-20, providing a visual representation of the experimental setup for monitoring and analyzing force distributions and potential torsional effects.

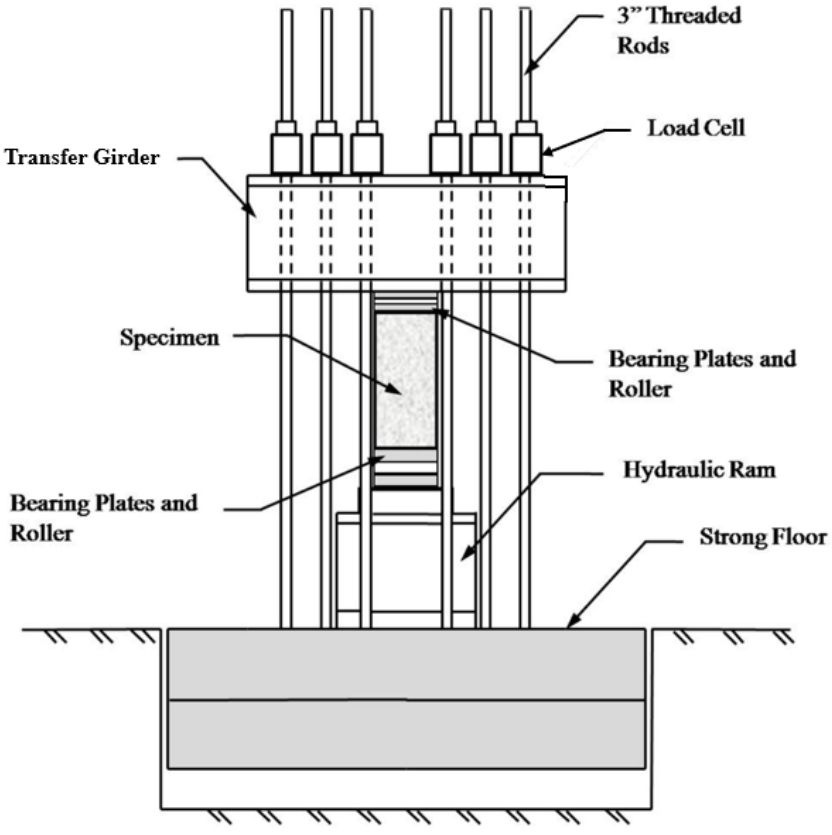

Figure 5-20 Supporting frame of the test setup (Re

Four 6-inch linear potentiometers were employed to monitor the displacement of the specimen at critical locations during the experiment. These potentiometers were strategically positioned under the supports, load point, and centerline of the entire beam to capture key

displacement data. An additional 2-inch linear potentiometer was attached to monitor the displacement of the strong floor beneath the primary ram. This setup was designed to account for potential deformation of the strong floor, ensuring accurate measurement of the actual specimen deformation at the loading point. The locations of the linear potentiometers are depicted in Figure 5-21.

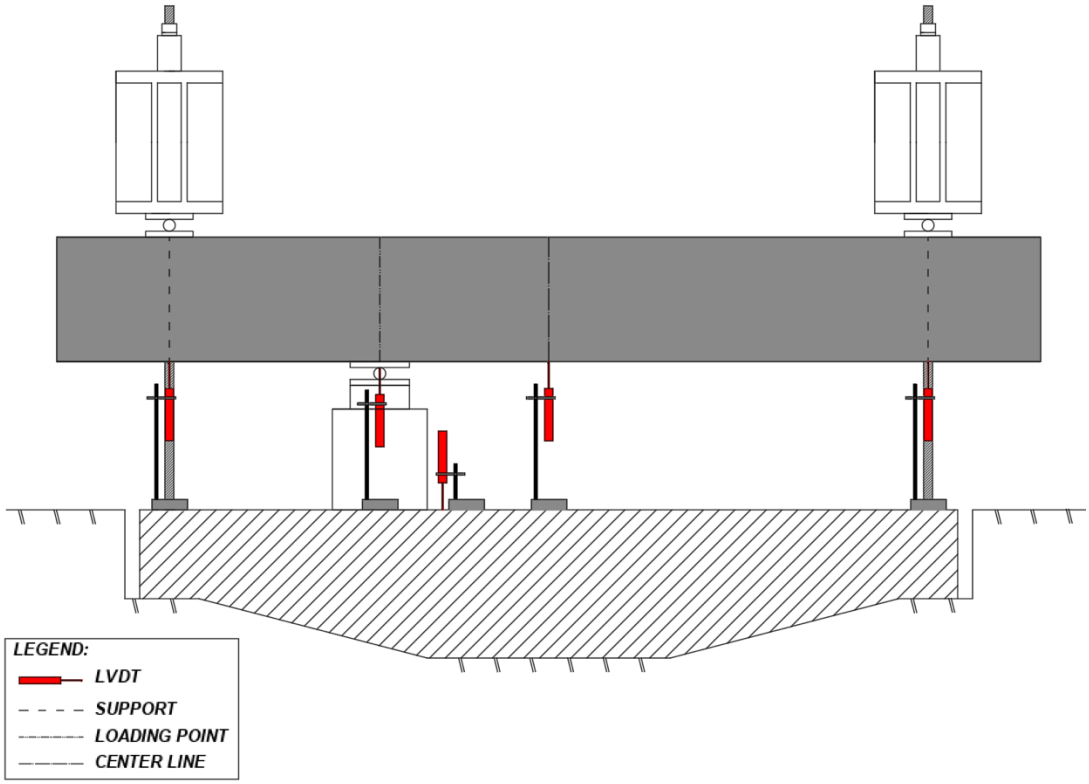

Figure 5-21 Locations of linear potentiometers

5.6.2.2. Strain Measurements

Strain gauges were attached to both legs of the stirrups and all the horizontal web reinforcement along the idealized strut line and the cold joint. The strain gauges positioned along the idealized strut line aimed to measure the strain response of web reinforcement along or adjacent to the primary crack as the compression strut approached failure. The strain response of the reinforcement was used to evaluate the strain of concrete within the compression strut. Based on the strain of concrete at failure, the development of concrete strength along the strut was quantified, facilitating the determination of the governing failure mode for each specimen.

Strain gauges were positioned at the intersection of reinforcement and the cold joints to investigate the interface shear behavior. For specimens with horizontal cold joints, strain gauges were attached to both legs of the stirrups at their intersection with the cold joints. In specimens with vertical cold joints, strain gauges were placed on the horizontal web reinforcement and longitudinal reinforcement at locations where these rebars intersected the cold joints. This

comprehensive arrangement of strain gauges enabled detailed monitoring of strain distribution at critical locations, providing insight into the impact of reinforcement on the structural response of cold joints.

Additional five sets of strain gauges were instrumented along the longitudinal reinforcement in the outermost layer to monitor the strain response at five different sections. Three sets of strain gauges were applied to the longitudinal bars within the testing region to measure the tensile strain in the reinforcing tie. Two sets of strain gauges were installed outside the testing region to investigate the anchorage efficiency of the development length region. Each set of strain gauges included two strain gauges positioned on the corner bars and two strain gauges attached to the center bars. The locations of strain gauges in specimens with a horizontal and a vertical cold joint are presented in Figure 5-22(a) and Figure 5-22(b), respectively.

To identify strain gauge data from various locations, a systematic labeling nomenclature was developed and consistently applied throughout the instrumentation process. Each label contains three components: the reinforcement type, the specific bar or side location, and the gauge section along the member. The first letter of each label indicates the type of reinforcement to which the strain gauge was attached: "L" for longitudinal reinforcement, "V" for vertical stirrups, and "H" for horizontal web reinforcement. The second letter specifies a particular reinforcing bar to which the strain gauge was affixed. For strain gauges on the longitudinal reinforcement, four rebars on the top layer, designated from west to east as bars A, B, C, and D, were instrumented. For stirrup and horizontal web reinforcement, the letter indicates the side of the specimen: side C refers to the face where cracks were visually marked during the experiment, and side D corresponds to the face monitored by the Digital Image Correlation (DIC) system. The number at the end of each label indicates the section along the member where the strain gauge was attached. Longitudinal reinforcement was instrumented with strain gauges in five different sections, as shown in Figure 5-22. For stirrups and horizontal web reinforcement, lower the numbers corresponds to locations closer to the support. Strain gauges instrumented along the cold joint followed the same labeling scheme with the addition of the suffix "CJ".

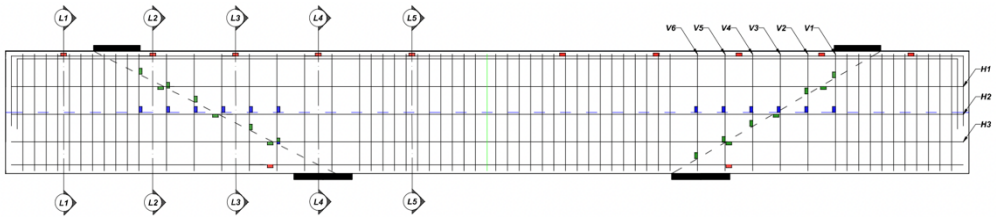

(a) Horizontal cold joint (DB-1.85-03-H & DB-1.4-03-H)

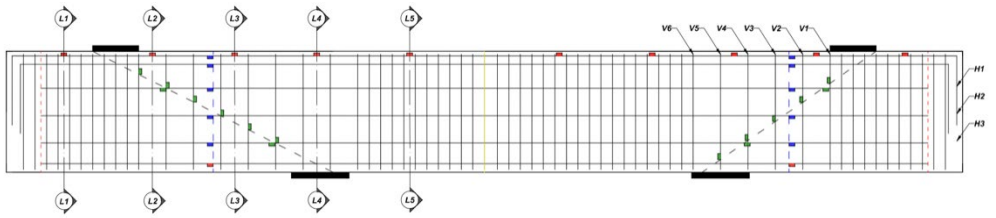

(b) Vertical cold joint (DB-1.85-03-V & DB-1.2-03-V)

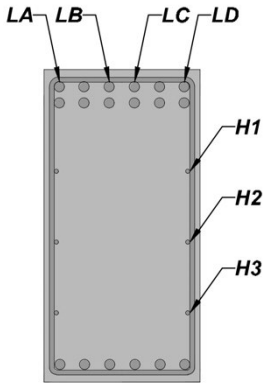

(c) Sectional diagram

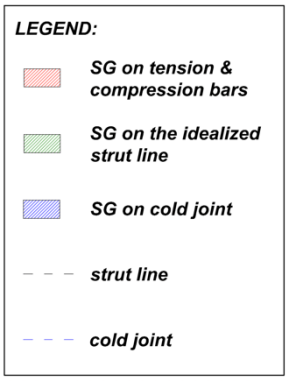

(d) Legend

Figure 5-22 Strain gauge location

5.6.2.3. Crack Width Measurements

Crack widths were measured after each load step using a standard crack comparator. The crack comparator features solid lines of predefined thicknesses that are visually compared against the observed cracks to estimate their widths. Since the comparison process involves a degree of subjective judgment, all crack width measurements were consistently performed by the same student throughout the experimental program to ensure the consistency and reliability of data. The crack comparator, shown in Figure 5-23, served as a visual aid for accurate crack widths assessment during the experiment.

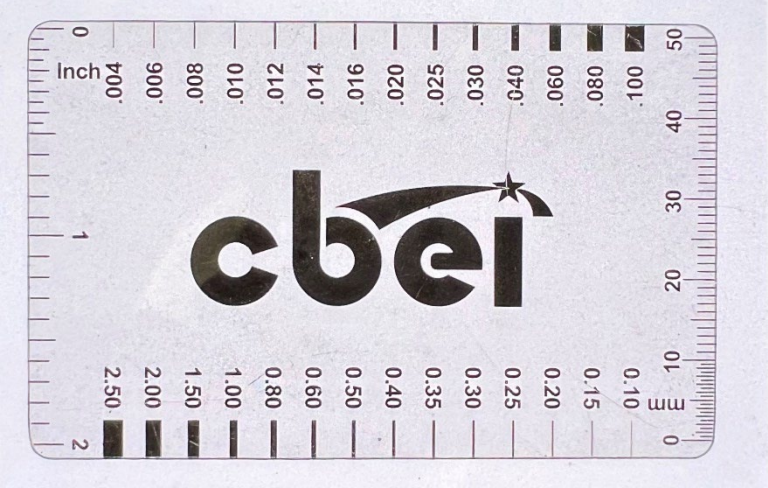

Figure 5-23 Crack comparator

5.6.2.4. Non-contact Instrumentation

A Digital Image Correlation (DIC) system was integrated into the experiment to monitor the strain field and crack propagation within the testing region. DIC utilizes two high-speed cameras to capture the images of speckle patterns applied to the surface of the testing region. These images were analyzed based on the virtual spatial coordinate systematic calibrated using customized calibration equipment. The calibration equipment provided predefined data that were used to unify the projection coordinates of each camera, allowing the system to accurately convert image differences into actual displacement measurements.

A reference image was selected for the DIC system to calculate deformation within the monitored area by analyzing the coordinate differences of speckle patterns in images taken at specific time intervals. This analysis enables the system to generate displacement and strain contours for the region of interest, facilitating the observation of crack propagation and identifying discontinuities in the strain profile. The components of the DIC system are detailed in Figure 5-24, which shows the setup and technology used to capture and analyze strain and displacement response during the experiment.

(a) Speckle pattern on the testing region

(b) High speed cameras

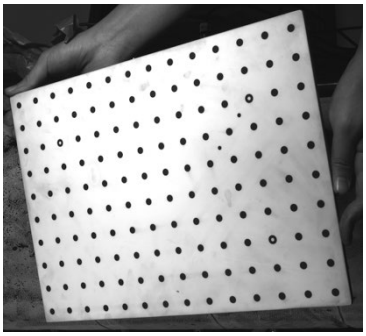

(c) Calibration board

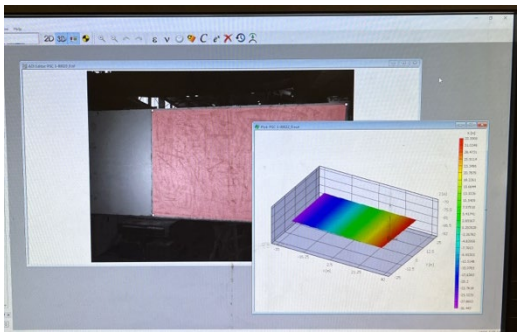

(d) Image data projection

Figure 5-24 DIC setup and equipment

5.6.3. Testing Procedure

The specimens were loaded monotonically in 50-kip increments of shear force at a constant loading rate of 10 kips/min until failure. The load increments were determined from the near-end reaction force, ensuring the shear force in the testing regions of specimens with various shear spans are comparable at each load step. This load increment represented approximately 15% of the average nominal capacity of the specimens. At each load stage, cracks were carefully marked throughout the beam, and the widths of cracks in the testing regions were measured and labeled alongside the cracks. Photographs were taken at each load stage to document the crack widths, locations, and geometries. These images were subsequently used to develop crack maps that illustrated the progression of cracks over the course of loading.

Each beam specimen was subjected to two tests. Prior to each test, the beam was loaded using two hydraulic rams to ensure proper contact with both reaction frames. The primary ram, used to apply load during the experiment, was positioned at the designated loading point in the testing region. The auxiliary ram was located near the far-end support. Both rams were extended simultaneously until full engagement was confirmed by a total load cell reading of approximately 10 kips on each reaction frame. Subsequently, the primary ram was further extended to reach the

first load increment. The auxiliary ram was then retracted and disengaged from the specimen to prevent potential interference with the experimental boundary conditions.

The behavior of the specimen was carefully monitored until shear failure occurred in the testing region. Prior to the second test, external clamps were applied to confine the shear failure region from the first test, preventing the existing failure from influencing the response of the subsequent experiment. The primary ram was repositioned to the designated loading point of the second testing region. The testing procedure described above was repeated, and the behavior of the second testing region was monitored until failure. The photograph of this testing procedure is presented in Figure 5-25.

(a) Test setup for the first test

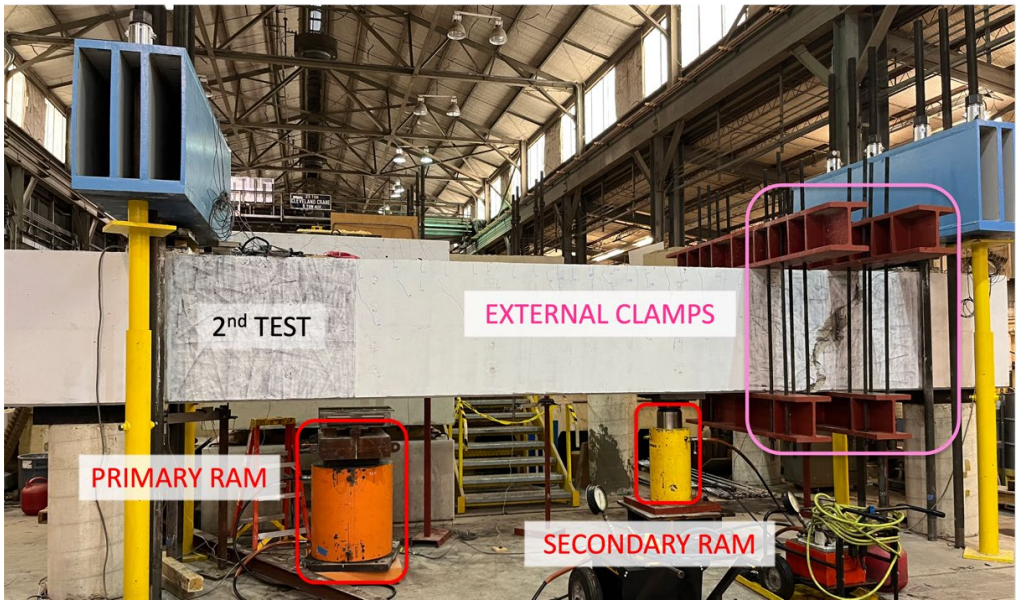

(b) Test setup for the second test

Figure 5-25 Experimental procedure for conducting two tests in one beam

5.7. Experimental Results

In this section, the experimental results of Task 5 are presented and discussed in detail. Specifically, the following aspects of the deep beam experiments are addressed:

- The shear behavior and capacity of deep beam specimens (Section 5.7.2 & 5.7.3)
- The crack pattern and failure mode (Section 5.7.4)
- The evolution of reinforcement strain (Section 5.7.5)
- The serviceability evaluation based on the measured crack width (Section 5.7.6)
- The displacement and strain contour of the test region (Section 5.7.7)

Finally, a summary of the experimental results is presented and pivotal information is highlighted to standardize the response and facilitate an in-depth discussion on the research findings.

5.7.1. Summary of Experimental Results

The experimental results are summarized in Table 5-6, and the design details of each specimen are previously provided in Table 5-2. The ultimate shear strength, V_{test}, is defined as the shear force acting on the mid-span of testing region corresponding to the maximum applied load, including the contribution from the self-weight of the specimen and the transfer girders. Additionally, the experimental results of two specimens from previous research (Birrcher et al., 2009) are included in Table 5-6. These two deep beam specimens were cast monolithically without the presence of cold joints. With dimensions and reinforcement details identical to the specimens in current study, these specimens serve as control specimens for investigating the influence of cold joints on structural behavior. To facilitate a direct comparison across specimens while eliminating the effect of material strength and sectional dimensions, the ultimate shear strengths were normalized by the compressive strength of the weaker concrete layer, $f_{c,min}$, and the sectional area, $b_w d$, as presented in Table 5-6.

The definition of variables in Table 5-6 are listed as follows:

$f'_{c,min} =$ compressive strength of the weaker concrete layer measured in accordance with ASTM C39/C39M-21, psi.

$\rho_{cj} =$ ratio of reinforcement intersecting cold joint.

$a/d =$ shear-span-to-depth ratio

V_{crack} = shear at mid-span of testing region when the first diagonal crack was observed, kip

V_{test} = maximum shear force at the mid-span of test region, including the estimated self-weight of the specimen and transfer girders, kip. Specific details regarding the determination of maximum shear force are presented later in Section 5.7.3

b_w = beam width, in.

d = distance from extreme compression fiber to centroid of tensile reinforcement, in.

δ_{peak} = deformation of specimen corresponding to peak load, in.

Table 5-6 Test results of deep beam experiments

Beam ID	$f'_{c,min}$ (ksi)	ρ_{cj}	a/d	V_{crack} (kips)	V_{test} (kips)	$\frac{V_{test}}{f'_{c,min}b_w d}$	δ_{peak} (in.)	$\frac{V_{test}}{\delta_{peak}}$ (kips/in.)
I-1.85-03-H	3.10	0.003	1.85	121	404	0.16	0.60	673
I-1.4-03-H	3.10	0.003	1.4	-	680	0.27	0.70	969
I-1.0-03-H	2.07	0.003	1.0	-	820	0.49	0.81	1019
II-1.85-00-H	2.17	0	1.85	122	296	0.17	0.62	480
III-1.85-00-V	4.60	0	1.85	123	416	0.11	0.76	550
III-1.85-00-V^{R}	4.73	0	1.85	-	642	0.17	1.18	543
IV-1.85-03-V	4.19	0.003	1.85	125	494	0.15	0.88	432
IV-1.2-03-V	4.07	0.003	1.2	-	526	0.16	0.62	851
V-1.85-00-V^{D}	4.19	0	1.85	-	67	0.03	0.29	231
V-1.85-03-V^{D}	4.07	0.003	1.85	-	78	0.03	0.14	557
III-1.85-03b^{M}	3.30	-	1.85	114	471	0.18	-	-
III-1.2-03^{M}	4.22	-	1.2	-	829	0.24	-	-

Note: H = specimen with horizontal cold joint

V = specimen with vertical cold joint

^{R} = specimen with intentionally roughened cold joint

^{D} = specimen with cold joint intersected by dowel reinforcement

^{M} = monolithic specimen from TxDOT Project 0-5253 (Birrcher et al., 2009)

5.7.2. Load-Deflection Response

To obtain the load-deflection response of specimens, the displacement measured from the loading point must be meticulously processed to account for all possible displacement of components in the test setup. As previously mentioned in Section 2.4.2.1, linear potentiometers were installed at the critical loading points to measure the displacement of the specimen during the experiment. This measured displacement consists of the settlement of the strong floor and the uplifting of the transfer girders, as illustrated in Figure 5-26. The uplifting displacement of transfer girders were measured from the linear potentiometers located under the supports. The displacement of girders resulted in the rigid body motion of specimens. Therefore, the displacement at the loading point from the rigid body motion of specimens was calculated by linear interpolating the measured displacement of two girders. The actual deflection of beam at the loading point was then determined by eliminating the rigid body motion and the settlement of the strong floor, as per Equations (5-4) and (5-5).

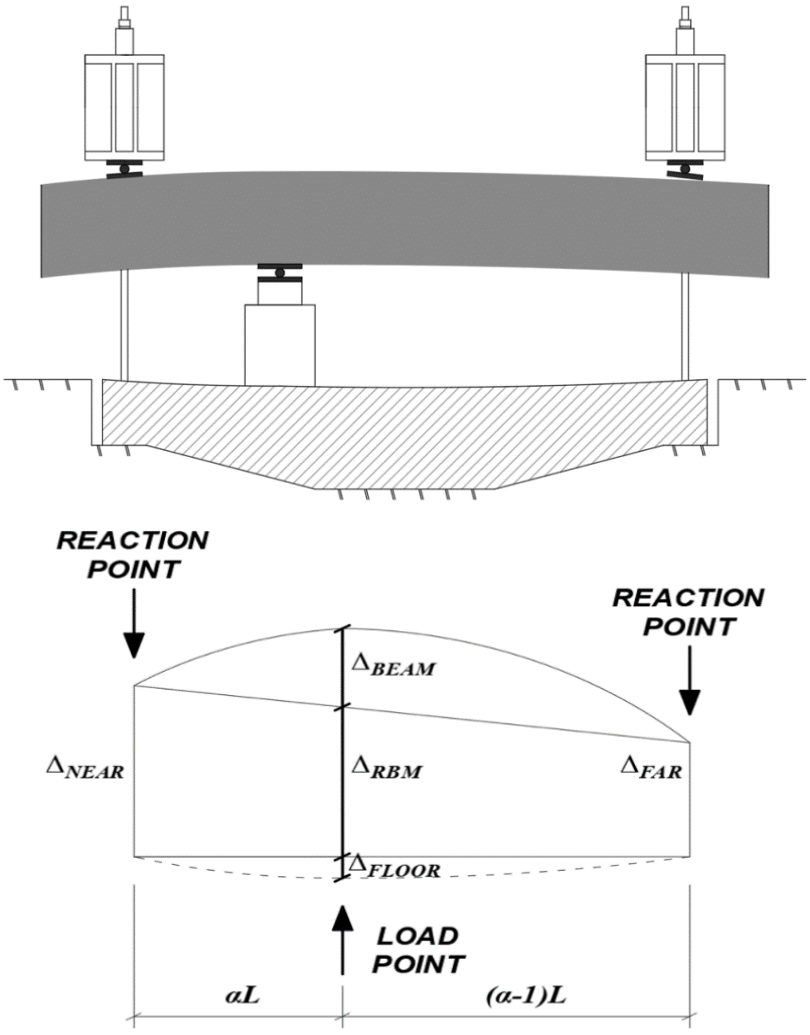

Figure 5-26 Diagram of beam displacements due to rigid body motion and flexural and shear deformations

$$\Delta_{RBM} = \Delta_{FAR} + (1 - \alpha) \cdot (\Delta_{NEAR} - \Delta_{FAR}) \quad (5\text{-}4)$$

$$\Delta_{BEAM} = \Delta_{LOAD} - \Delta_{RBM} - \Delta_{FLOOR} \quad (5\text{-}5)$$

The load-deflection responses measured from the experiments are presented in Figure 5-27. To compare the responses between specimens without the effect of material strength and sectional dimensions, the normalized shear-deflection responses of specimens with an a/d ratio of 1.85 are presented in Figure 5-28.

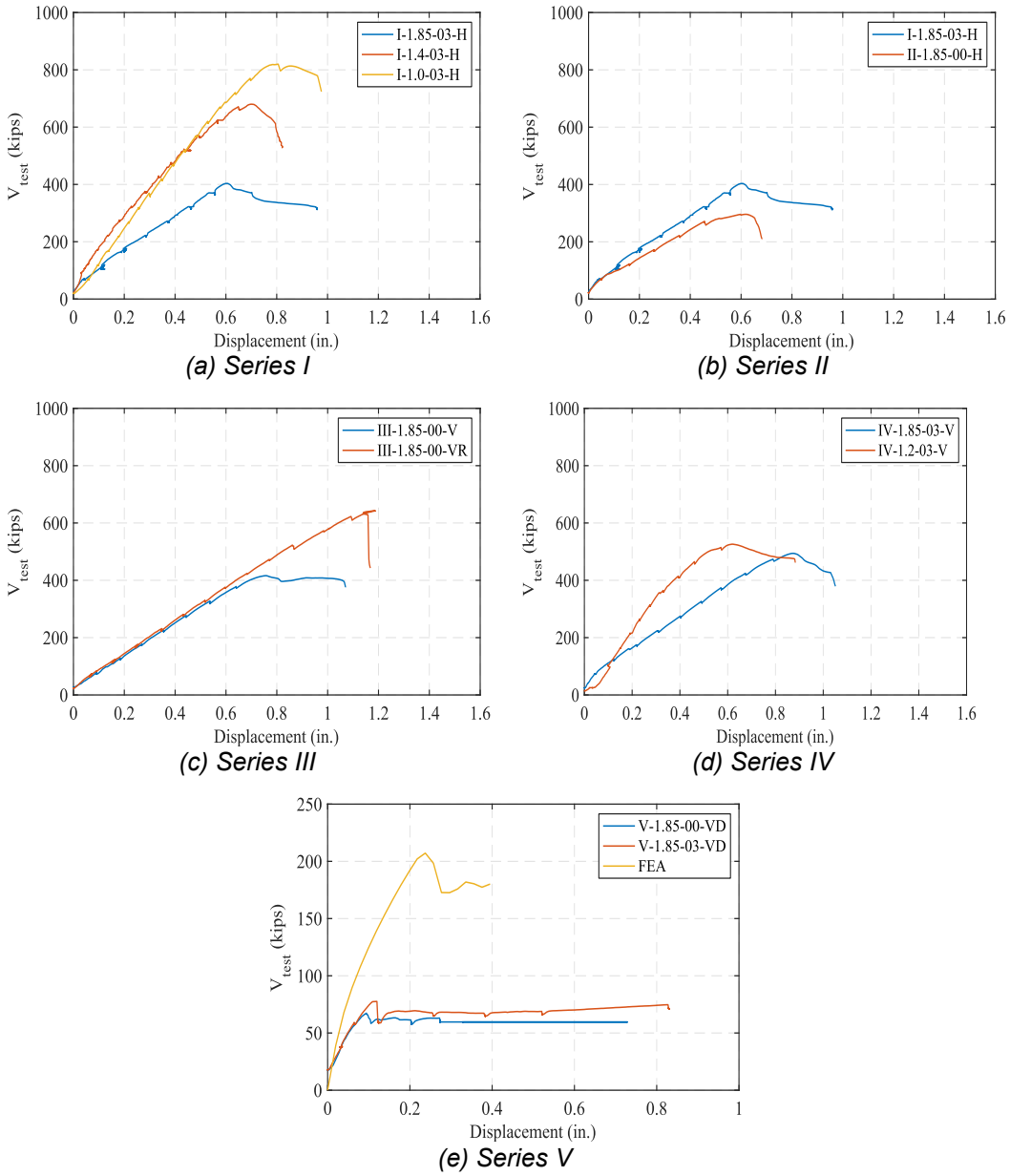

Figure 5-27 Load-deflection response

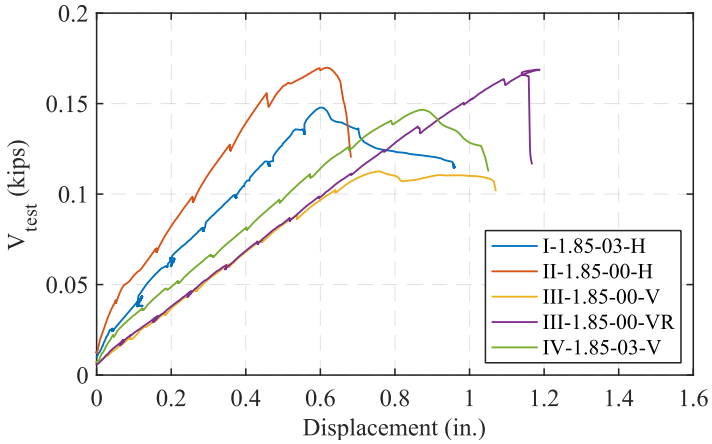

Figure 5-28 Normalized shear-deflection response of specimens with a/d ratio of 1.85

From the load-deflection responses of specimens in Series I shown in Figure 5-27(a), the reduction in the a/d ratio was observed to enhance the stiffness of the specimens. The load-deflection responses were also used to assess the behavior of cold joints. Based on the small-scale cold joint experiments, such as the slant-shear tests in Task 4, a significant increase in slip of the cold joints was observed when the applied shear approached the ultimate capacity of the interface. Therefore, deep beams with cold joint failure were also expected to exhibit a significant increase in deformation due to the increasing slip of cold joints at ultimate load. However, the continuous and stable deflection responses indicate that no substantial increase in slip along the horizontal cold joints. Without the slip required to mobilize the maximum shear resistance at the cold joints, it is concluded that the shear capacity of the horizontal cold joints was not fully developed at failure.

To investigate the effect of web reinforcement, the response of Specimen I-1.85-03-H was compared to that of Specimens II-1.85-00-H. Since the two specimens were cast using different batches of concrete, the comparison was made based on their normalized shear-deflection responses presented in Figure 5-28. Based on the comparison, no significant negative effect on the stiffness or the shear capacity of deep beams was observed in specimens without web reinforcement intersecting the horizontal cold joint.

Specimen III-1.85-00-V exhibited a nonlinear load-deflection response following the peak load, as shown in Figure 5-27(c). As the deflection increased beyond the ultimate load, the applied load remained relatively constant. A comparative evaluation of all specimens with an a/d ratios of 1.85, as presented in Figure 5-28, reveals that all specimens except III-1.85-00-V experienced brittle shear failure, characterized by a rapid reduction in normalized shear after reaching peak load. In contrast, Specimen III-1.85-00-V demonstrates a more gradual reduction in shear load, resulting in a relatively ductile post-peak response. This ductile nonlinear behavior of Specimen III-1.85-00-V is attributed to the slip along the nonroughened, unreinforced vertical cold joint, which influenced the deflection behavior of specimen and governed the failure mechanism. The

nonlinear behavior was not observed in Specimen III-1.85-00-VR, which features a roughened cold joint interface.

A similar nonlinear response is also observed in Specimen IV-1.2-03-V, as shown in Figure 5-27(d). Despite exhibiting greater initial stiffness due to its lower shear-span-to-depth ratio compared to Specimen IV-1.85-03-V, the applied load remained relatively constant as the deflection increased beyond the peak load. The post-peak behavior of both Specimen III-1.85-00-V and Specimen IV-1.2-03-V underscore the need for further investigation into cold joint behavior to understand the influence of cold joints on the overall structural response and shear capacity of deep beams.

The load-deflection responses of Specimen V-1.85-00-VD and V-1.85-03-VD exhibit substantially weaker capacities with a significant post-peak ductility, as shown in Figure 5-27(e). After reaching the peak load, the shear load remained relatively constant as the displacement continued to increase. This behavior significantly deviates from the post-peak response of other specimens characterized by shear failure.

A preliminary finite element analysis was conducted to evaluate the response of specimens with post-installed reinforcement. The model assumed a bonding strength between the reinforcement and chemical adhesive equivalent to nominal bond strength summarized in Table 5-5. The load-deflection response from the analysis, also presented in Figure 5-27(e), is significantly different from the experimental observations. This indicates that the actual bonding strength between the dowel bars under tension and the chemical adhesive is incomparable with the nominal bonding strength. Additional discussions and explanations are provided in the following paragraphs, focusing on various aspects of structural behavior for specimens with post-installed reinforcement.

5.7.3. Evaluation of Strength Data

The shear strength of the specimens, V_{test} in Table 5-6, was determined by the shear at the critical section under maximum applied load. The critical section was identified as the midpoint between the support and the loading point in the testing region, as shown in Figure 5-29. To accurately calculate the shear at this location, the self-weight of the specimen and the weight of the transfer girders were incorporated with the load cell measurement. Figure 5-29 illustrates the location of the critical section and the shear diagram of the specimens during the experiment. The reaction forces measured by load cells are denoted as R_A and R_B, where P_{TR} refers to the weight of the transfer girder. The unit self-weight of the specimen, denoted as ω_{DL}, is specified on the beam. The applied load, P_L, was calculated as the sum of all force components mentioned above.

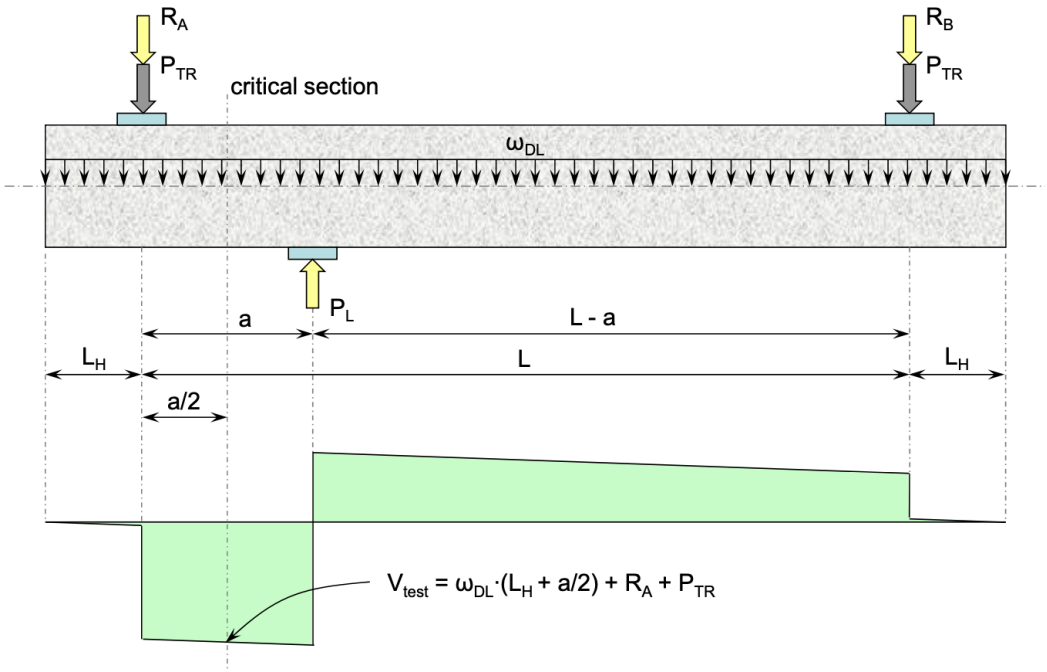

where, R_A = reaction force measured at the near support, kips

R_B = reaction force measured at the far support, kips

P_{TR} = weight of the transfer girder, kips

ω_{DL} = unit self-weight of specimen, kips/in

P_L = total applied load, kips

L_h = distance from the end of the beam to the support, in.

a = shear span of the testing region, in.

L = distance between two supports, in.

Figure 5-29 Force and shear force diagram for deep beam tests

To evaluate the behavior of all specimens cast with different batches of concrete, the shear strength was normalized by the material strength of concrete and the sectional dimensions of the specimens. For reinforced concrete members governed by shear failure, it is common to associate the shear strength with the tensile strength of concrete by normalizing the structural capacity based on the square root of concrete compressive strength,$\sqrt{f_c'}$. However, to better assess the effect of the cold joints on the compression capacity of concrete struts, the shear strength was normalized by the compressive strength of concrete, f_c', in this research. This evaluation approach aligns with the strut-and-tie method (STM), which uses the concrete compressive strength, f_c', to assess the compression capacity of the strut-to-node interface.

The experimental results of deep beams without cold joints from previous project (Birrcher et al., 2009) designed identically to specimens in this research are also listed in Table 5-6 to serve as control specimens. The maximum shear measured from these prior experiments were

normalized using the same approach mentioned in the previous paragraph. By respectively comparing the normalized shear strength of Specimen I-1.85-03-H and I-1.4-03-H to Specimens III-1.85-03b and III-1.2-03, no significant reduction in capacity was observed in specimens with horizontal cold joints.

Specimen II-1.85-00-H exhibits normalized shear strength identical to that of Specimen I-1.85-03-H. This indicates that the influence of web reinforcement intersecting horizontal cold joints is insignificant to the shear capacity of deep beams. Combining the conclusion drawn from the shear capacities of specimens in Series I, it is concluded that the effect of horizontal cold joint is generally negligible.

For specimens with vertical cold joints, Specimen III-1.85-00-V exhibits 35% reduction in normalized shear capacity comparing to Specimen III-1.85-03b from TxDOT Project 0-5253 (Birrcher et al., 2009). By roughening the interface of the cold joint or providing web reinforcement intersecting the cold joint, Specimen III-1.85-00-VR and IV-1.85-03-V demonstrate normalized shear capacity approximately identical to monolithic deep beam. In conclusion, for specimens with a/d ratios of 1.85, the shear capacity was negatively influenced by the nonroughened, unreinforced vertical cold joints. However, the implementation of interface roughening and 0.3% of web reinforcement crossing the interface have shown to pronouncedly enhance the shear capacity, neutralizing the detrimental effect of cold joints on shear behavior of deep beams.

Despite the presence of web reinforcement across the cold joint, Specimen IV-1.2-03-V exhibits 33% reduction in normalized shear capacity comparing to monolithically cast deep beam, III-1.2-03. Since the reduction in a/d ratio results in the decrease in the inclination between the compression load path and the cold joint, the experimental results also indicate that the shear capacity decreases with the reduction in the inclination. Identical results were drawn from the slant shear tests in Task 4, where the reduction of inclination between the load path and the cold joints negatively influenced the shear capacity. This effect is due to the interaction between the inclination and the force components applied perpendicularly and parallelly to the cold joint. The decrease in inclination reduces the perpendicular force component that contributed to the shear resistance and the enhances in the parallel force component transferred through the interface. This reduction in shear capacity and simultaneous enhancement in shear demand of cold joints result in the decrease in deep beam capacity.

Both specimens with dowel bars exhibited a significant reduction in capacity. Specimen V-1.85-00-VD and V-1.85-03-VD showed an 87% decrease in normalized shear strength compared to specimen III-1.85-03b. This substantial strength reduction highlights the inefficiency of dowel bars installed across the cold joint. The underlying causes of this reduction in shear strength will be further examined and elaborated in the following paragraphs, with a focus on the failure pattern observed from the experiments.

5.7.4. Crack Pattern and Failure Mode

During the experiments, the propagations of cracks were marked and recorded with photographs at each load step. The photographs focused only on the testing region where the loading point is at the bottom and support is on the top. For Specimen I-1.85-03-H, minor cracks along the cold joint were initially observed when the reaction force reached 50 kips, as shown in Figure 5-30(a). Subsequently, multiple flexural cracks on the top and diagonal shear cracks in the testing region developed at 100 kips, as presented in Figure 5-30(b). These existing cracks widened as the applied load increased, accompanied by the propagation of diagonal shear cracks throughout the specimens. Notably, no additional cracks were observed along the cold joint after the reaction force reached 150 kips. When the near-end reaction force reached 300 kips, diagonal shear cracks were observed in the non-testing region near the far-end support, pre-cracking the testing region of the subsequent experiment. The primary shear crack developed progressively from the loading point to the support, leading to shear failure of specimen when the shear load at the critical section reached 404 kips, as presented in Figure 5-30(c) and illustrated in Figure 5-30(d).

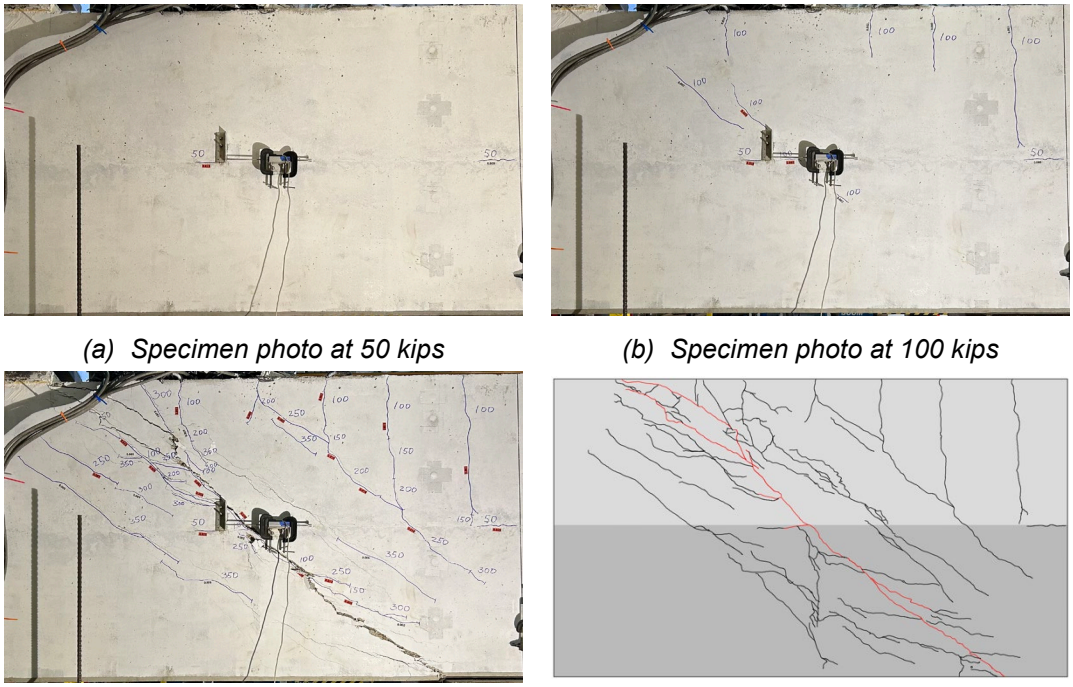

(a) Specimen photo at 50 kips

(b) Specimen photo at 100 kips

(c) Specimen photo at failure

(d) Crack map at failure

Figure 5-30 Experimental photographs and crack map of I-1.85-03-H

For Specimen I-1.4-03-H, diagonal shear cracks were observed at the first load step. These diagonal shear cracks initiated from the pre-existing cracks induced by the first experiment, as shown in Figure 5-31(a). No minor cracks were observed along the cold joint in this experiment at the first load step. The increase in load was predominantly accompanied by the development of shear cracks, with only a few short and thin flexural cracks appearing at 250 kips, as shown in Figure 5-31(b). The specimen ultimately failed when the shear load at the critical section reached 680 kips. The failure was governed by the primary shear crack that penetrated through the testing region. The crack patterns at failure are presented in Figure 5-31(c) and illustrated in Figure 5-31(d). The loading point and support of Specimen I-1.4-03-H are located at the bottom left corner and the top right corner, respectively.

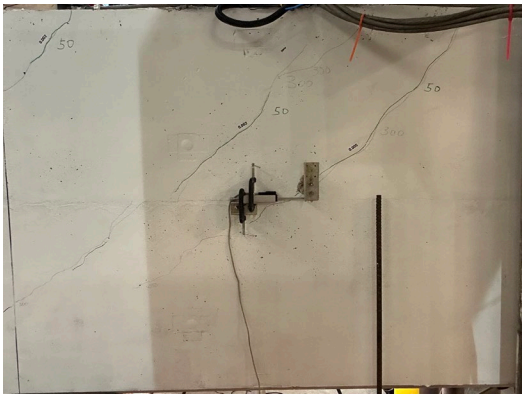

(a) Specimen photo at 50 kips

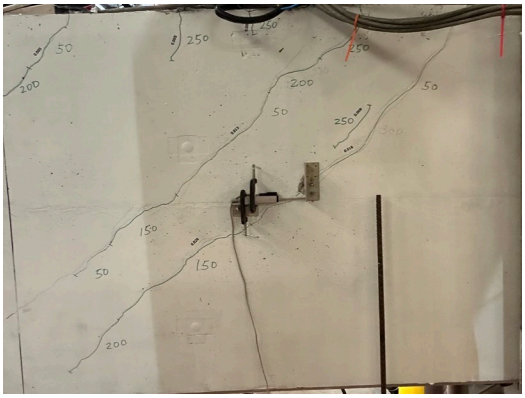

(b) Specimen photo at 250 kips

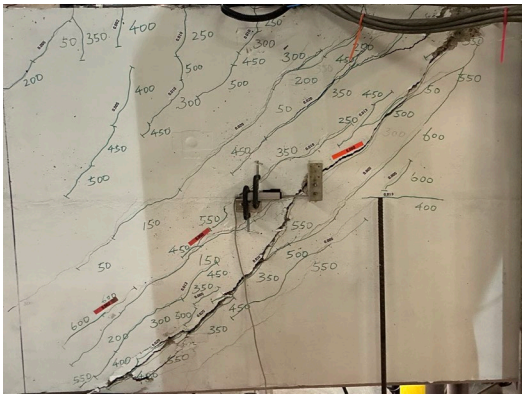

(c) Specimen photo at failure

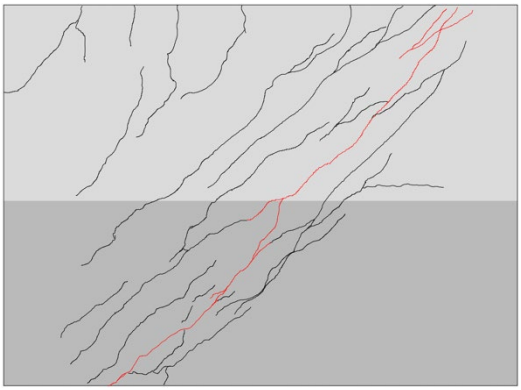

(d) Crack map at failure

Figure 5-31 Experimental photographs and crack map of I-1.4-03-H

For specimen I-1.0-03-H, no significant effect of cold joint was observed from the crack patterns and the governing failure mode. The first flexural crack appeared at 50 kips, as shown in Figure 5-32(a), followed by the occurrence of a diagonal shear crack at 150 kips, as shown in Figure 5-32(b). The specimen ultimately failed when the shear load at the critical section reached 820 kips. The failure crack patterns, presented in Figure 5-32(c) and (d), resemble the patterns of a typical deep beam, with shear cracks propagating from the loading point to the support.

(a) Specimen photo at 50 kips

(b) Specimen photo at 150 kips

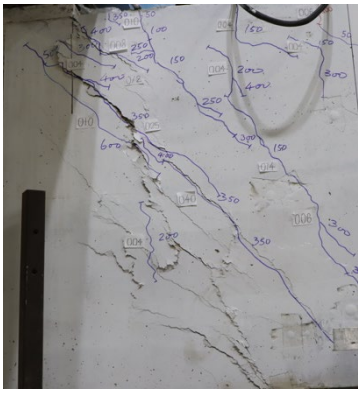

(c) Specimen photo at failure

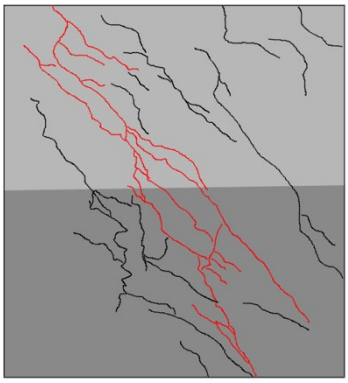

(d) Crack map at failure

Figure 5-32 Experimental photographs and crack maps of I-1.0-03-H

For specimen II-1.85-00-H, the absence of web reinforcement resulted in the development of significantly wider cracks at each load step. The first flexural crack occurred at 50 kips, as shown in Figure 5-33(a). The diagonal shear cracks began to develop at 100 kips, as shown in Figure 5-33(b). The measured width of the initial shear crack was 0.030”, which is substantially wider than the average initial shear cracks, 0.006”, measured from other specimens. This comparison highlights the effect of web reinforcement in restraining the development of shear cracks. The specimen failed when the shear load at the critical section reached 296 kips, and the crack patterns are presented in Figure 5-33(c) and (d). Despite the wider cracks observed during the experiment, no significant effect of the unreinforced horizontal cold joint was observed on the crack patterns and the governing failure mode.

(a) Specimen photo at 50 kips

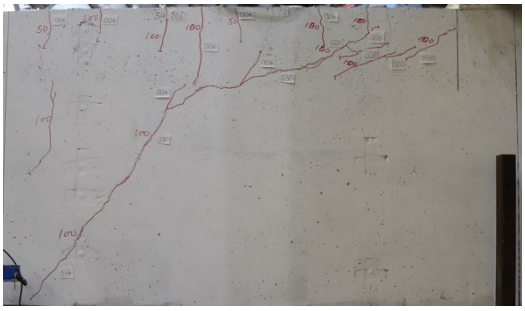

(b) Specimen photo at 100 kips

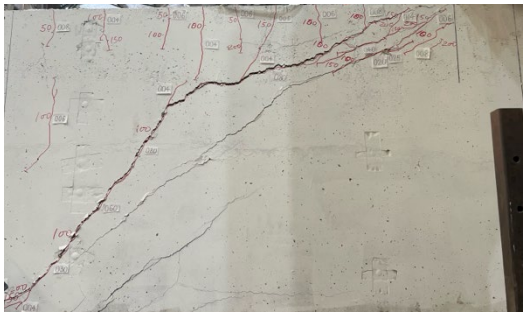

(c) Specimen photo at failure

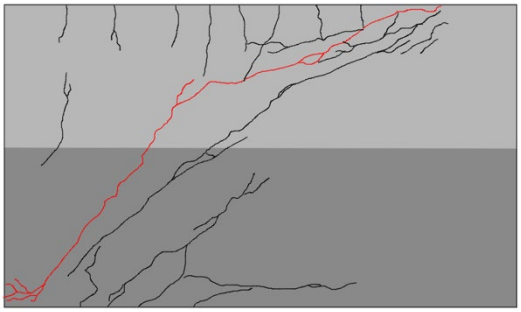

(d) Crack map at failure

Figure 5-33 Experimental photographs and crack maps of II-1.85-00-H

Unlike typical shear cracks in deep beams that develop directly from the loading to the supporting point, a transition section of shear crack propagated along the cold joint was observed in Specimen III-1.85-00-V, as presented in Figure 5-34(a). This crack pattern indicates that a localized region of cold joint was engaged in the shear resisting mechanism of deep beam. The shear crack developed along the cold joint widen as the load increase, eventually resulting in the failure of structure, as shown in Figure 5-34(c) and (d). Additionally, comparing to monolithic cast deep beams in which the shear cracks distributed uniformly along the load path throughout the testing region, the failure crack pattern of Specimen III-1.85-00-V focused significantly on the widest shear crack developed along the cold joint. This observation indicates that the stress redistribution along the compression load path was incomplete when the localized shear failure at the cold joint occurred, resulting in shear failure prior to the crushing of concrete strut.

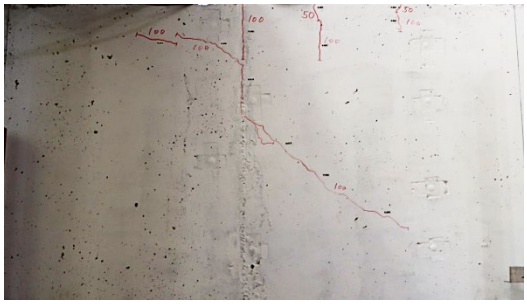

(a) Specimen photo at 100 kips

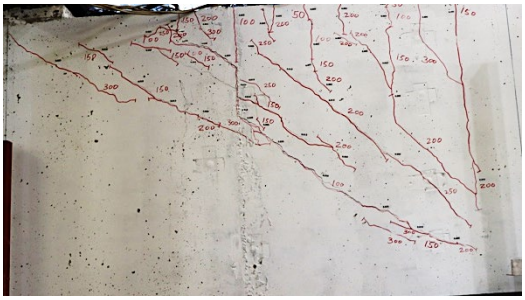

(b) Specimen photo at 350 kips

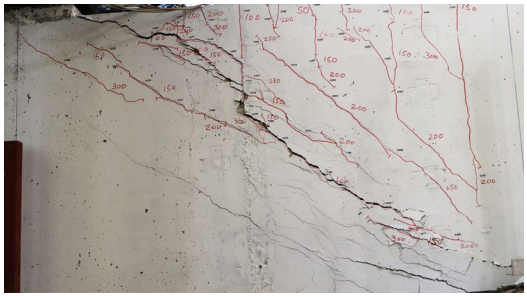

(c) Specimen photo at failure

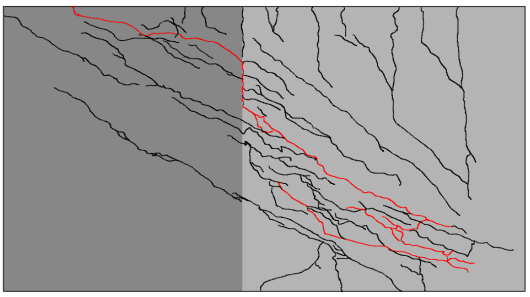

(d) Crack map at failure

Figure 5-34 Experimental photographs and crack map of III-1.85-00-V

Despite being pre-cracked by the previous test on the same beam prior to the experiment, the same shear crack development along the cold joint was not observed in Specimen III-1.85-00-VR. The shear crack was observed propagating along the existing crack at the cold joint in the first two load steps, as shown in Figure 5-35(a). As the applied load reached 500 kips, a more uniform distribution of shear crack without significant discontinuity along the cold joint was observed, as shown in Figure 5-35(b). According to the failure crack patterns shown in Figure 5-35(c) and (d), the damage of the compressive strut region is more pronounce through visual inspection comparing to Specimen III-1.85-00-V. The discontinuity of the widest shear crack along the cold joint was not observed at failure in Specimen III-1.85-00-VR and the overall shear cracks were evenly distributed throughout the testing region.

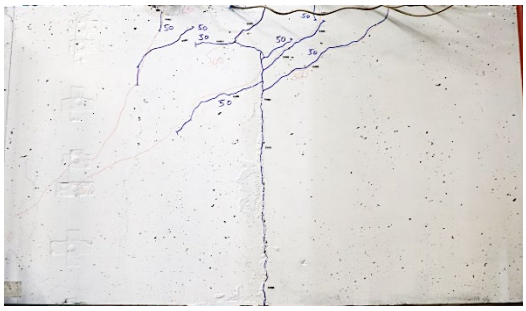

(a) Specimen photo at 50 kips

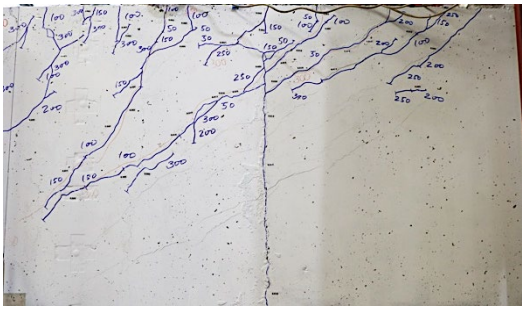

(b) Specimen photo at 500 kips

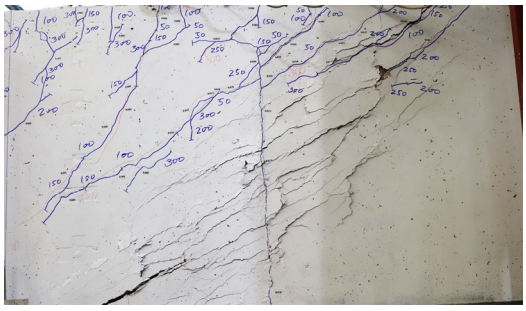

(c) Specimen photo at failure

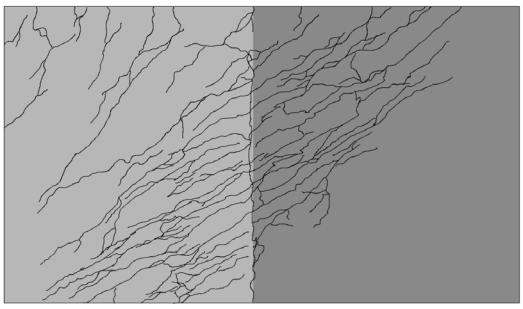

(d) Crack map at failure

Figure 5-35 Experimental photographs and crack map of III-1.85-00-VR

Shear failure along the cold joint was insignificant for IV-1.85-03-V. As shown in Figure 5-36(a), flexural crack along the cold joint occurred at 50 kips. Multiple shear cracks developed along the existing cracks from previous experiment when the applied load reached 100 kips, as demonstrated in Figure 5-36(b). Despite the presence of a pre-cracked cold joint, the development of shear cracks was independent to the path of existing cracks. As the load reached 450 kips, no significant discontinuity along the interface was observed in the widest shear crack that eventually governed the failure of specimen. The failure crack patterns are presented in Figure 5-36(c) and illustrated in Figure 5-36(d). This indicates that by providing 0.3% of reinforcement intersecting the cold joint, the increase of interface shear resistance allows the compressive strength of strut to fully developed before the failure of cold joint. Accordingly, the structural capacity and the response of IV-1.85-03-V are similar to deep beams without cold joints.

(a) Specimen photo at 50 kips

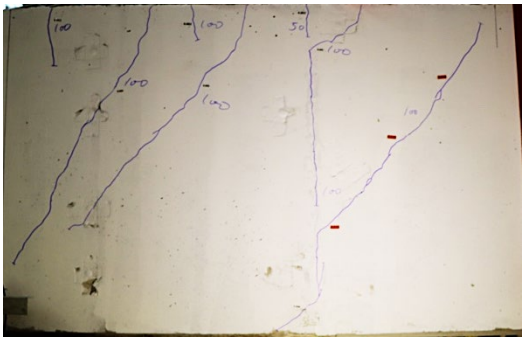

(b) Specimen photo at 100 kips

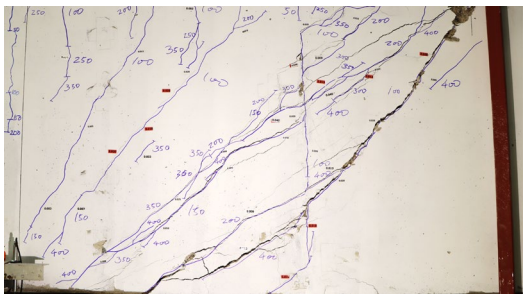

(c) Specimen photo at failure

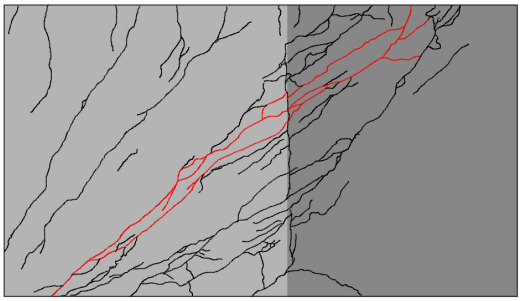

(d) Crack map at failure

Figure 5-36 Experimental photographs and crack map of IV-1.85-03-V

Specimen IV-1.2-03-V exhibited significant shear failure along the cold joint. As presented in Figure 5-37(a), flexural cracks on top of the specimen and shear cracks along the cold joint were observed when the reaction force reached 50 kips. The discontinued shear crack propagated from the cold joint towards both the supporting and loading points as the applied load increased. Additionally, when the reaction force reached 350 kips, as shown in Figure 5-37(b), the discontinued section of shear crack further developed along the cold joint. This shear crack propagation indicated that a wider range of the interface was engaged in the shear resisting mechanism. The failure occurred when the shear load at the critical section reached 526 kips. The crack patterns and crack map diagram at failure, presented in Figure 5-37(c) and (d), exhibit a significant shear crack developed along the intersection of the compression load transferring path and the cold joint.

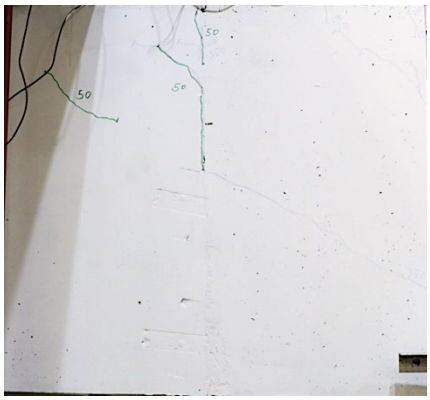

(a) Specimen photo at 50 kips

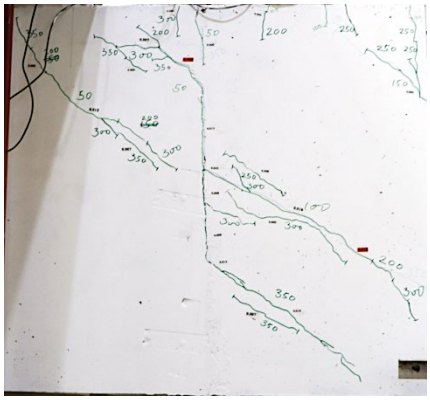

(b) Specimen photo at 350 kips

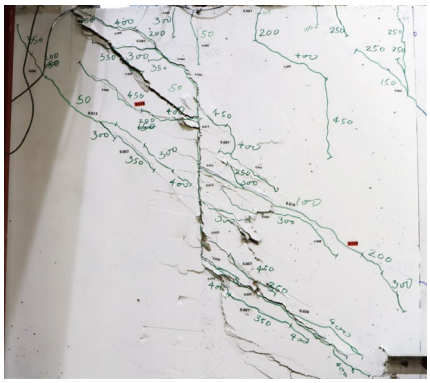

(c) Specimen photo at failure

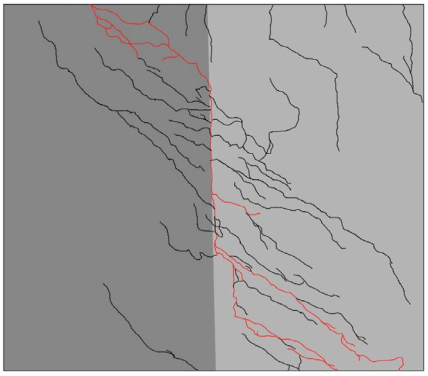

(d) Crack map at failure

Figure 5-37 Experimental photographs and crack map of IV-1.2-03-V

The failure of specimens with post-installed reinforcement were governed by anchorage failure of post-installed reinforcement instead of the crushing of concrete strut. For specimen V-1.85-00-VD, the cold joint cracked due to self-weight prior to the experiment, as shown in Figure 5-38(a). This observation suggests that the unreinforced cold joint section is highly susceptible to cracking, even under minimal construction or service loads. Therefore, reinforcement should be incorporated throughout the cold joints to facilitate load transfer and ensure the serviceability of the structure. During the experiment, failure occurred before reaching the first load step. A horizontal crack originated from the cold joint at the location where post-installed reinforcement was implemented. As the applied displacement increased, this crack further propagated from the cold joint into the interior section of the specimen, as shown in Figure 5-38(b). The observed horizontal crack pattern indicates anchorage failure between the chemical adhesive and the post-installed reinforcement, resulting in pullout of the tension-transferring reinforcement from the surrounding concrete in the interior section.

(a) Crack at cold joint under self-weight *(b) Specimen photo at failure*

Figure 5-38 Experimental photographs of V-1.85-00-VD

Specimen V-1.85-03-VD exhibits the same failure mode as Specimen V-1.85-00-VD. Based on the observation from Specimen V-1.85-00-VD, load increments were reduced from 50 kips to 20 kips for Specimen V-1.85-03-VD to better measure and record the development of failure cracks. The first flexural crack occurred at the cold joint when the reaction force reached 20 kips, as shown in Figure 5-39(a). Additional flexural cracks continued to develop as the load increased. At 60 kips, anchorage failure cracks began to propagate from the cold joint toward the chemical-bonded section, as shown in Figure 5-39(b). Once the anchorage failure was initiated, no additional flexural resistance was provided by the specimen as the post-installed rebars began to slip, dissipating tension forces to other components. The experiment continued by increasing the displacement until significant spalling of concrete occurred at the anchorage region, exposing the post-installed reinforcement, as shown in Figure 5-39(c) and (d).

Due to the anchorage failure, the effect of post-installed reinforcement at cold joint intersected by the compressive strut remain inconclusive. Notably, no crack was observed along the cold joint with 0.3% of post-installed web reinforcement under self-weight before and after the experiment, demonstrating an improvement in restraining interface cracks compared to Specimen V-1.85-00-VD.

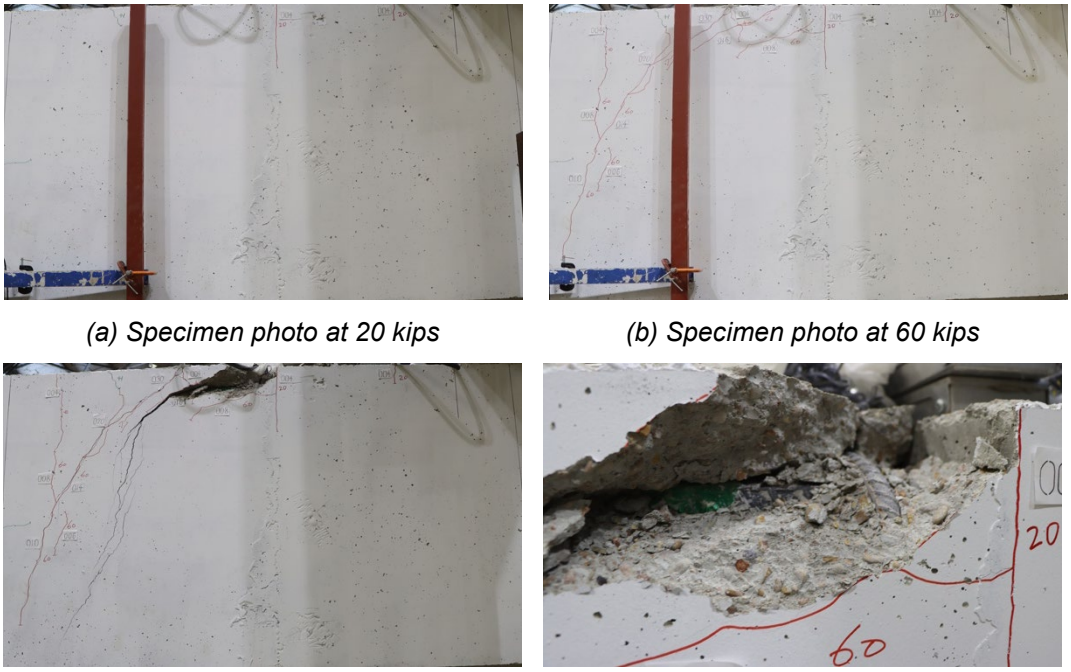

(a) Specimen photo at 20 kips *(b) Specimen photo at 60 kips*

(c) Specimen photo at failure *(d) Reinforcement exposure*

Figure 5-39 Experimental photographs of V-1.85-03-VD

All specimens with cast-in-place reinforcement experienced failure governed by shear failure. The shear failure of deep beam is equivalent to the crushing of the concrete strut in the strut-and-tie model, where the model resist shear through compression strength of concrete. For specimens with horizontal cold joints, the failure-inducing cracks developed from the loading point to the support without propagating along the cold joints. The crack patterns observed in these specimens are similar to the crack patterns observed from previous experiments from TxDOT Project 0-5253 (Birrcher et al., 2009). This observation suggests that the influence of horizontal cold joints is insignificant on the shear behavior of deep beams.

The localized shear failure of cold joints was observed to accompany the strut failure of Specimen III-1.85-00-V and Specimen IV-1.2-03-V. The interface failure was prevented by applying interface roughening and 0.3% of web reinforcement across the interface. In conclusion, beams with nonroughened, unreinforced vertical cold joints and specimens with smaller a/d ratios demonstrated failure mechanism associated with the localized failure of cold joints.

The anchorage failure observed in both specimens with post-installed reinforcement suggests that the anchorage provided by the chemical adhesive is insufficient to transfer tension across cold joints. The finite element analysis also demonstrated that with the nominal bonding strength and the anchorage length designed for the specimen, the expected capacity of specimens with post-installed reinforcement is substantially greater than the experimental results. Accordingly, alternative design approaches, such as sectional expansion and the application of fiber-reinforced polymer, should be investigated to provide a more reliable design for cold joints with substantial tension demand.

5.7.5. Strain Gauge Data

The strain of reinforcement measured by the strain gauges are presented in Figure 5-40 to Figure 5-46, along with the corresponding rebar configurations and failure patterns of each specimen. To facilitate the comparison across specimens, the specimen orientations in the figures are consistent in this section with the loading point located at the top right corner and the support positioned at the bottom left corner. The locations of strain gauges are indicated by rectangles shaded with color according to the ratio of strain at ultimate load to the yielding strain. For specimens with horizontal cold joints, yielding of reinforcement was measured by strain gauges located along the strut-line. In contrast, no yielding was recorded by the strain gauges positioned along the cold joint. This comparison indicates that the reinforcement in the strut region was more engaged in the load-resisting mechanism than the reinforcement crossing the cold joint at peak load. The conclusion is consistent with the failure modes identified from the crack patterns, suggesting that the failure mechanism of specimens I-1.85-03-H, I-1.4-03-H, and I-1.0-03-H were all governed by the crushing of concrete strut.

Although the horizontal cold joint was found to have a negligible effect on the overall failure modes of the specimens, the stirrups crossing the cold joint within the strut region eventually yielded during the experiments. This observation suggests that the cold joints remained subjected to compression and shear forces transmitted through the testing region. Accordingly, further evaluation is necessary to assess the structural integrity of the discontinuous interface.

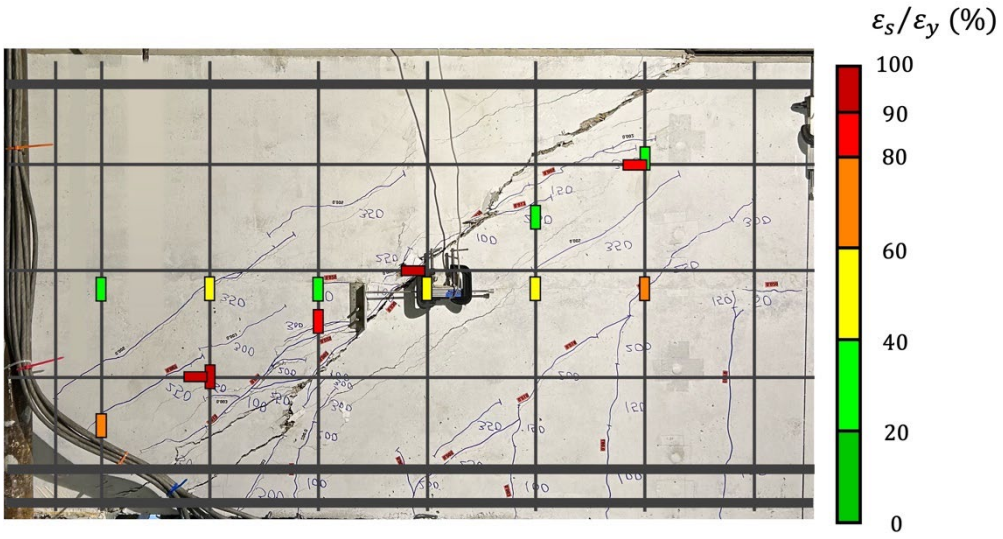

(a) Strain distribution in web reinforcement and failure pattern at ultimate load

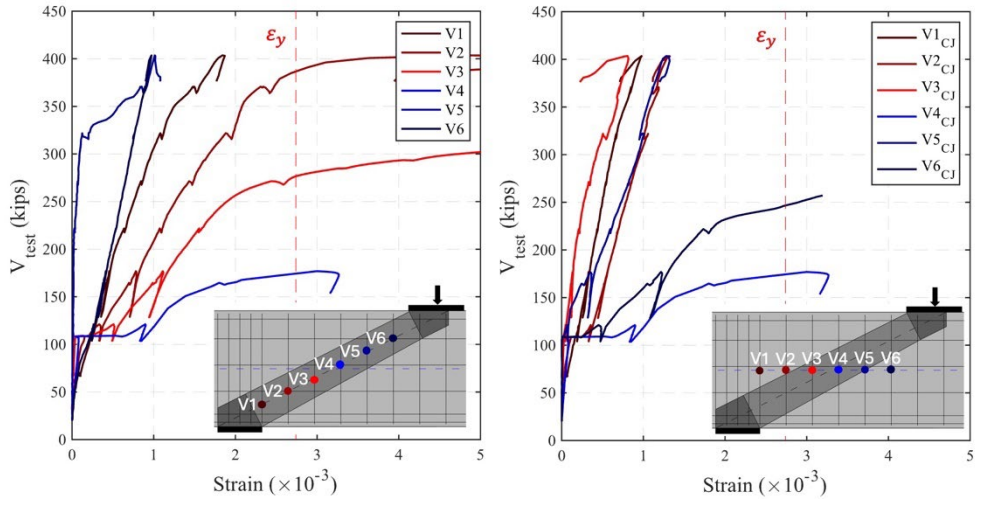

(b) Strain development along strut line *(c) Strain development along cold joint*

Figure 5-40 Strain gauge response of Specimen I-1.85-03-H

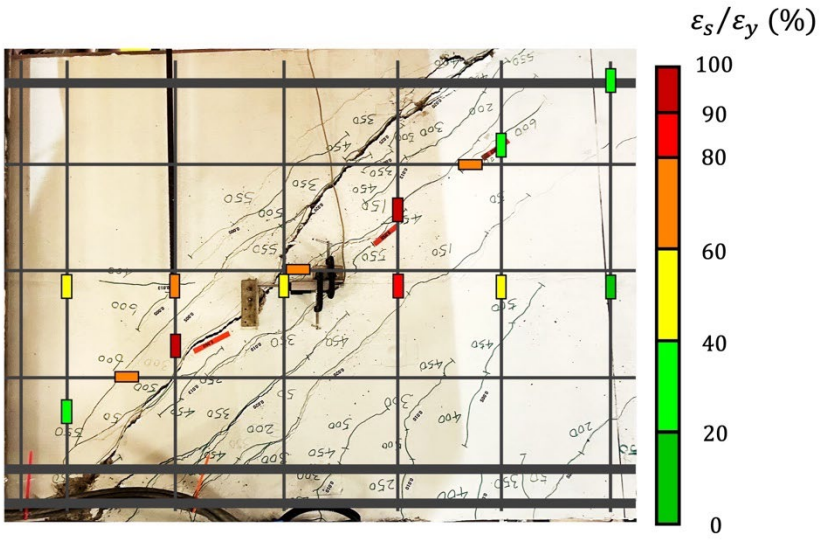

(a) Strain distribution in web reinforcement and failure pattern at ultimate load

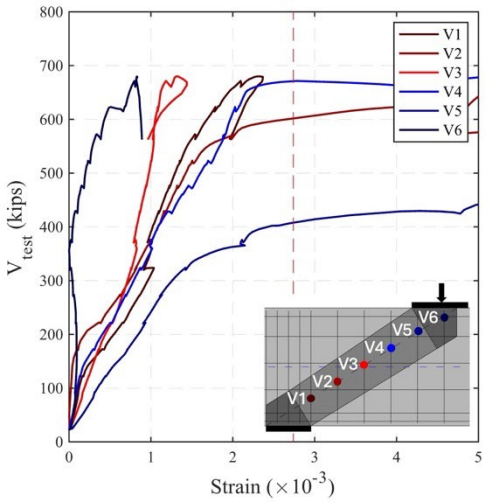

(b) Strain development along strut line

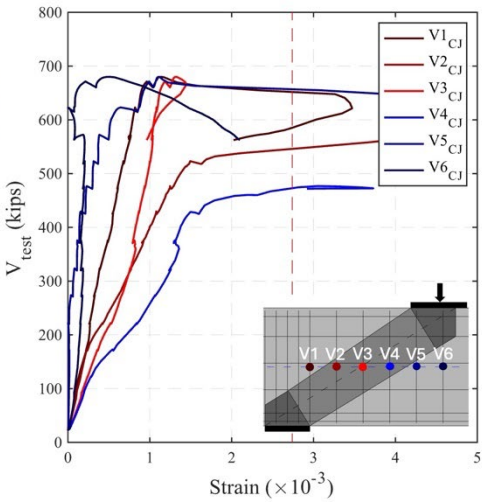

(c) Strain development along cold joint

Figure 5-41 Strain gauge response of Specimen I-1.4-03-H

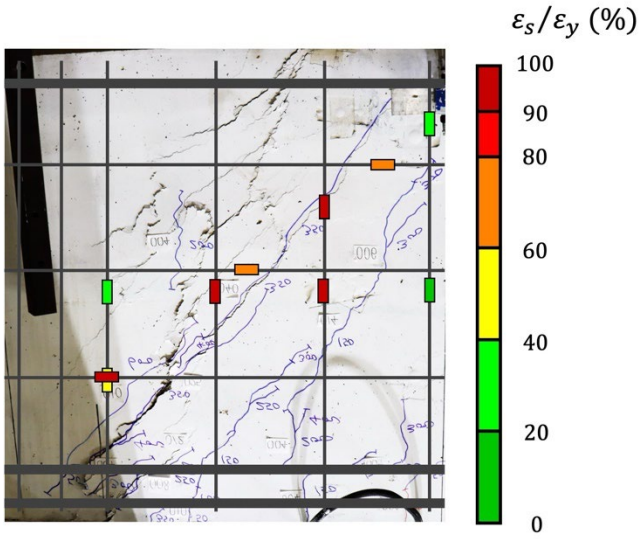

(a) Strain distribution in web reinforcement and failure pattern at ultimate load

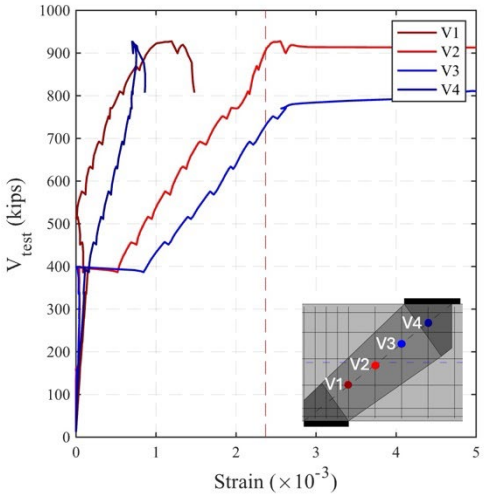

(b) Strain development along strut line

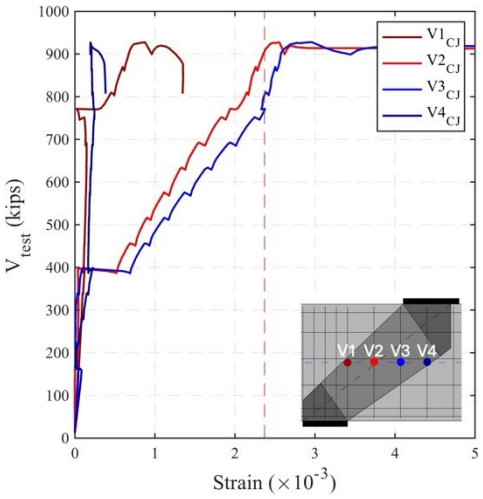

(c) Strain development along cold joint

Figure 5-42 Strain gauge response of Specimen I-1.0-03-H

For specimens with vertical cold joints, the strain developed along the strut-line was compared to across four specimens. In Specimen III-1.85-00-V and Specimen IV-1.2-03-V, three out of eight and two out of eight strain gauges, respectively, recorded yielding of rebar. For Specimen III-1.85-00-VR and Specimen III-1.85-03-V, five out of eight strain gauges along the strut-line exhibited yielding. These results suggest that the compression strain in the strut region was less developed in Specimen III-1.85-00-V and Specimen IV-1.2-03-V at peak load, implying that failure of these two specimens occurred before the compression capacity of strut was fully mobilized.

Strain gauges along the vertical cold joint were available only in Specimen IV-1.2-03-V. Among these strain gauges, yielding of reinforcement was observed exclusively at the intersection of the strut and the cold joint. This indicates that the localized portion of cold joint within the strut region was specifically engaged in the load resisting mechanism at ultimate load. However, since Specimen III-1.85-00-V and Specimen III-1.85-00-VR were designed without reinforcement intersecting the cold joint, no strain gauges measurement can be used to further validate the strain condition along the cold joint. This highlights the importance of non-contact instrumentation, which enables a more in-depth investigation of strain and displacement profiles at cold joints.

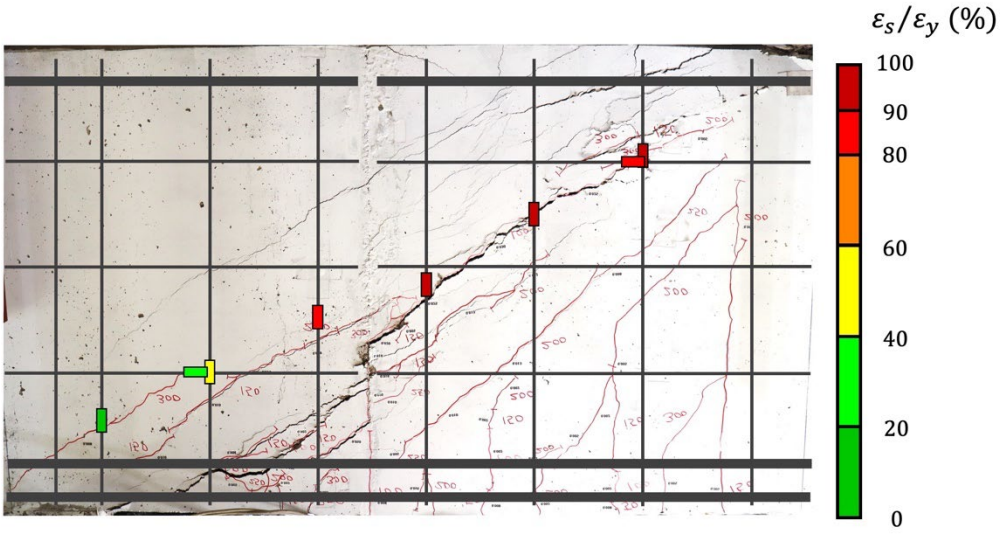

(a) Strain distribution in web reinforcement and failure pattern at ultimate load

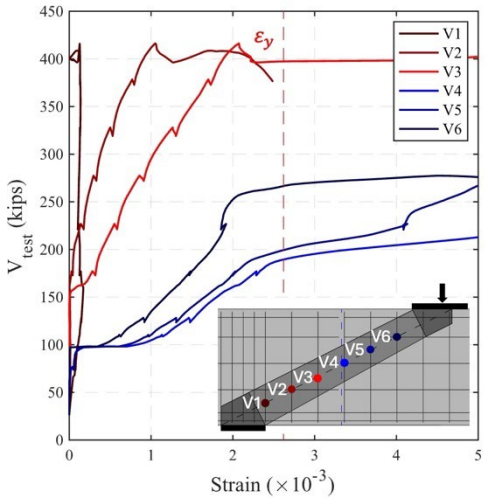

(b) Strain development along strut line

Figure 5-43 Strain gauge response of Specimen III-1.85-00-V

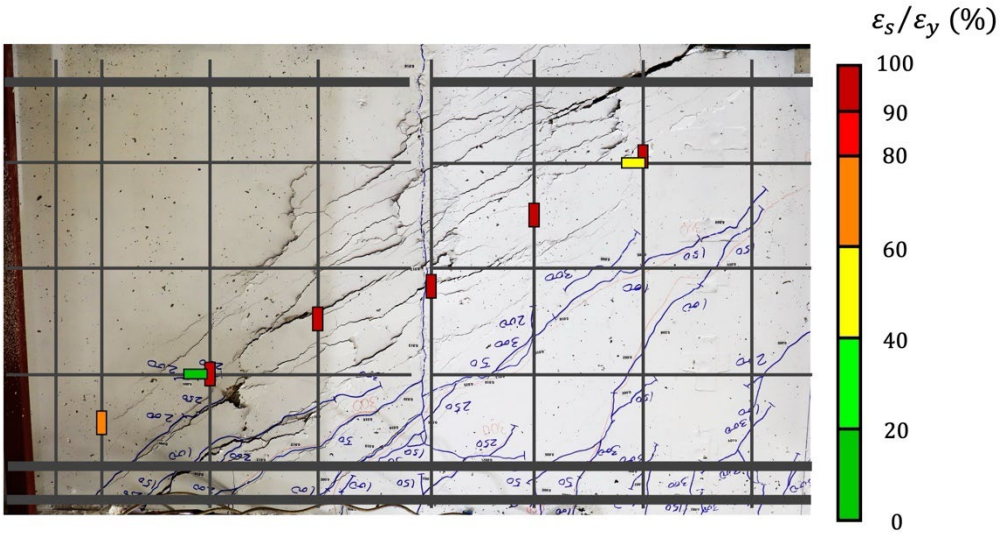

(a) Strain distribution in web reinforcement and failure pattern at ultimate load

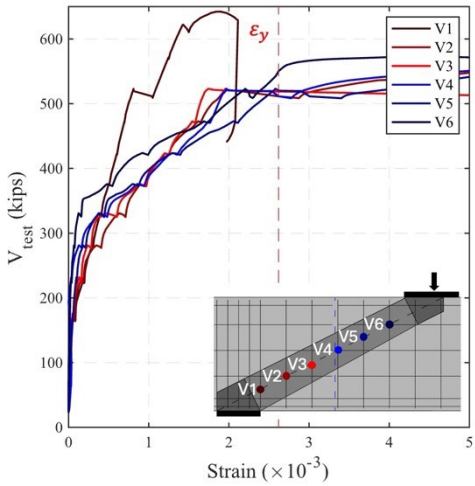

(b) Strain development along strut line

Figure 5-44 Strain gauge response of Specimen III-1.85-00-VR

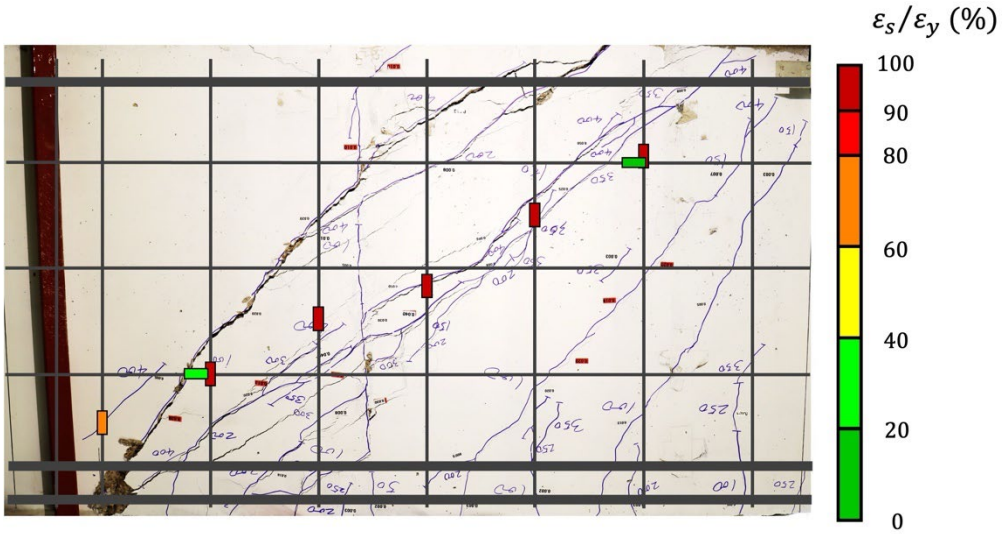

(a) Strain distribution in web reinforcement and failure pattern at ultimate load

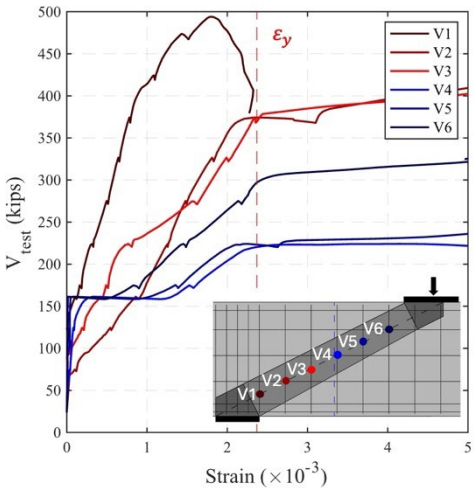

(b) Strain development along strut line

Figure 5-45 Strain gauge response of Specimen IV-1.85-03-V

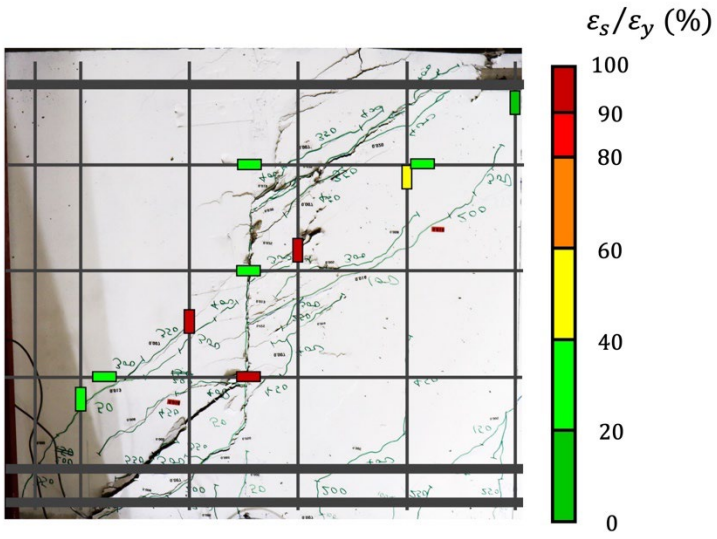

(a) Strain distribution in web reinforcement and failure pattern at ultimate load

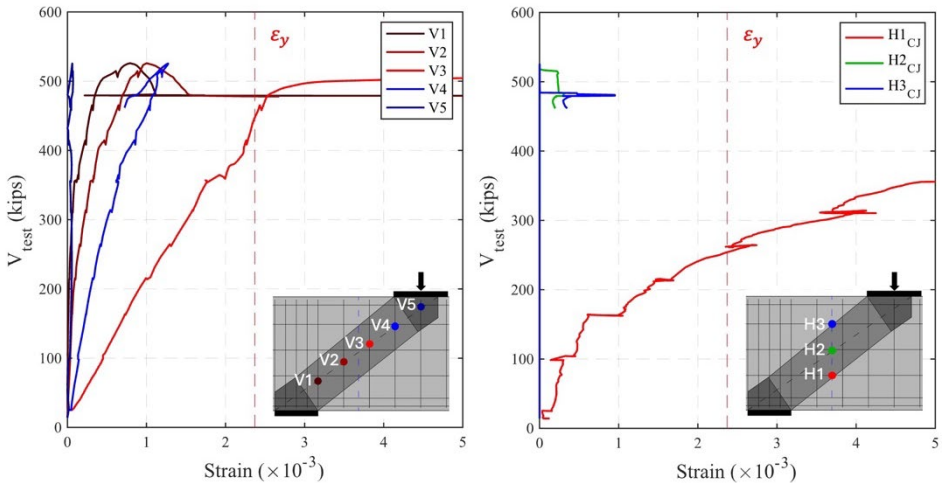

(b) Strain development along strut line *(c) Strain development along cold joint*

Figure 5-46 Strain gauge response of Specimen IV-1.2-03-V

5.7.6. Evaluation of Serviceability Data

The widths of the widest diagonal shear cracks at each load step were used to evaluate the serviceability of specimens. The second testing region of each beam was potentially cracked during the first test, initiating the shear cracks at an earlier stage along the pre-existing cracks during the second test. Therefore, only the crack data from the specimens tested first in each beam were used to evaluate the serviceability performance. The shear load corresponding to the occurrence of the first diagonal shear crack for four specimens are listed in Table 5-6. The diagonal crack widths measured at each load step are plotted in Figure 5-47.

The level of service load and the benchmark crack width, plotted in Figure 5-47, were estimated based on the formulation proposed by previous research (Birrcher et al., 2009) to facilitate the evaluation of structural serviceability. To estimate the service load, assumptions regarding the governing load case, the percentage of live and dead load, and the ratio of nominal to experimental capacity were outlined in Figure 5-48. In conclusion, the service load was estimated to be 33% of the maximum applied load, in accordance with the load and resistance factors in AASHTO LRFD (2024).

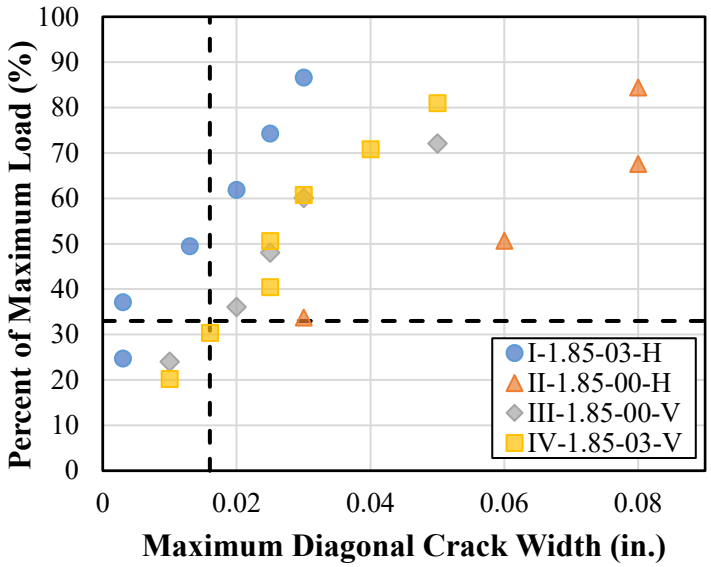

Figure 5-47.Maximum diagonal crack width at each load step of four specimens

$$\phi \text{ Nominal Capacity} \approx \eta \text{ Service Load}$$

$$\frac{\phi}{\eta} \approx \frac{\text{Service Load}}{\text{Nominal Capacity}}$$

Assumptions:
1). Load Case: 1.25DL + 1.75LL
2). DL = 75% of Service Load
LL = 25% of Service Load
3). Nominal = 2/3 Experimental

$\eta = 1.4$

$$2/3 \quad \frac{0.70}{1.4} = \boxed{0.33} \approx \frac{\text{Service Loads}}{\text{Experimental Capacity}}$$

ϕ = strength reduction factor, 0.70
η = load factor
DL = dead load
LL = live load

Figure 5-48 Estimated service load based on experimental capacity

The benchmark crack width of 0.016 in. was used to evaluate the serviceability performance of specimens. According to ACI 224R-01, a reasonable width for flexural crack under a dry air or protective membrane exposure condition is listed as 0.016 in. Considering that other exposure conditions require a smaller acceptable crack width, 0.016 in. was taken as the upper limit for tolerable shear crack width in this research to secure structural serviceability and long-term durability.

The maximum diagonal crack widths for specimens tested first in each beam are presented in Figure 5-47. At every load step, Specimen III-1.85-00-V and Specimen IV-1.85-03-V exhibited larger diagonal crack widths than Specimen I-1.85-03-H. In both III-1.85-00-V and IV-1.85-03-V, the widest cracks propagated along the vertical cold joint. This suggests that, in comparison to Specimen I-1.85-03-H, the crack restraint provided by the vertical cold joint was insufficient, regardless of the presence of reinforcement crossing the interface

For specimen without web reinforcement, the diagonal cracks in Specimen II-1.85-00-H were significantly wider than those observed in other specimens. However, based on the observed crack patterns, the development of crack in this specimen is not associated to the presence of the horizontal cold joint. Accordingly, it is concluded that the ineffectiveness on crack restraint is primarily attributed to the absence of web reinforcement.

5.7.7. Displacement and Strain Contour

To authenticate the observed load transfer mechanism, the analysis results from the Digital Image Correlation (DIC) was employed to provide additional insight into the displacement and strain field of the testing region. These data were specifically used to compare the strain distribution along the cold joint and the idealized strut line across the specimens. To ensure consistency in the comparison, the images were rotated so that the specimens shared a uniform

orientation where the loading point was positioned in the top right corner and the support in the bottom left corner.

Specimens with vertical cold joints exhibited significant shear crack developed along the cold joints. The displacement contours of these specimens are specifically investigated to evaluate the localized behavior of the intersection between the load transferring path and the cold joint. The displacement contours measured by the DIC system prior to failure are presented in Figure 5-49. Specimen III-1.85-00-V and Specimen IV-1.2-03-V demonstrated significant difference of displacement along the cold joint due to the slip of the interface when experiencing localized failure. On the other hand, displacement difference can only be observed along the diagonal shear crack in Specimen III-1.85-00-VR and Specimen IV-1.85-03-V without specific difference along the cold joints. This observation validates the conclusion drawn from the crack maps, where Specimen III-1.85-00-V and Specimen IV-1.2-03-V exhibited localized failure at the intersection of strut and cold joint. More importantly, the localized interface shear failure indicated that the force transferred through the compression strut to the cold joints was primarily resisted by part of the interface. This conclusion facilitates the development of an analytical approach that focus on evaluating the localized shear behavior of cold joints.

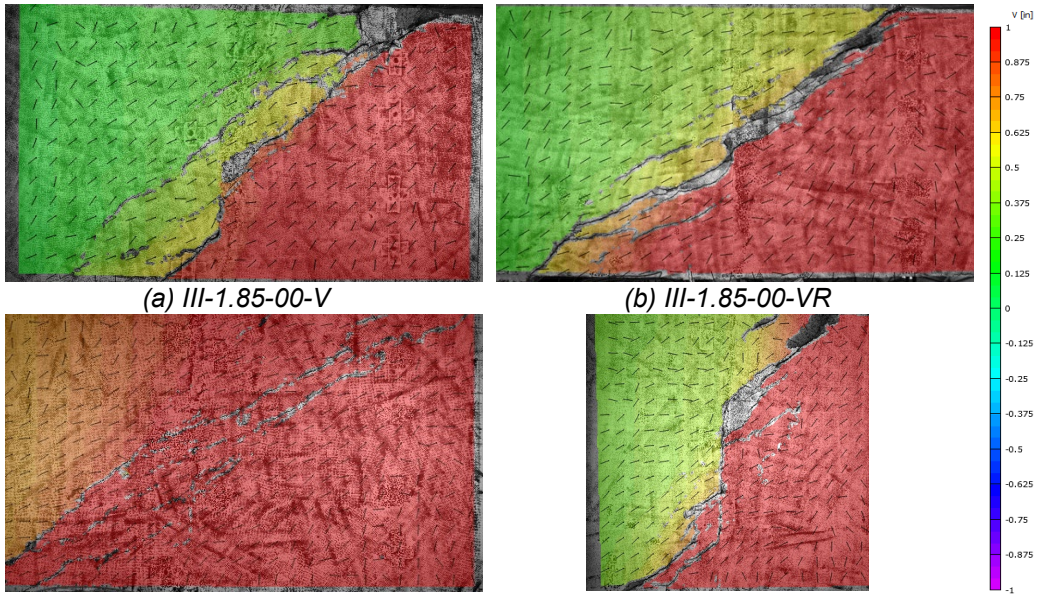

(a) III-1.85-00-V *(b) III-1.85-00-VR*

(c) IV-1.85-03-V *(d) IV-1.2-03-V*

Figure 5-49 Displacement contour at onset of failure

The strain contours captured immediately prior to failure of the specimens are depicted in Figure 5-50. For Specimens I-1.85-03-H, I-1.4-03-H, I-1.0-03-H and II-1.85-00-H, the principal compression strain analysis indicates that the strain was primarily concentrated along the diagonal compression strut. Only minor strain distribution was observed along the cold joints. Based on the strain profile obtained from the DIC and the experimental results discussed in the preceding sections, the influence of horizontal cold joint on the shear behavior of deep beams was determined to be inconsequential.

It is important to note that the non-testing regions of these specimens were intentionally fortified with dense confining reinforcement to ensure that failure manifested within the designated testing regions. This design potentially contributed to the limited influence observed from the horizontal cold joints. Accordingly, future research is recommended to explore a broader range of design parameters to advance the understanding of deep beam behavior featuring cold joints with various orientations.

Strain concentrations were observed along the vertical cold joints in all specimens, regardless of whether the global behavior was governed by cold joint failure. This consistent strain localization indicates that cold joints act as critical stress-transfer regions within the structure. Even when the overall capacity was not significantly compromised, the cold joint influenced the internal force distribution and deformation response. These findings highlight the importance of addressing cold joint behavior in design and analysis. Accordingly, the development of specific design guidelines and analytical methods is essential to accurately evaluate cold joint response and ensure the structural integrity of reinforced concrete members incorporating discontinued concrete placement.

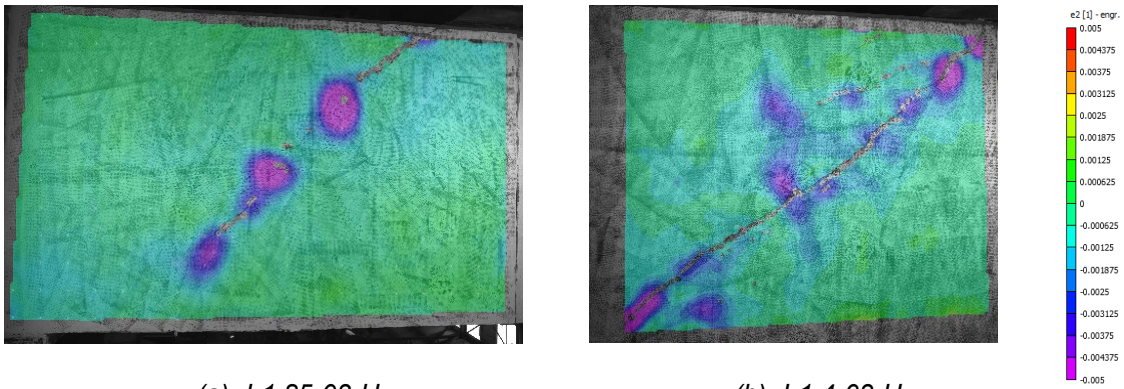

(a) I-1.85-03-H *(b) I-1.4-03-H*

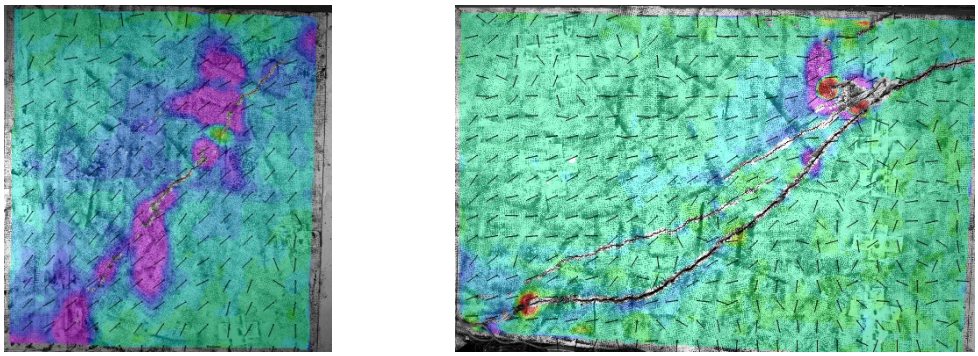

(c) I-1.0-03-H *(d) II-1.85-00-H*

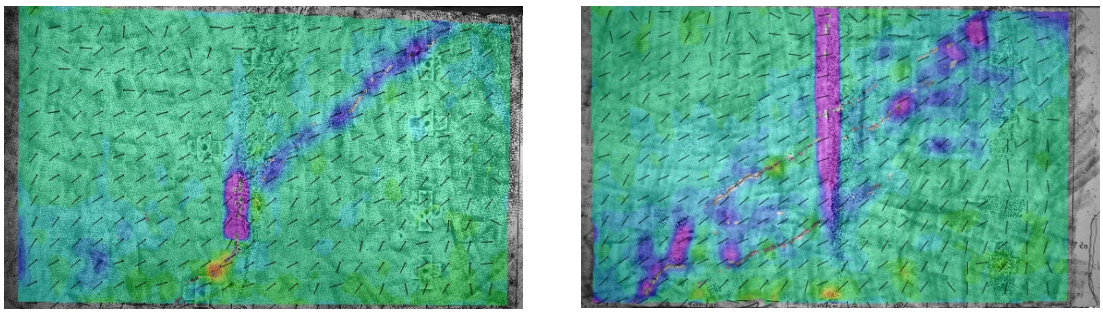

(e) III-1.85-00-V *(f) III-1.85-00-VR*

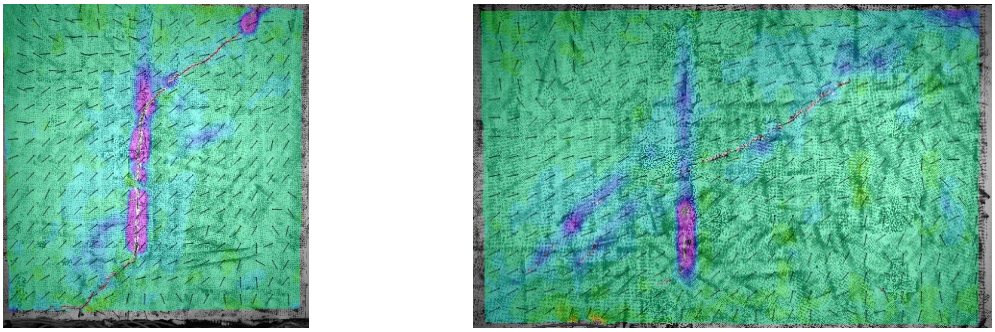

(g) IV-1.2-03-V *(h) IV-1.85-03-V*

Figure 5-50 Strain contours at onset of failure

5.8. Summary

This chapter summarizes the experimental program conducted on deep beams with cold joints. A total of 10 specimens were designed in accordance with current STM specifications to investigate the behavior of cold joints within disturbed regions of reinforced concrete members. The specimens featured various cold joint configurations to evaluate key variables identified as influential to the interface shear behavior in the slant shear tests. The failure mode of these specimens was intentionally designed to be governed by the crushing of concrete struts, with the overarching aim of developing design guidelines for evaluating the strength of struts crossing cold joints.

Section 5.7 presents the experimental results of all 10 specimens. When comparing the normalized shear capacities of specimens with horizontal cold joints to those from a previous project (Birrcher et al., 2009) with similar designs, no significant reduction was observed in the capacity of strut crossing horizontal cold joint. For deep beams with vertical cold joints, significant reductions in shear strength were observed in Specimen III-1.85-00-V with nonroughened, unreinforced interface and Specimen IV-1.2-03-V with a smaller shear-span-to-depth ratio. This negative influence of cold joints on the shear strength was effectively mitigated either by intentionally roughening the interface or by providing 0.3% of reinforcement intersecting the cold joint. The tension transfer efficiency of the post-installed reinforcement was found to be inadequate, leading to the anchorage failure in both specimens with dowel bars crossing the cold joint.

To validate this observation, crack patterns, strain gauge data, displacement and strain profiles were meticulously examined. In Specimen I-1.85-03-H, although minor cracking along the horizontal cold joint was observed during the initial loading stage, the experimental data demonstrated no significant influence of the horizontal cold joint on the failure pattern or the overall load transfer mechanism. For specimen exhibiting significant interface failure, the displacement contours revealed notable slip along the cold joint, indicating that the localized region of cold joint contributed significantly to the shear resistance. Additionally, strain concentrations were consistently observed along the vertical cold joints in all relevant specimens, regardless of whether cold joint failure governed the overall response. These findings underscore the importance of cold joint behavior in influencing the global structural response and load transfer mechanism.

The experimental results highlighted the influence of cold joints on the behavior of deep beams and emphasized the need for explicit design and analytical methods to address the unique characteristic of cold joint behavior. However, considering that the specimens in this research were intentionally designed to ensure failure within the testing region, further experimental studies incorporating a broader range of design configurations and boundary conditions are necessary to more comprehensively evaluate the structural implications of cold joints and to support the development of reliable and practical design guidelines.

Chapter 6. Experimental Program: Drilled-Shaft Footing with Cold Joint

6.1. Overview of Experimental Program

The objective of Phase III testing is to investigate the effect of cold joints on the strength of struts in three-dimensional (3D) reinforced concrete members. The load transfer mechanism in a reinforced drilled shaft footing cap can be conceptualized as a 3D truss system, where compression loads are transferred from the column to the drilled shafts through concrete struts, while tension loads are resisted by reinforcing steel ties, as illustrated in Figure 6-1. Cold joints intersecting the strut-and-tie system were deliberately introduced to the testing region to evaluate their impact on the structural response. The drilled shaft footing specimen was designed such that the failure mode is governed by the crushing of the concrete struts, facilitating the investigation of the strength of 3D struts crossing cold joints. Consequently, the influence of cold joints can be assessed by comparing the strength of struts in specimens with cold joints to those in specimens without cold joints tested in prior studies (Yi et al., 2022).

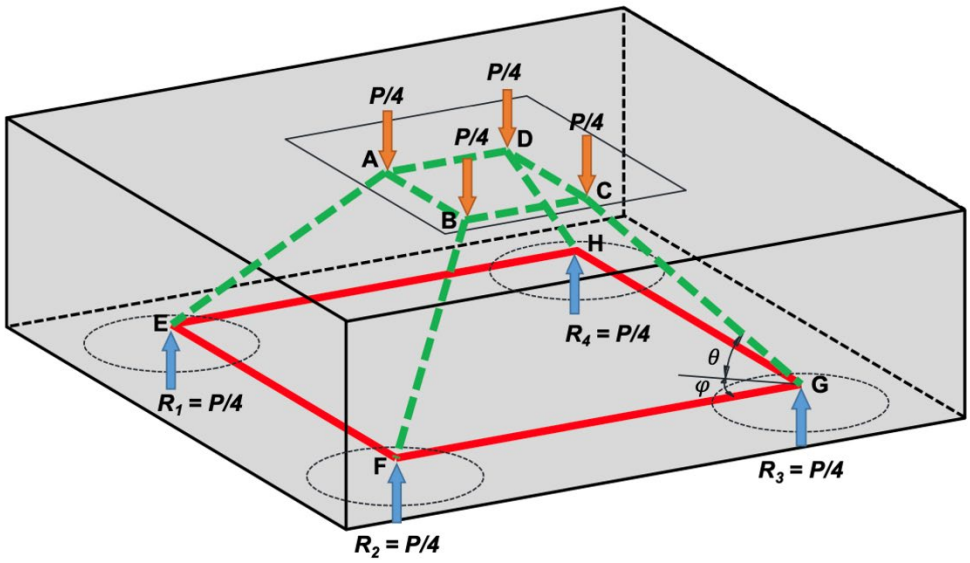

Figure 6-1 3D STM of drilled shaft footing cap under uniform compressive loading (Reprinted from Yi et al., 2022)

The Phase III experimental program consists of a drilled shaft footing cap designed to investigate the behavior of struts crossing cold joints. A square footing cap with a side length of 96 inches and a depth of 32 inches was designed to ensure consistent loading conditions for all struts within the system through symmetrical geometry and boundary conditions. Conventional reinforced concrete member design typically relies on sectional analysis by assuming *plane sections remain plane*. However, this assumption does not hold in the D-regions of a structure,

characterized by the disturbed strain fields. The behavior of a drilled shaft footing cap with a shear-span-to-depth ratio (*z/d* ratio) below 2.5 is primarily influenced by nonlinear stress fields, which are induced from the vicinity of the applied load and the reaction forces at the supports. Therefore, the three-dimensional strut-and-tie method (3D-STM) was employed for both the design and evaluation of the drilled shaft footing specimen.

6.2. Overview of 3D Strut-and-Tie Modeling

The 3D-STM idealizes the stress distribution in RC members with a representative truss system comprised of compression resisting elements (*struts*) and tension resisting elements (*ties*). The intersections of struts and ties are referred to as *nodes*. To maintain equilibrium within the truss system, deliberate consideration must be given to the angles between struts and ties, as well as the dimensions of each element. Thus, the load demand on each component can be determined based on the applied loads, facilitating the subsequent design process.

The initial phase in developing a strut-and-tie model involves establishing the relationship between the applied load and the reaction forces. This process requires calculating the proportion of the applied load to the reaction force at each support, which varies depending on the boundary conditions. To investigate the effect of cold joints on the strength of each strut transferring the applied load to the support, each support was designed to carry an identical portion of the applied load. Additionally, the specimen was designed with symmetrical boundary and loading conditions to minimize the impact of the internal load transferring mechanism on the experimental results and analysis. By subjecting the specimen to pure compression force through the loading plate without eccentricity, a uniform compressive stress distribution can be achieved at the bearing face where load was applied to simulate the axial load transferred by the column to the footing in practice. Consequently, struts with identical dimensions and loading conditions are established to uniformly transfer the applied load to each support. The distribution of the applied load, along with the idealized strut-and-tie model of a drilled shaft footing cap are illustrated in Figure 6-1. This idealized design ensures that all struts in the specimen intersect the cold joint at the same location, creating identical intersecting areas. This design and load applying strategy facilitates the determination of load transfer through the struts and the corresponding stress profile at the cold joints.

Within the framework of STM, various truss system configurations can be developed while maintaining equilibrium. However, the load generally follows the path of least resistance and deformation. As a result, the model with the fewest ties often provides a more accurate representation, as ties typically exhibit greater deformation capacity compared to concrete struts. Furthermore, it is essential to ensure that the angle, θ, between struts and ties exceeds 25 degrees to avoid interference between the development of tensile stress in the reinforced ties and compression stress in the concrete struts. Empirical data from previous study (Yi et al., 2022) indicated that the nodes beneath the column can be assumed at 0.1 times the height of the specimen,

while the nodes above the drilled shafts are positioned at the centroid of the bottom reinforcing mat. Based on these requirements and assumptions, the magnitude of the member forces and the dimensions of each component can be computed to establish the 3D-STM system.

6.2.1. Proportioning 3D STM elements

Given that all struts and ties are connected through multiple nodes, it is essential to determine the dimensions of these nodes to calculate the forces transferred within the nodal regions. Nodes are categorized into three distinct types based on the intersecting elements: *CCC*, *CCT*, and *CTT* nodes. *CCC* nodes refer to nodes intersected only by struts, *CCT* nodes represent intersections where a single tie intersects along with struts, and *CTT* nodes refer to nodes where ties intersect in multiple directions.

In the specimen for Task 6, as illustrated in Figure 6-1, node A, B, C and D are classified as a *CCC* node at the location of the applied load, while node E, F, G and H are classified as a *CCT* node at the supports. The following sections will focus on elucidating the proportioning of *CCC* and *CCT* nodes.

6.2.1.1. Proportioning the CCC node

Given the pure axial compression applied to the specimen and the symmetrical boundary conditions, it is evident that each drilled shaft will provide an equal reaction force. Therefore, the bearing face of each node, located between the applied load and the compression strut, can be determined as a quadrant of the column area. The diagram of two types of nodes in the drilled shaft footing is presented in Figure 6-2, and the length of each side of the equivalent bearing face, l_b, can be calculated using Equation (6-1). This configuration enables the uniform transfer of compression forces through each strut, maintaining equilibrium within the internal system.

To calculate the interface dimension between the strut and the *CCC* node, a 3D node configuration was established, as shown in Figure 6-2(a). To calculate the compression resistance at the strut-to-node interface corresponding to the load transfer from the *CCC* node at the bearing column to the *CCT* node at the support, the equivalent bearing face was projected onto a plane perpendicular to the orientation of the strut. Based on the assumption that the node beneath the column is located at 0.1 times the total height of the specimen, $0.1h$, the height of the back face can be determined as twice the distance from the top surface to the node, $0.2h$. Subsequently, the height of the strut-to-node interface, l_s, can be determined using Equation (6-2), incorporating the side length of the equivalent bearing face, l_b, the height of the back face, $0.2h$, and the angle between strut and tie, θ. The width of the node was assumed to remain the same in the direction perpendicular to the strut. Hence, the width of the equivalent bearing face, l_b, is identical to the width of the strut-to-node interface, $\frac{\sqrt{A_c}}{2}$.

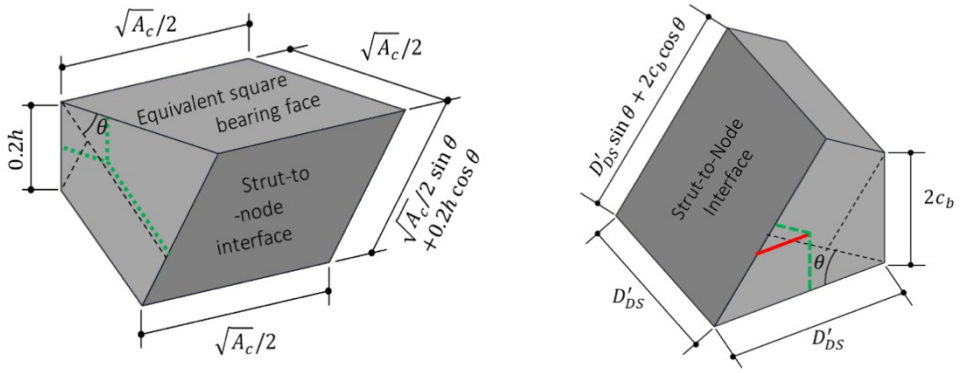

(a) CCC Node *(b) CCT Node*

Figure 6-2 Nodal geometries (Reprinted from Yi et al., 2022)

$$l_b = \frac{\sqrt{A_c}}{2} \tag{6-1}$$

$$l_s = \frac{\sqrt{A_c}}{2} \cdot sin\theta + 0.2h \cdot cos\theta \tag{6-2}$$

where, A_c = area of the column (loading point), in^2
h = height of the specimen, in.
θ = angle between strut and tie, °.

6.2.1.2. Proportioning the CCT node

A *CCT* node is depicted in Figure 6-2(b). In the 3D strut-and-tie model employed to analyze the drilled shaft footing, *CCT* nodes were utilized to calculate the capacity of nodal regions located above the supporting drilled shafts. The circular bearing face between the footing cap and each drilled shaft was represented by an equivalent square interface with an identical interface area. The side length of the equivalent square interface for the drilled shaft is calculated using Equation (6-3). The orientation of the equivalent square bearing face at the *CCT* nodes was also projected to establish a strut-to-node interface that is perpendicular to the strut.

Since the *CCT* node serves as the intersection of the compression load carried by the strut and the tension load transferred through the ties, it is necessary to locate the *CCT* node at the centroid of the bottom mat reinforcement that was designed to resist all the tension load. The dimensions of the strut-to-node interface can be determined by Equation (6-4), incorporating the side length of the equivalent square bearing face, D'_{DS}, the distance from the bottom concrete face to the centroid of the reinforcement, c_b, and the angle between strut and tie, θ. Similar to *CCC* nodes, the width of the *CCT* nodes is assumed to be identical to the width of the equivalent square

bearing face. Consequently, the area of the strut-to-node interface can be determined to assess the bearing capacity.

$$D'_{DS} = D_{DS}\sqrt{\frac{\pi}{4}} \tag{6-3}$$

$$l_{DS} = D'_{DS} \cdot sin\theta + 2c_b \cdot cos\theta \tag{6-4}$$

where, D_{DS} = diameter of the drilled shaft (support), in.
D'_{DS} = side length of the equivalent square interface, in.
c_b = distance from the centroid of bottom mat reinforcement to the bottom face of the specimen, in.
θ = angle between strut and tie, °.

6.2.1.3. Proportioning the ties

Based on the findings from the TxDOT Project 0-6953 (Yi et al., 2022), all well-anchored bottom mat reinforcement can be incorporated into the calculation of tie resistance regardless of the reinforcement configuration. After establishing the 3D strut-and-tie model, the tension resistance of all ties in one direction is determined by the total area of bottom mat reinforcement that is parallel to these ties. To be more specific, for the specimen in Task 6, the bottom mat reinforcement in each direction was evenly distributed to two parallel ties that transfer tension from one support to another. For demonstration purposes, the bottom mat reinforcement contributing to the strength of the tie on the west side is illustrated in Figure 6-3. Consequently, the reinforcement area used to calculate the strength of each tie corresponds to half of the total area of the bottom mat reinforcement parallel to the respective tie.

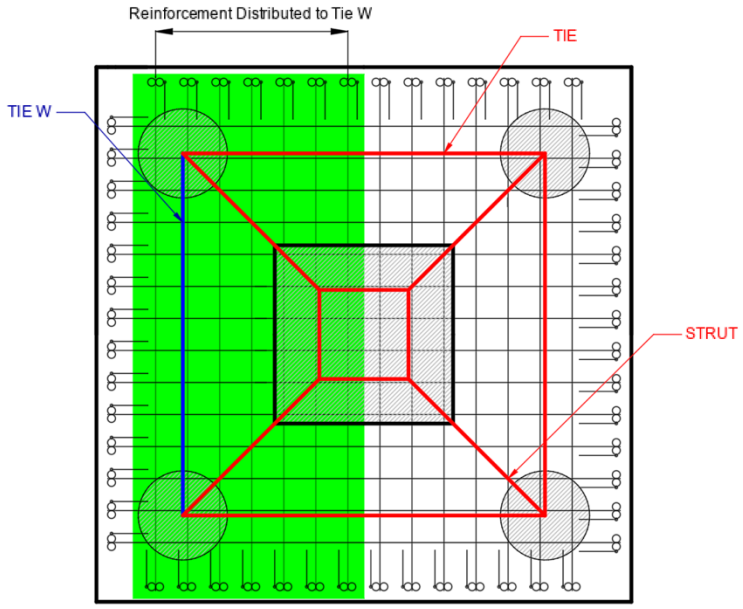

Figure 6-3 Distributing the bottom mat reinforcement to ties

6.2.2. Calculating the Capacity of 3D STM elements

6.2.2.1. Strut Nominal Strength

The specimen in Task 6 was designed in accordance with AASHTO LRFD 2020. The nominal resistance of the node face is calculated using Equation (6-5). The compressive stress at the node face, f_{cu}, is determined using Equation (6-6), where m represents the confinement modification factor, v is the concrete efficiency factor and f_c' indicates the compressive strength of concrete. The determination of the confinement modification factor and the concrete efficiency factor are discussed in the following sections.

$$P_n = f_{cu} \cdot A_{cn} \tag{6-5}$$

$$f_{cu} = m \cdot v \cdot f_c' \tag{6-6}$$

where, A_{cn} = effective cross-sectional area of the node face, in.^{2}
m = confinement modification factor
v = concrete efficiency factor
f_c' = compressive strength of concrete, ksi
P_n = nominal resistance of a node face, kips

6.2.2.1.1. Confinement Modification Factor

The confinement modification factor, m, is implemented in the calculation of nodal strength to account for the confinement effect arising from the distribution of bearing stress. According to AASHTO LRFD 2020, the confinement modification factor is calculated using Equation (6-7), with an upper limit of 2.0 applicable to uniformly distributed bearing stresses. The notional area, A_2, and the bearing area, A_1, in Equation (6-7) are defined as shown in Figure 6-4. However, according to the suggestion made by the TxDOT Project 0-6953 (Yi et al., 2022), the upper limit of the confinement modification factor should be increased to 3.0 for *CCC* nodes due to the triaxial confinement effect provided by the struts intersecting those regions.

$$m = \sqrt{\frac{A_2}{A_1}} \leq \begin{cases} 3.0 \text{ for } CCC \text{ node} \\ 2.0 \end{cases} \tag{6-7}$$

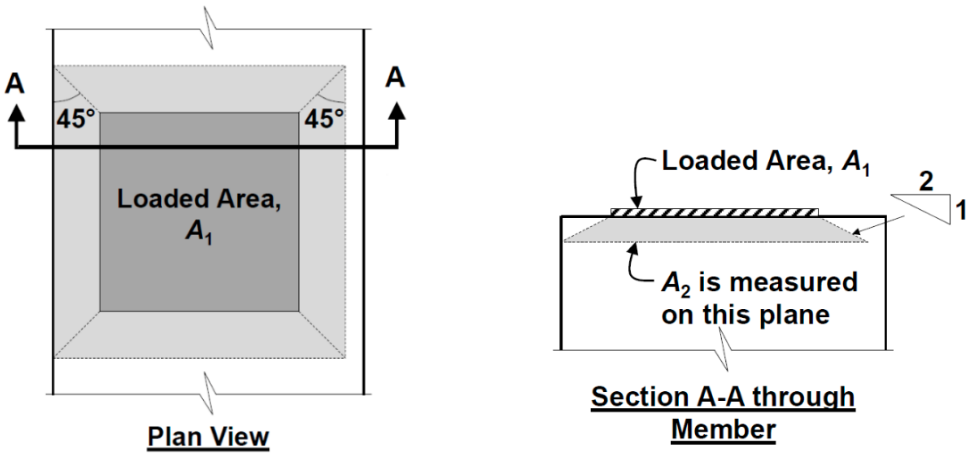

Figure 6-4 Determination of notional area (AASHTO LRFD, 2024)

6.2.2.1.2. Concrete Efficiency Factor

According to AASHTO LRFD 2020, the concrete efficiency factor is specified as 0.45, unless sufficient crack control reinforcement is provided for the nodes. The efficiency factor for nodes with crack control reinforcement is determined according to Table 6-1. Although the requirement of crack control reinforcement is not mandated for footing structures per AASHTO LRFD 2020, previous experiments (Yi et al., 2022) have demonstrated that a slightly higher capacity with a ductile failure mode can be achieved by the implementation of side face reinforcement. The side face reinforcement facilitates the redistribution of internal stresses between two supported regions, engaging resistance and confinement from surrounding concrete and reinforcement.

Additionally, previous experimental program (Yi et al., 2022) also indicated that specimens with 0.18% side face shrinkage and temperature control reinforcement demonstrated greater capacity and ductility than both specimens and analytical models with side face reinforcement less than 0.18%. Therefore, it is suggested that the concrete efficiency factor used for 2D structures with crack control reinforcement is also applicable to 3D structures with side reinforcement exceeding 0.18%, as outlined in Table 6-1.

Table 6-1 Efficiency factors for nodes with crack control reinforcement

	Node Type		
Face	***CCC***	***CCT***	***CTT***
Bearing Face	0.85	0.70	$0.85 - \frac{f'_c}{20\ ksi}$ $0.45 \leq v \leq 0.65$
Back Face			
Strut-to-Node Interface	$0.85 - \frac{f'_c}{20\ ksi}$ $0.45 \leq v \leq 0.65$	$0.85 - \frac{f'_c}{20\ ksi}$ $0.45 \leq v \leq 0.65$	

6.2.2.2. Tie Nominal Strength and Anchorage

To ensure the full development of ties, the bottom mat reinforcement must be adequately anchored. Previous research (Yi et al., 2022) has shown that the concept of the extended nodal zone is also applicable when determining the anchorage length for 3D STM. Figure 6-5 demonstrates a diagram of a *CCT* node with tension transfer ties intersecting. In particular, Figure 6-5(b) and Figure 6-5(c) show the extended nodal zone within a *CCT* node on a plane parallel to the tie, showing the projected strut line. The critical section on the plane of the strut is defined as the point where the centroid of the tie intersects the extended nodal zone.

With the extended nodal zone defined, the available development length can be calculated using Equation (6-8). For the #11 bars used in the design of the specimen, a 90-degree or 180-degree hook is required to fully develop the bars within the available development length, as dictated by the design parameters. Once the bars are properly anchored, the tension resistance of each tie can be calculated according to Equation (6-9).

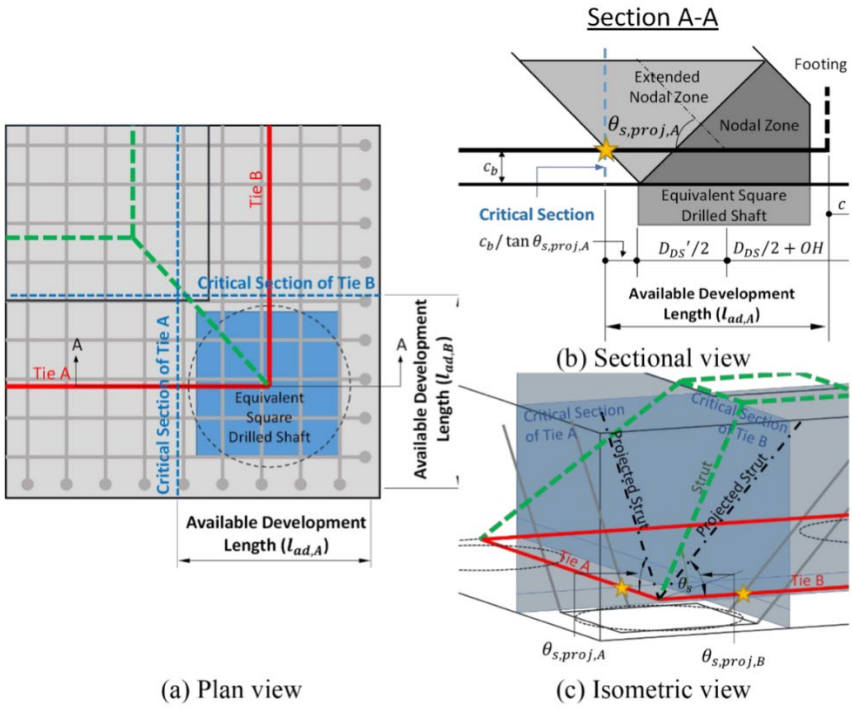

Figure 6-5 Available length of anchorage of bottom mat reinforcement (Reprinted from Yi et al., 2022)

$$l_{ad} = \frac{c_b}{tan\theta_{s,proj}} + \frac{D_{DS}{}'}{2} + \frac{D_{DS}}{2} + OH \tag{6-8}$$

$$P_n = f_y A_{st} + A_{ps}\left[f_{pe} + f_y\right] \tag{6-9}$$

where, l_{ad} = available development length, in.

c_b = distance from bottom surface to the centroid of bottom mat reinforcement, in.

$\theta_{s,proj}$ = projected strut angle on the plane parallel to ties, °

OH = the minimum distance from the edge of the drilled shaft to the closest exterior face of the footing, in.

c = clear cover between bottom mat reinforcement and the side face, in.

A_{st} = total area of longitudinal non-prestressed reinforcement distributed to the tie, in.^{2}

A_{ps} = area of prestressing steel distributed to the tie, in^2

f_y = yield strength of non-prestressed longitudinal reinforcement, ksi

f_{pe} = effective stress in prestressing steel after losses, ksi

6.3. Specimen Design

To investigate the strength of struts crossing cold joints, the specimen was intentionally designed to fail through compressive failure of the struts. Although there are currently no specific design guidelines indicating the methodology for calculating the strength of struts crossing cold joints, it was anticipated that the strength would decrease compared to the strength of a monolithic strut. Since the design objective is to create a condition where the strut experiences failure before other components in the STM system, the design of the specimen was conducted neglecting the possible strength reduction introduced by the cold joints.

Experimental results from a previous project (Yi et al., 2022) indicated that using 28-#9 bars in one direction of the bottom mat reinforcement still resulted in failure governed by the yielding of the reinforcement. To ensure that the failure of the specimen would be dominated by the strut crushing rather than yielding of the ties, 28-#11 bars were provided for the bottom mat reinforcement in each direction, thereby promoting strut failure as the governing mode.

The dimensions and design parameters of specimen DSF1 in Task 6 are shown in Figure 6-6. The column stub, measuring 32 × 32 × 5 inches, was designed to apply a compressive load during the experiment, simulating the axial force transferred from a column to a footing in a structural system. To accommodate 28 #11 bars in the bottom mat reinforcement in each direction, pairs of #11 bars were bundled together to meet the minimum clear cover and spacing requirements between the reinforcing bars. The #11 bars were bent with 180-degree hooks to provide adequate anchorage for the bottom mat reinforcement without reducing the top clear cover. For the side face reinforcement, horizontal and vertical reinforcement ratios of 0.3% were achieved using #3 and #6 bars, respectively. This configuration allowed the utilization of maximum efficiency factors for calculating the strength of concrete compressive strut in the 3D strut-and-tie model as discussed in the previous section.

In order to investigate the influence of cold joint in the D-regions of three-dimensional structures, the cold joint in specimen DSF1 was designed to intersect the middle of each strut in the 3D strut-and-tie model. This design created a configuration where the cold joint enclosed the loading column, necessitating the transfer of applied loads through the cold joint before reaching the drilled shafts. The cold joint separated the specimen into two sections: the internal section with the loading column and the external section with the drilled shafts. The internal section measured 37 × 37 inches in length and width, with a height of 32 inches, matching the overall height of the specimen. The design parameters are detailed in

Table 6-2.

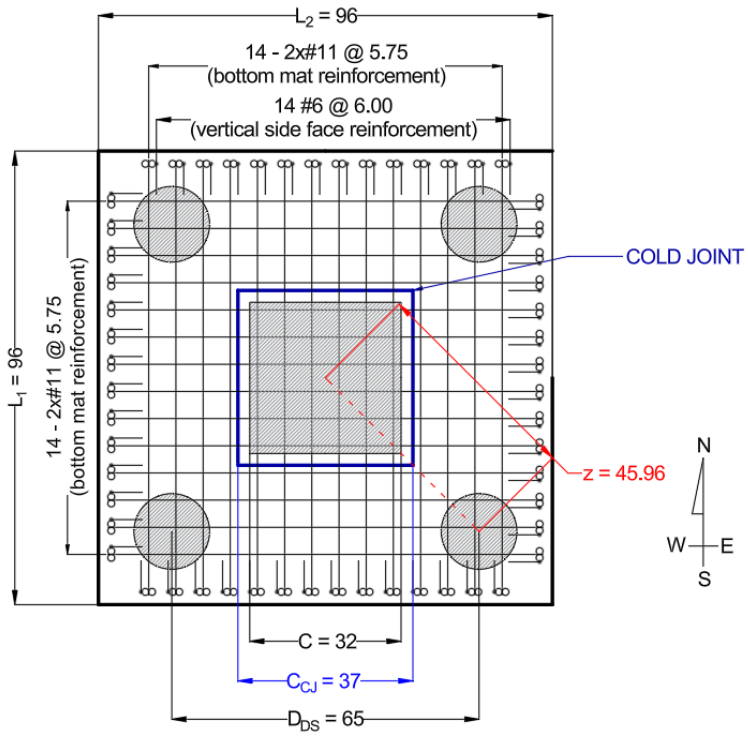

(a) Plan view

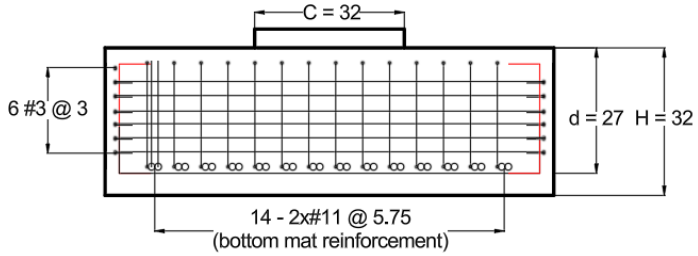

(b) Side view

Figure 6-6 Design diagram of DSF1

Table 6-2 Summary of reinforcement detail

Bottom Mat Reinforcement					Side Face Reinforcement		
Layout	Anchorage	Direction		ρ_s (%)	Horizontal	Vertical	ρ_v&ρ_h (%)
		NS	EW				
Grid	180-Hook	14-2×#11 @ 5.75 in.	14-2×#11 @ 5.75 in.	1.71	#3@ 3 in.	#6 @ 6 in.	0.31

6.4. Fabrication Procedure

6.4.1. Fabrication of Steel Cage

This section outlines the general fabrication procedure employed for the steel cages and the concrete placement of the drilled-shaft footing specimen. The fabrication process commenced with the attachment of strain gauges at designated locations, which will be further detailed in Section 6.6.1.2. To ensure the fidelity of data obtained from the strain gauges, the subsequent fabrication protocol is rigorously followed during the construction phase. Initially, a sequence of three grinding levels, progressing from coarse to fine, was implemented on the designated strain gauge locations on the rebars. Following this, acetone was applied to these prepared areas to establish a pristine interface for strain gauge attachment. Subsequently, strain gauges were mounted onto the reinforcement, which was coated with three layers of M-coat to provide insulation against water ingress during casting. SB tape and VM tape were then applied over the strain gauges to shield the wiring while mitigating heat transmission to the gauges. Finally, electrical tape was employed to encase the entire region as a protective layer, and epoxy was applied on the electrical tape to forestall potential collisions among rebars during construction. The strain gauge installation procedure is presented in Figure 6-7.

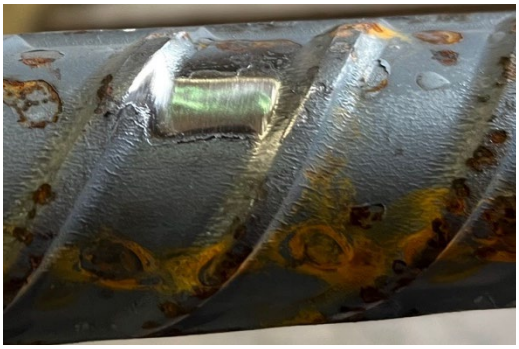

(a) Rebar surface after grinding

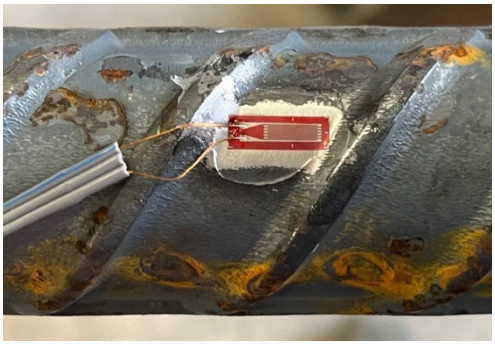

(b) Strain gauge with 3 layers of M-coat

(c) SB tape for wire protection

(d) VM tape for heat insulation

(e) Electrical tape wrapping

(f) Epoxy coating

Figure 6-7 Strain gauge installation

Rebars with strain gauges attached were strategically assembled in specific order, utilizing customized equipment to create cold joints at the designated locations. The fabrication of steel cage was organized into two phases, the first phase focused on constructing the bottom mat reinforcement for the internal section, and the second phase involved assembling the bottom mat reinforcement and the side face reinforcement for the external section.

To create vertical cold joints surrounding the loading column, a wooden formwork was meticulously fabricated prior to the construction of the steel cage in the first phase. The wooden formwork was designed as a box with tight connection at the edges of each face to prevent concrete leakage during the placement of the internal section. Also, to ensure the continuity of bottom mat

reinforcement, holes with diameter identical to the #11 reinforcing bars were drilled at designated locations. These drilled holes were later separated into the top and bottom segments, as shown in Figure 6-8. Once the steel cage fabrication of the first phase was completed, the entire wooden formwork was assembled, allowing the bottom mat reinforcement to cross the cold joints after the first concrete placement. The wooden formwork was then affixed to another steel formwork previously used for casting footings from prior projects with identical dimensions. This arrangement maximized the rigidity of the system during concrete placement by transferring the concrete pressure from the wooden formwork to the mechanically fastened steel formwork. The first-phase bottom mat reinforcement and the wooden formwork assembly are presented in Figure 6-9.

Figure 6-8 First phase bottom mat reinforcement fabricated on top of the bottom segment of wooden formworks

Figure 6-9 Wooden formworks with the bracings and the bottom mat reinforcement

A customized steel formwork was employed for casting the drilled-shaft footing specimen. This steel formwork consisted of four components: the bottom soffit, a pair of side forms, a pair of end forms, and a pair of bolt caps. To integrate the steel cage and wooden formwork with the steel formwork, the fabricated steel cage was positioned on the soffit. Subsequently, the side forms, one end form and one bolt cap were placed adjacent to each side of the soffit. Wooden bracings were installed on the top and between the steel and the wooden formwork, leveraging the pressure exerted by the concrete during the placement to secure the wooden formwork at the center of the entire specimen. The dimensions of the steel formwork were maintained by two top ties across the side forms and six impact bolt connections on each end form and bolt cap. The assembled steel and wooden formwork with bracings are shown in Figure 6-10.

(a) *(b)*

Figure 6-10 (a) Steel and wooden formworks fastened by (b) the wooden bracing

6.4.2. Concrete Placement

To create cold joints, the concrete placement for the drilled-shaft footing specimen was performed in two stages. The first concrete placement occurred after the wooden formwork and bottom mat reinforcement were constructed. Seven days after the initial placement, concrete cylinders were tested to ensure that the material strength satisfied the requirement for demolding. The wooden formwork was then dismantled, exposing the cold joint and facilitating the subsequent fabrication efforts. Meanwhile, the remaining portion of the steel cage was fabricated outside the casting area, and the steel formwork used for the first cast was cleaned to prevent any concrete or cement debris from contaminating the second placement. Afterward, the newly constructed steel cage and the existing section of the specimen were repositioned onto the soffit in preparation for the second placement. The second placement was scheduled 28 days after the first cast, allowing concrete in the internal section to properly cure before the placement of the external section. This difference in casting age was designed to replicate conditions where expansion or retrofitting of structure is required after the existing structure has been in service for a certain period. Figure 6-11 demonstrates the fabrication procedure and the configuration of the cold joints.

(a) Steel cage and wooden formwork fabricated for the internal section

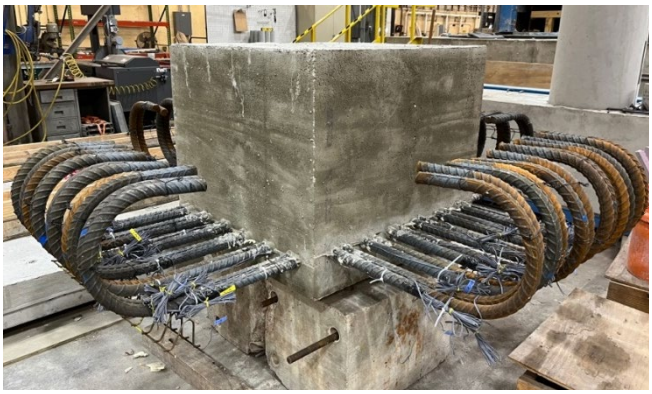

(b) The internal section after concrete placement

(c)Steel cage fabricated for the external section

(d) Concrete placement of the external section

Figure 6-11 Concrete placement procedure for specimens with vertical cold joints

To determine the material properties of the specimens, 24 cylindrical concrete samples measuring 4 inches in diameter and 8 inches in height were cast for each concrete placement. On the day of testing, material tests were conducted to measure the compression strength and the modulus of elasticity of the concrete. For each section, three cylinders were tested to ensure the reliability of material properties.

To replicate the load-transfer mechanism in a drilled-shaft footing, a column stub with steel frame was cast using high-strength grout, enabling the application of compression load to the specimen during the experiment. The column stub ensured uniform distribution of the applied load, while the high-strength grout, with a nominal compression strength of 10 ksi, prevented local crushing failure at the loading column. The steel jacketing and the reinforcement design of the column stub are shown in Figure 6-12.

Figure 6-12 Steel jacketing and reinforcement detail of the column stub

6.5. Materials

6.5.1. Concrete

To align with the material strength commonly used in practice, the design concrete strength was specified as 4 ksi. The mixture design provided by the concrete supplier to achieve the nominal strength of the specimen is presented in Table 6-3. This mixture design is also consistent with the concrete mixture used for deep beam specimens in Task 5, ensuring uniform material properties for comparative analysis and evaluation.

Table 6-3 Concrete mixture design

Material	Mass / Volume/ Properties
Type I/II L cement (lb/yd^3)	451
Class F fly ash (lb/yd^3)	113
Fine aggregate (lb/yd^3)	1369
Coarse aggregate (lb/yd^3)	1700
Water (lb/yd^3)	267
Hydration retarder (oz/100 lb CM)	1~8
High range water reducer (oz/100 lb CM)	1~6
Water-to-cementitious ratio	0.47
Maximum aggregate size (in.)	0.375
Nominal Slump (in.)	8.0 ± 1.0

The mechanical properties of each batch of concrete were determined through a series of material tests. Several 4×8 in. cylinders were fabricated for each batch of concrete to obtain essential mechanical properties, including 28-day concrete strength, compressive strength on the test day, modulus of elasticity (MOE) on the test day, and the complete stress-strain response. The compressive strength test was performed in accordance with ASTM C39, while the MOE data was obtained through the full stress-stain curve measured during the experiment. Testing frames in accordance with ASTM C469, as shown in Figure 6-13, were used for the instrumentation of linear variable differential transformers (LVDT), facilitating the measurement of strain throughout the compressive strength test. Three cylinders were tested for each batch, and the material properties were calculated following the requirement outlined in ASTM C39. The concrete compressive strength of each layer is summarized in Table 6-4.

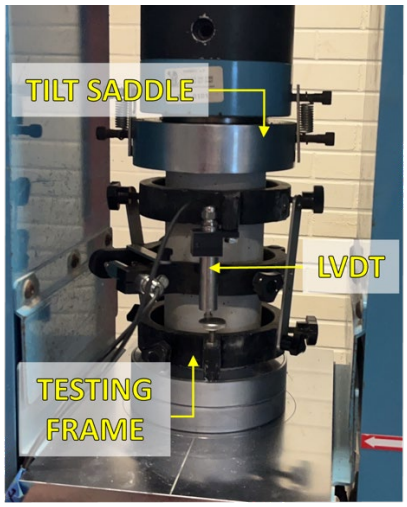

Figure 6-13 Test setup for concrete material tests

Table 6-4 Concrete material properties

Specimen	Footing region	28-day f'_c (ksi)	Test day f'_c (ksi)	Test day modulus of elasticity E_c (ksi)
DSF1	Internal	3.01	3.58	3337
	External	5.53	5.18	4564

6.5.2. Reinforcing Bars

Three steel reinforcement samples were tested for each reinforcing bar size used in the construction of the footing specimen, in accordance with ASTM A370. A summary of the average mechanical properties obtained from these tests is provided in Table 6-5, and photographs of the test setup and the experimental procedure are presented in Figure 6-14. To measure the strain values during the first stage of testing, an extensometer was attached to record the displacement corresponding to the applied load, as shown in Figure 6-14 (a). The yield stress, yield strain, and modulus of elasticity were determined from the full stress-strain response obtained during this stage. After the measured strain reached 0.02, the extensometer was removed, and the second stage of the test proceeded until the specimen ruptured, as shown in Figure 6-14 (b).

Table 6-5 Steel material properties

Bar Size	Yield Strength (ksi)	Yield Strain (10^{-3})	Tensile Strength (ksi)
#6	63.7	2.32	102.2
#11	64.1	2.61	97.1

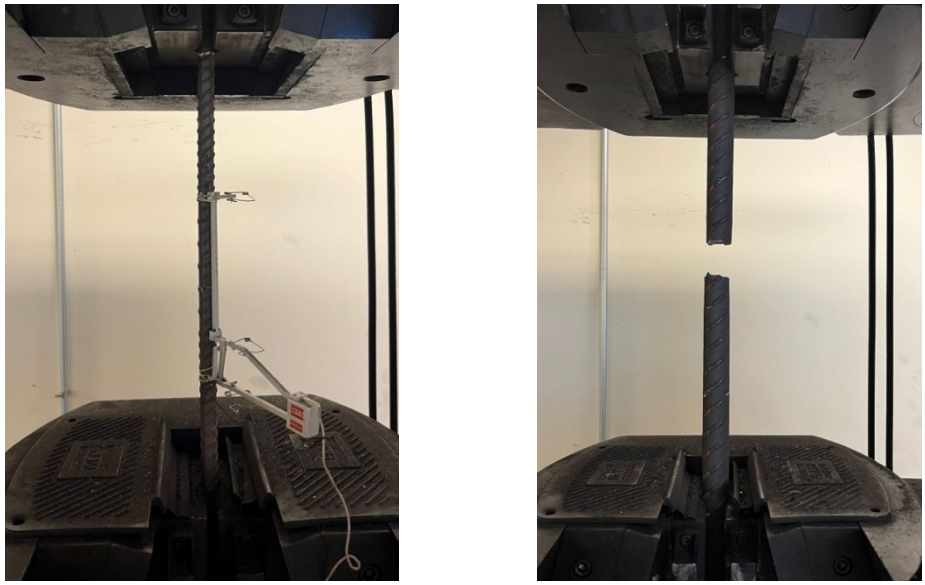

(a) First stage with extensometer *(b) Second stage until rupture*

Figure 6-14 Test setup for steel reinforcement sample

6.6. Test Setup

The specimen in Task 6 was subjected to a centrally applied load uniformly distributed across the column stub to simulate the compression load transferring from the column to the drill-shaft footings. The load was applied using two 2000-kip hydraulic rams positioned at the center of the specimen. To achieve a uniform compressive load, a steel spreader beam was employed to transfer the load from the two rams to the column stub. The reaction force was resisted by another blue transfer beam, which transferred the load to two red steel beams. These red beams were supported by eight threaded rods, each fitted with a pair of fasteners. During the experiment, the upper fasteners on the rods reacted against the rams, transferring the load through the threaded rods down to the strong floor. The test setup of the drilled-shaft footing is presented in Figure 6-15.

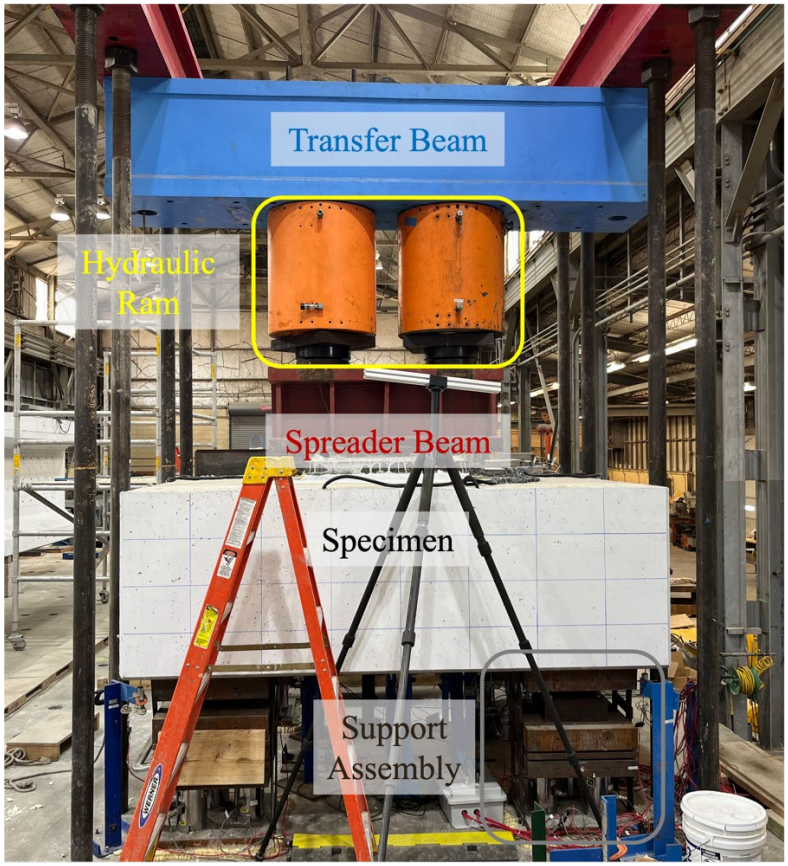

Figure 6-15 Test setup for drilled-shaft footing cap specimen

To replicate the reaction forces provided by the drilled shafts, four supports were assembled and positioned at the designated locations for each shaft. The design and configuration of each support were determined to prevent any additional fixtures from providing unexpected lateral and rotational restraint. Thus, the support system consists of one 3D pinned support, one two-way roller at the corner opposite to the pinned support, and two one-way rollers with the

degree of freedom perpendicular to each other at the corners adjacent to the pinned support. Steel round plates with a diameter of 16 in. were set on the top of each support to replicate the circular interface between the drilled shafts and the footing cap. Finally, rubber bearing sheets were positioned in between the specimen and the steel plates to ensure a uniform connection at each support. The supporting system is presented in Figure 6-16.

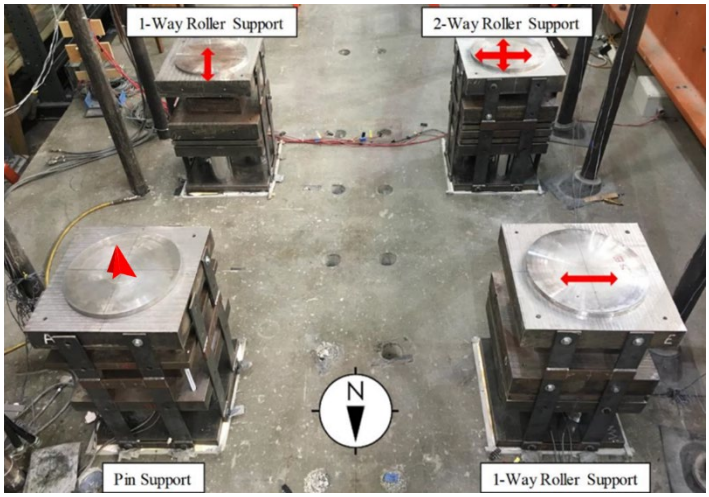

Figure 6-16 Layout of the supporting system (Yi et al., 2022)

6.6.1. Instrumentation

6.6.1.1. Load and Displacement Measurements

The reaction force provided by each support was measured using three load cells. Three 500-kips load cells were arranged at the base of each support, with their centroid aligned with the center of the designated drilled shafts. The steel plates on both the top and bottom of the load cell assembly were precisely fabricated by milling and machining to ensure the rigidity and levelness of the overall supporting system, maintaining the idealized boundary condition necessary for the post-analysis of experimental data. The components of a one-way support assembly are presented as an example in Figure 6-17.

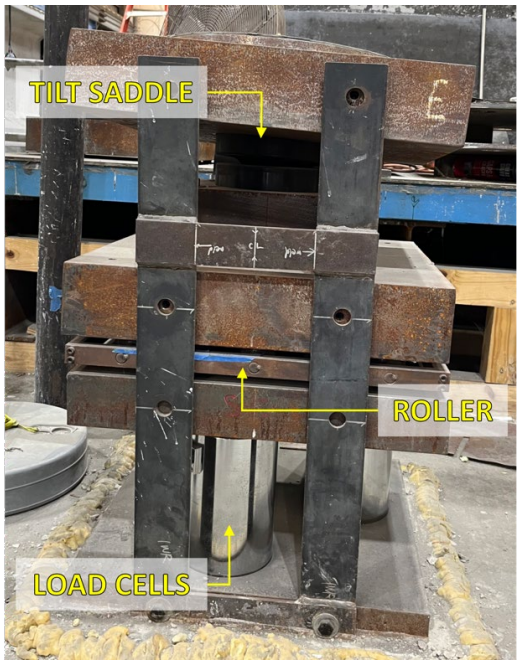

Figure 6-17 Assembly of a one-way support

Linear potentiometers were employed to monitor the displacement of the specimen at critical locations during the experiment. These potentiometers were strategically positioned at the center of the specimen, near the supports, and at the bottom of the cold joints to capture displacements that characterized the behavior of the footing. The linear potentiometer at the center of the specimen was utilized to measure the maximum deflection during the experiment, while two linear potentiometers at each support were used to interpolate the support settlement. Eight pairs of linear potentiometers were located at the cold joint to measure the displacement difference between the internal and external regions of the footing, allowing for the assessment of slip at each side and corner throughout the test. The locations of the linear potentiometers are depicted in Figure 6-18.

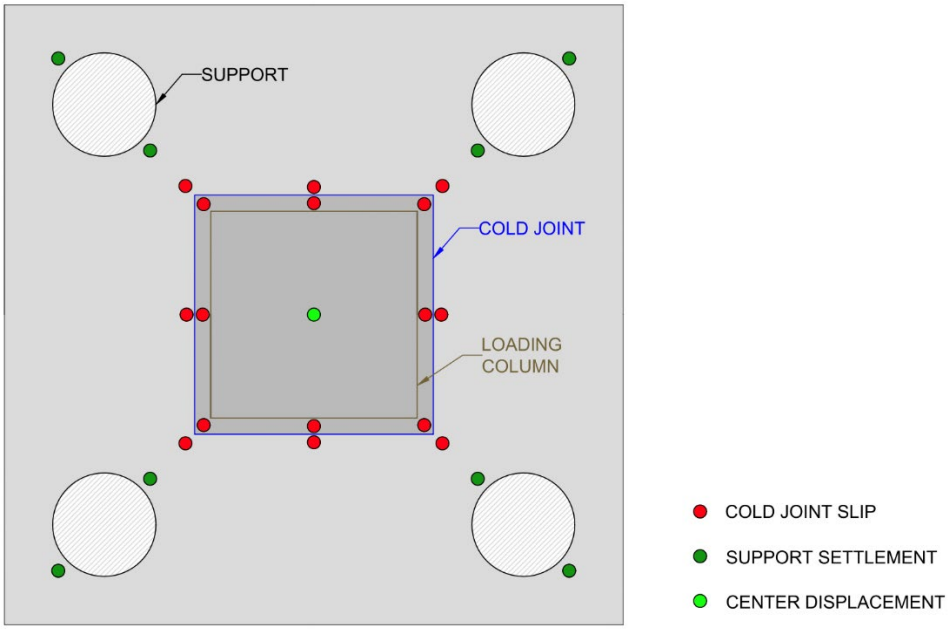

Figure 6-18 Location of linear potentiometers through the bottom view of the specimen

6.6.1.2. Strain Measurements

Strain gauges were attached to the bottom mat reinforcement, focusing on the region where ties intersect with the cold joints. The placement of strain gauges aimed to measure the strain in the bottom mat reinforcement throughout the specimen at each load step. Additionally, the governing failure mode of the specimen can be examined through the strain gauge data by determining whether yielding of the bottom mat reinforcement occurred during the experiment. However, unlike specimens in Task 5 where cold joints, which included crack control reinforcement in the strut region, there was no reinforcement in the idealized intersection of struts and the cold joints. Therefore, no strain data could be obtained from the strain gauges at the struts crossing cold joints.

To differentiate strain gauge data from various locations, a labeling nomenclature was developed and consistently applied throughout the instrumentation process. The first letter of each label indicates the type of reinforcement to which the strain gauge was attached. Labels were then assigned according to the location of the bottom mat reinforcement relative to the center of the specimen. For example, strain gauges installed on rebar north of the specimen's center were labeled with an "N". The subsequent letter specified the specific reinforcement bar, with smaller numbers assigned to bars positioned closer to the center of the specimen. The final number in the label denoted the portion of the footing where the strain gauge was attached. For gauges instrumented at the cold joints, the same labeling system was used, with "CJ" appended to clearly indicate their placement. The arrangement of strain gauges is shown in Figure 6-19.

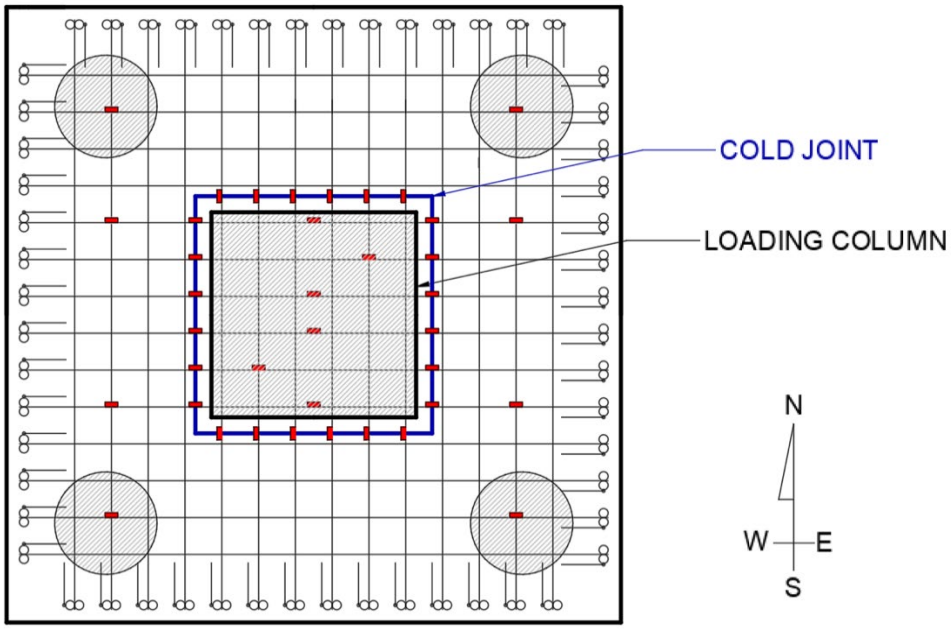

Figure 6-19 Strain gauge locations

6.6.1.3. Crack Measurements

Cracks were marked and the crack widths were measured using a standard crack comparator after each load step. The crack comparator features solid lines of specific thickness that are used to visually compare with the width of the cracks. To ensure consistency and reliability in the measurement process, all crack width assessments were conducted by the same student throughout the experimental program, mitigating the influence of subjective judgment. The crack comparator, depicted in Figure 6-20, serves as a visual aid for accurately assessing crack widths during the testing process.

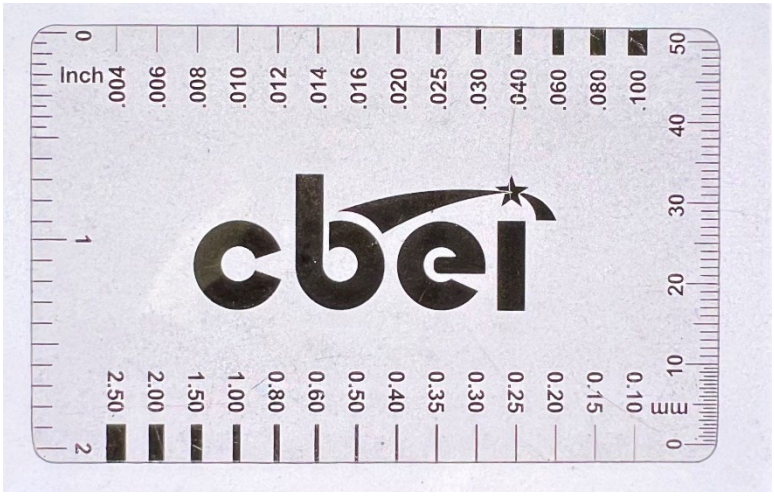

Figure 6-20 Crack comparator

6.6.1.4. Non-contact Instrumentation

A Digital Image Correlation (DIC) system was integrated into the experiment to monitor the strain field and crack development on one edge of the cold joint. The DIC system employs two high-speed cameras to capture the speckle pattern applied to the surface of the testing region. To enable accurate measurement and analysis, the DIC system undergoes systematic calibration using specific calibration equipment. This calibration process ensures that the DIC system can accurately project the area of interest onto a virtual spatial coordinate.

Once a reference image is selected, the DIC system calculates deformation within the monitoring area by analyzing the coordinate differences of each speckle. This allows the system to compute displacement and strain contours, facilitating the observation of crack development through the analysis of images and the identification of discontinuities in the strain profile. The components of the DIC system used in the experiment are detailed in Figure 6-21, illustrating the setup and technology employed to capture and analyze displacement and crack behavior during the test.

(a) Speckle pattern on the testing region

(b) High speed cameras

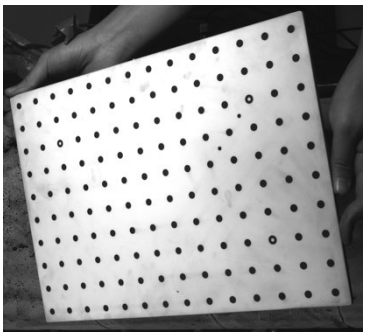

(c) Calibration board

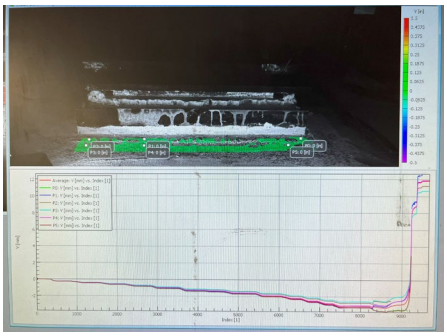

(d) Speckle image projection and displacement data collection

Figure 6-21 DIC setup and equipment

6.6.2. Testing Procedure

To ensure uniform contact between the specimen and each supporting assembly, the heights of the supports were adjusted, and the load cells were calibrated after the specimen was

positioned in the setup. Prior to the specimen placement, all load cells were tared with no external loads applied to the supports. Subsequently, the total loads measured by the load cells in each support were monitored during the placement of specimen. The height of each support assembly was then adjusted with thin aluminum sheets to ensure that each support made firm contact and provided reaction force to support the self-weight of the specimen before the experiment. The calibration process and results are shown in Figure 6-22.

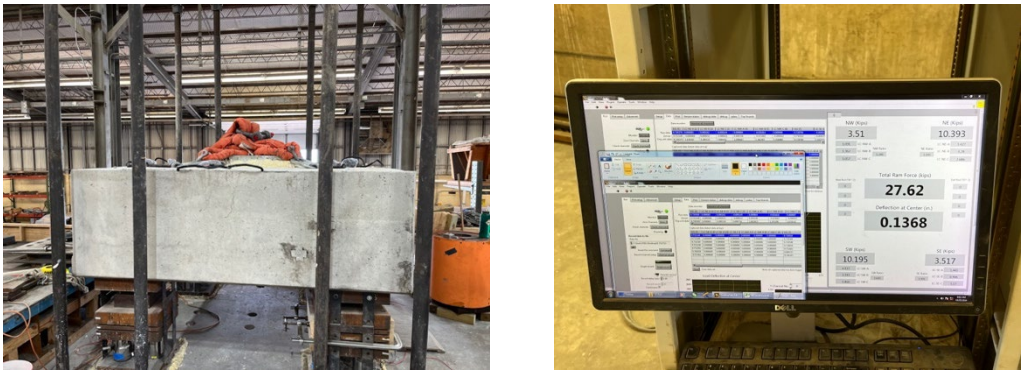

(a) Support adjustment under self-weight *(b) Reaction after contact calibration*

Figure 6-22 Load cell calibration before the experiment

During the experiment, the specimen was subjected to monotonic loading in increments of 200 kips, with a loading rate of 25 kips/min, until failure occurred. This load increment was set to approximately 10% of the nominal capacity of the specimen. Upon reaching each predefined load stage, cracks were meticulously marked, and the width of each crack in the testing regions was measured and documented in correspondence with the load step. Photos of each face were taken at every load stage, which were subsequently used to create crack maps illustrating the progression of cracks throughout the experiment. The behavior of the specimen was closely monitored until failure occurred, facilitating a comprehensive assessment of the structural behavior and failure mechanism under the specified loading conditions.

6.7. Experimental Results

In this section, the experimental results of the drilled-shaft footing cap from the test program are presented and discussed in detail. Specifically, the following aspects are addressed:

- The capacity of drilled-shaft footing with vertical cold joint (Section 3.1)
- The crack pattern and failure mode (Section 3.2)
- The evolution of reinforcing bars strain (Section 3.3)

A summary of the experimental results is presented and pivotal information is highlighted to standardize the response and facilitate an in-depth discussion of the findings.

6.7.1. Summary of Experimental Results

The experimental results are presented in Table 6-6, while the design detail of the specimen was previously provided in Section 2. Photographs of cracks on the north, east and west side of the specimen at every load step are presented in Appendix F. The variables used in Table 6-6 are defined as follows:

A_{col} = Area of loading column, in^2.

f'_c = Compressive strength of concrete at the time of testing measured in accordance with ASTM C39/C39M-21, psi.

f_{yb} = Yield strength of bottom mat reinforcement measured in accordance with ASTM A370-24 (Section 3.4.1), ksi.

f_{ysf} = Yield strength of vertical side face reinforcement measured in accordance with ASTM A370-24 (Section 3.4.1), ksi.

P_{STM} = Load capacity calculated using 3D-STM introduced in Section 2.1 without considering the effect of cold joint, kips.

P_{cr} = Load at which cracking was observed on the side face, kips.

P_u = Ultimate applied load, including the self-weight of the specimen and transfer girders, kips.

$P_{u,N}$ = Normalized ultimate applied load ($\frac{P_u}{f'_{c,int}A_{col}}$), kips

z = Distance from the center of column to the center of shaft, in.

Δ_m= Measured deflection under the center of loading area, in.

Δ_{supp}= Average settlement of four supports, in.

Δ= Deflection under the center of the loading area, adjusted for the average settlement of the supports ($\Delta_m - \Delta_{supp}$), in.

Δ_{max}= Deflection under the center of the loading area adjusted for the average settlement of the supports at ultimate load, in.

$\Delta_{max,N}$= Normalized deflection under the center of the loading area adjusted for the average settlement of the supports at ultimate load ($\frac{\Delta_{max}}{z}$), in.

Table 6-6 Test results of DSF1

Material Properties				Test results				
$f'_{c,int}$	$f'_{c,ext}$	f_{yb}	f_{ysf}	P_{cr}	P_u	$P_{u,N}$	Δ_{max}	$\Delta_{max,N}$
3.58	5.18	64.1	63.7	427	2693	0.68	0.34	7.40

6.7.1.1. Evaluation of Strength Data

The maximum applied load, denoted as P_u in Table 6-6, was defined as the capacity of the specimen. To accurately calculate the applied load, the self-weight of the specimen was included

alongside the load cell data. To evaluate the behavior of the specimen, the load capacity, P_u, was normalized by the compressive strength of the concrete, $f'_{c,int}$, and the dimensions of the loading column, A_{col}. Similarly, the normalized displacement of the specimen, Δ_N, was also calculated through dividing the displacement measured at the center of the specimen, Δ, by the distance from the center of the loading column to the center of the drilled shafts, z. For reinforced concrete (RC) members governed by shear failure associated with the tensile strength of concrete, it is common to normalize the shear capacity by $\sqrt{f'_c}$.However, to more effectively assess the influence of the cold joint on the compression capacity of the concrete struts, the applied load was normalized by $'$ in this research. This evaluation method reflects the crushing failure observed during the experiment and aligns with the concept implemented in the Strut-and-Tie Method (STM), which uses f_c' to calculate the compression capacity of the concrete strut.

6.7.1.2. Load-Displacement Response

The applied load versus center displacement response of the specimen is presented in Figure 6-23. The initial flexural crack occurred at an early stage when the applied load reached approximately 20% of the ultimate load capacity. As the applied load approached the ultimate capacity, the load-displacement response transitioned from a linear trend to a plateau phase characterized by minimal increase in strength despite increase in displacement. This plastic plateau observed in the load-displacement response was attributed to the slipping of the cold joints. The occurrence of cracking and subsequent slip at these joints prior to failure resulted in significant downward displacement at the center of the specimen. This displacement was primarily due to the relative movement between the internally loaded portion of the footing and the external supporting portion until failure occurred.

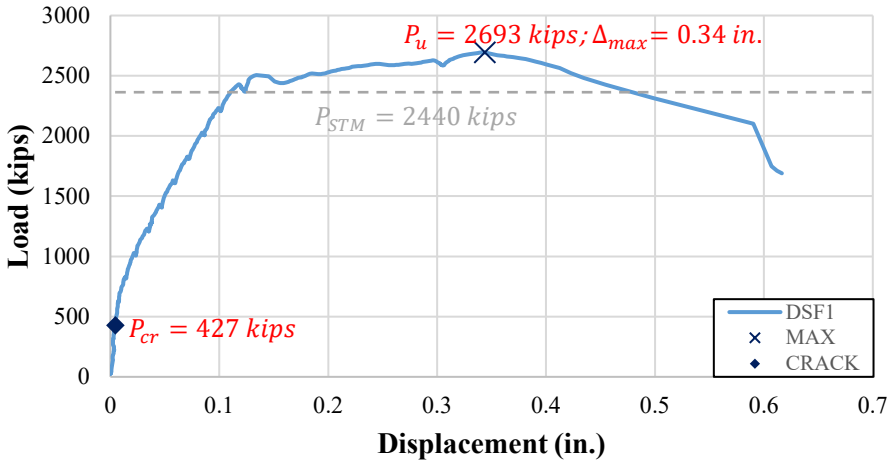

Figure 6-23 Load-displacement response

To gain a deeper understanding of the behavior of cold joints, slip measurements from eight pairs of linear variable differential transformers (LVDTs) positioned on the bottom surface of the specimen is presented in Figure 6-24. The displacement difference recorded by each pair of

LVDTs was interpreted as slip at specific cold joint locations. Results were organized according to the orientation of each pair of LVDTs relative to the center of the specimen. Notably, slip measurements at the corners of the cold joint were significantly greater than those along the edges, consistent with the idealized load-transfer paths of 3D-STM. This observation suggests that the stress transferred from the loading point to the support was concentrated in the strut regions, particularly at intersections of struts and cold joints, leading to a pronounced structural response at those points. As illustrated in Figure 6-24, substantial slip was measured at approximately 2500 kips of applied load, coinciding with the onset of increased displacement without a corresponding load increase. This finding further validates the existence of significant slip at the cold joints, which influenced the overall response of the specimen at its limit state.

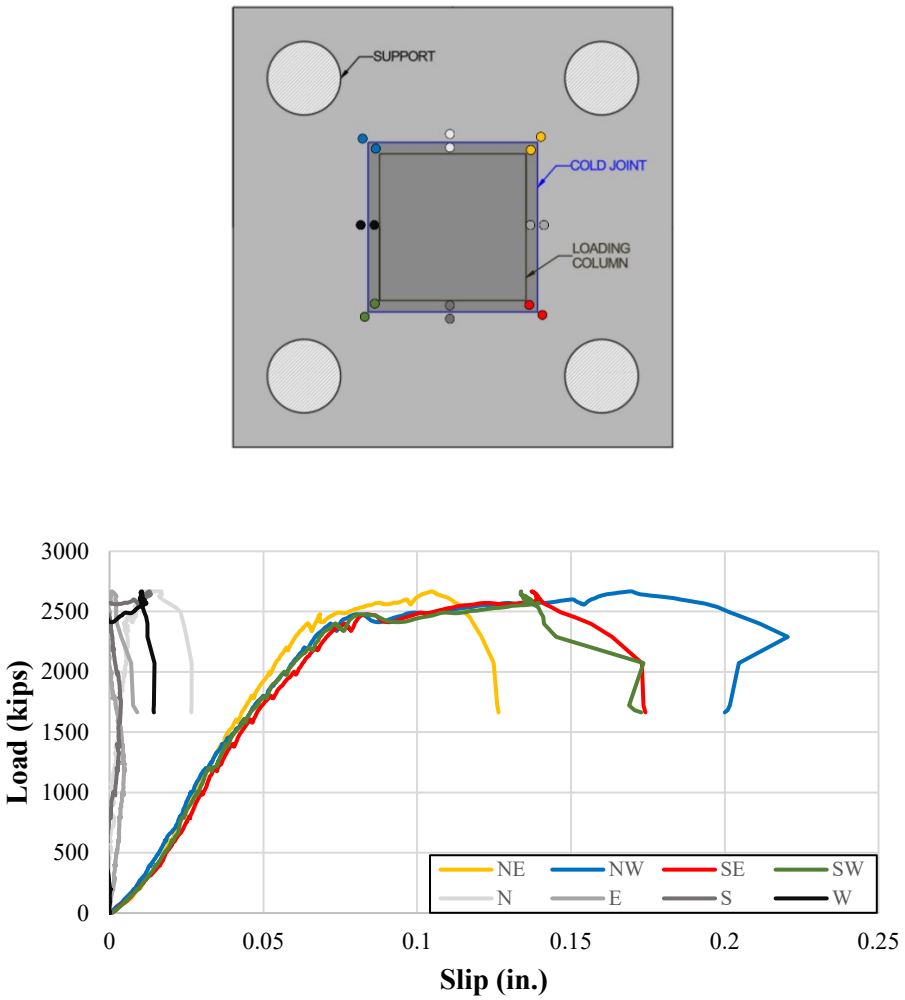

Figure 6-24 Slip at the cold joints

6.7.2. Crack Pattern and Failure Mode

During the experiment, crack development was marked and recorded with photographs after each predetermined load step. The widths of the largest cracks at each step were measured

and documented for each face of specimen to further evaluate the response of the structure. For specimen DSF1, the first flexural cracks occurred on the east and west faces of the structure when the applied load reached 400 kips, as shown in Figure 6-25(a). Additional flexural cracks were observed at the subsequent load step on the north and south faces of the specimen when the applied load reached 600 kips, as presented in Figure 6-26(b).

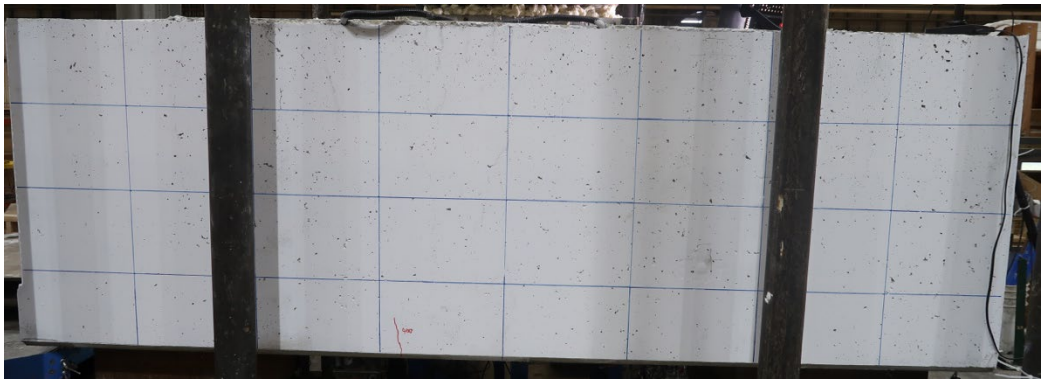

(a) 400 kips

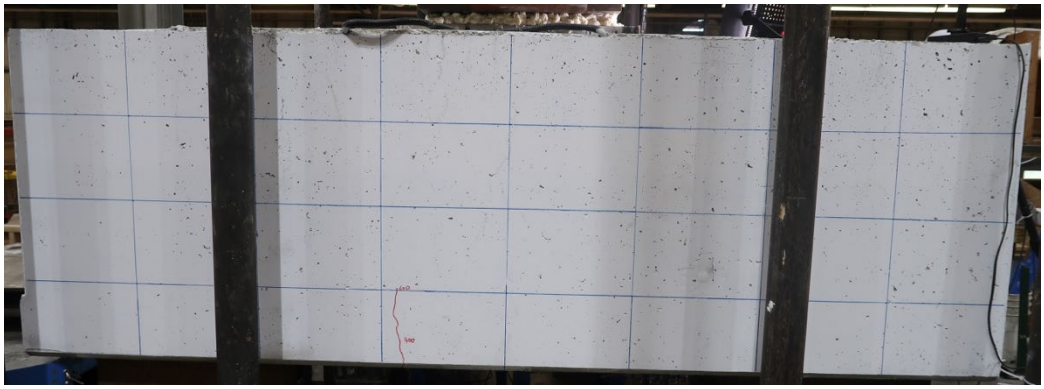

(b) 600 kips

Figure 6-25 West side face of DSF1

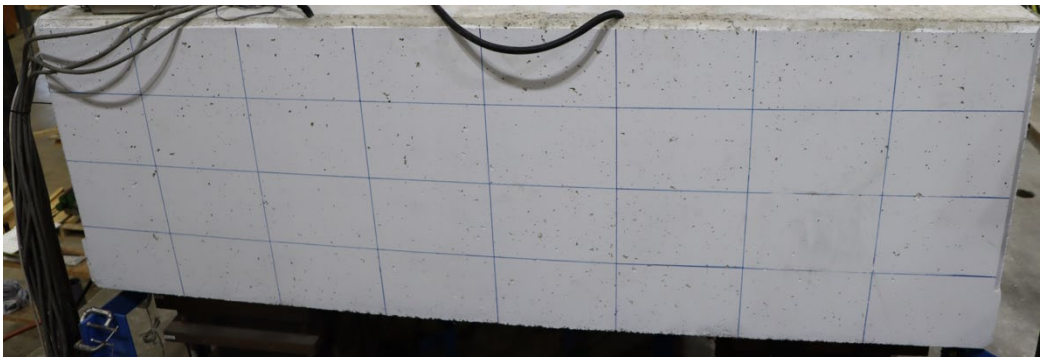

(a) 400 kips

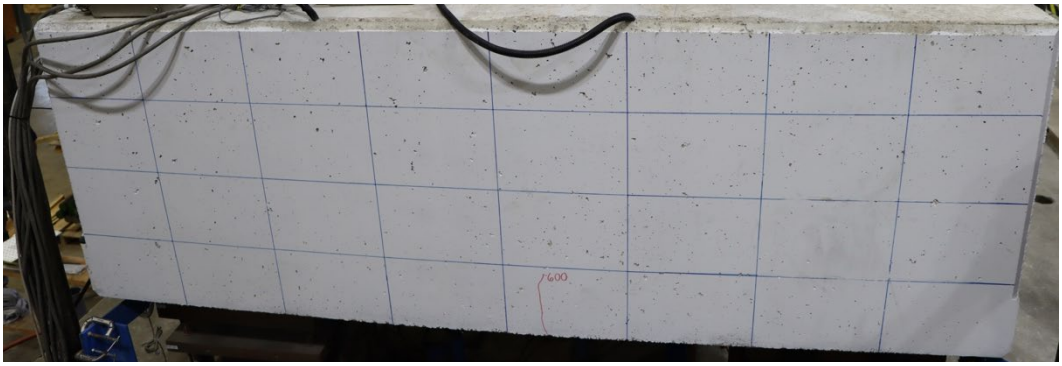

(b) 600 kips

Figure 6-26 North side face of DSF1

When the applied load reached 1600 kips, diagonal shear cracks began to develop along the idealized strut-lines on all faces of the specimen, as shown in Figure 6-27. It is also noteworthy that flexural cracks occurred in two distinct locations: at the mid-span of the footing, where the maximum moment occurred during the experiment, and along the projection lines from the cold joints to the side faces, which exhibited the lowest tensile capacity before cracking. As the load increased, additional shear cracks developed, and cracks along different strut-lines on the same surface began to connect, resulting in an arch-shaped crack pattern on the side surfaces of the specimen. The crack patterns observed at 2400 kips are shown in Figure 6-28, where the distribution of cracks is in agreement with previous experimental results from specimen without cold joints (Yi et al., 2022).

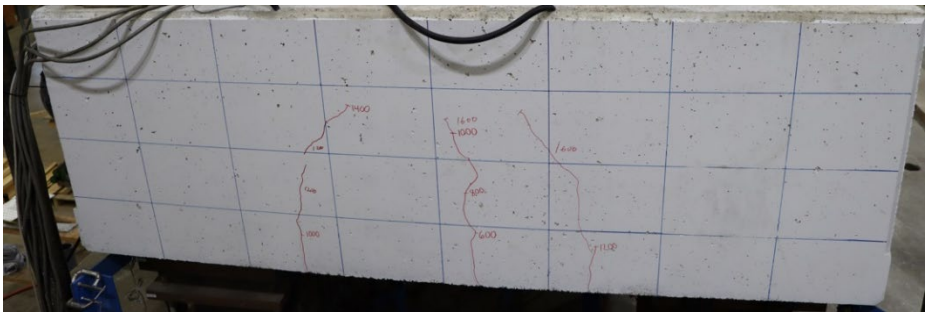

(a) North

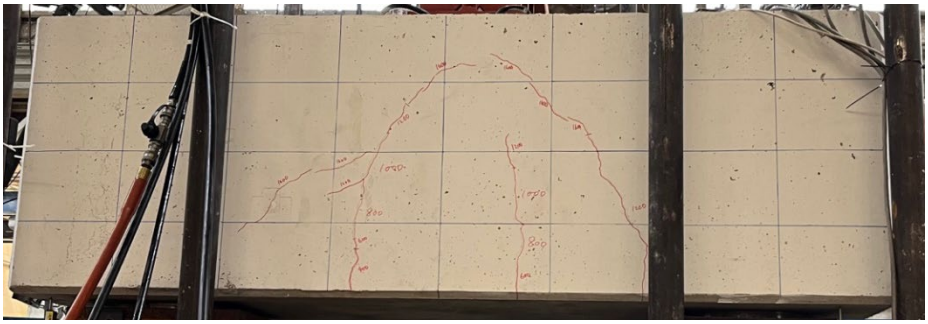

(b) East

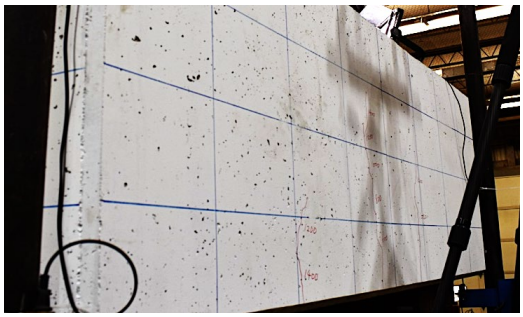

(c) South

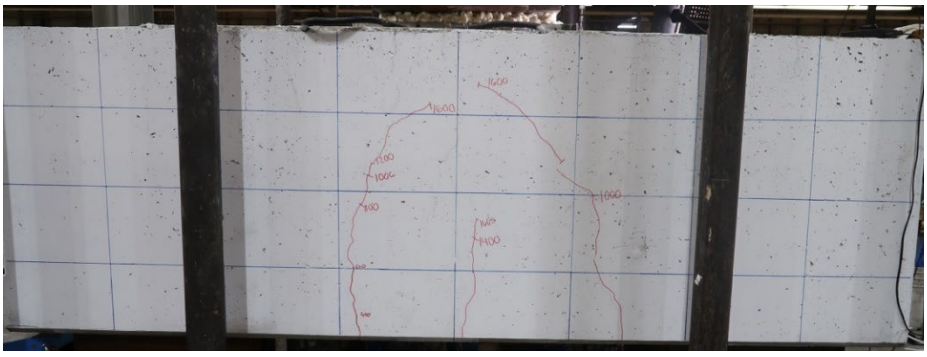

(d) West

Figure 6-27 Crack patterns at 1600 kips

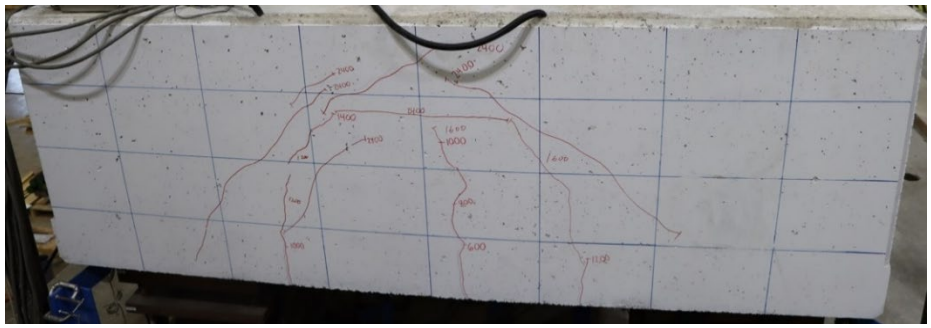

(a) North

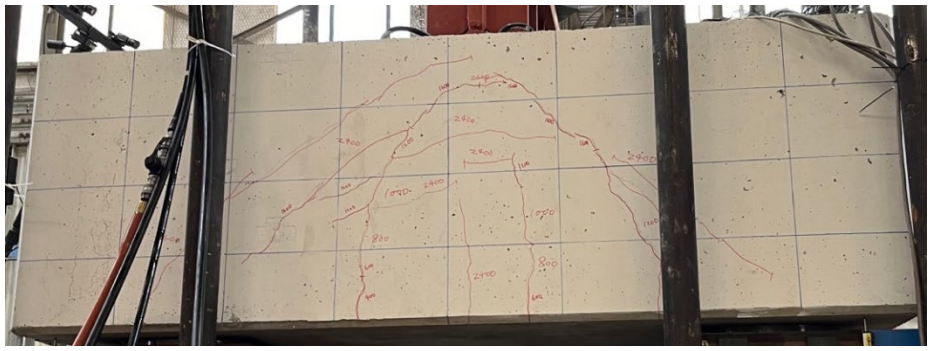

(b) East

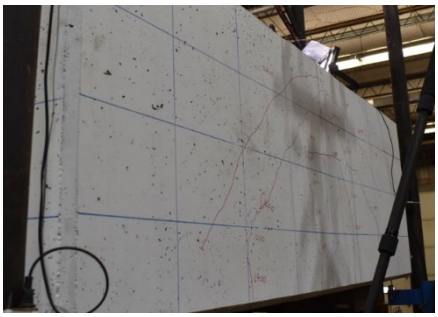

(c) South

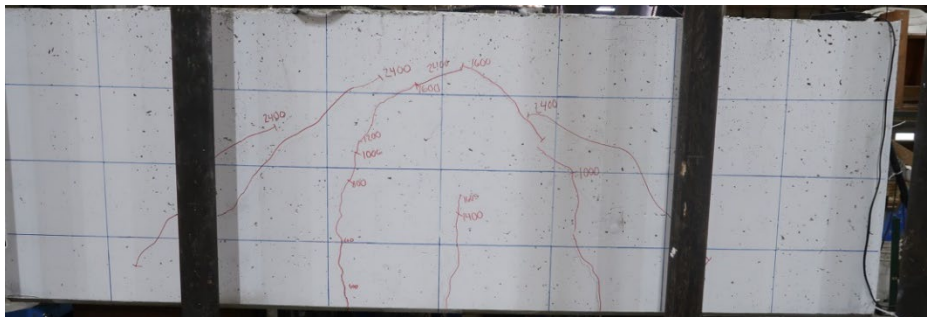

(d) West

Figure 6-28 Crack patterns at 2400 kips

The separation between the internal and external portions of the footing remained subtle throughout the experiment. Photographs of the top of the specimen were captured at each load step to monitor the behavior of cold joints, as shown in Figure 6-29. When the applied load reached 2000 kips, minor cracks began to form along the cold joints, and a slight settlement of the internal section was observed on the top surface of the specimen. Although the slip of the cold joint was not pronounced one load step before failure (2400 kips), significant separation and settlement were evident after failure. Furthermore, cracks along the cold joints propagated to the shear cracks along the idealized strut-line. This observation aligns with the load-displacement response and the measured slip at the bottom of the specimen, where substantial slip occurred as the load approached failure. The flexural cracks developed along the cold joint and the separation of the internal section were also observed from the crack patterns of the bottom surface after failure, as shown in Figure 6-30.

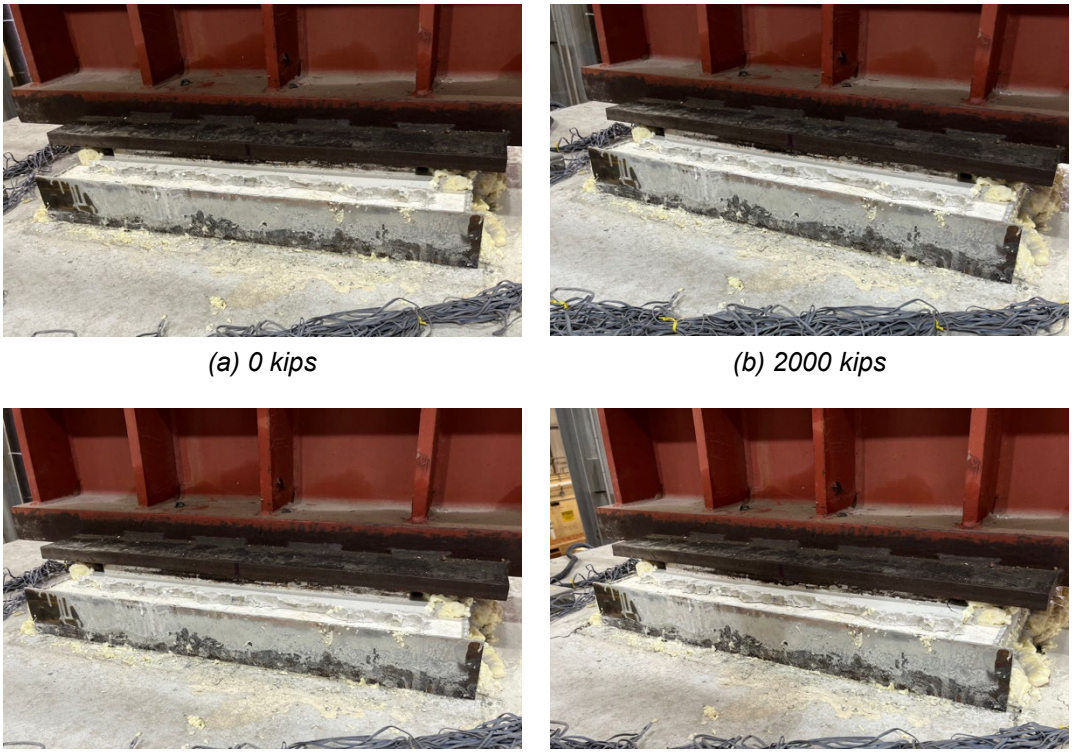

(a) 0 kips *(b) 2000 kips*

(c) 2400 kips *(d) Failure*

Figure 6-29 Slip of cold joints on the top surface

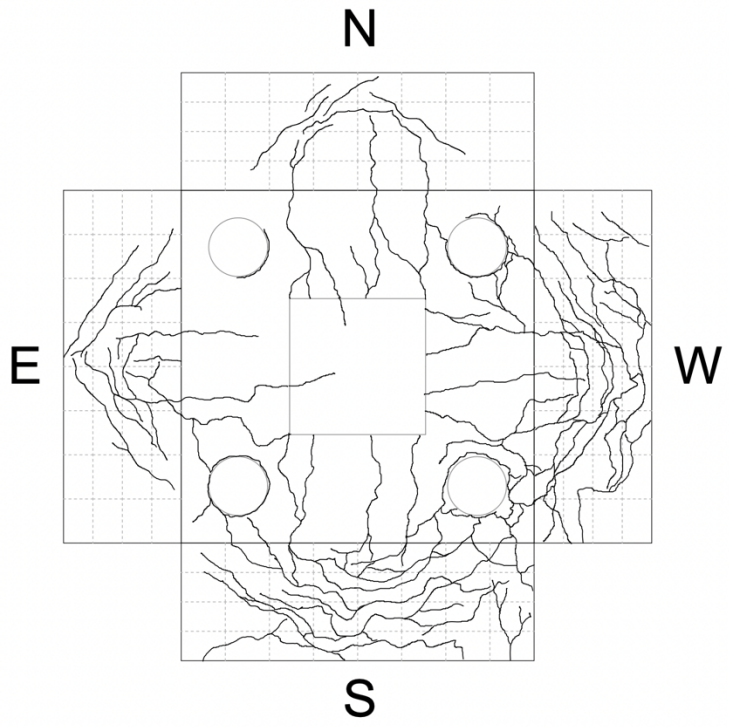

Figure 6-30 Crack map of the bottom surface after failure

Following the experiment, a sectional cut was made through the specimen. During testing, the cold joint on the south side experienced the most significant settlement among all sides, prompting the decision to focus the cut in this region to better examine the failure pattern. As shown in Figure 6-31(a), the observed crack pattern along the idealized strut-line and the intersection of the strut and cold joint indicated the development of cracks due to the compression force transferred from the strut through the cold joint. A similar crack pattern at the intersection of struts and cold joints was observed in the deep-beam experiments conducted in Task 5.

(a) Crack patterns at the cold joints after sectional cut

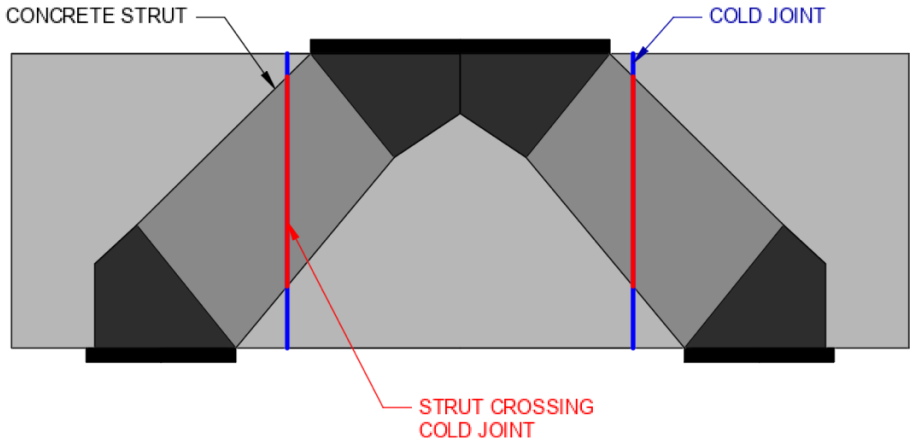

(b) Idealized projection of struts crossing cold joint

Figure 6-31 Development of compression strut crossing cold joints

By comparing the crack patterns from the sectional cut with the idealized projection of the cold joint along the strut-line, as shown in Figure 6-31, a significant failure characteristic of the cold joint was identified at the intersection of the struts and cold joints. Major delamination was concentrated at these intersections, indicating localized failure of the cold joints. In contrast, minor separation and slip were observed in the top compressive region and the bottom tension region. These observations indicate that the shear failure mechanism of the cold joints is most pronounced where forces are transferred through the compressive struts.

6.7.3. Strain Gauge Data

The strain gauge data measured at the ultimate load is presented in Figure 6-32. The strain measured at the intersection of the bottom mat reinforcement and the cold joint is greater than the strain measured at other locations. This strain distribution supports the observed failure mode,

where the failure was governed by the crushing of the strut without yielding of the ties. Additionally, the data revealed that the reinforcement outside of the cold joint did not reach its full strength before failure, whereas the reinforcement at the cold joint contributed more significantly at the ultimate load. This finding confirms that the failure was concentrated at the cold joints, preventing the complete development of the structural capacity of the entire footing, and further highlights the importance of evaluating the strength of cold joints in the D-region of 3D structures.

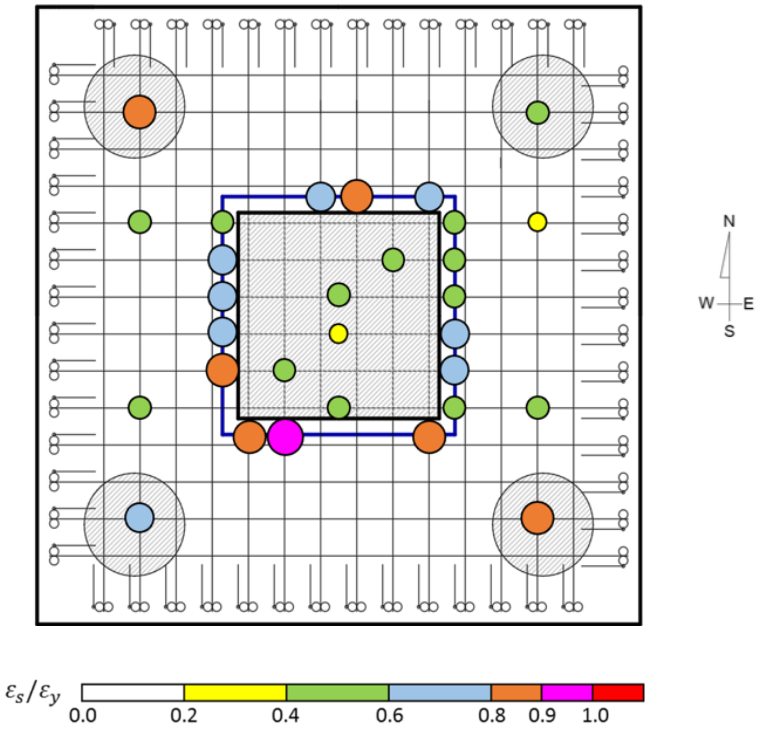

Figure 6-32 Strain distribution in bottom mat reinforcement at the ultimate load

6.8. Summary

This chapter presented the experimental program of Task 6-Drilled-Shaft Footing Test. A comprehensive structural evaluation was conducted to examine the influence of cold joints in a reinforced concrete member with a predominately three-dimensional behavior, including the assessment of load displacement response, slip at the cold joint, crack and failure patterns, and the strain in the bottom mat reinforcement. A significant plastic response measured during the experiment was found to be associated with the local slip of cold joints. Moreover, the crack and failure patterns of the side faces and the sectional cut indicated that the ultimate state of the structure was governed by the shear failure of cold joints. The strain measured in the bottom mat reinforcement also suggested that the overall structural capacity did not reach the ultimate state at failure, with strain primarily concentrated at the cold joints. In conclusion, the key findings of the drilled-shaft footing experiment are listed as follows:

- A plastic characteristic in the load-displacement response was observed and attributed to the slip occurring at the cold joints.
- The failure pattern observed on each side face and in the sectional cut indicated that shear failure was concentrated at the intersections of struts and the cold joints.
- Strain gauge data and comparative analyses revealed that the failure of the specimen was primarily localized at the cold joints, without exceeding the capacity of other components in the structure.

Chapter 7. Numerical Analysis and Design Recommendations

7.1. Proposed Analytical Method

This section introduces an STM-based analytical approach for evaluating the capacity of members with cold joints. The analysis focuses on calculating the shear capacity of the cold joint, integrated within the strut-and-tie method framework.

The load-resisting mechanism of members with cold joints was found to exhibit characteristics associated with both the strut-and-tie model and the interface shear behavior. Accordingly, the proposed methodology integrates principles from both STM and interface shear theory to accurately capture the structural response.

The approach distinguishes between two cases: Cold Joints not Intersected by STM Ties and Cold Joints Intersected by STM Ties. In this context, ties refer to tension members in the strut-and-tie model (STM) that transfer tensile forces across the cold joint. When a tie intersects a cold joint, the induced tensile force can cause local opening of the interface, rendering a portion of the cold joint ineffective in resisting shear. This phenomenon necessitates separate treatments of these two configurations in the analysis. The methodology is formulated for a single-panel model.

Figure 7-1 (a) and (b) illustrate the force distribution in a single-panel model incorporating a cold joint. In the strut-and-tie model (STM) idealization, compressive forces are transmitted along the diagonal strut. The portion of the cold joint intersecting the strut is designated as the effective area, within which the demand for the cold joint is evaluated. In addition to the contribution of the effective area to interface shear resistance, the regions adjacent to it, within the single-panel model, also participate in the shear-resisting mechanism.

Among these two different cases (Cold Joints not Intersected by STM Ties and Cold Joints Intersected by STM Ties), the evaluation of the shear resistance of the effective area is performed in a similar manner, and detailed in the following section. The difference lies in the treatment of the contribution to the shear capacity of the adjacent regions, elaborated in the subsequent sections.

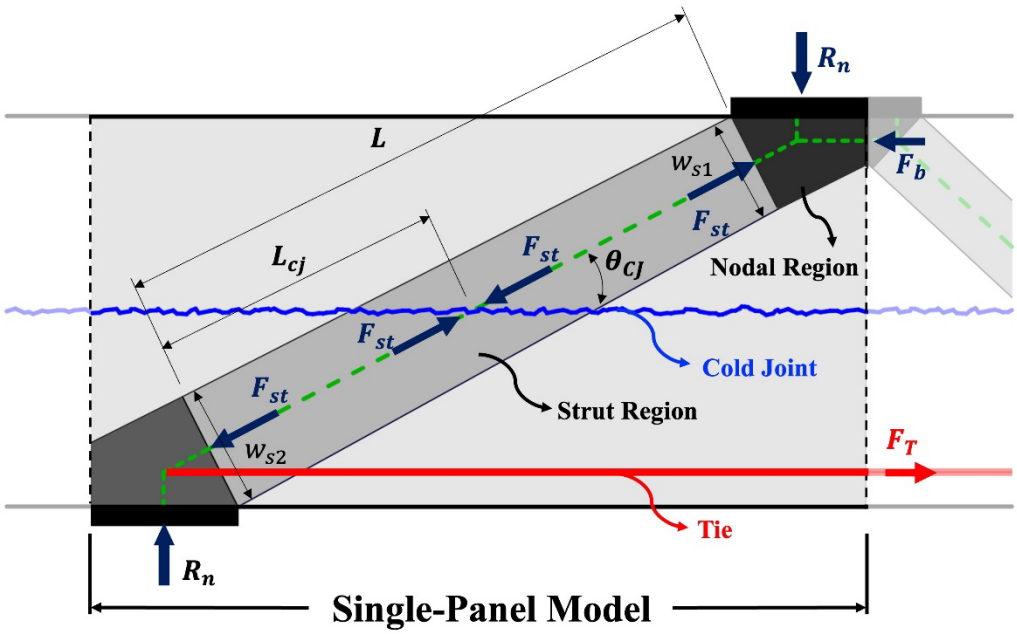

(a) Cold joints not intersected by STM ties

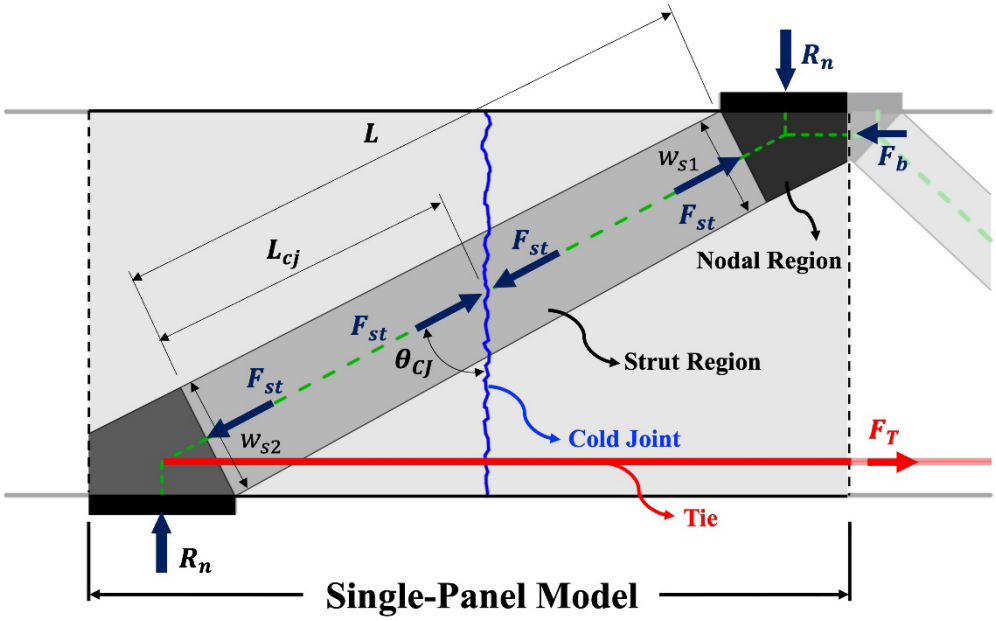

(b) Cold joints intersected by STM ties

Figure 7-1. Load transfer mechanism of deep beams with cold joints

7.1.1. Nominal Shear Resistance of the Cold Joint within the Effective Area

To evaluate the shear capacity of the cold joint within the effective area, the size of the effective area, A_{eff}, is determined based on the assumption of prismatic struts. Initially, the dimensions of each nodal face, w_{s1} and w_{s2}, are determined in accordance with the current STM provisions (AASHTO, 2024). The length of the effective area, w_{CJ}, is calculated using linear interpolation, as per Equation (7-1). To facilitate the linear interpolation, the length of the strut, L, and the distance from the strut-to-node face to the cold joint, L_{cj}, are incorporated into Equation (7-1). Subsequently, the effective area can be calculated as the multiplication of the length of the effective area, w_{CJ}, and the width of the beam, b_w, as per Equation (7-2).

$$w_{CJ} = \frac{w_{s1} - \frac{L_{cj}}{L} \cdot (w_{s1} - w_{s2})}{sin\theta_{CJ}} \tag{7-1}$$

$$A_{\text{eff}} = w_{CJ} \cdot b_w \tag{7-2}$$

To calculate the force distribution within the effective area, the force transferred through the strut is decomposed into components acting perpendicular, N_i, and parallel, V_i, to the cold joint, as expressed in Equation (7-3) and (7-4). The shear demand of the effective area is determined by the force component acting parallel to the cold joint.

$$N_i = F_{st} \cdot sin\theta_{CJ} \tag{7-3}$$

$$V_i = F_{st} \cdot cos\theta_{CJ} \tag{7-4}$$

The interface shear resistance of the effective area, V_{eff}, is calculated according to the interface shear formulation from AASHTO LRFD 2024 (AASHTO, 2024), as shown in Equation (7-5). The contribution of the force acting perpendicular to the cold joint, N_i, is incorporated in this expression. To ensure the consistency between the proposed approach and the current design specifications, the shear capacity of the effective area is limited by the same upper bounds prescribed in AASHTO LRFD 2024 (AASHTO, 2024), as per Equation (7-6) and (7-7).

$$V_{\text{eff}} = c \cdot A_{\text{eff}} + \mu \cdot (A_{\text{s,CJ}} \cdot f_y + N_i) \tag{7-5}$$

$$V_{\text{eff}} \leq K_1 f_c' A_{\text{eff}} \tag{7-6}$$

$$V_{\text{eff}} \leq \text{K}_2 A_{\text{eff}} \tag{7-7}$$

where c is the cohesion factor, μ is the friction factor, $A_{\text{s,CJ}}$ is the area of reinforcing bars intersecting the cold joint, f_y is the yielding strength of reinforcing bars, f_c' is the concrete compressive strength of the weaker concrete on either side of the cold joint, K_1 is the fraction of concrete strength available to resist interface shear, and K_2 is the limiting interface shear

resistance. Factors c, μ, K_1, and K_2 are determined according to Article 5.7.4.4 in AASHTO LRFD (AASHTO, 2024).

7.1.2. Nominal Shear Resistance of Cold Joints not Intersected by STM Ties

To determine the nominal shear resistance of cold joints not intersected by STM ties, the proposed approach considers the relevant failure mechanisms and associated restraint conditions within a single panel, as illustrated in Figure 7-2. The failure mode illustrated in Figure 7-2 (a) represents crushing of the concrete strut prior to the full engagement of the cold joint resistance. The proposed approach captures this failure mechanism by evaluating the demand-to-capacity ratio at the strut-to-node interface, ensuring that localized crushing is identified independently of the interface shear capacity. The strut-to-node interface capacity is calculated according to Equation 5.8.2.5.1-1 and Section 5.8.2.5 from AASHTO LRFD 2024 (AASHTO, 2024).

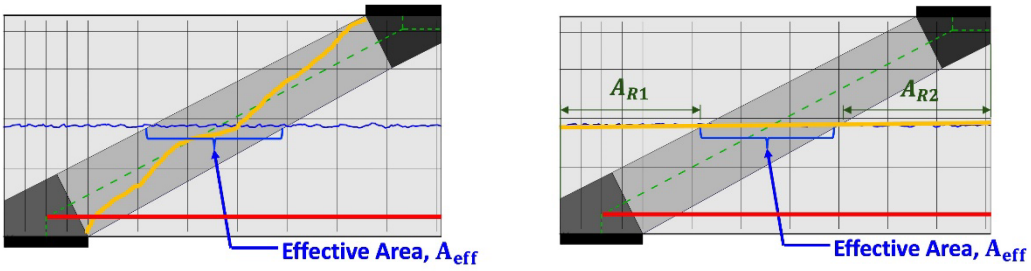

(a) Strut failure *(b) Cold joint failure*

Figure 7-2 Potential failure mechanisms for deep beams with horizontal cold joints

When the capacity of strut exceeds the shear capacity of the cold joint, failure may initiate along the cold joint interface, as shown in Figure 7-2 (b). Experimental evidence suggests that stress redistribution can activate regions of the cold joint beyond the immediate strut zone, allowing adjacent areas of the cold joint interface to contribute in the load-carrying mechanism. In this case, failure occurs when the combined shear capacity of the cold joint, within both the effective area and the adjacent regions is fully mobilized. To account for this behavior, the analysis incorporates both the shear resistance of the cold joint within the effective area, V_{eff}, and the shear resistance of the adjacent regions, V_{R1} and V_{R2}, calculated as per Equation (7-8). The shear resistance of each region should individually satisfy the upper limit of interface shear resistance in accordance with AASHTO LRFD 2024 (AASHTO, 2024), as per Equation (7-9) and (7-10).

$$V_{R1,2} = c \cdot A_{R1,2} + \mu \cdot \rho_{R1,2} \cdot A_{R1,2} \cdot f_{yR1,2} \quad (7\text{-}8)$$

$$V_{R1,2} \leq K_1 f_c' A_{R1,2} \quad (7\text{-}9)$$

$$V_{R1,2} \leq K_2 A_{R1,2} \quad (7\text{-}10)$$

where $V_{R1,2}$ is the effective restraint provided by the two adjacent regions, c is the cohesion coefficient, $A_{cj,R1,2}$ is the area of the adjacent region, μ is the friction coefficient, $\rho_{R1,2}$ is the reinforcement ratio within the adjacent regions, and $f_{yR1,2}$ is the yielding strength of reinforcement in the adjacent region.

The total shear resistance of the cold joint is calculated as the sum of the contributions of the effective area and the adjacent areas:

$$V_{ni} = V_{\text{eff}} + V_{R1} + V_{R2} \tag{7-11}$$

7.1.3. Nominal Shear Resistance of Cold Joints Intersected by STM Ties

The concept of external restraint provided by the adjacent regions also applies to cold joints intersected by STM ties; however, additional considerations arise when a tension-transferring tie intersects the interface. In such cases, the tensile force carried by the tie induces opening along a portion of the cold joint, rendering part of the interface ineffective in resisting shear. As a result, the potential governing failure mechanisms must consider both localized cold joint failure within the strut region and the influence of a partially-opened interface caused by tie-induced cracking. These potential failure modes are identified and illustrated in Figure 7-3.

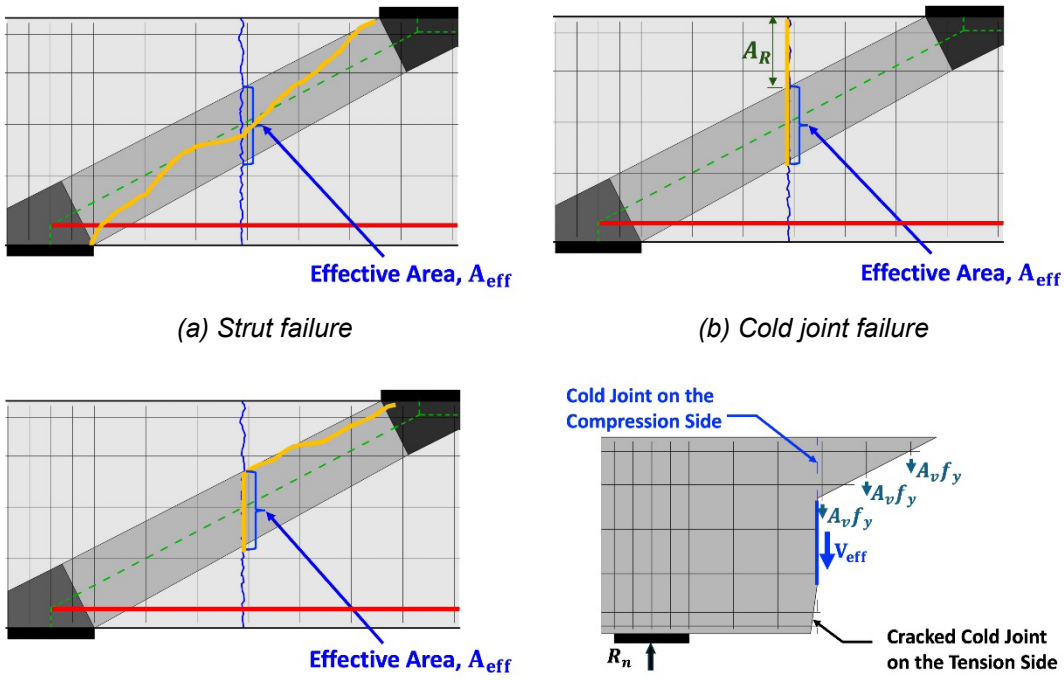

(a) Strut failure

(b) Cold joint failure

(c) Localized cold joint and partial strut separation

(d) Free body diagram for localized cold joint and partial strut separation

Figure 7-3 Potential failure mechanisms for deep beams with vertical cold joints

A potential failure mechanism includes compression failure of the strut, as illustrated in Figure 7-3 (a). Alternatively, a failure mechanism may occur prior to crushing of the strut, involving shear failure of the cold joint, as shown Figure 7-3 (b). In this case, the portion of the cold joint interface adjacent to the effective area, on the tie side is assumed to be fully cracked and thus, ineffective in resisting shear. Consequently, the shear resistance provided by the cold joint includes the effective area and the contribution of the adjacent region on the strut side, A_R. The effective restraint side is calculated as Equation (7-12). This effective restraint is also limited by the interface shear resistance upper bound per Equation (7-13) and (7-14).

$$V_R = c \cdot A_R + \mu \cdot \rho_R \cdot A_R \cdot f_{yR} \tag{7-12}$$

$$V_R \leq K_1 f_c' A_R \tag{7-13}$$

$$V_R \leq K_2 A_R \tag{7-14}$$

where A_R, ρ_R, f_{yR} and are respectively the area, the reinforcement ratio, and the reinforcement yielding strength of the uncracked cold joint, in the effective restraint region.

Therefore, the total shear resistance is determined as the sum of the shear resistance of cold joint within the effective area and the contribution from the adjacent interface outside the strut, in the effective restraint region:

$$V_{ni} = V_{eff} + V_R \tag{7-15}$$

A third potential failure mechanism is illustrated in Figure 7-3 (c). This involves a localized failure mode in which the cold joint fails in shear within the effective area, followed by separation of the strut from the effective restraint region. In this case, failure occurs before the adjacent interface restraint is fully mobilized. When the cold joint in the effective restraint region provides sufficient resistance to delay interface failure, local separation of the strut may govern the response. As a result, conventional strut-and-tie methods, which assume full strut mobilization, are not applicable. No existing STM-based formulation currently accounts for this type of partial strut separation.

A simplified expression is proposed to account for the effective restraint provided by the portion of strut adjacent to the effective area. The critical load path associated with the partial failure of strut is assumed to initiate at the boundary of the nodal region and extend toward the effective area of cold joint, aligning with the edge of the idealized prismatic strut. The resistance is derived from the contribution of reinforcement intersecting the critical load path, as shown in Figure 7-3 (d). The dowel contribution of the reinforcing bars intersecting the failure plane is excluded from the analysis due to its negligible influence on the overall resistance. The resistance, V_R, is calculated as the tensile strength of bars parallel to the slipping direction, as per Equation (7-16):

$$V_R = n \cdot A_v \cdot f_y \tag{7-16}$$

where n is the number of reinforcing bars, A_s is the area of each bar, and f_y is the yielding strength of reinforcing bars. Accordingly, the total shear capacity is determined by combining the shear resistance of cold joint in the effective area, V_{ni}, and the effective restraint, V_R, as previously shown in Equation (7-15).

7.2. Validation Based on Experimental Observation

7.2.1. Experimental Observation

To facilitate the following discussion, the experimental results from Task 5 are summarized in Table 7-1 for reference. For specimens with vertical cold joints, a significant decrease in shear capacity was observed in Specimen III-1.85-00-V and IV-1.2-03-V compared to monolithic specimens from prior research projects (D. B. Birrcher et al., 2009). These specimens also exhibited discontinuity of diagonal shear cracks, displacement, and strain field along the cold joints, as shown in Figure 7-4. Therefore, it was concluded that the shear capacity of cold joints in the strut region has a pivotal impact on the load transfer mechanism of deep beams.

Table 7-1 Summary of experimental results from Task 5

Beam ID	$f'_{c,min}$ (ksi)	ρ_{cj}	a/d	V_{crack} (kips)	V_{exp} (kips)	$\frac{V_{exp}}{f_{c,min}{}'b_w d}$	δ_{peak} (in.)	$\frac{V_{exp}}{\delta_{peak}}$ (kips/in.)
I-1.85-03-H	3.10	0.003	1.85	121	404	0.16	0.60	673
I-1.4-03-H	3.10	0.003	1.40	-	680	0.27	0.70	969
I-1.0-03-H	2.07	0.003	1.00	-	820	0.49	0.81	1019
II-1.85-00-H	2.17	0	1.85	122	296	0.17	0.62	480
III-1.85-00-V	4.60	0	1.85	123	416	0.11	0.76	550
III-1.85-00-V^{R}	4.73	0	1.85	-	642	0.17	1.18	543
IV-1.85-03-V	4.19	0.003	1.85	125	494	0.15	0.88	432
IV-1.2-03-V	4.07	0.003	1.20	-	526	0.16	0.62	851
III-1.85-03b^{M}	3.30	-	1.85	114	471	0.18	-	-
III-1.2-03^{M}	4.22	-	1.20	-	829	0.24	-	-

Note: $f'_{c,min}$ = concrete compressive strength of the weaker layer
ρ_{cj} = ratio of reinforcement crossing the cold joint
a/d = shear-span-to-effective-depth ratio
V_{crack} = shear force at first diagonal crack
V_{exp} = experimentally measured maximum shear strength
b_w = cross-sectional width of the specimen
d = effective depth of the specimen
δ_{peak} = peak load displacement at the point of load application
^{R} = specimens with roughened cold joints
^{M} = monolithic specimens from previous research (Birrcher et al., 2009)

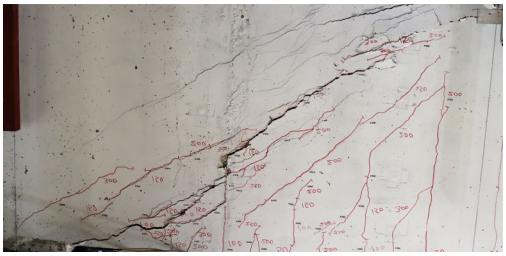

(a) Crack patterns of III-1.85-00-V

(b) Crack patterns of IV-1.2-03-V

(c) Displacement field of III-1.85-00-V

(d) Displacement field of IV-1.2-03-V

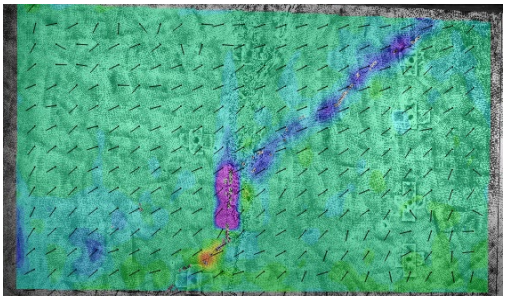

(e) Strain field of III-1.85-00-V

(f) Strain field of IV-1.2-03-V

Figure 7-4 Crack patterns, displacement and strain fields at peak load of Specimen III-1.85-00-V and IV-1.2-03-V

7.2.2. Crack Patterns and Local Failure Zone

In the proposed analytical approach, the effective area was determined by modeling the compression strut as prismatic. However, prior research suggested that the bottle-shaped strut can better represent the compression field in the strut-and-tie model. To evaluate the validity of the prismatic assumption, both prismatic and bottle-shaped strut geometries were incorporated into the analytical model to calculate the length of the effective area for Specimen III-1.85-00-V and IV-1.2-03-V, both of which exhibited localized cold joint failure. The corresponding effective lengths calculated using the prismatic and bottle-shaped assumptions, $w_{CJ,p}$ and $w_{CJ,b}$, are summarized in Table 7-2 alongside the experimentally measured length of the cold joint failure region, $w_{CJ,exp}$, for comparison.

Table 7-2 Comparison between calculated and measured effective length

Specimen	$w_{CJ,p}$ (in.)	$w_{CJ,b}$ (in.)	$w_{CJ,exp}$ (in.)
III-1.85-00-V	14.16	24.31	11.46
IV-1.2-03-V	17.79	18.53	13.50

The derivation of effective length in a prismatic strut, as shown in Figure 7-5, is previously discussed in Section 7.1.1, and should be calculated according to Equation (7-1). Since the vertical cold joints of all specimens are located at the mid-span of the testing region, the effective area of a cold joint intersected by a bottle-shaped strut is determined using the strut width at the mid-span and the inclination between the strut and the cold joint. For the bottle-shaped strut, the strut width is calculated based on the approximate expression proposed by Schlaich and Weischede (Schlaich & Weishede, 1982), as presented in Figure 7-6 and Equation (7-17) and (7-18). Subsequently, the calculated strut width is projected onto the cold joint using the strut-to-cold-joint inclination, θ_{CJ}, to obtain the effective area corresponding to the cold joint orientation, as per Equation (7-19).

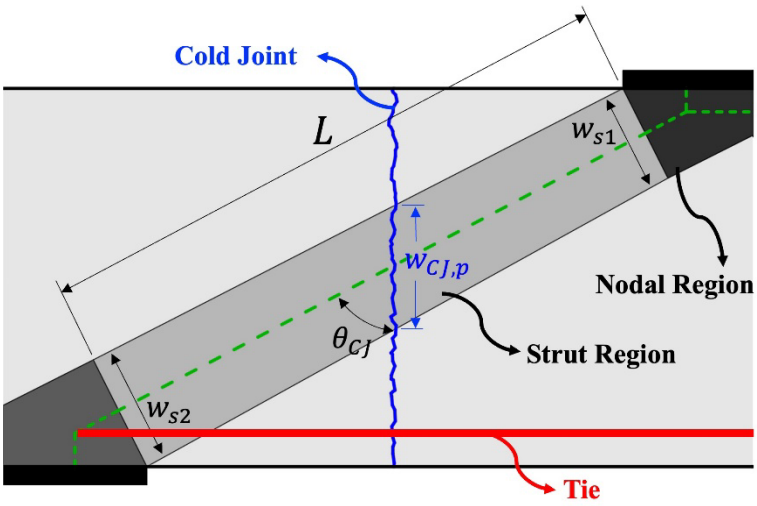

Figure 7-5 Cold Joint Intersected by A Prismatic Strut

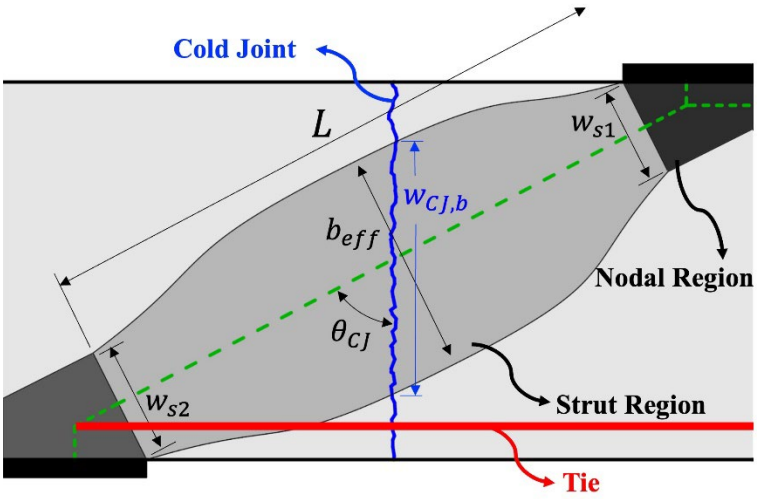

Figure 7-6 Cold Joint Intersected by A Bottle-Shaped Strut

$$w_{s,min} = min(w_{s1}, w_{s2}) \tag{7-17}$$

$$b_{eff} = \begin{cases} L/3, & for\ w_{s,min} < L/3 \\ L/6 + w_{s,min}, & for\ w_{s,min} \geq L/3 \end{cases} \tag{7-18}$$

$$w_{CJ,B} = \frac{b_{eff}}{sin\theta_{CJ}} \tag{7-19}$$

The experimentally observed region of localized failure along the cold joint was identified using the DIC based on the area exhibiting significant displacement differentials across the cold joints, as demonstrated in Figure 7-7. By comparing the calculated effective length to the experimentally measured length of the localized failure region, it is concluded that the length

calculated using the prismatic strut assumption yields better agreement with the experimental measurement. Conversely, the calculation based on the bottle-shaped assumption tends to overestimate the effective length in certain cases. Accordingly, the application of the prismatic strut model is recommended for evaluating the effective area of cold joints within the strut regions.

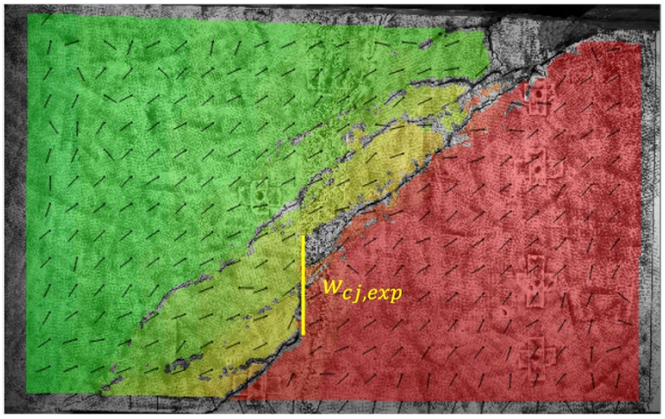

Figure 7-7. Experimentally observed region with localized cold joint failure

7.2.3. Shear Capacity and Failure Mode

The shear capacities of the specimens tested in this study, calculated using the modified analytical approach, $V_{STM,CJR}$, are summarized in Table 7-3. This approach incorporates the contribution of effective restraint and accounts for the associated potential failure mechanisms. All previously discussed failure mechanisms were evaluated for each specimen, and the governing failure mode was identified as the mechanism associated with the lowest calculated capacity. For comparison, the experimental results are provided in Table 7-3, along with the shear capacity and failure modes calculated using the current STM without considering the effect of the cold joint. To evaluate the level of conservatism of the proposed approach for deep beams with cold joints, experimental data and analytical results using the current STM from two monolithic control specimens reported in prior research (D. B. Birrcher et al., 2009) are also summarized in Table 7-3.

Table 7-3 Comparison of Analytical and Experimental Failure Modes and Shear Capacity

Specimen	V_{STM} (kips)	$V_{STM,CJR}$ (kips)	V_{test} (kips)	$\frac{V_{test}}{V_{STM}}$	$\frac{V_{test}}{V_{STM,CJR}}$	M_{STM}	$M_{STM,CJR}$	M_{test}
I-1.85-03-H	253	253	404	1.60	1.60	Strut	Strut	Strut
I-1.4-03-H	328	258	680	2.07	2.64	Strut	CJ	Strut
I-1.0-03-H	277	277	820	2.96	2.96	Strut	Strut	Strut
II-1.85-00-H	123	90	296	2.41	3.29	Strut	CJ	Strut
III-1.85-00-V	309	274	416	1.35	1.52	Strut	CJ	CJ
III-1.85-00-VR	341	341	642	1.88	1.88	Strut	Strut	Strut
IV-1.85-03-V	331	331	494	1.49	1.49	Strut	Strut	Strut
IV-1.2-03-V	426	336	526	1.23	1.57	Strut	CJ	CJ
III-1.85-03b^{P}	271	-	471	1.74	-	Strut	-	Strut
III-1.2-03^{P}	459	-	829	1.81	-	Strut	-	Strut

Note: V_{STM} = shear strength calculated using current STM specifications
$V_{STM,CJR}$ = shear strength calculated using the proposed approach
V_{test} = shear strength measured from the experiment
M_{STM} = failure mode identified using current STM specifications
$M_{STM,CJR}$ = failure mode identified using the proposed approach
M_{test} = failure mode observed from the experiment

To numerically determine the failure modes of the specimens, the capacities of all strut-and-tie components were calculated. These components include the bearing capacities of all the nodal faces and the tensile capacities of ties. For deep beams with cold joints, the shear capacity of cold joints in the effective area was also evaluated in accordance with the proposed analysis approach. Subsequently, the corresponding applied load at which the internal force demand exceeded the nominal capacity was calculated for each component. The component with the lowest corresponding applied load was identified as the critical element, and the failure mechanism associated with the critical element was determined as the governing failure mode.

For specimens with cold joints that are not intersected by STM ties, the proposed approach successfully identified the governing failure mode in two of the four specimens. The experimental-to-calculated shear strength ratios are consistent with the monolithic specimens when the contributions of effective area and adjacent regions are included.

Compared to the shear strength calculated using the current STM, the average experimental-to-calculated shear strength ratios for specimens that experienced cold joint failure, namely IV-1.2-03-V and III-1.85-00-V increased from 1.23 and 1.35 to 1.57 and 1.52, respectively when evaluated using the proposed approach. These ratios calculated using the proposed approach are comparable to the 1.74 ratio derived from the monolithic specimen evaluated using conventional STM. This indicates that the level of conservatism of the proposed approach remains uncompromised in the assessment of deep beams with cold joints.

Failure modes determined by the proposed approach for specimens with cold joints intersected by STM ties exhibit strong agreement with the experimental observations. In the design of Specimen III-1.85-00-VR and III-1.85-03-V, the total shear capacity of the cold joint within the effective area and the adjacent regions remains sufficient at the ultimate load, and failure is governed by the bearing capacity of the strut-to-node face. This indicates a strut governing failure

mode, which is consistent with the crushing of concrete in the strut region observed from the experiment.

In contrast, for Specimens III-1.85-00-V and IV-1.2-03-V, the shear demand across the cold joint exceeds the total shear capacity of the effective area and the adjacent regions at ultimate load, while the capacities of the strut-to-node faces remain adequate. The critical components identified through the proposed approach align with the localized cold joint failures observed in the experiments, underscoring the validity and effectiveness of the proposed approach in capturing the governing failure mechanisms of deep beams with cold joints.

Within the experimental program, Specimen IV-1.2-03-V was unique in exhibiting a compound failure, characterized analytically by both shear failure in the effective area and partial strut separation. Correspondingly, the observed crack patterns revealed no damage on the compression side of the cold joint outside the strut region at failure, as shown in Figure 7-4(b). This observation indicates that failure occurred before the full engagement of the restraint provided by the cold joint on the compression side. Rather, failure initiated along a critical load path extending from the edge of the loading region through the effective area of cold joint. Accordingly, the assumptions underlying the proposed failure mechanism used to define the effective restraint are supported by the experimental results.

The proposed analytical approach offers a more representative evaluation of the shear behavior of deep beams with vertical and horizontal cold joints. This method is grounded in a detailed assessment of potential failure mechanisms corresponding to the location and stress profile of cold joints. The analysis indicates that the cold joint orientation is not the primary factor influencing structural capacity and behavior. Instead, the stress distribution and the configuration of surrounding structural components are the critical factors influencing the structural response, resulting in significant variation in failure modes and overall performance among specimens. This research accounts for the difference in the stress profiles of the vertical and horizontal cold joints using a unified model, facilitating the development of a universally applicable approach for analyzing deep beams with cold joints.

7.3. Nonlinear Finite Element Analysis

This section introduces the nonlinear finite element analysis (NLFEA) modeling approach developed for reinforced concrete structures with cold joints. The methodology was validated based on the experimental results presented in previous chapters. The validated NLFEA modeling approach was employed to conduct a numerical parametric analysis, extending the investigation to a broader range of design parameters that were identified as influential to the response of deep beams with cold joints. The finite element analysis results were compared with the calculated strengths obtained using the STM-based analytical approach proposed in this chapter to evaluate the efficiency of the proposed approach in reflecting the influence of key design parameters.

7.3.1. Nonlinear Finite Element Model

The nonlinear finite element analysis program VecTor2 was used to develop numerical models for the deep beam specimens. This program incorporates advanced constitutive relations for reinforced concrete elements developed based on the Modified Compression Field Theory (MCFT) and the Disturbed Stress Field Model (DSFM). The methodology accounts for various influential behavioral mechanisms, including compression softening and tension stiffening. Compression softening represents the reduction of concrete compressive strength due to transverse cracking induced by principal tensile stresses in the orthogonal direction. Tension stiffening considers the contribution of uncracked concrete between cracks due to the bond mechanism between the concrete and the reinforcement. Building upon the MCFT, DSFM introduces additional refinements by explicitly modeling the shear slip deformation along the crack surfaces. Further details on the numerical approach can be found elsewhere (Wong et al., 2013).

The finite element model developed for analyzing the deep beam specimen is shown in Figure 7-8. A mesh size of 2 in. × 2 in. was used, resulting in a total of 4208 elements, with 22 elements employed through the depth of the beam. These elements include 3842 rectangular elements, 344 truss elements, and 22 contact elements. The eight-degree-of-freedom rectangular elements were used to model the concrete and the steel bearing plates. The vertical and horizontal web reinforcement was modeled as smeared reinforcement within the concrete elements. All longitudinal reinforcing bars were explicitly modeled using truss elements. The cold joints were modeled using contact elements, allowing for localized interface slip and opening, independent of the behavior of the surrounding elements.

The steel bearing plates were modeled using two types of materials. The outer layer was modeled as Grade 60 structural steel and the layer in contact with the surface of the beam was modeled as bearing material. The bearing material only provides stiffness in the loading direction, ensuring that no unintended confinement was introduced at the interface between the bearing plate and the concrete specimen.

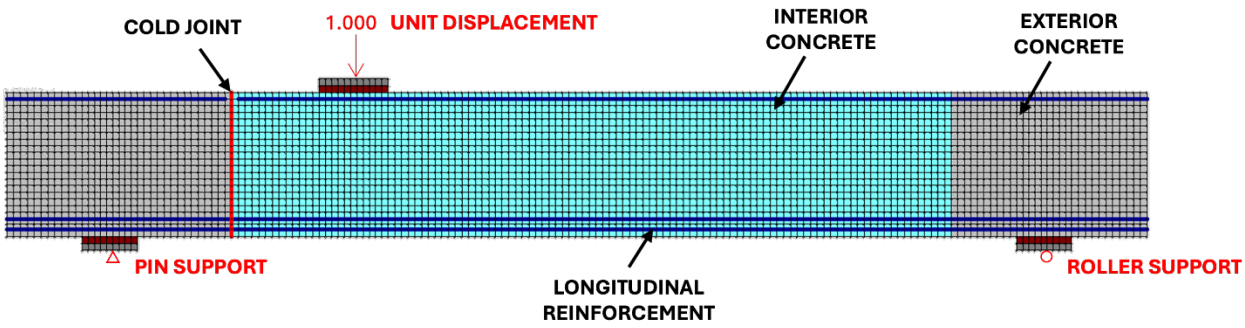

Figure 7-8 Nonlinear finite element analysis model for deep beams with cold joints

The cold joints were modeled using the constitutive relation proposed by Li et al. (2025), which was developed based on the shear-slip models for cracks in monolithic concrete elements. The model incorporates key variables influential to cold joint behavior, including interface roughness, aggregate size, normal forces acting on the interface, concrete compressive strength, clamping effect of reinforcement, and dowel action from reinforcement crossing the cold joint. By accounting for these critical parameters, the model effectively captures the interface behavior observed in the previous experiments (Alimran, 2023; Barbosa et al., 2017; Figueiredo et al., 2022; Harries et al., 2012; Hu et al., 2020; Kahn & Mitchell, 2002; Saldanha et al., 2013; Santos & Júlio, 2011; Shaw & Sneed, 2014).

The concrete and reinforcement properties were assigned according to the material test results reported in Table 5-4. The analysis was conducted by applying displacement-controlled loading at the center of the loading plate, as shown in Figure 7-8. The displacement was incremented by 0.04 in. per step until failure. Approximately 40 steps were applied throughout the course of the analysis, corresponding to the average displacement at failure measured from the experiments.

7.3.2. FE Analysis Results and Validation with Experimental Data

The analysis focuses on deep beams with various cold joint configurations to validate the ability to capture the influence of key variables on the shear behavior of deep beams. Three specimens with different cold joint designs were examined: Specimen III-1.85-00-V with a non-roughened unreinforced cold joint, Specimen III-1.85-00-VR with a roughened unreinforced cold joint, and Specimen IV-1.85-03-V with a non-roughened reinforced cold joint. These specimens were selected to isolate the influence of surface roughening and interface reinforcement.

Table 7-4 summarizes the experimental and numerical shear strengths for these three deep beam specimens. The average ratio of experimental-to-calculated shear strengths was 1.18 and the coefficient of variation was 12.7 %. These results demonstrate reasonable accuracy and validate the effectiveness in capturing the influences of interface roughness and interface reinforcement on cold joint behavior.

Table 7-4 Finite element analysis and experimental results

Specimen	$b_w \times d$ (in. × in.)	$f'_{c,min}$ (ksi)	V_{test} (kips)	V_{FEA} (kips)	$\frac{V_{test}}{f'_{c,min} b_w d}$	$\frac{V_{FEA}}{f'_{c,min} b_w d}$	$\frac{V_{test}}{V_{FEA}}$
III-1.85-00-V	21 × 38.3	4.598	416	411	0.112	0.111	1.01
III-1.85-00-VR	21 × 38.3	4.733	642	468	0.169	0.123	1.37
IV-1.85-03-V	21 × 38.3	4.190	494	432	0.147	0.128	1.14

Note: b_w = width of the deep beam
d = depth of the deep beam
$f'_{c,min}$ = concrete compressive strength of the weaker layer
V_{test} = shear strength measured from the experiment
V_{FEA} = shear strength from finite element analysis

For specimen containing a cold joint without roughening and interface reinforcement (III-1.85-00-V), the model exhibited excellent agreement with the experimental behavior. The crack propagation from the analysis closely aligns with the experimental observed crack patterns, as shown in Figure 7-9. For the specimens with either intentional roughening or interface reinforcement, the analyses underestimated the peak loads. However, the numerical analysis successfully captured the relative strength enhancements provided by these design features. Overall, the strength ratios and crack patterns obtained from the analysis indicate that the NLFEA model provides a reliable representation of both the shear capacity and the failure behavior in deep beams with vertical cold joints.

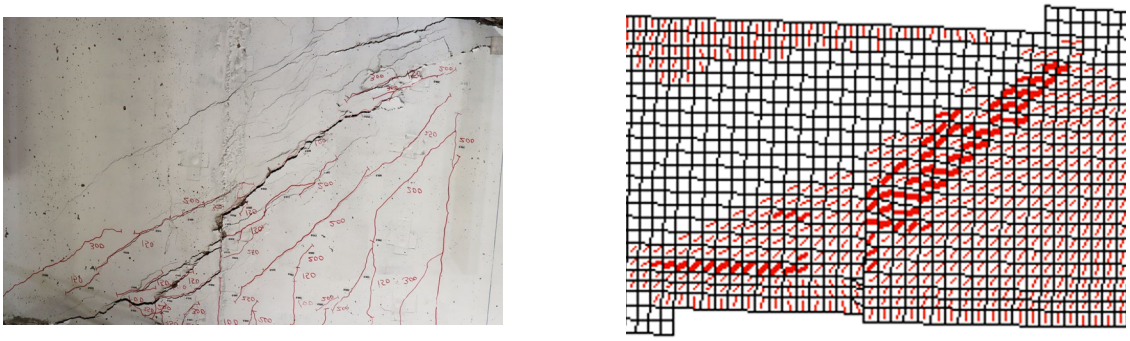

(a) Experimentally observed pattern *(b) Finite element analysis*

Figure 7-9 Crack patterns of Specimen III-1.85-00-V

7.3.3. Parametric Analysis

The validated NLFEA model was used to conduct a comprehensive parametric investigation into the influence of key variables on the behavior of deep beams with cold joints. Five additional models were developed, incorporating various cold joint reinforcement configurations and interface roughness amplitudes. The strengths of these five novel designs were also calculated using the STM-based analytical approach introduced in Section 7.1. The STM-

calculated strengths were compared with the FE-based ones to assess the reliability and accuracy of the proposed approach across a wider range of practical design scenarios.

7.3.3.1. Cold Joint Reinforcement Ratio

According to the experimental results, the normalized capacity of Specimen IV-1.85-03-V, featuring 0.3% of web reinforcement intersecting the cold joint, was found to be 35% greater than that of Specimen III-1.85-00-V with no interface reinforcement. This enhancement was also observed in the finite element analysis. However, Specimen IV-1.85-03-V also consisted of compression reinforcement intersecting the cold joint in the compression region, as shown in Figure 7-10 (a). These compression bars were found to provide additional restraint and increased the structural capacity.

To isolate the effect of web reinforcement, two additional finite element models were developed: Specimen 1.85-03-VNC, with 0.3% web reinforcement and no compression bars crossing the cold joint, and Specimen 1.85-015-VNC, with 0.15% web reinforcement and no compression bars intersecting the cold joint. The model with no compression bars intersecting the cold joint is presented in Figure 7-10 (b). These models were designed to evaluate the influence of various interface reinforcement ratios by comparing their ultimate capacities to that of the specimen with unreinforced cold joint.

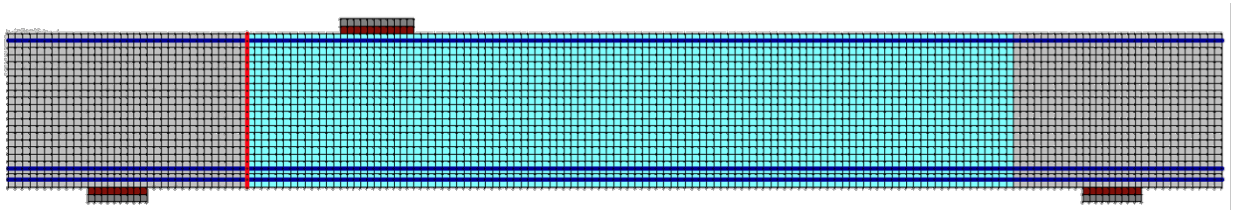

(a) Model for Specimen IV-1.85-03-V

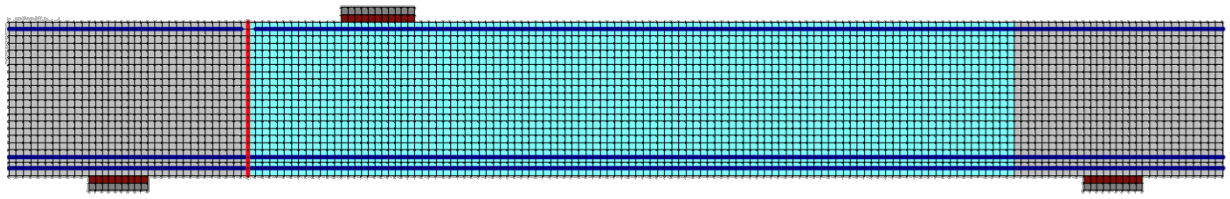

(b) Model with no compression bar intersecting the cold joint

Figure 7-10 Finite element model with various web reinforcement intersecting the cold joint

Table 7-5 Finite element analysis on different interface reinforcement ratios

Specimen	$b_w \times d$ (in. × in.)	$f'_{c,min}$ (ksi)	V_{FEA} (kips)	$V_{STM,CJR}$ (kips)	$\frac{V_{FEA}}{f'_{c,min} b_w d}$	$\frac{V_{STM,CJR}}{f'_{c,min} b_w d}$	$\frac{V_{STM,CJR}}{V_{FEA}}$
III-1.85-00-V	21 × 38.3	4.598	411	274	0.111	0.074	0.67
IV-1.85-03-V	21 × 38.3	4.190	432	331	0.128	0.098	0.77
1.85-03-VNC	21 × 38.3	4.190	418	296	0.124	0.089	0.71
1.85-015-VNC	21 × 38.3	4.190	400	284	0.119	0.084	0.71

The analysis results are summarized in Table 7-5. The capacities of specimens from the analysis were normalized based on the compressive strength of concrete to facilitate direct comparison across the specimens. The normalized capacity of Specimen 1.85-03-VNC was 11% higher than that of Specimen III-1.85-00-V, while Specimen 1.85-015-VNC exhibited a 7% increase in normalized capacity comparing to that of Specimen III-1.85-00-V. These analysis results confirm the effectiveness of web reinforcement in enhancing the capacity of deep beams with cold joints, independent of additional compression reinforcement. Moreover, the capacity increase was found to be approximately proportional to the interface reinforcement ratio. When comparing the analysis results of Specimen 1.85-03-VNC and 1.85-015-VNC to the specimen with an unreinforced cold joint, the increase in capacity observed in the specimen with 0.3% web reinforcement intersecting the cold joint is more significant than that of the specimen with 0.15% of cold joint reinforcement.

The STM-based analytical approach discussed in Section 7.1 was applied to calculate the capacities of Specimen 1.85-03-VNC and Specimen 1.85-015-VNC. The calculated capacities are summarized in Table 7-5. For both specimens, the ratios of the capacities calculated using the proposed approach to the capacities obtained from the finite element analysis are consistently 0.71. This consistency indicates that the STM-based analytical approach successfully captures the influence of cold joint reinforcement while maintaining a consistent level of conservativeness in capacity calculations across various interface reinforcement ratios.

7.3.3.2. Interface Roughness

This subsection introduces the investigation into the effect of cold joints roughness amplitudes on the shear capacity of deep beams. Based on the experimental results, deep beams consisting of a roughened cold joint with a 0.25 in. amplitude exhibited a shear capacity equivalent to the capacity of a monolithically cast deep beam. The 0.25 in. roughness amplitude was designed to satisfy the minimum requirement for a roughened interface as specified by AASHTO LRFD (AASHTO, 2024). According to AASHTO LRFD, cold joints with roughness amplitudes below this threshold are classified as smooth interfaces, and the contribution of interface roughness to interface shear resistance is disregarded in the design calculations.

To evaluate the effect of intermediate roughening with amplitudes below the required threshold, three NLFEA deep beam models were developed with roughness amplitudes of 0.06, 0.125, and 0.188 in. These models are referred to as 1.85-00-V0.06R, 1.85-00-V0.125R, and 1.85-

00-V0.188R, respectively. The analysis results, summarized in Table 7-6, indicate that shear capacity increases with the roughness amplitude, disregarding whether the amplitude satisfied the requirement to be treated as a roughened interface by current AASHTO specifications. Notably, the model with a 0.188 in. amplitude achieved a capacity equivalent to that of the specimen with 0.25 in. roughening.

Table 7-6 Finite element analysis on different interface roughness

Specimen	$f'_{c,min}$ (ksi)	V_{FEA} (kips)	$V_{STM,CJR}$ (kips)	$V_{STM,LIF}$ (kips)	$\frac{V_{FEA}}{f'_{c,min}b_w d}$	$\frac{V_{STM,CJR}}{f'_{c,min}b_w d}$	$\frac{V_{STM,LIF}}{f'_{c,min}b_w d}$	$\frac{V_{STM,CJR}}{V_{FEA}}$	$\frac{V_{STM,CJR}}{V_{FEA}}$
III-1.85-00-V	4.598	411	274	274	0.111	0.074	0.074	0.67	0.67
III-1.85-00-VR	4.733	468	341	341	0.123	0.090	0.090	0.73	0.73
1.85-00-V0.06R	4.733	435	274	331	0.114	0.074	0.087	0.63	0.76
1.85-00-V0.125R	4.733	447	274	341	0.118	0.074	0.090	0.61	0.76
1.85-00-V0.188R	4.733	467	274	341	0.123	0.074	0.090	0.59	0.73

The capacities of these three specimens were calculated using the STM-based approach proposed in Section 7.1 and summarized in Table 7-6. Since the roughening amplitude of cold joints in these three specimens are below the required amplitude specified by AASHTO LRFD (2024), these cold joints were treated as smooth interface when calculating their interface shear resistance. The calculated capacities failed to reflect the influence of interface with intermediate roughness and underestimated the shear capacities predicted by the finite element analysis.

To address this inefficiency, the LIF approach proposed in Section 4.5.3.1.2 was implemented in the interface shear calculation for the STM-based approach. The shear capacities calculated using the LIF approach are also summarized in Table 7-6. The LIF approach successfully captured the enhancement in capacities of specimens attributed to the intermediate interface roughness. The average ratio of capacities calculated from the STM-based approach to the capacities obtained from the finite element analysis for three specimens with intermediate roughness increased from 0.61 to 0.75 when using the LIF approach. This increment indicate that the accuracy of STM-based approach was improved by the implementation of the LIF approach in shear calculation.

7.3.4. Conclusion

A NLFEA model was developed to analysis the behavior of deep beams with cold joints. This model integrated the constitutive relations for concrete, reinforcement, and cold joints within a finite element analysis framework grounded in MCFT and DSFM. The analysis results exhibited strong alignment with the shear capacities and the crack patterns measured from the experiments, validating the accuracy and reliability of the model.

This validated model was used to conduct a parametric study focusing on the effect of cold joint reinforcement ratio and the interface roughness on structural performance. The analysis results indicate that the amount of web reinforcement intersecting the cold joint results in a proportional increase in deep beam capacity. Additionally, cold joints with roughness amplitudes below the requirement from AASHTO LRFD (2024) were found to significantly enhance the shear capacity of deep beam.

The STM-based analytical approach proposed in section 7.1 was applied to calculate the capacities of the models included in the parametric study. The STM-based approach effectively captured the influenced of interface reinforcement, but conservatively underestimated the capacities of specimens with intermediate roughness. The accuracy of capacities calculated using the STM-based approach of specimens with intermediate roughness was improved by implementing the LIF approach in interface shear calculation. These results confirm that the calculations from STM-based approach with LIF modification maintain a reasonable level of conservativeness while effectively capturing the influences of key parameters on cold joint behavior.

7.4. Design Recommendation

To incorporate the proposed approach into the strut-and-tie design, a systematic procedure is introduced for evaluating the capacity of deep beams with cold joints. For ties intersecting the cold joints, the reinforcement crossing the cold joint must be adequately designed to resist the tension demand. For strut intersecting the cold joints, the design procedure is summarized in the flowchart shown in Figure 7-11.

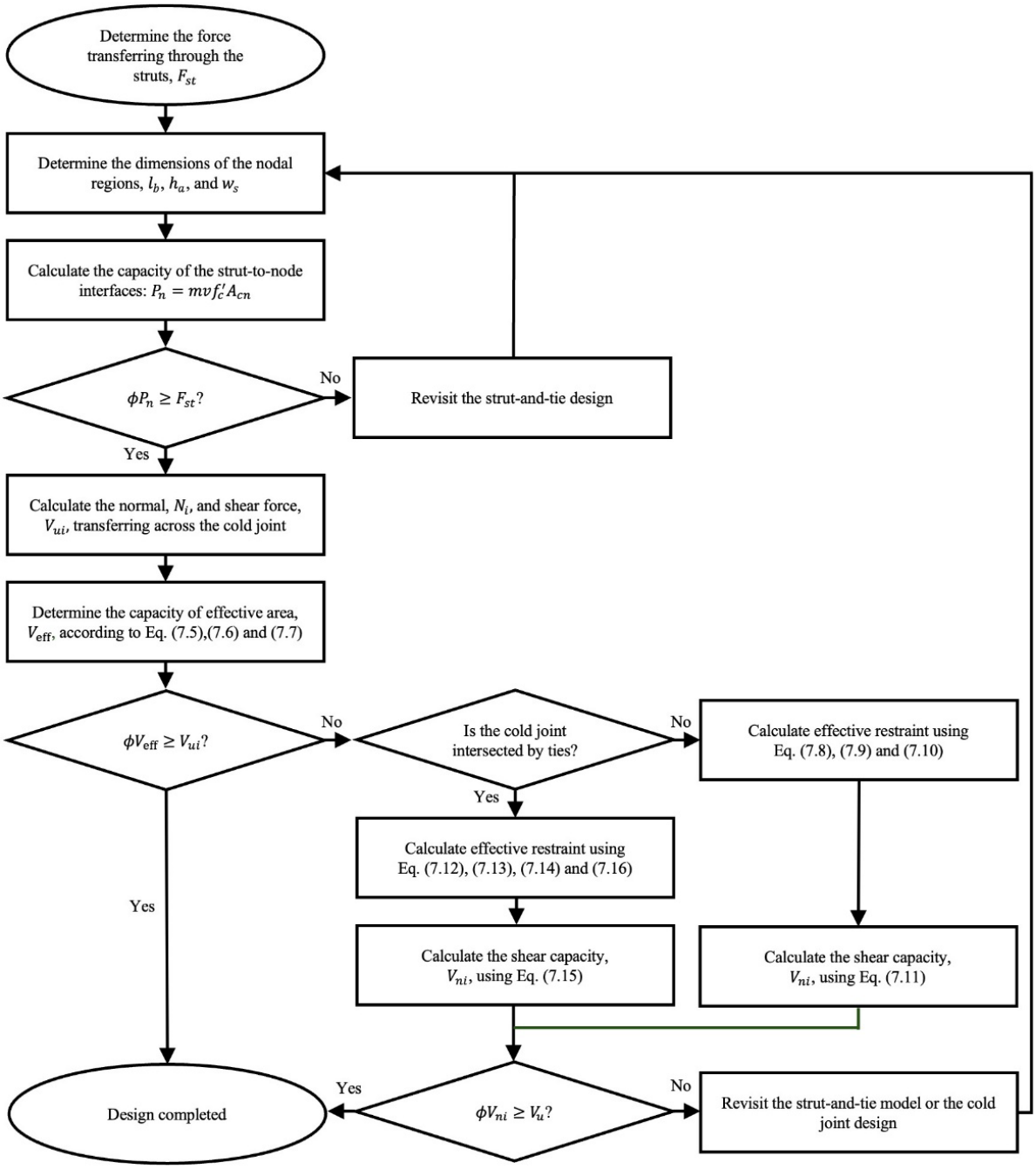

Figure 7-11 Design recommendation for struts intersecting by cold joints

The design begins by identifying the force demand in the compression strut. Based on the strut-and-tie model and the size of the bearing components, the dimensions of nodal regions are then determined. According to the confinement conditions and the web reinforcement design, the capacity of the strut-to-node interface is calculated. If the load demand in the strut exceeds the strut-to-node face capacity, the strut-and-tie model should be revised to ensure the load resisting capacity. The dimension and capacity of the nodal regions are determined following Section 5.8.2 in AASHTO LRFD 2024 (AASHTO, 2024).

Once the strength of the strut-to-node interface is confirmed to satisfy the force demand in the strut, the shear capacity of cold joint is evaluated. The force in the strut is decomposed into force components acting perpendicular and parallel to the cold joint using Equation (7-3) and (7-4). The component perpendicular to the cold joint is used to compute the interface shear resistance, while the parallel component defines the shear demand along the cold joint. The interface shear in the effective area is calculated following Equation (7-5), (7-6), and (7-7). If the calculated interface shear resistance exceeds the shear demand of the cold joint, the design is completed, and the strut is considered adequate for the applied. However, it is important to apply appropriate load factors to each force component to accurately account for their respective effects on the demand and capacity of structures. The resistance factor of interface shear is calculated according to Equation (5.5.4.2-2) in AASHTO LRFD 2024 (AASHTO, 2024), and can be conservatively taken as 0.75.

If the interface shear resistance of the cold joint in the strut region is insufficient, external restraint provided by adjacent structural components is allowed to be considered in the strength calculation. To determine the effective restraint, it is necessary to evaluate whether the cold joint is intersected by tension-transferring ties, which may result in different potential failure modes. For cold joints not intersected by STM ties, the effective restraint is calculated according to Equation (7-8), (7-9), and (7-10). For cold joints intersected by STM ties, the effective restraint is determined using Equation (7-12), (7-13), (7-14), and (7-16). Based on the identified failure mechanism and the restraint calculation, the total shear capacity of the cold joint is determined by the sum of the shear resistance in the effective area and the effective restraint. Consequently, the design is considered satisfactory as the total shear resistance is sufficient for the shear demand across the cold joint. A design example for a deep beam specimen tested in this research is presented in Appendix G using the proposed design recommendation.

7.5. Summary

This chapter presents an analytical approach for evaluating deep beams with cold joints. A mechanical model was proposed to represent the load transfer mechanism across the cold joints in the strut-and-tie method. This model includes the evaluation of the interface shear resistance of cold joints in the strut region and the effective restraint provided by surrounding structural elements. The proposed approach was validated by comparing the calculated shear strength and failure modes against the experimental results from Task 5. Compared to conventional STM, the proposed approach demonstrated improved agreement with both the observed structural behavior and measured shear strength. Notably, the proposed approach captured failure mode initiated by localized failure of cold joint, offering a more representative analysis of structural behavior.

To quantify effective restraint provided by the adjacent regions, a series of potential failure mechanisms were evaluated to identify critical load paths. Recognizing that tension ties intersecting cold joints influence both crack propagation and interface stress profiles, the methodology differentiates between cases with and without STM ties intersecting the cold joints, providing explicit procedures for each case.

A design procedure is subsequently developed to integrate the proposed analytical model into the practical strut-and-tie design workflow. The design procedure incorporates the interface shear resistance expressions in accordance with current specifications into the strut-and-tie design method. The proposed recommendation provides guidance for designing structures in D-regions with cold joints using strut-and-tie model, enhancing the reliability of the design and the accuracy of structural assessment.

Chapter 8. Summary and Conclusions

8.1. Project Summary

Cold joints are formed at the interfaces between layers of concrete placed at different times. Whether introduced deliberately or unintentionally, cold joints create a potential plane of weakness within the reinforced concrete structures. To evaluate the shear capacity of cold joints, shear friction theory was implemented into current design expressions to quantify the shear capacity of cold joints under sectional analysis. However, cold joints occur frequently in the disturb regions of structures, where the strut-and-tie method is commonly employed in the design and analysis to account for the intricate stress-transfer mechanisms. Although the 2016 interim revisions of AASHTO LRFD requires the verification for the shear-friction capacity of cold joints when intersected by a strut, no explicitly design guidelines is available to address the approach for evaluating struts intersecting cold joints. The primary objective of this research is to investigate the effect of cold joints in D-regions of structures, and develop reliable and applicable analytical approach and design guidelines based on the strut-and-tie model.

The research team comprehensively developed and conducted a series of tasks to accomplish those objectives. Each chapter of this report presents the detailed procedure to attained valuable information from each task, and the critical research findings are summarized at the end of each chapter. The summary and featured conclusions of each research tasks are as follows:

1. Research Background and Literature Review: A state-of-the-art literature review on the shear friction theory for cold joint capacity and the concepts used to develop the strut-and-tie method were comprehensively reviewed. Previous research revealed that current design expressions for interface shear capacity are generally conservative. However, the database analysis suggests a potential concern about the reliability of existing formulations. The available model presented in FIP Practical Design of Structural Concrete 1999 was revisited, serving as a potential inspiration for the establishment of proposed analytical model. Lastly, the application in practice of cold joints intersecting struts were discussed, underscored an urgent need of a reliable and applicable design specifications for these cases.

2. Industrial Survey: Based on the 22 responses received from DOTs spanning across the country, design practices and experience of cold joints are concluded. The respondents agreed that cold joints occur more often in D-region than B-region. However, the respondents also addressed limited experience designing D-region of structures with STM. To enhance friction along the interface, interface roughening and shear key are two commonly employed construction approaches. However, no standardize method was used to inspect and quantify the level of interface roughness. Common

reinforcement details intersecting the cold joints were found to be straight bars, bars with 90-degree hook, and post-installed reinforcement.

3. Slant Shear Experiments: In total 54 slant shear tests were designed and conducted in this experimental program. Six key design parameters were examined: cold joint inclination, interface roughness, variation in concrete compressive strength between layers, casting age difference, aggregate size, and reinforcement crossing the interface. According to the test results, the interface roughness and aggregate size were the most influential parameters affecting interface shear resistance. The difference in failure modes of specimens corresponding to various inclinations also demonstrate the influence of force components acting perpendicular and parallel to the interface. A database analysis containing 124 slant shear tests was composed to examine the accuracy and relevance of design expressions. A modification approach on determining the friction and cohesion coefficient using linear interpolation based on the interface roughness amplitude was proposed and proven to improve the accuracy of the calculation. Four large-scale slant shear experiments are also conducted to investigate the size effect on interface shear resistance and the development of strain profile along the cold joint under monotonic loading. The size effect of cold joint resistance was confirmed by the reduction of ultimate shear stress observed in the large-scale slant shear experiments.

4. Deep Beam Experiments: An experimental program consists of 10 deep beam specimens was designed to replicate practical scenarios where cold joints occur in the D-region of structures. Pivotal variables concluded from the previously mentioned tasks were implemented in the experimental program, including cold joint orientation, interface roughness, and reinforcement ratio. By evaluating the load-deflection response, shear capacity, failure mode, reinforcement response, serviceability and displacement and strain contour, the horizontal cold joints were concluded to have insignificant effect on the deep beam behavior. However, the absence of interface roughening and intersecting reinforcement, and the decrease of a/d ratio was found to significantly reduce the shear capacity of deep beams. Additionally, the failure crack pattern, reinforcement response along the compression load path, and the displacement field of these two specimens demonstrated that a specific section of cold joint was particularly engaged in the shear resisting mechanism. The conclusion drawn from this experimental program highlighted the need for further investigation on the effect of cold joint on the shear transferring mechanism of deep beam structure.

5. Drilled-Shaft Footing Experiments: A drill-shaft footing specimen was designed to investigate the behavior of three-dimensional struts intersected by cold joints, replicating commonly design cases of footing expansion. The specimen was design with cold joint enclosing the loading point, forcing the load to transfer through compressive strut through the cold joints. According to the load-deflection response,

this drilled-shaft footing specimen demonstrated a more ductile response than footings without cold joint. The ductile response suggested that failure was not governed by brittle shear failure, but the shear slip response of the cold joints. The failure patterns observed from each side of the specimen and the post-cut section revealed that failure concentrated along the portion of cold joints intersected by strut. The strain gauge exhibited no yielding of bottom mat reinforcement, suggesting that the failure occurred before fully mobilizing the capacity of reinforced ties. These results supported the conclusion drawn from the deep beam experiments, indicating the strut capacity was influenced by the shear resistance of cold joint, especially in a localized region within the compression strut.

6. Numerical Analysis and Design Recommendations: An analytical approach was developed based on the experimental results and the proposed mechanical model. This approach considers the potential failure mechanisms and the effective restraint using a single panel strut-and-tie model. The shear capacity and failure mode predicted by the proposed model demonstrated improvement comparing to the calculation using conventional STM that neglected the cold joint effects. A series of design procedures were subsequently recommended for practical application.

8.2. Concluding Remarks

In this research program, behavior of deep beams and drilled-shaft footing cap with cold joints was intensively investigated. The experimental results demonstrated that the strut-and-tie method remains valid to analyze the load transfer mechanism of D-regions with cold joints. Additionally, the cold joints intersecting struts demonstrated significant failure patterns focusing within the strut region, indicating the need quantify the contribution of cold joint resistance on the strut capacity. The comprehensive behavior analysis further explores potential shear resisting mechanism based on the strut-and-tie model, resulting in the establishment of an analytical approach applicable to design in practice. The proposed approach was validated by the shear capacity and failure mode of the experiments conducted in this research. Eventually, a step-by-step design procedure was recommended, providing an explicit guideline quantifying the shear resistance of cold joint in the strut region and the corresponding structural capacity based on current strut-and-tie model.

However, there is limited research available focusing on the structural implication of cold joints in D-regions. The proposed analysis and design approach should be further validated with more experimental or analytical data to ensure its reliability in various cases. The available restraint corresponding to different cold joint stress profile and the potential failure mode also requires further investigation for various cases with additional failure mechanisms. The key variables influential to the shear behavior of cold joints should be more widely investigated when implemented according to practical structural design, providing a more general design guideline

for not only the strength of strut crossing cold joints, but the comprehensive behavior of new and old structures connected by cold joints.

Chapter 9. Value of Research

This research provides critical advancements in the structural engineering field by addressing the lack of design methodologies for reinforced concrete elements containing cold joints, particularly in disturbed regions (D-regions) where conventional design assumptions are often invalid. Cold joints are a common but complex condition in construction, arising from unintentionally interrupted or strategically staged concrete placement. When cold joints intersect with primary load paths, such as compression struts in deep beams or footing caps, they can significantly affect structural performance and reliability.

The project contributes to the profession in several key ways:

- Mechanically Grounded Design Framework: By integrating interface shear behavior into the strut-and-tie modeling (STM) approach, the research provides a unified and rational framework for evaluating the behavior of RC members with cold joints under complex stress conditions.

- Experimental Validation: Through a comprehensive experimental program, including slant shear tests, full-scale deep beam tests, and footing cap tests, the research delivers high-quality data to validate the proposed analytical models and design procedures.

- Practical Design Recommendations: The proposed analytical approach is compatible with current design specifications and can be directly implemented by practitioners, offering clear and applicable guidance for addressing cold joints in real-world structures.

- Industry Relevance: Insights from a national survey of DOT engineers highlight the limited existing guidance and inconsistent treatment of cold joints in current practice, reinforcing the need for the design tools and recommendations developed in this project.

Overall, this research enhances the safety, consistency, and economy of concrete structure design by filling a critical gap in the treatment of cold joints, especially in regions where failure could be catastrophic. It provides a practical, validated solution that supports engineers, agencies, and code committees in making informed, performance-based design decisions.

References

AASHTO. (2014). *AASHTO LRFD Bridge Design Specifications* (7th ed.). American Association of State Highway and Transportation Officials.

AASHTO. (2024). *AASHTO LRFD Bridge Design Specifications* (10th ed.). American Association of State Highway and Transportation Officials.

ACI Committee 318. (1999). *Building Code Requirements for Structural Concrete (ACI 318-99) and Commentary (ACI 318R-99)*. American Concrete Institute.

ACI Committee 318. (2025). *Building Code Requirements for Structural Concrete (ACI 318-25) and Commentary (ACI 318R-25)*. American Concrete Institute.

Alimran, A. A. A. (2023). Effects of High-Strength Reinforcement on Shear-Friction with Different Interface Conditions and Concrete Strengths. *Purdue University Graduate School. Thesis*.

ASTM C39/C39M. (2021). *ASTM C39/C39M-Standard Test Method for Compressive Strength of Cylindrical Concrete Specimens*.

ASTM C882/C882M. (2020). *ASTM C882/C882M- Standard Test Method for Bond Strength of Epoxy-Resin Systems Used With Concrete By Slant Shear*.

Barbosa, A. R., Trejo, D., & Nielson, D. (2017). Effect of High-Strength Reinforcement Steel on Shear Friction Behavior. *Journal of Bridge Engineering*, *22*(8), 04017038. https://doi.org/10.1061/(ASCE)BE.1943-5592.0001015

Bayrak, O. (2020, Fall). Concrete Bridge Technology—Strength of Structures with Struts Crossing Cold Joints—Beginning the Discussion. *ASPIRE, The Concrete Bridge Magazine*, 32–33.

Birkeland, P. W., & Birkeland, H. W. (1966). Connections in Precast Concrete Construction. *ACI Journal Proceedings*, *63*(3). https://doi.org/10.14359/7627

Birrcher, D. B., Tuchshcerer, R. G., Huizinga, M., Bayrak, O., Wood, S., & Jirsa, J. (2009). *Strength and Serviceability Design of Reinforced Concrete Deep Beams.* (Nos. 0-5253–1). Center for Transportation Research, The University of Texas at Austin.

Brown, M. D., Sankovich, C. L., Bayrak, O., Wood, S., & Jirsa, J. (2006). *Design for Shear in Reinforced Concrete Using Strut-and-Tie Models* (No. FHWA/TX-06/0-4371-2). Center for Transportation Research.

Collins, M. P., & Mitchell, D. (1980). Shear and Torsion Design of Prestressed and Non-Prestressed Concrete Beams. *PCI Journal*, *25*(5), 32–100. https://doi.org/10.15554/pcij.09011980.32.100

Collins, M. P., Mitchell, D., Adebar, P., & Vecchio, F. J. (1996). A General Shear Design Method. *ACI Structural Journal*, *93*(1), 36–45. https://doi.org/10.14359/9838

CRD-C164-92- Standard test method for direct tensile strength of cylindrical concrete or mortar specimens. (1992).

CSA Standard A23.3-14. (2014). *Design of Concrete Structures* (6th ed.).

CSA Standard A23.3-19. (2019). *Design of Concrete Structures* (7th ed.).

Diab, A. M., Abd Elmoaty, A. E. M., & Tag Eldin, M. R. (2017). Slant shear bond strength between self compacting concrete and old concrete. *Construction and Building Materials*, *130*, 73–82. https://doi.org/10.1016/j.conbuildmat.2016.11.023

Drucker, D. C. (1961). On Structural Concrete and The Theorems of Limit Analysis. *IABSE Publications, 21*, 49–59. https://doi.org/10.5169/SEALS-18246

European Committee for Standardization. (2005). *EN 1992-1-1 Eurocode 2: Design of concrete structures—Part 1-1: General ruels and rules for buildings*. EN,CEN.

Farzad, M. S., & Azizinamini, A. (2019). Experimental and Numerical Study on Bond Strength between Conventional Concrete and Ultra High-Performance Concrete (UHPC). *Engineering Structures*, *186*, 297–305. https://doi.org/10.1016/j.engstruct.2019.02.030

Fédération Internationale de la Précontrainte (FIP). (1999). *Practical design of structural concrete*.

fib International. (2024). *Fib Model Code for Concrete Structures 2020*.

Figueiredo, P., Garcia, S. L., Cossetti, R., & Leite, A. (2022). Bond Performance between Normal-Strength Concrete and Sand-Lightweight Concrete. *ACI Structural Journal*, *119*(1), 199–213. SciTech Premium Collection. https://doi.org/10.14359/51733007

Harries, K. A., Zeno, G., & Shahrooz, B. (2012). Toward an Improved Understanding of Shear-Friction Behavior. *ACI Structural Journal*, *109*(6). https://doi.org/10.14359/51684127

Hennebique, F. (1898). Construction of Joists, Girders, and The Like. *United States Patent Office*, *No. 611,907*.

Hermansen, B. R., & Cowan, J. (1974). Modified shear-friction theory for bracket design. *ACI Journal Proceedings*, *71*(2), 55–60.

Hofbeck, J. A., Ibrahim, I. O., & Mattock, A. H. (1969). Shear transfer in reinforced concrete. *ACI Journal Proceedings*, *66*(2), 119–128.

Hu, B., Li, Y., & Liu, Y. (2020). Dynamic slant shear bond behavior between new and old concrete. *Construction and Building Materials*, *238*, 117779. https://doi.org/10.1016/j.conbuildmat.2019.117779

Kahn, L. F., & Mitchell, A. D. (2002). Shear Friction Tests with High-Strength Concrete. *ACI Structural Journal*, *99*(1). https://doi.org/10.14359/11040

Kahn, L. F., & Slapkus, A. (2004). Interface Shear in High Strength Composite T-Beams. *PCI Journal*, *49*(4), 102–110.

Kupfer, H. (1964). Erweiterung der MÖRSCH'schen Fachwerkanalogie mit Hilfe des Prinsips vom Minimum der Formänderungaarbeit. *Comité Euro-International Du Béton*, *CEB Bulletin*(No. 40), 45–57.

Lampert, P. (1970). *Bruchwiderstand von Stahlbetonbalken unter Torsion und Biegung*. ETH Zürich.

Lampert, P., & Thürlimann, B. (1971). Ultimate Strength and Design of Reinforced Concrete Beams in Torsion and Bending. *IABSE Publications*, *31*, 107–131. https://doi.org/10.5169/SEALS-24211

Lang, M. (2011). *Analysis of the AASHTO LRFD Horizontal Shear Strength Equation*. Virginia Polytechnic Institute and State University.

Leondardt, F. (1965). Reducing the Shear Reinforcement in Reinforced Concrete Beams and Slabs. *Magazine of Concrete Research*, *17*(53), 187–198.

Li, B., Wang, H. C., Ferche, A. C., & Bayrak, O. (2025). Mechanics-Based Model for Cold Joints in Reinforced Concrete Members. *(Under Review)*.

Loov, R., & Patnaik, A. (1994). Horizontal Shear Strength of Composite Concrete Beams With a Rough Interface. *PCI Journal*, *39*, 48–69. https://doi.org/10.15554/pcij.01011994.48.69

MacGregor, J. G. (n.d.). Derivation of Strut-and-Tie Models for The 2002 ACI Code. *Examples for the Design of Structural Concrete with Strut-and-Tie Models, 208*, 7–40.

MacGregor, J. G. (1976). Safety and Limit States Design for Reinforced Concrete. *Canadian Journal of Civil Engineering*, *3*(4), 484–513.

Marti, P. (1985). Basic Tools of Reinforced Concrete Beam Design. *ACI Journal*, *82*(1), 46–56.

Mast, R. F. (1968). Auxiliary Reinforcement in Concrete Connections. *Journal of the Structural Division*, *94*(6), 1485–1504. https://doi.org/10.1061/JSDEAG.0001977

Mattock, A. H. (1974). Shear Transfer in Concrete Having Reinforcement at an Angle to the Shear Plane. *American Concrete Institute, Farmington Hills, MI*, *11*(46).

Mattock, A. H. (1977). Considerations for the Design of Precast Concrete Bearing Wall Buildings to Withstand Abnormal Loads (Reader Comments). *PCI Journal*, *22*(3), 105–106.

Mattock, A. H. (2001). Shear Friction and High-Strength Concrete. *ACI Structural Journal*, *98*(1). https://doi.org/10.14359/10146

Mattock, A. H., & Hawkins. (1972). Shear transfer in reinforced concrete—Recent research. *PCI Journal*, *17*(2), 55–75.

Mattock, A. H., Johal, L., & Chow, H. C. (1975). Shear Transfer in Reinforced Concrete with Moment or Tension Acting across the Shear Plane. *PCI Journal*, *20*(4), 76–93.

Mattock, A. H., Li, W. K., & Wang, T. C. (1976). *Shear transfer in lightweight reinforced concrete*. *21*(1), 20–39.

Mörsch, E. (1902). Der Eisenbetonbau, Seine Theorie und Anwendung. *Konrad Wittwer*.

Patnaik, A. K. (1999). Longitudinal Shear Strength of Composite Concrete Beams with a Rough Interface and No Ties. *Australian Journal of Structural Engineering*, *SEI*(3), 157–166.

Piancastelli, E. M., Magalhães, A. G., Silva, F. J., Rezende, M. A. P., Santos, W. J., Carrasco, E. V. M., & Mantilla, J. N. R. (2017). Bond Strength between Old and New Concretes with Focus on the Strengthening of Reinforced Concrete Columns—Slant Shear Test versus Double Sleeve Test. *Applied Mechanics and Materials*, *864*, 324–329. https://doi.org/10.4028/www.scientific.net/AMM.864.324

Ramirez, J. A., & Breen, J. E. (1991). Evaluation of A Modified Truss-Model Approach for Beams in Shear. *ACI Structural Journal*, *88*(5), 562–571.

Randl, N. (2013). Design recommendations for interface shear transfer in fib Model Code 2010. *Structural Concrete*, *14*(3), 230–241. https://doi.org/10.1002/suco.201300003

Ritter, W. (1899). Die Bauweise Hennebique. *Schweizerische Bauzeitung*.

Rüsch, H. (1965). Über eine Erweiterung der Mörschschen Fachwerkanalogie. *IABSE Congress Report*, *7*, 353–369. https://doi.org/10.5169/SEALS-7974

Saldanha, R., Júlio, E., Dias-da-Costa, D., & Santos, P. (2013). A modified slant shear test designed to enforce adhesive failure. *Construction and Building Materials*, *41*, 673–680. https://doi.org/10.1016/j.conbuildmat.2012.12.053

Santos, P., & Júlio, E. (2011). Factors Affecting Bond between New and Old Concrete. *ACI Materials Journal*, *108*, 449–456.

Schlaich, J., Schafer, K., & Jennewein, M. (1987). Toward A Consistent Design of Structural Concrete. *PCI Journal*, *32*(3), 74–150. https://doi.org/10.15554/pcij.05011987.74.150

Shaw, D. M., & Sneed, L. H. (2014). Interface shear transfer of lightweight-aggregate concretes cast at different times. *PCI Journal*, *59*(3), 130–144.

Soltani, M., & Ross, B. E. (2017). Database Evaluation of Interface Shear Transfer in Reinforced Concrete Members. *ACI Structural Journal*, *114*(2). https://doi.org/10.14359/51689249

Thürlimann, B. (1979). Shear Strength of Reinforced and Prestressed Concrete—CEB Approach. *Concrete Design: US and European Practices*, *59*, 93–116.

Williams, C. S., Deschenes, D. J., & Bayrak, O. (2012). *Strut-and-Tie Model Design Examples for Bridges: Final Report* (No. FHWA/TX-12/5-5253-01-1). Center for Transportation Research.

Wong, P., Vecchio, F. J., & Trommels, H. (2013). *VecTor2 and Formworks Manual* (2nd ed.). University of Toronto.

Yi, Y., Kim, H., Boehm, R. A., Webb, Z. D., Choi, J., Wang, H.-C., Murcia-Delso, J., Hynryk, T. D., & Bayrak, O. (2022). *3D Strut-and-Tie Modeling for Design of Drilled Shaft Footings* (Nos. 0-6953–1). Center for Transportation Research, The University of Texas at Austin.

Appendix A. Qualtrics Reports

Full responses of the survey are summarized in Appendix A. Responses were collected and verified using the Qualtrics software. A total of 22 survey participants submitted complete responses.

Question 1 - Contact Information

Name:	Position/Title:	District/ State:	Organization/Unit:	Email:
David Madden	Bridge Design Engineer	SD	dave.madden@state.sd.us	dave.madden@state.sd.us
Trey Carroll	Project Engineer - Policy Development	North Carolina	NCDOT - Structures Management Unit	thcarroll1@ncdot.gov
Vickie Young	Structures Design Engineer	CO/Florida	FDOT/SDO	vickie.young@dot.state.fl.us
Kumar Selvakumar	Supervising Engineer	New Jersey	NJDOT	Kumar.Selvakumar@dot.nj.gov
Victoria McCammon	Transportation Engineer	TX	Bridge Division	victoria.mccammon@txdot.gov
Bijan Khaleghi	Bridge Design Engineer	WSDOT	Bridge	khalegb@wsdot.wa.gov
Mary Vittoria-Bertrand	Chief Civil Engineer	RI	Bridge Engineering	mary.bertrand@dot.ri.gov
Mark Hurt	State Bridge Engineer	US	KS DOT	mark.hurt@ks.gov
Kyle Kopper	Bridge Design Policy Specialist	Michigan	Department of Transportation	KopperK1@michigan.gov
Donn Digamon	State Bridge Engineer	Georgia	Georgia Department of Transportation	dodigamon@dot.ga.gov
Randall Scott Knieriem	Transportation Design Engineer	Maryland	Maryland State Highway Administration	rknieriem@mdot.maryland.gov
Robert Juliano	Project Engineer	New Hampshire	NH Department of Transportation	robert.a.juliano@dot.nh.gov
Andy Zickler	Program Manager Complex Structures and ABC support	VA	VDOT	andy.zickler@VDOT.virginia.gov
Andy Pott	PE II	CO	CDOT Staff Bridge	andrew.pott@state.co.us

Tracy Brown	Brown	West Virginia	WVDOT	tracy.w.brown@wv.gov
Matt Rink	Senior Design Engineer	UT	UDOT/Structures	mrink@utah.gov
Karl Johnson	Assistant Bridge Design Manual Engineer	Minnesota	MnDOT	karl.johnson@state.mn.us
Jim Pool	Staff Engineer	AR	Arkansas Department of Transportation	james.pool@ardot.gov
Kelly Kemp	Assistant Bridge Design Administrator	LA	LA DOTD - Bridge & Structural Design Section	kelly.kemp@la.gov
Andrew Cardinali	Transportation Principal Engineer	CT	Connecticut Dept of Transportation	andrew.cardinali@ct.gov
Mike Nop	Bridge Project Development Engineer	Iowa	Bridges and Structures Bureau	Michael.Nop@iowadot.us
Elmer Marx	Tech. Engr. 2	Alaska	Bridge	elmer.marx@alaska.gov

Question 2 - Please rate how frequently you work on new construction versus existing structures on a scale of 1–5 (1 is exclusively new construction and 5 is exclusively existing structures).

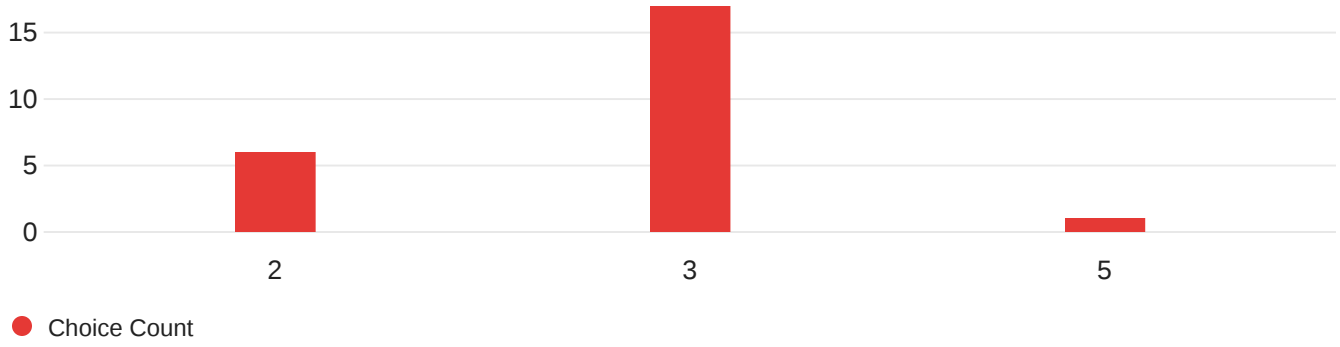

Question 3 - Has your state/district had experience with the design of struts crossing cold joints?

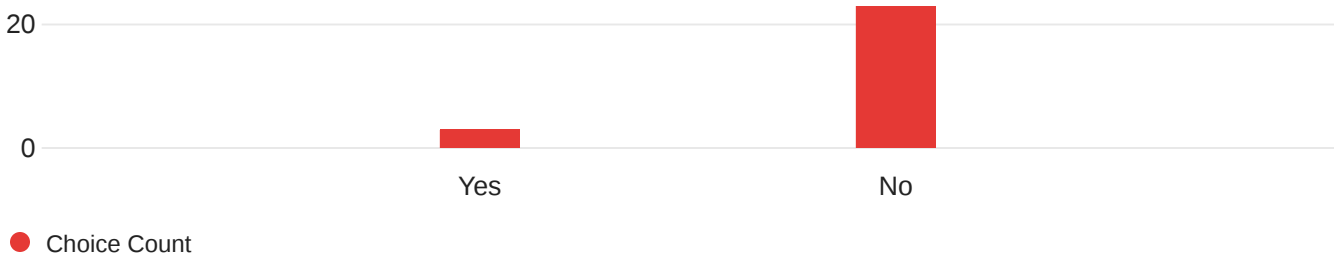

Question 4 - If Yes, please briefly explain the general approach used / interpretation of AASHTO LRFD Article C5.8.2.2.

Florida follows the design guidance provided AASHTO LRFD when analyzing the D-Regions. We recently worked on a bridge project where we used both methods for comparison purposes.

RIDOT LRFD bridge design manual refers designer to follow AASHTO LRFD Bridge Design Specifications. From our bridge design manual: "At the strength and extreme event limit states, the use of the strut-and-tie model should be considered to determine the internal forces near the supports; the points of application of concentrated loads; and for the design of deep footings and pile caps, all in accordance with the referenced Article of the AASHTO LRFD Bridge Design Specifications."

We use the same member dimensions, rebar size and spacing across the cold joint as the critical design location as the rest of the member.

Question 5 - If No, please explain why (e.g., sectional methods in Article 5.7.4 are used).

The few we have using strut and tie have not required a cold joint.

Sectional Methods are used.

We do not consider this in the design and make sure that the proper measures are taken to have proper boding with the new and old concrete.

We typically use sectional analysis to design bent caps using 5.7.3.4.2 for shear on prestressed sections and B5 for shear on conventionally reinforced sections, and check interface shear using 5.7.4. We do use 5.8 for footing and end zone design; footings only have cold joints in retrofit cases and end zones only have cold joints to repair poorly consolidated concrete. We treat struts through cold joints the same as monolithic concrete in these cases, but include an interface shear check where the cold joint is full depth.

not used

Traditional practice

MDOT's current design standards establish general locations for construction joints based on constructability and construction operations. This includes maximum volume of concrete in a footing, length of abutment wall or pier cap, and height of abutment wall.

Sectional methods used, but GDOT has just place into the bridge design manual to use strut and tie models for structures or situations that warrant the approach.

We generally avoid locating construction joints in D Regions. Most of the time we will design the individual stages as separate units with a pinned connection. We have little faith in our cold joints to carry moment or large amounts of shear.

Article 5.7.4 typically used

Consultants may be designing strut tie as a gut check, but traditional beam and frames are used internally and required from consultants.

Cases not fully analyzed yet, newer requirement

Methods from LRFD 5.7.4 are utilized for shear transfer. Sometimes the added portion of the substructure is isolated from the existing portion (separate pier cap, foundation, etc.).

When referring to pier caps, typically we do not place vertical cold joints in the pier caps. In the cases of staged construction, rehab bridge widenings, or very long pier caps, we prefer to place an open air gap in the pier cap instead of a cold joint.

It may happen on rare occasion, but we do not have a designated procedure for this design at MnDOT.

Also, sorry for the previous "blank" survey I filled out. I wanted to get a sense for the questions and didn't mean to turn in a blank survey.

We previously designed cold joints using sectional methods in Article 5.7.4. We have adopted the STM for about a year. I am unaware of any designs requiring a cold joint while using this design method.

Cold joints are not used often in bent caps. We would required a cap cold joint for a relatively long cap supported on (2) columns where the columns are short/stiff and curing/temperature strains in the cap are found to place excessive moments on the column and footing. We use sectional methods for flexural regions, and would verify with strut-and-tie for deep regions and for hammerheads.

Typically there is a significant area of reinforcing steel crossing the cold joint. This reinforcing steel contributes additional shear resistance across the cold joint.

We use sectional methods of design.

NDDOT is in the early stages of the strut and tie design method.

Rarely widen older bridges as they do not often satisfy modern AASHTO standards (e.g., seismic and liquefaction).

Question 6 - On average, do cold joints occur more frequently in B-regions (beam) or D-regions (disturbed, discontinuity, etc.)? See figure below for examples of B- and D-regions. D-regions typically occur near concentrated loads, supports, or changes in geometry (e.g., dapped-end beams). Is the proximity to disturbances/discontinuities usually considered when selecting the location of a cold joint? Separation of B- and D-regions (Birrcher et al., 2009)

B-region. Yes we would look at the proximity of the joint to the disturbed region.

Cold joints are more frequent in D regions. Proximity to disturbances is considered.

A. In B-Region

B. Due to steel reinforcement congestion in D region, cold joint in D region should be avoided.

Almost exclusively in D-regions.

Cold joints if needed are at low moment and shear regions.

Usually for us the cold joints are a factor of staged construction. I'd say mostly in the B region.

Typically at the edge of a D region.
Proximity to a disturbed region is not typically considered.
Primary consideration is phasing around whatever obstacle is preventing construction of the whole pier at once.

For substructure elements construction joints are typically located between beams to align with bolster steps in order to aid in forming and to minimize the risk of creating small, unreinforced sections of concrete. Because of this substructure construction joints will often times fall with D-Regions of the element.

D region

Typically between the edge of the B and D regions, but mostly B Regions...

location of cold joints often dictated by traffic control phasing

cold joints typically occur where required by stage construction. Otherwise pier caps are generally placed as a single operation from one end of the cap to the other.
when we have a choice we may try to place the joints near supports (d-regions). We do not generally want to have them under applied load locations, but that happens too.

D-Regions

Most typically D-regions.

B Regions. Yes.

As stated above, it is not a typical practice for MnDOT to have cold joints in our pier caps. However, if and when they do happen, it would be more likely in a "D" region.

We have limited designs using STM with none requiring cold joints. However, I would expect the cold joints would occur in the D-Region. Although we have yet to design a bridge that is to be widened using STM, I believe our typical practice of setting the joint location would cause it to be located in a D-Region as well.

Site constraints have limited joint locations, but the proximity to disturbances/discontinuities would be considered.

We do not frequently specify cold joints in caps. If a cold joint is required, we recommend placing it in an area of lower shear/moment.

An attempt is always made to place a cold joint at the optimal location however site constraints due to stage geometry and superstructure configurations restrict this flexibility. Because of the variability at each bridge a typical location can not be given.

Probably D regions. In general the location of a cold joint when it occurs is constrained by staging/geometry.

D-Regions

I suspect that D-regions are more frequently encountered

Question 7 - How is surface roughness typically detailed at cold joint interfaces? Select all that apply and, if possible, estimate the percentage of projects for which each interface has been specified.

23 Responses

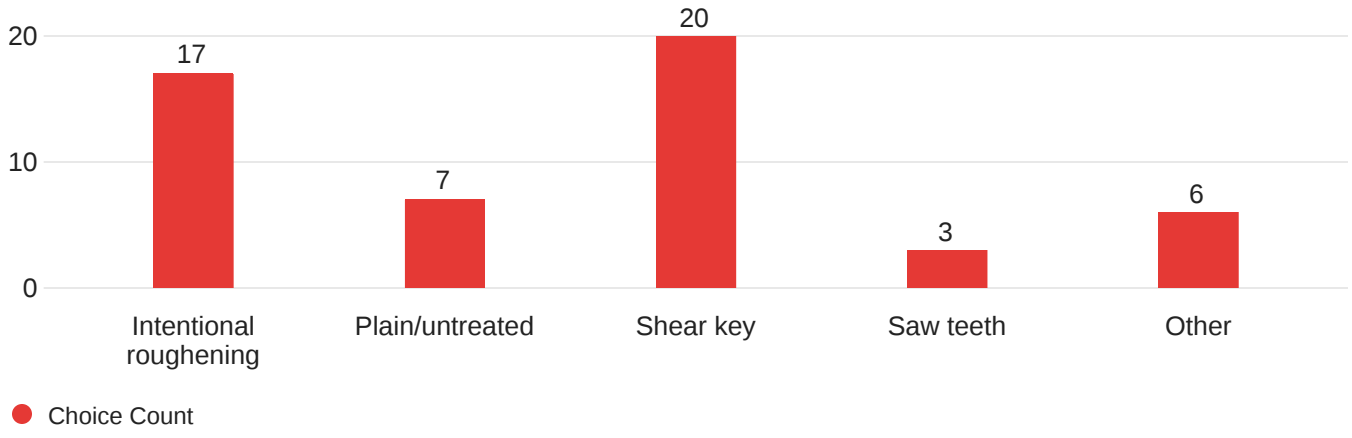

Question 7_Other

Other - Text

There may be unique projects where other interface surfaces are needed

95% apply epoxy

5

multiple shear keys (similar to PT segments)

Open air joint (not a cold joint)

Our specifications require epoxy on the vertical surfaces of all construction joints.

Question 8 - Please explain the factors that affect the type of interface chosen. If intentional roughening was selected and the application was specified, then please describe how surface roughness was applied (e.g., sandblasting, hydro-blasting, brush hammer with sandblasting, etc.).

we always use intentionally roughened joints in substructure units.

NCDOT has had success with detailing shear key in the cap at cold joint interfaces.

Type depends on whether it’s a vertical (shear key) or horizontal joint (intentionally roughened to a certain amplitude), redundancy, structure type, new construction or widening. For roughened surfaces (girders for example), use a coarse brush or metal tine.

The FDOT Structures Design Guidelines contains design provisions when using shear friction with intentionally roughened surface (Section 1.15).

For a retrofit, bushing hammer is typically used. We don't typically specify intentional roughening otherwise.

member depth and location

We use standard shear keys for all segmentally constructed super and substructure elements.

MDOT's current bridge design standards call for keyways to be used at all construction joints for newly constructed elements. If a bridge is being widened to accommodate additional lanes, wider shoulders, etc. the existing face that the widened portion it to be built against is left as is, and is usually plain/untreated with adhesive anchored reinforcement tying the existing and new portions together. If a unique project requires a specific type of interface the requirements will be included in the Contract plans and often times in a project specific special provision.

epoxy application to vertical surface immediately prior to concrete pour.

N/A

precast components often intentionally roughened, cast-in-place typically incorporate a shear key

the VDOT Road and Bridge Specifications have guidance for construction joints. This is the default method. other methods would only be specified if the designer has specific concerns.

Construction Joints: Construction joints that are not detailed on the plans shall be placed as directed or approved by the Engineer. The Contractor shall use shear keys or inclined reinforcement where necessary to transmit shear or bond the two sections together. Joints shall be constructed so that feather edging does not occur.
For construction joints in deck slabs, a 2 by 1 1/2-inch shear key shall be provided between mats of reinforcing steel.
Construction joints against which earth fill is placed shall be protected by a heavy coat of asphalt conforming to Section 213 applied for a distance of 3 inches on each side of the joint and continuous throughout its length.
In construction joints exposed to view, a waterstop conforming to Section 212 shall be inserted. The waterstop shall be placed at least 3 inches from the face of the concrete and shall extend at least 2 inches into each section of concrete.
Longitudinal or transverse construction joints may be used to facilitate placing concrete in continuous slab spans. Longitudinal joints shall be spaced so that each concrete placement will be at least 10 feet in width. Transverse joints shall be placed at the centerlines of piers provided they are located infrequently, permitting simultaneous longitudinal screeding of as many spans as possible.
Concrete shall be placed in one continuous operation between construction joints. The volume of concrete in any one placement shall be not less than the volume of concrete in one end span.

methodology left to contractor

The existing concrete is normally removed in order to get development length for the reinforcing. In these cases the roughened profile resulting from the removal process is used. In some rare cases a shear key will be specified, possibly if mechanical rebar splices were being utilized.

sandblasting, hydro-blasting, scarifying and brushing.

As stated previously, most joints in pier caps are not cold joints, but open air joints (which I marked as other).

However, I would assume if we were to have cold joints on rehab pier caps, they would be intentionally roughened.

If they were on new construction, I assume we would use a shear key.

Our typical practice is to leave the surface untreated.

We do not dictate means & methods for roughening, so we do not have records showing how it was done. We only inspect the final result.

The Department's Standard Specifications do not require a specific type of joint and allow the contractor a choice unless specified on the plans. Some factors such as accessibility, interference, design loads, cross section or other site constraints may drive a reason for selecting a specific joint type.

Shear keys have been the most common method probably because it is more likely to get done in the field according to the plan and won't be forgotten. Intentional roughening is not as likely to be constructed as consistently. In general means and methods are left to the contractor in terms of intentional roughening. The plans may simply call for roughening at a cold joint or possibly call for an roughening amplitude.

Bush hammer

501-3.11 CONSTRUCTION JOINTS.

Unless otherwise noted, locate construction joints where specified in the Contract documents. Obtain approval before adding, deleting, or relocating construction joints specified in the Contract documents. Make requests for such changes in writing, accompanied by a drawing depicting the joint. The Engineer will evaluate the proposed construction joint to determine if the joint will affect the strength or durability of the concrete. Joints noted as "permissible" do not need the Engineer's approval before deleting. When permitted, place the joints where they will not be exposed to view in the finished structure.

At horizontal construction joints, place gage strips 1-1/2 inches thick inside the forms along exposed faces to give the joints straight lines.

Do not use wire mesh forming material.

If the Plans require a roughened surface on the joint, create grooves at right angles to the length of the member. Make grooves that are 1/2 to 1 inch wide, 1/4 to 1/2 inch deep, and spaced equally at twice the width of the groove. Terminate the grooves within 1-1/2 to 2 inches from the edges of the joint.

If the Plans require a smooth surface on the joint, provide a trowel finish.
Include shear keys at the joint when the Contract documents do not require a roughened surface or a smooth surface. Make shear keys of formed depressions with slight beveling to ensure ready form removal. Do not use raised shear keys. Make shear keys that meet the following:

1. For tops of beams, at the tops and bottoms of boxed girder webs, in diaphragms, and in crossbeams, use shear keys 1-1/2 inches deep, 8 inches long, and spaced at 16 inches.

2. In other locations, use shear keys at least 1-1/2 inches deep and 1/3 of the joint width.

Terminate the shear keys within 1-1/2 to 2 inches of the joint edge.

Clean construction joints of surface laitance and other foreign materials before fresh concrete is placed against the surface of the joint. Flush construction joints with water and allow the joint to dry to a surface-dry condition immediately prior to placing concrete.

Question 9 - How is surface roughness typically checked prior to the second cast? Select all that apply.

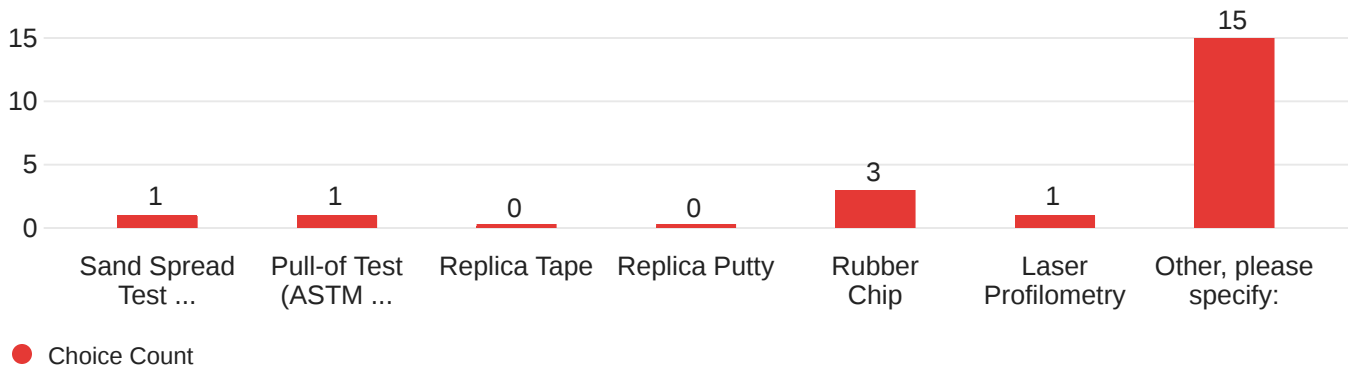

Question 9_Other

Other, please specify: - Text

N/A
Other, FDOT does not use a specific method to check surface roughness meets what's specified in the Plans (nothing listed within our Construction Specifications).
Visual
visual/tactile
Left to contractor means and method for construction of shear keys
It is not MDOT standard practice to verify the surface roughness of concrete on a typical project.
No measurement
no testing specified
None of these is used.
Roughness not usually quantified other than visual observation.
Visual inspection.
Unsure, as this is not a standardized practice.
Visual inspection
Visually

visual

Question 10 - How is the longitudinal reinforcement across the interface typically detailed (refer to the figure below)? Select all that apply and, if possible, estimate the percentage of projects for which each detail has been specified.

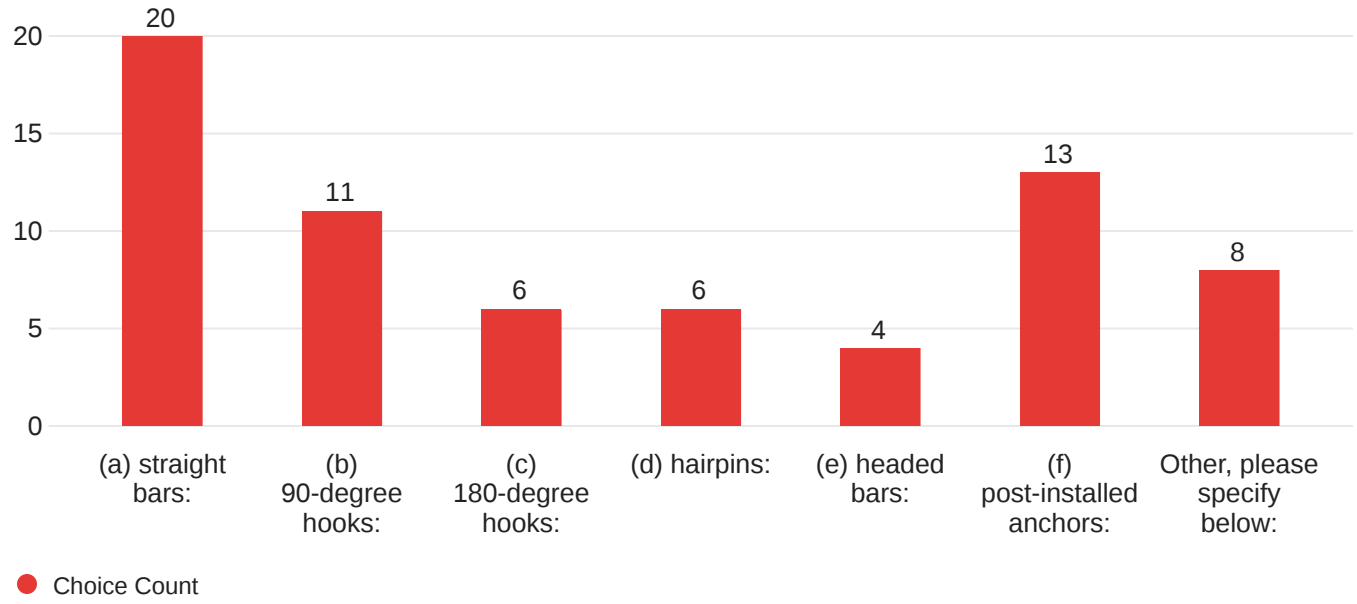

Question 10_Other

Other, please specify below: - Text
5% Mechanical Couplers when lap splices are not feasible
mechanical coupler
typically we use couplers for pier beams
0%
lap bars with threaded couplers
we are using 180 deg bars (not hairpins) that are full depth of the cap on one project and there is research underway as well.
50

combinations of the above

Question 11 - Please elaborate on the detailing of the interface reinforcement if necessary. If possible, include information regarding average bar diameter, bar spacing, and reinforcement ratio.

These numbers are very a rough estimate since we do not have a lot of experience in this area.

Reinforcement size and spacing depends on component type (generally larger bars for substructure, smaller bars for superstructure).

For a widened cap, we typically dowel in a few bars at the interface (assumed hinge for design). For phased construction, we typically extend the bars a lap length (for the smaller bars - #3 through #6), or far enough to weld splice (larger bars - #9 or #11), then splice the next phase of reinforcement to the extensions. The smaller bars are typically temperature reinforcing; the larger bars are the main flexural reinforcing. There is no typical spacing or reinforcement ratio, except we try to use a maximum spacing of 12" and a minimum based on 5.10.3.

Per AASHTO

Typically an epoxy coated #6 bar is the minimum bar diameter used in substructures on MDOT projects. The maximum spacing is 1'-6". For pier caps and integral abutments this spacing is often times considerably less than the maximum, and varies based on project specific conditions.

For post-installed adhesive anchors MDOT's Standard Specifications for construction require a minimum embedment of 12 times the bar diameter if reinforcing bars are used. For anchor rods or bolts a minimum embedment of 9 times the bar diameter is required.

NA

rehabilitation projects involve use of post-installed anchors

formsavers

180 degree hooks are normally used in order to achieve development length more efficiently. #8 bars at 3" are common.

See answer to first question.

As mentioned previously, we typically would have an open air gap in a wide or staged pier cap (not a cold joint). But assuming we have a cold joint, I feel any but the headed or hairpin bar would be used. The choice would be depended on the needed development and if it were new or rehab construction (rehab would be more likely to use post installed anchors). But it would be taken on a project by project basis.

Typical practice is to use a lapped splice. For widening projects, if the existing structure cannot be removed to incorporate a lapped splice, then anchors will be post-installed.

These requirements are per the design and not standardized.

Provide development length beyond interface joint.

Designed in accordance with LRFD article 5.7.4.3 (interface shear / shear friction).

Question 12 - Have you had any constructability issues related to cold joints?

No due to minimal use.

I am not aware of any issues.

Yes, honeycomb forming, especially in deep thin members (PT segmental bridge box girder) and integral diaphragm (in steel I girder bridges).

Reduced available space created some field changes.

No

No, with the exception of potential for leakage depending on where the cold joint is located.

no

No significant issues. There have been instances where steel bulkheads have been used at construction joints that were not braced properly and were displaced during concrete pours. This issue is usually not encountered.

none

not that I'm aware of...

congestion

Not so far

None to our knowledge other than some isolated issues of small voids along the joint interface due to poor concrete consolidation.

Yes, didn't roughen to amplitude required in our specs. Located cold joint in wrong location.

Not to my knowledge, but again, they are not common practice.

I am not aware of any issues.

No. We do not use them often in caps and prefer to avoid them.

No

Not aware of any issues.

No

Not that we are aware

Appendix B. Wood Stand Drawings

The schematic of the wood stands for the small-scale and large-scale slant shear specimens at an interface angle of 30° is presented in this appendix. Note, additional wood stands were designed and constructed for the rest of the interface angle alternatives (40°, 45°, 60°) accordingly.

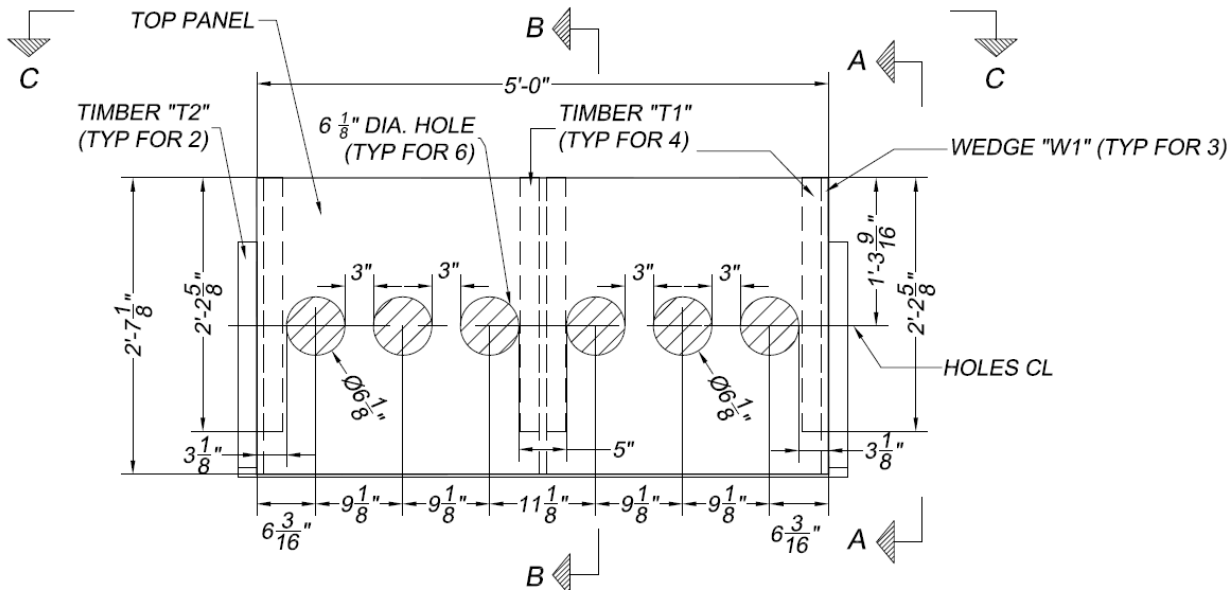

(a) Plan View

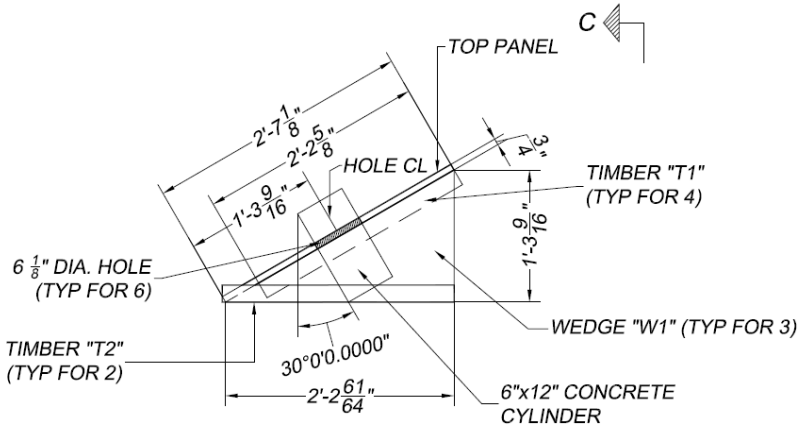

(b) Section A-A

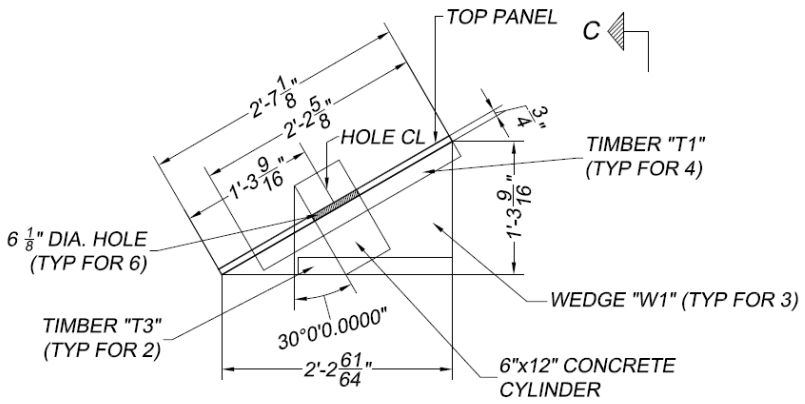

(c) Section B-B

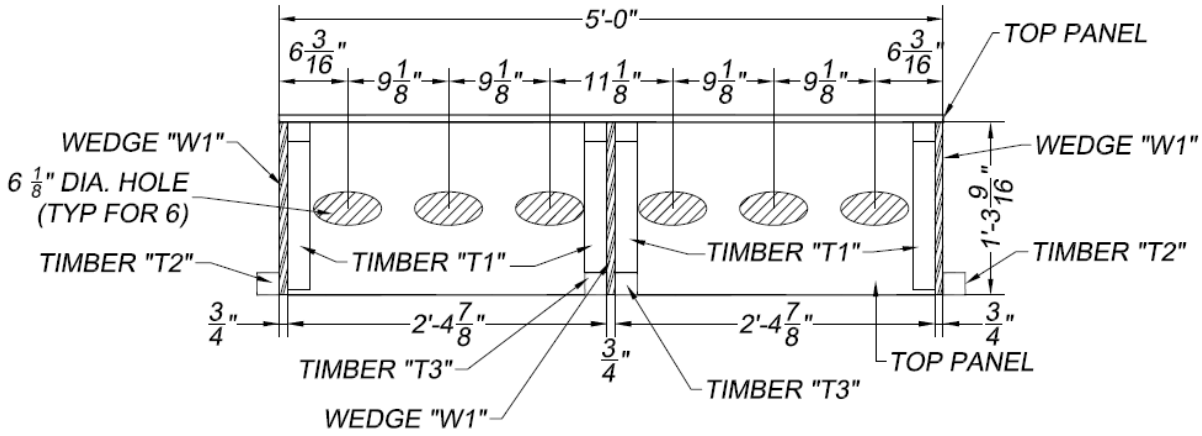

(d) Elevation View (Section C-C)

Figure B.1 Wood stand for 6×12-in. cylinders

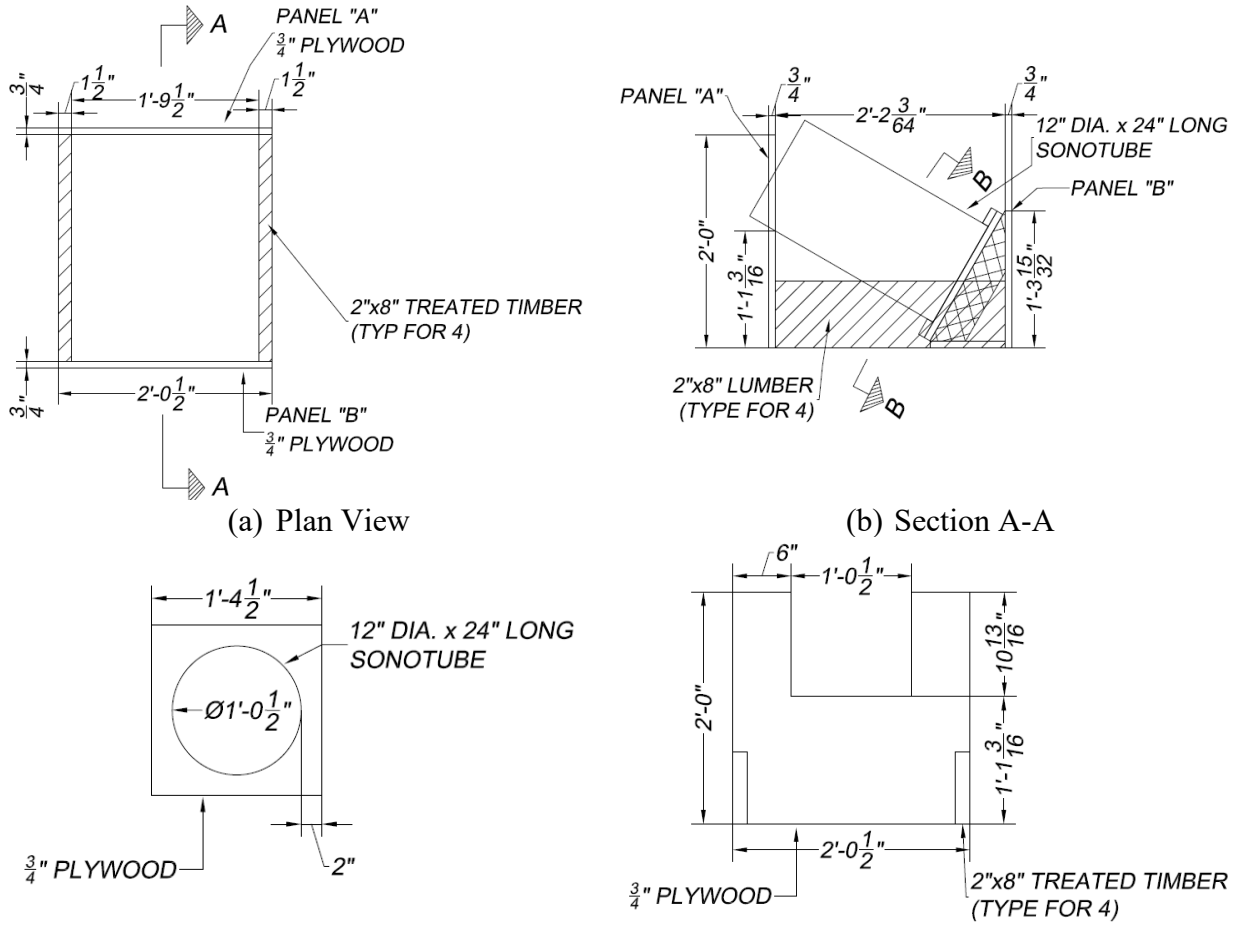

Figure B.2 Wood stand for 12×24-in. cylinders

Appendix C. Failure Modes of Slant Shear Tests

Failure mode photos for all the slant shear specimens are presented in this appendix.

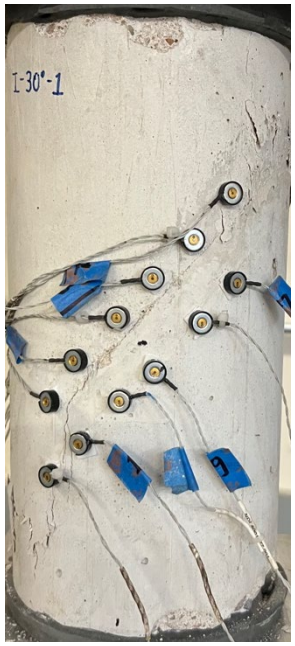

I-40-1

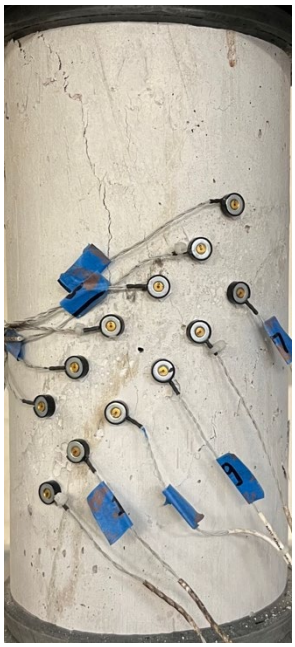

I-40-2

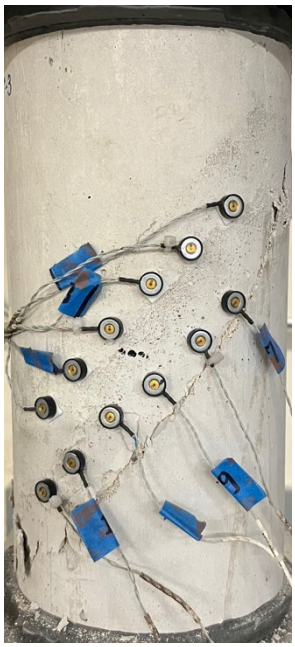

I-40-3

Figure C.1 Failure modes of I-40

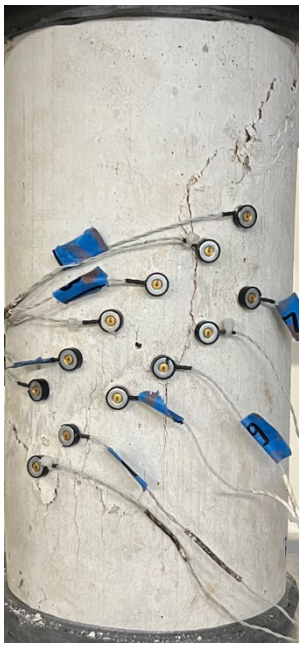

I-45-1

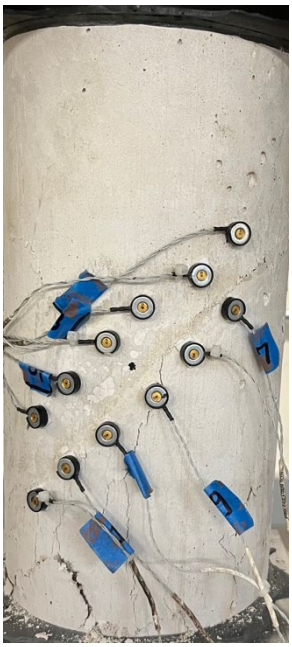

I-45-2

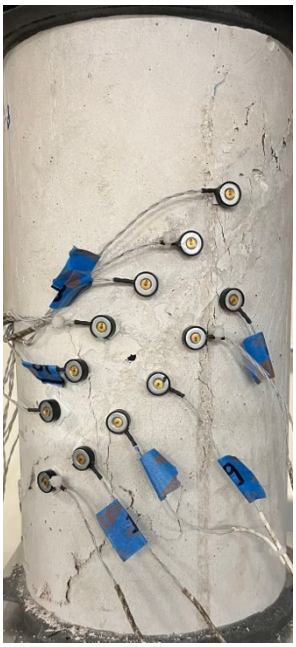

I-45-3

Figure C.2 Failure modes of I-45

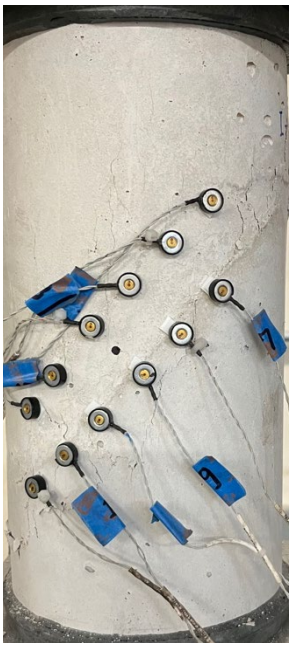

I-50-1

I-50-2

I-50-3

Figure C.3 Failure modes of I-50

I-60-1

I-60-2

I-60-3

Figure C.4 Failure modes of I-60

II-M-1

II-M-2

II-M-3

Figure C.5 Failure modes of II-M

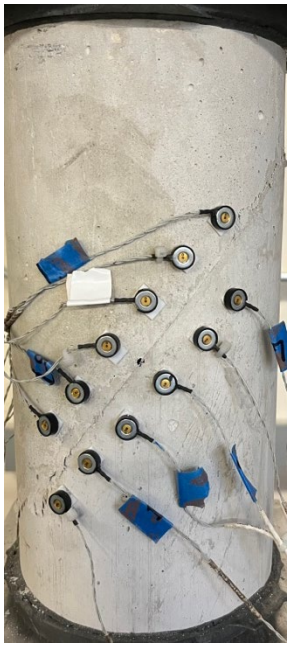

II-NR-1

II-NR-2

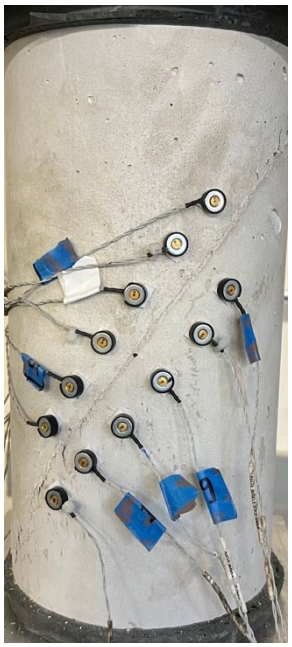

II-NR-3

Figure C.6 Failure modes of II-NR

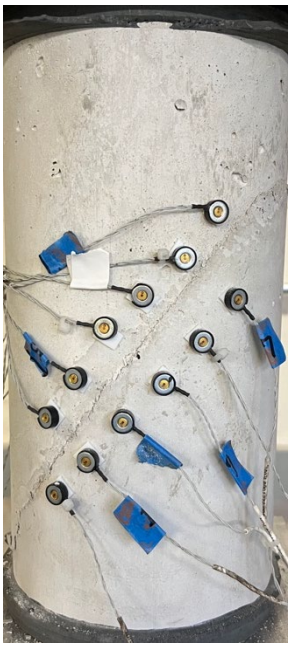

II-R1-1

II-R1-2

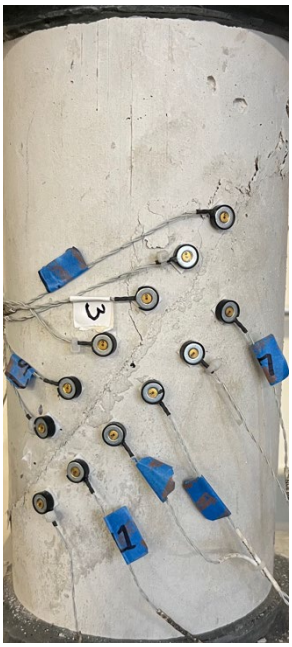

II-R1-3

Figure C.7 Failure modes of II-R1

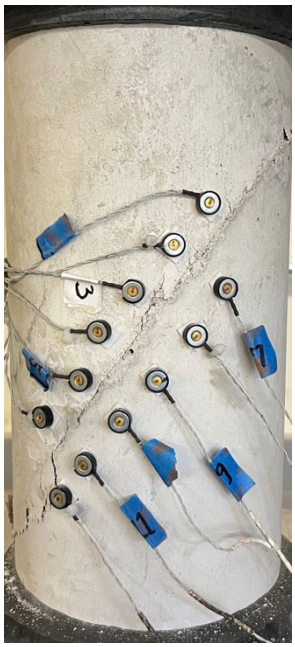

II-R2-1

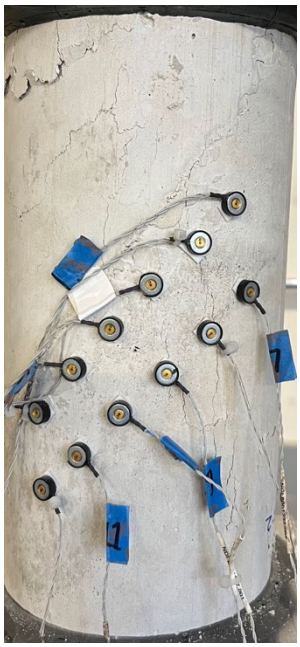

II-R2-2

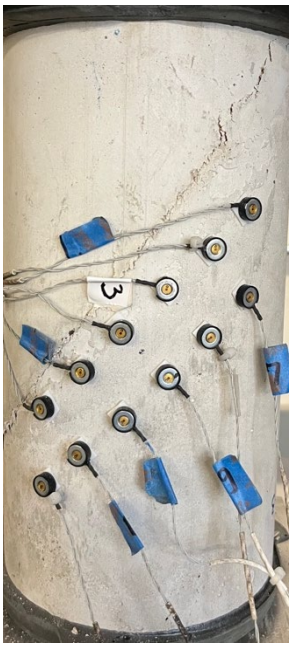

II-R2-3

Figure C.8 Failure modes of II-R2

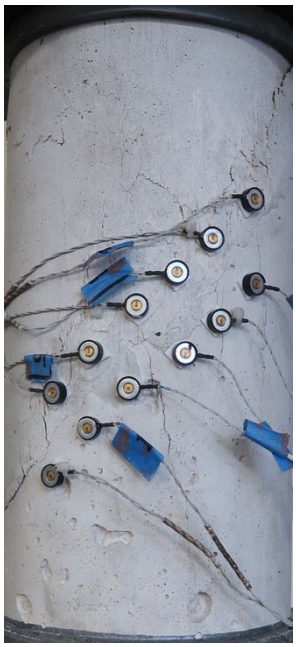

III-H1-1

III-H1-2

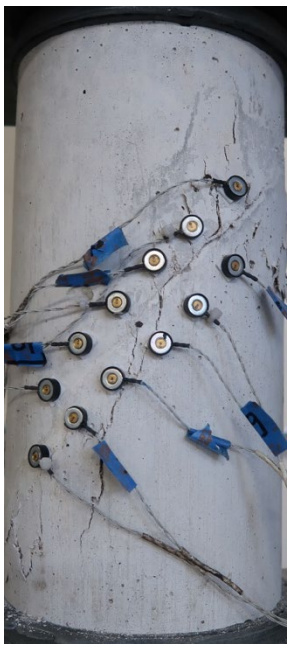

II-H1-3

Figure C.9 Failure modes of III-H1

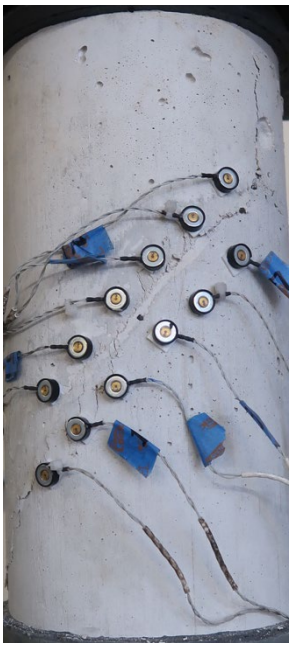

III-H2-1

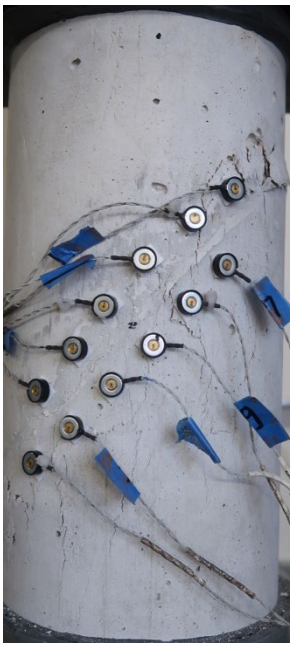

III-H2-2

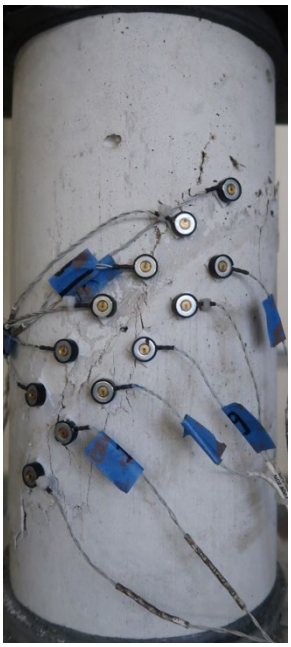

III-H2-3

Figure C.10 Failure modes of III-H2

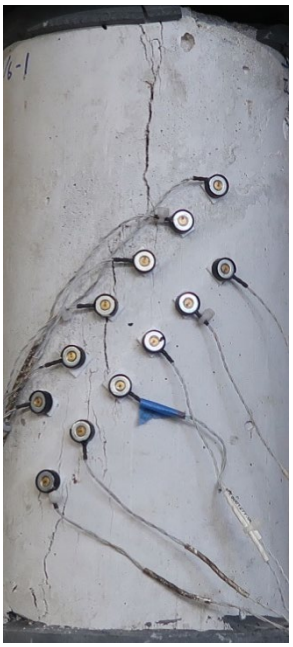

IV-1/6-1

IV-1/6-2

IV-1/6-3

Figure C.11 Failure modes of IV-1/6

IV-28-1

IV-28-2

IV-28-3

Figure C.12 Failure modes of IV-28

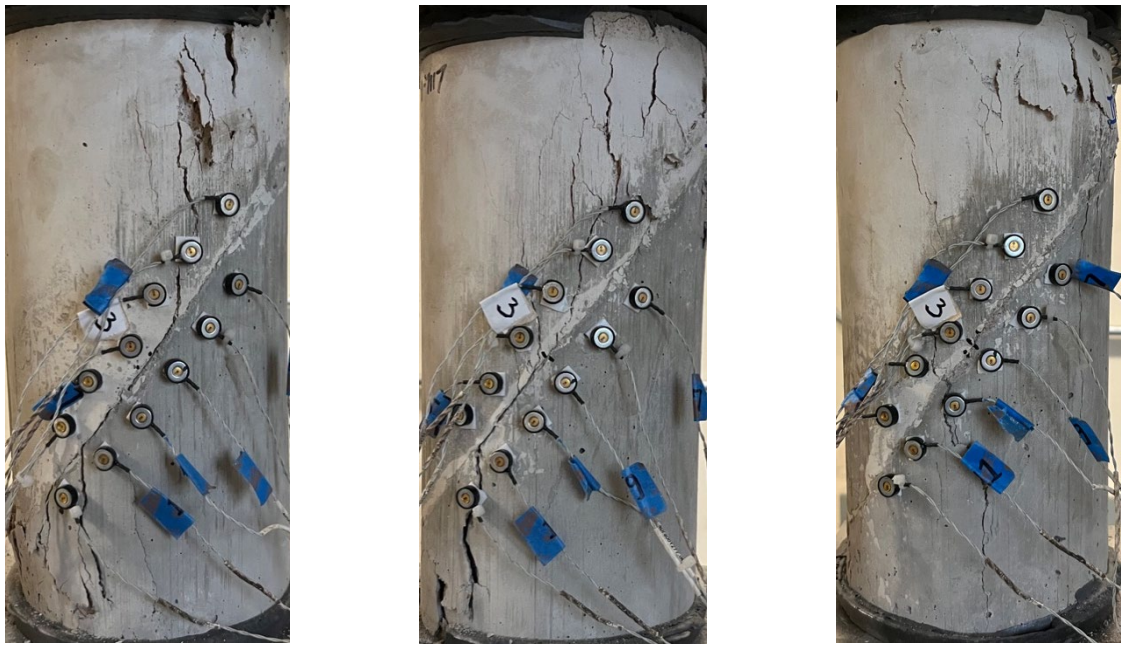

IV-56-1 IV-56-2 IV-56-3

Figure C.13 Failure modes of IV-56

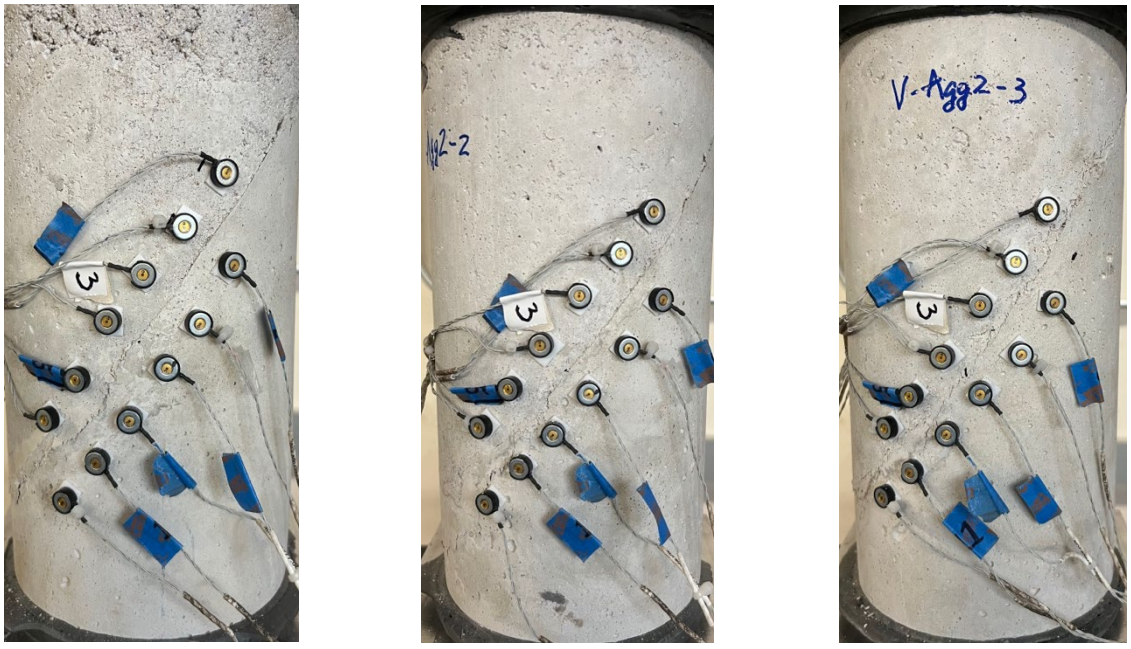

V-A2-1 V-A2-2 V-A2-3

Figure C.14 Failure modes of V-A2

V-A3-1

V-A3-2

V-A3-3

Figure C.15 Failure modes of V-A3

VI-40-1

VI-40-2

VI-40-3

Figure C.16 Failure modes of VI-40

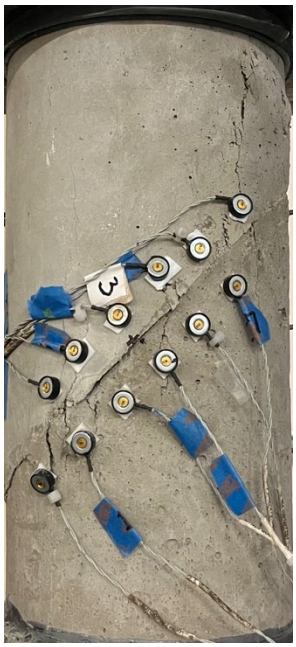

VI-45-1

VI-45-2

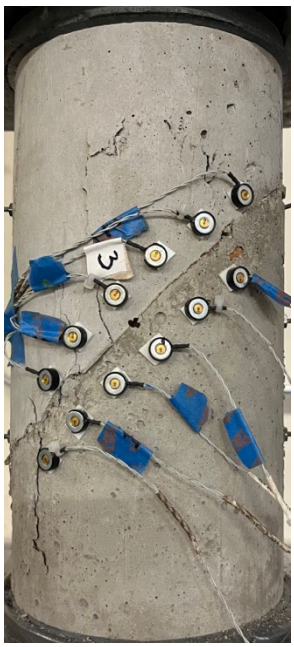

VI-45-3

Figure C.17 Failure modes of VI-45

VI-60-1

VI-60-2

VI-60-3

Figure C.18 Failure modes of VI-60

VII-30 VII-30-NR VII-45 VII-60

Figure C.19 Failure modes of Series VII

Appendix D. Shear Force versus Slip Plots

The shear force-slip plots of the small-scale slant shear specimens governed by SS are presented in this appendix.

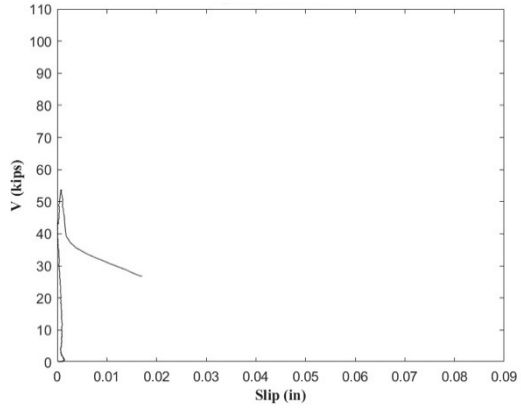

(a) I-40-1

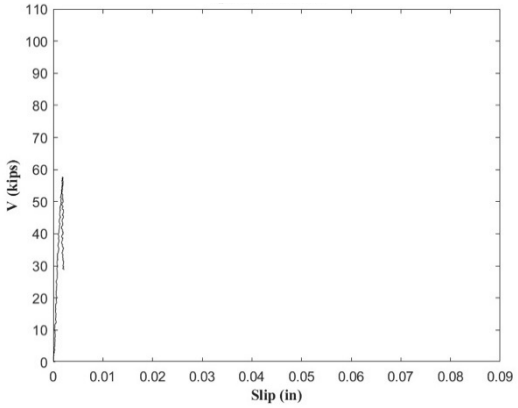

(b) I-40-3

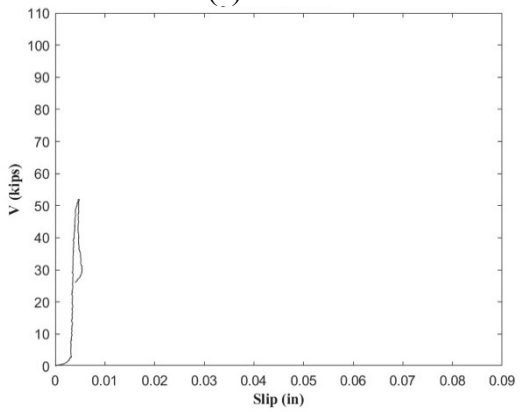

(c) I-45-1

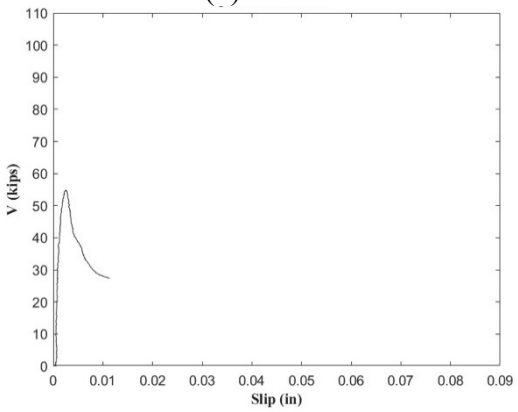

(d) I-45-2

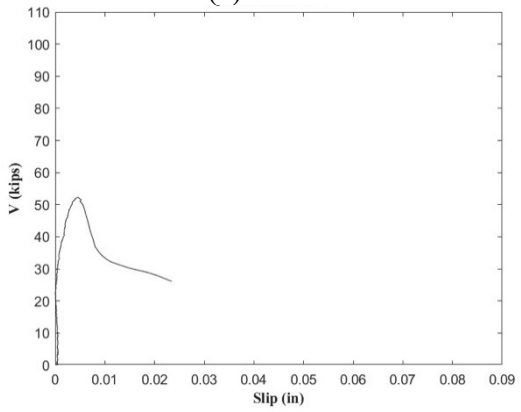

(e) II-R1-1

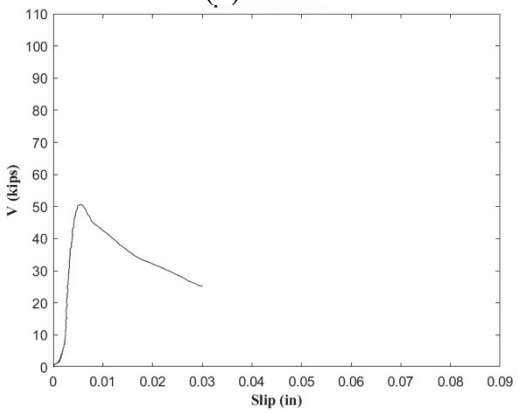

(f) II-R1-2

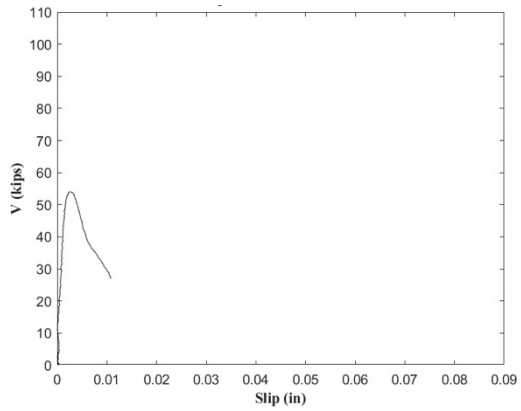

(g) II-R1-3

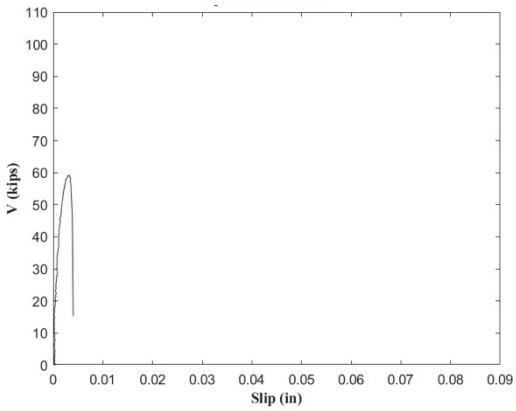

(h) II-R2-1

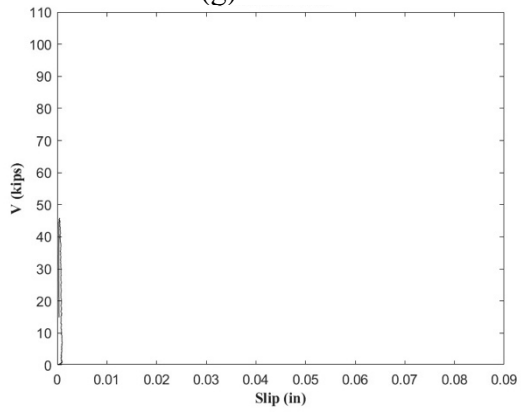

(i) II-R2-3

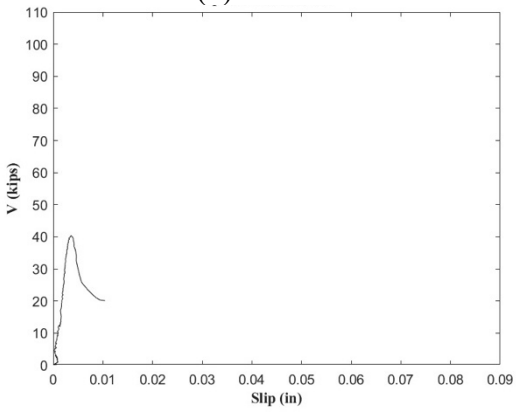

(j) II-NR-1

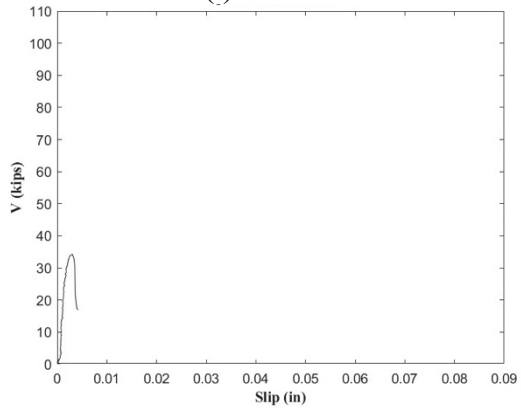

(k) II-NR-2

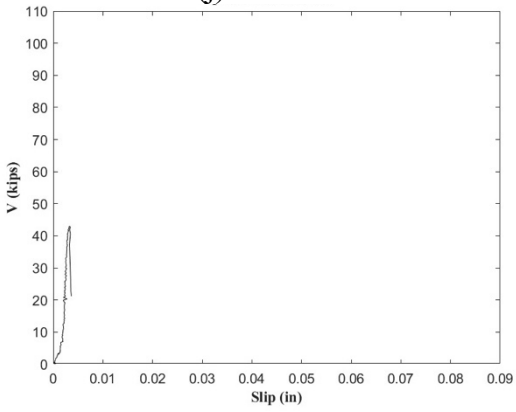

(l) II-NR-3

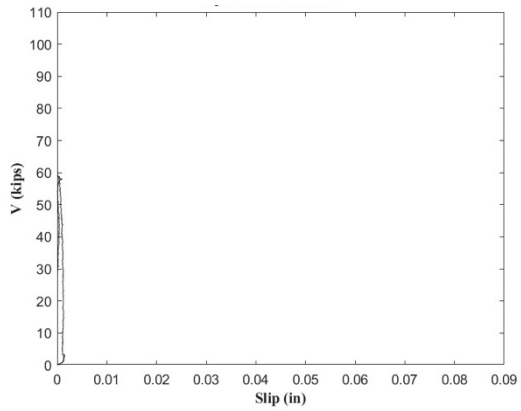

(m) III-H2-3

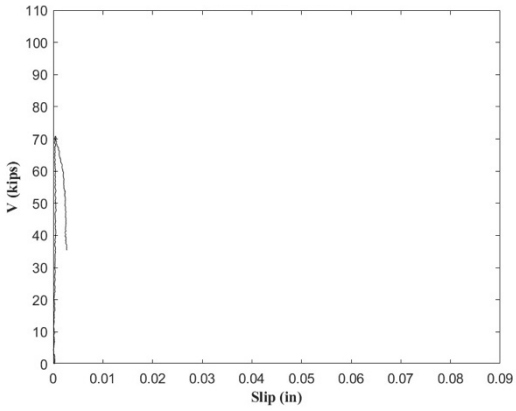

(n) IV-28-1

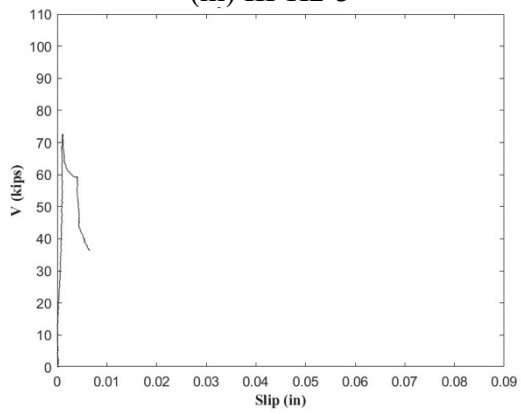

(o) IV-28-2

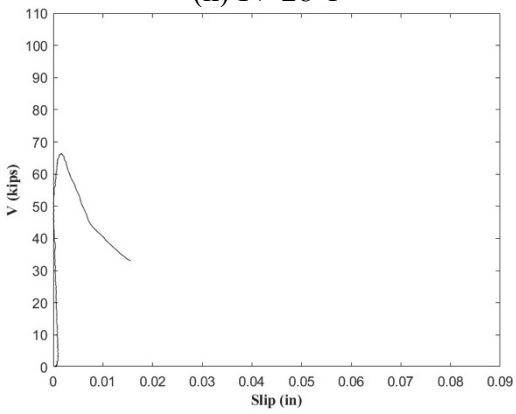

(p) IV-28-3

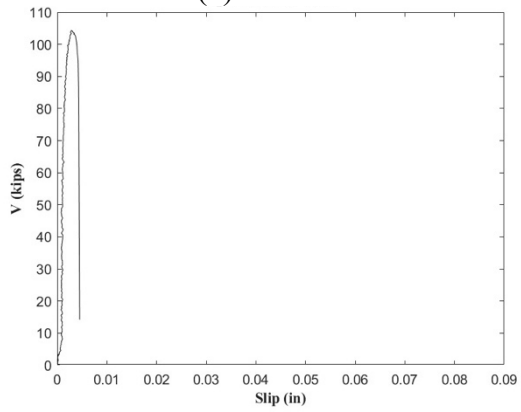

(q) IV-56-1

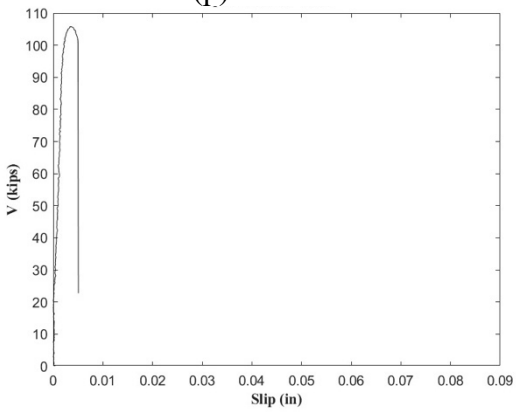

(r) IV-56-2

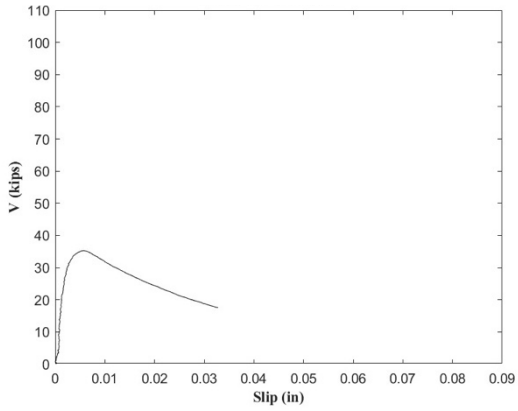

(s) V-A2-1

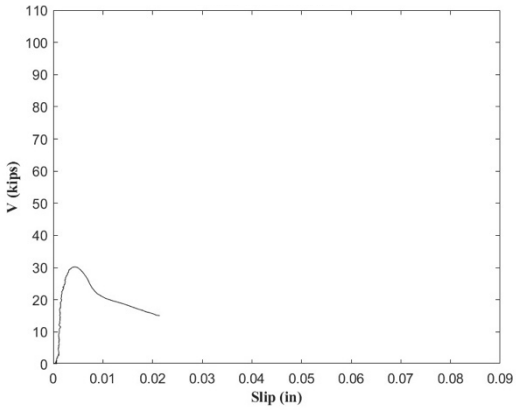

(t) V-A2-2

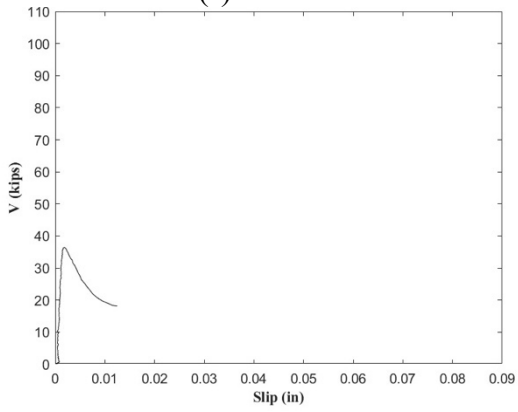

(u) V-A2-3

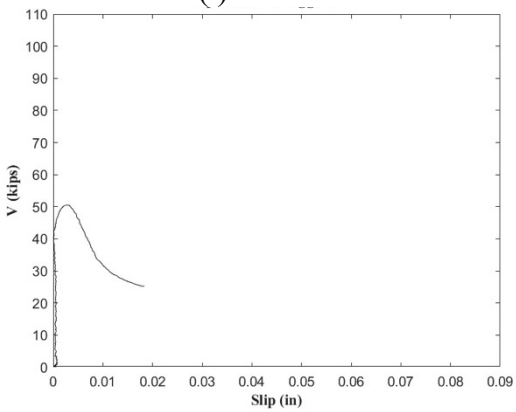

(v) V-A3-2

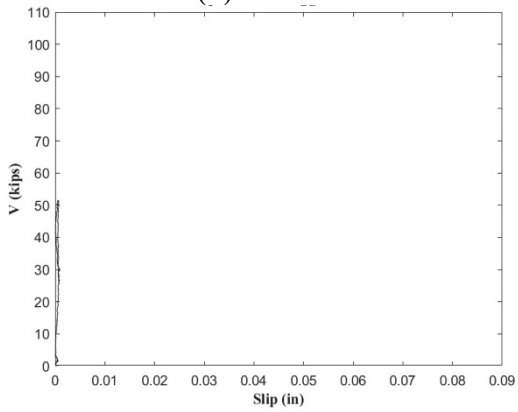

(w) V-A3-3

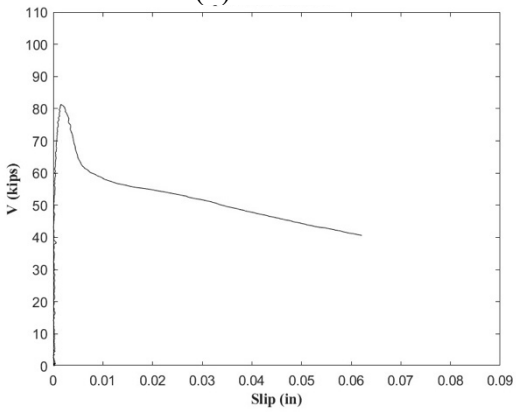

(x) VI-40-1

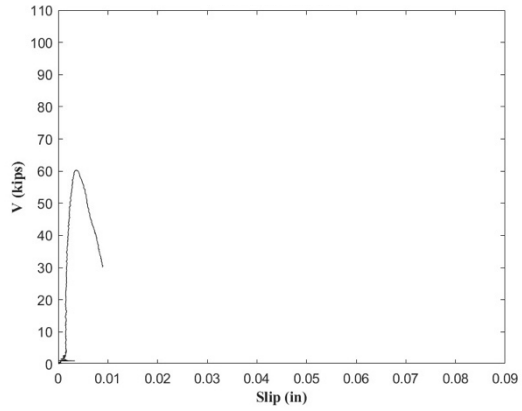

(y) VI-40-2

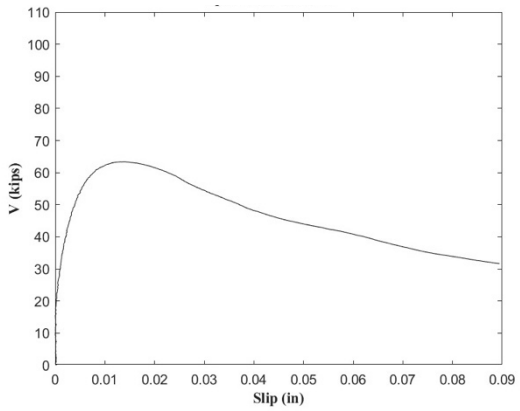

(z) VI-45-1

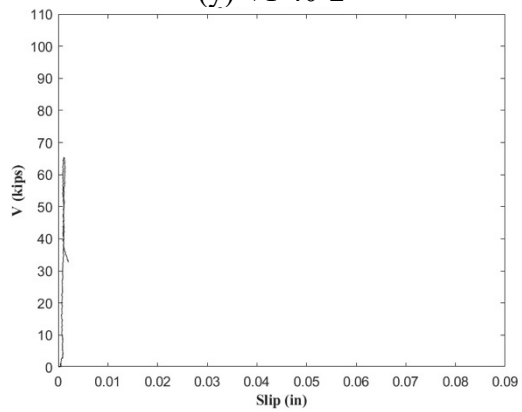

(aa) VI-45-2

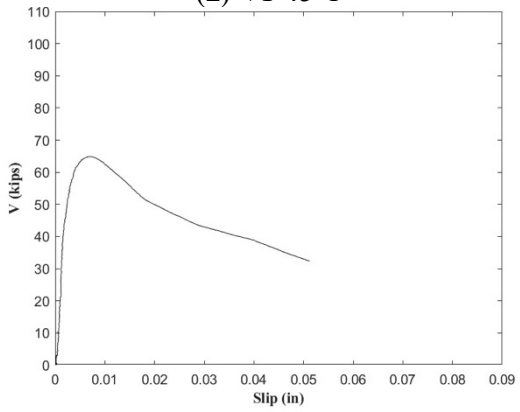

(ab) VI-45-3

Figure D.1 Shear force versus slip plots for small-scale slant shear specimens governed by SS

Appendix E. Test Data from Shear Friction Database

Normal and shear stress under peak load reported by previous research or determined from the inclination of shear interface were listed in Table D.1. The interface roughness of each group of specimens was also listed in Table D.1 for code validation.

Table E.1 Previous test results

Source	Specimen	R_a (in.)	σ (ksi)	τ (ksi)
Figueiredo et al.	NSC-NSC-S	0.034	2.126	2.138
	NSC-NSC-V	0.098	1.986	1.983
	NSC-NSC-R1	0.165	1.635	1.643
	NSC-NSC-R2	0.207	1.842	1.852
	NSC-NSC-R3	0.224	1.867	1.877
	NSC-25-V	0.098	1.331	1.321
	NSC-25-R2	0.207	1.443	1.432
	NSC-25-R3	0.224	1.517	1.505
	NSC-50-S	0.034	1.184	1.220
	NSC-75-S	0.034	1.030	1.004
	NSC-75-V	0.098	1.062	1.034
	NSC-100-S	0.034	0.915	0.947
	NSC-100-V	0.098	0.949	0.982
Santos & Júlio	L28LAC	0.01	0.380	0.658
	L28WB	0.038	0.435	0.753
	L28SAB	0.048	0.673	1.165
	L56LAC	0.01	0.378	0.654
	L56WB	0.038	0.565	0.979
	L56SAB	0.048	0.703	1.217
	L84WB	0.038	0.745	1.290
	E28LAC	0.01	0.318	0.550
	E56WB	0.038	0.365	0.632
	E84LAC	0.01	0.503	0.870
	E84WB	0.038	0.520	0.901
Diab et al.	3mm	0.12	0.980	1.697
	6mm	0.24	1.206	2.089
Saldanha et al.	HSMSST-1	0.59	0.963	1.668
	HSMSST-2	0.59	1.022	1.769
	HSMSST-3	0.59	0.938	1.624
	WMSST-1	0.20	1.013	1.755
	WMSST-2	0.20	0.913	1.581
	WMSST-3	0.20	0.955	1.653
Hu et al.	SL30R1A1S	0.12	1.072	1.858
	SL30R2A1S	0.24	1.259	2.181
	SL30R1A2S	0.12	1.212	2.100
	SL30R2A2S	0.24	1.278	2.213

R_a = amplitude of roughness
σ = normal stress acting on the interface
τ = shear stress acting on the interface

Appendix F. Photographs of Drilled-Shaft Footing Specimen at Different Load Steps

(a) 0 kips

(b) 200 kips

(c) 400 kips

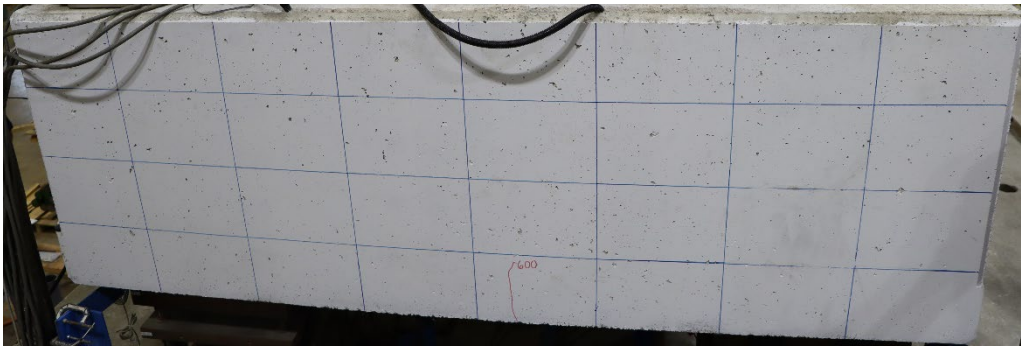

(d) 600 kips

(e) 800 kips

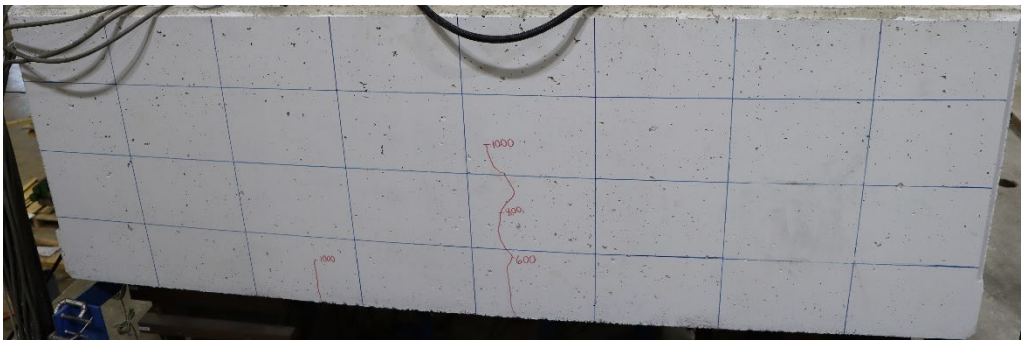

(f) 1000 kips

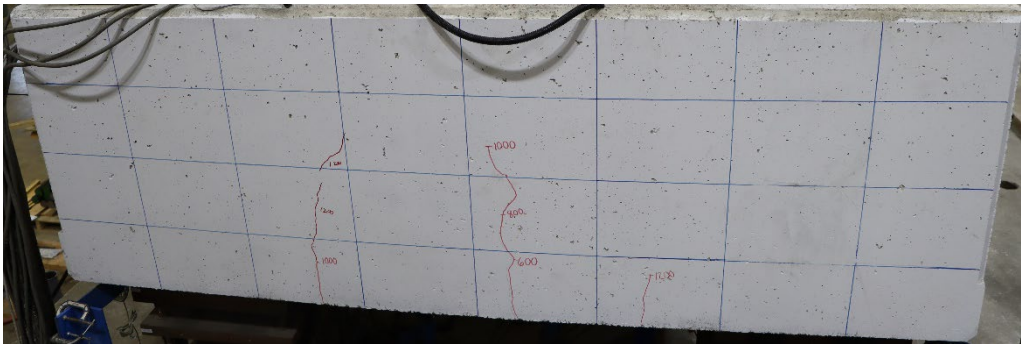

(g) 1200 kips

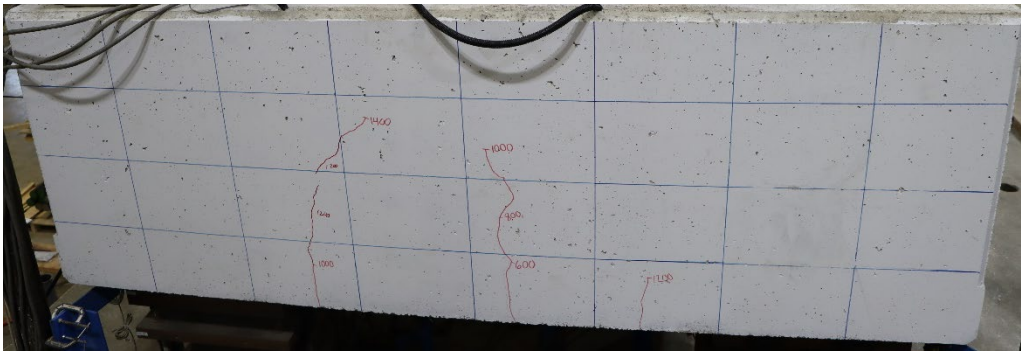

(h) 1400 kips

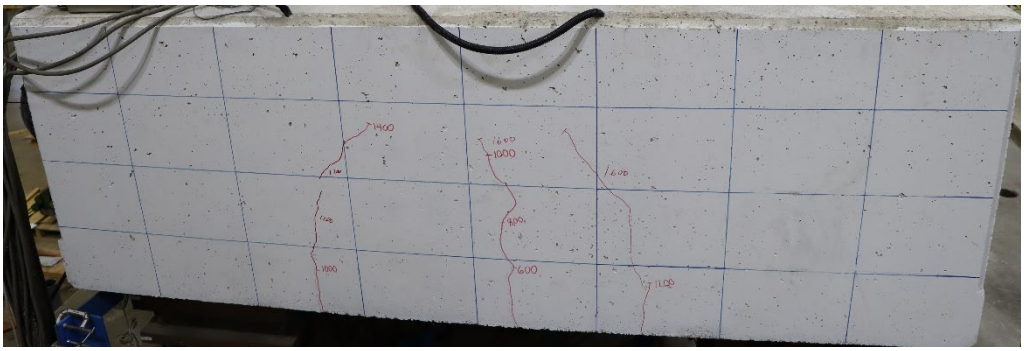

(i) 1600 kips

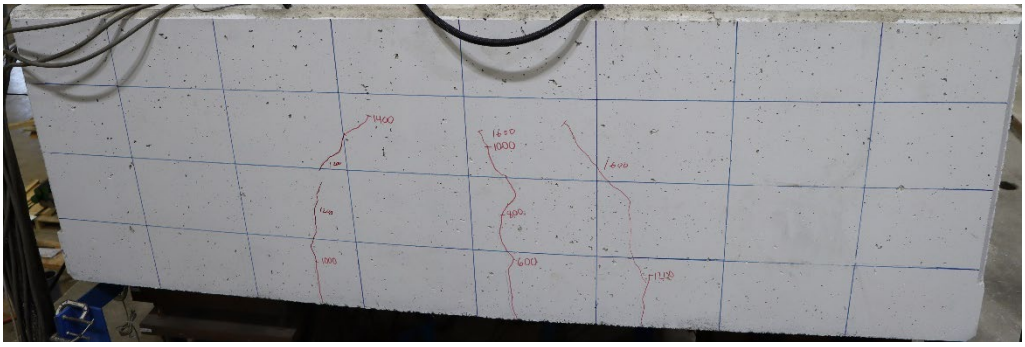

(j) 1800 kips

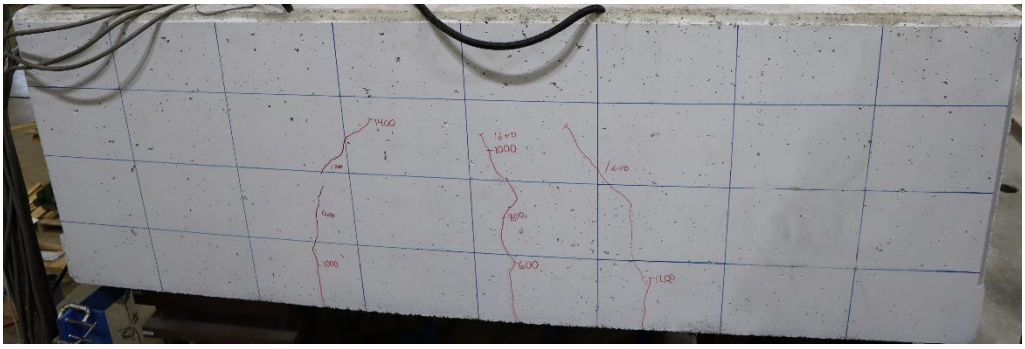

(k) 2000 kips

(l) 2200 kips

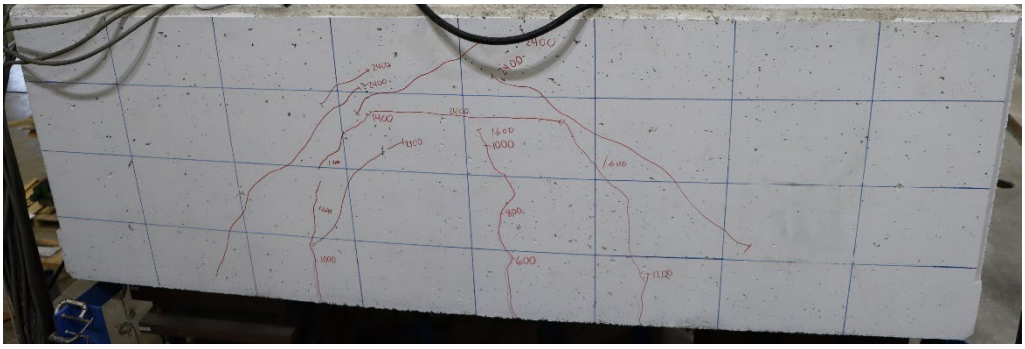

(m) 2400 kips

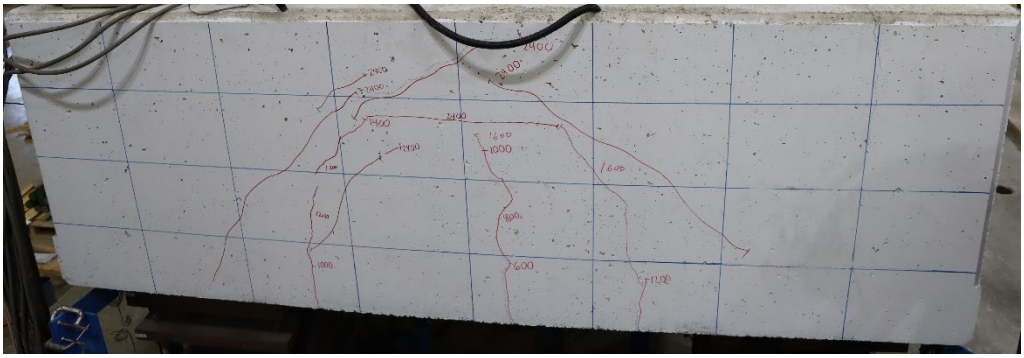

(n) Failure

Figure F.1 North side face of DSF1 at each load step

(a) 0 kips

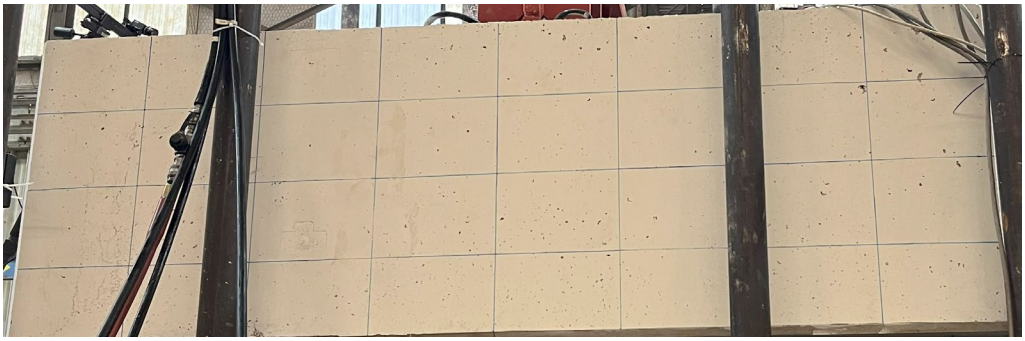

(b) 200 kips

(c) 400 kips

(d) 600 kips

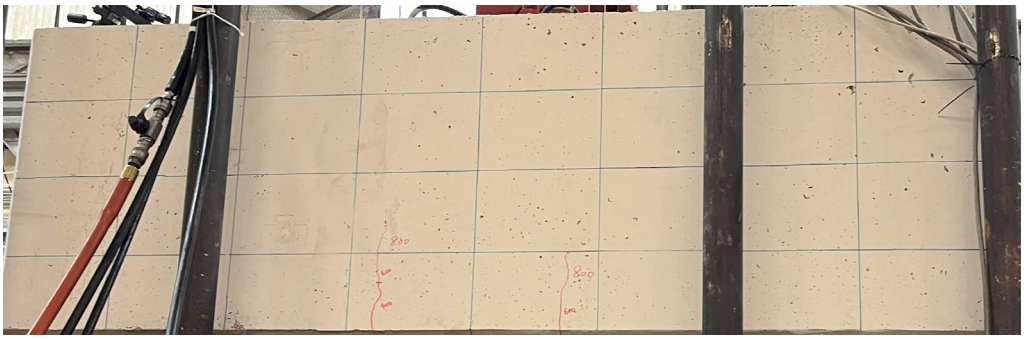

(e) 800 kips

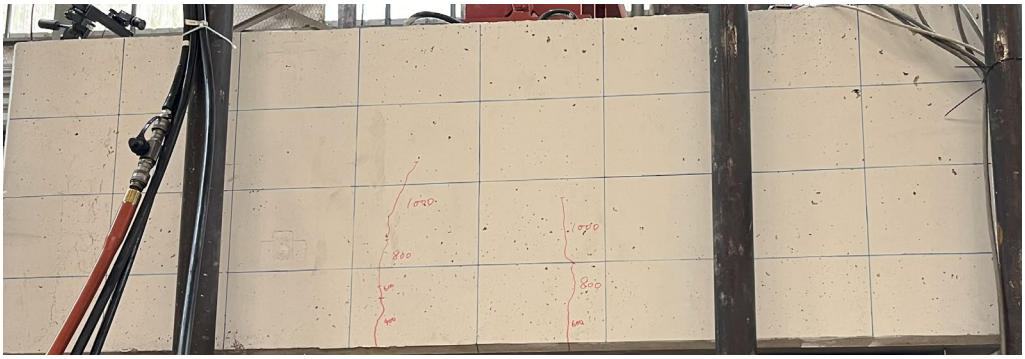

(f) 1000 kips

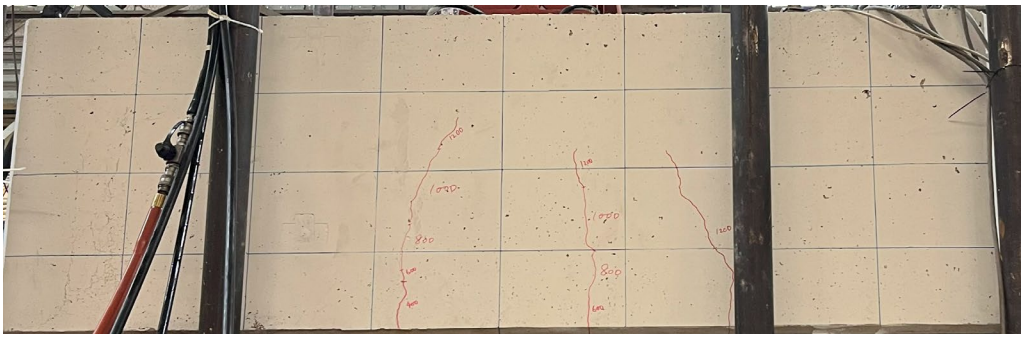

(g) 1200 kips

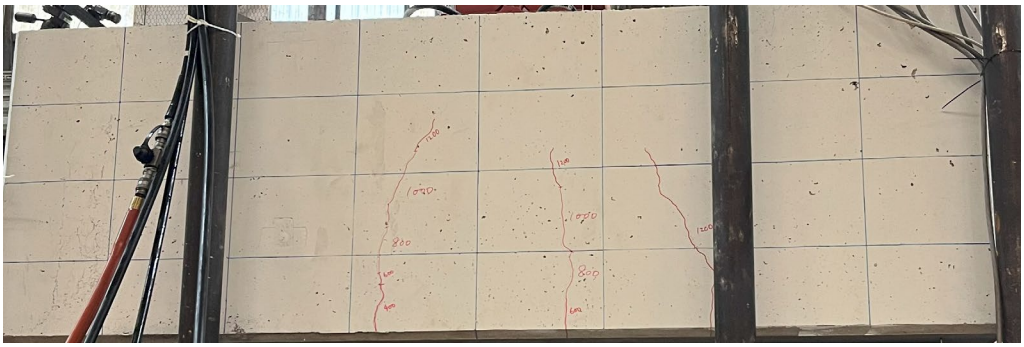

(h) 1400 kips

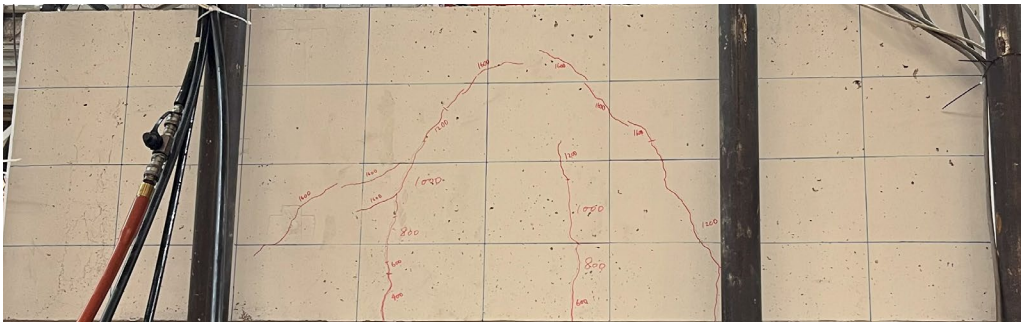

(i) 1600 kips

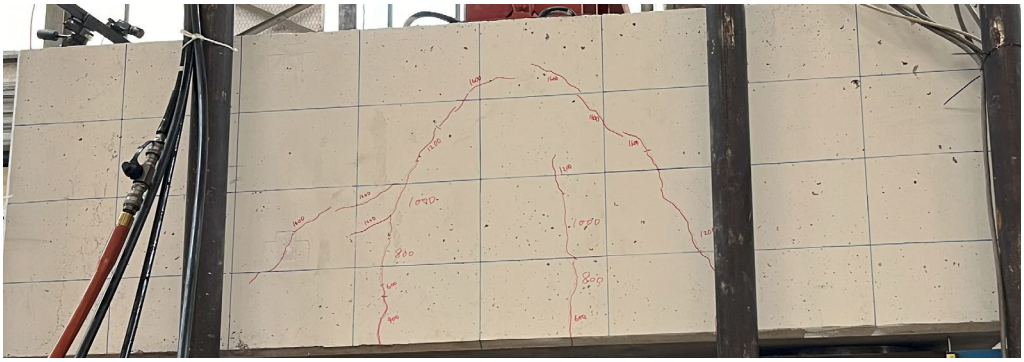

(j) 1800 kips

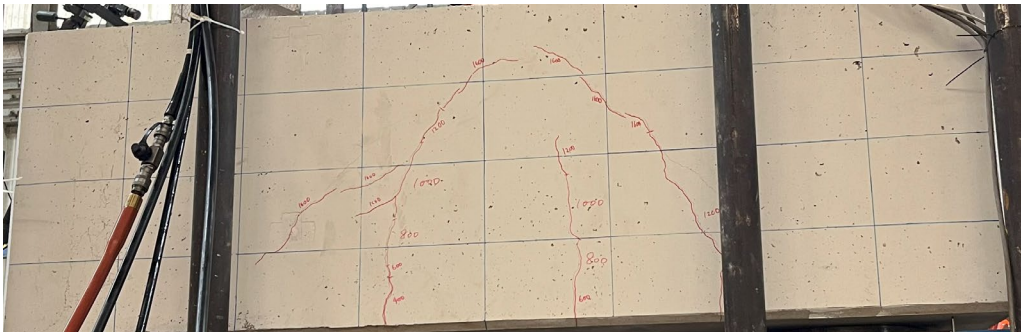

(k) 2000 kips

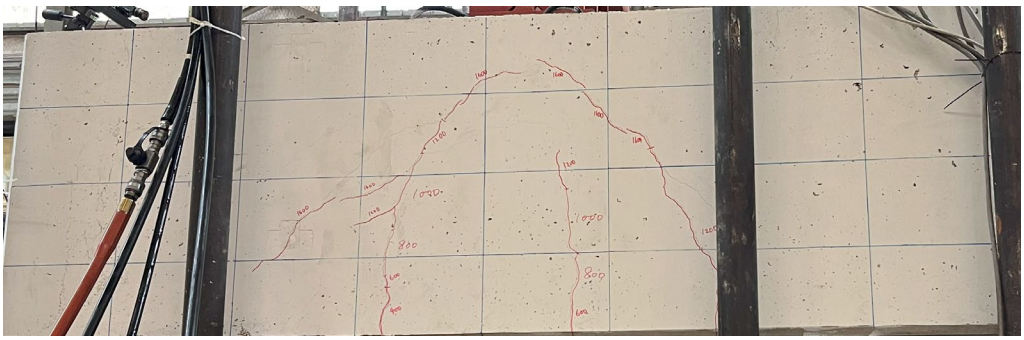

(l) 2200 kips

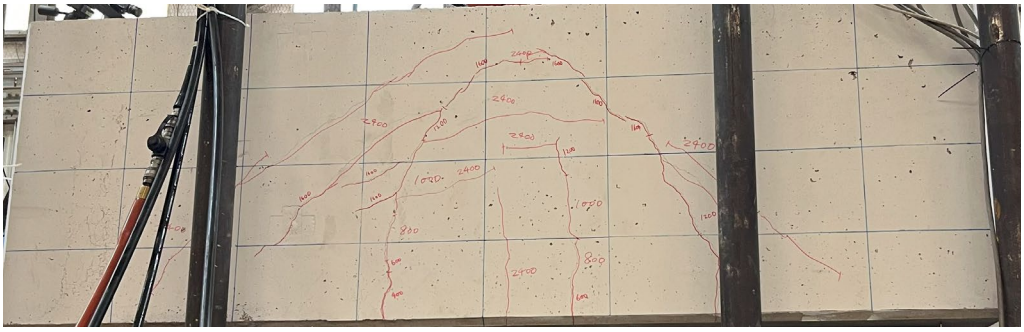

(m) 2400 kips

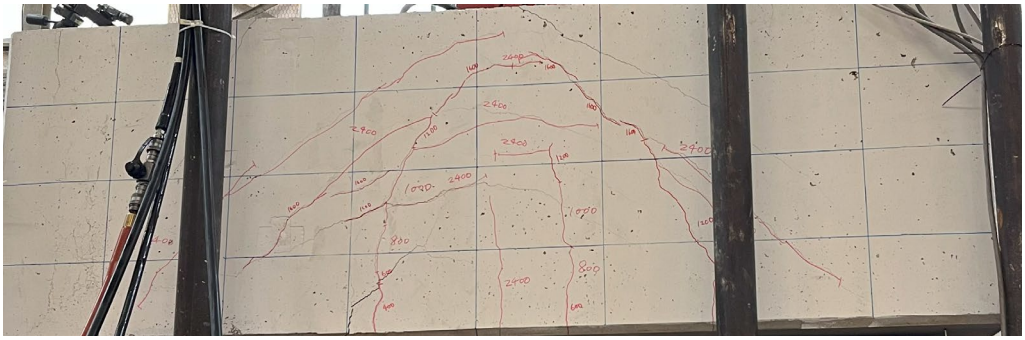

(n) Failure

Figure F.2 East side face of DSF1 at each load step

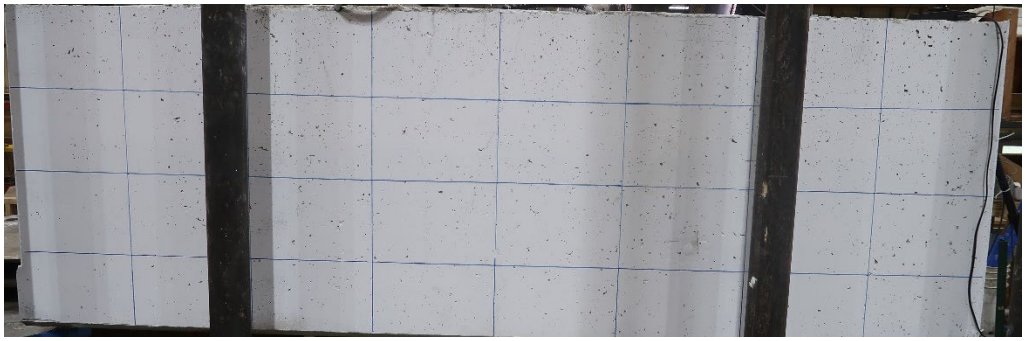

(a) 0 kips

(b) 200 kips

(c) 400 kips

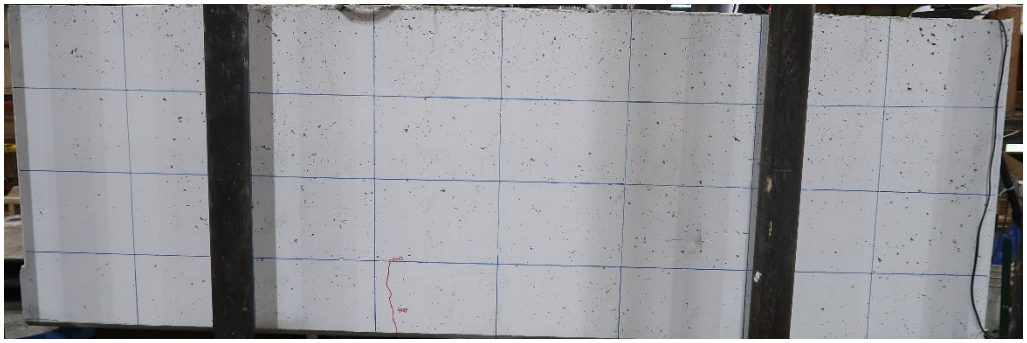

(d) 600 kips

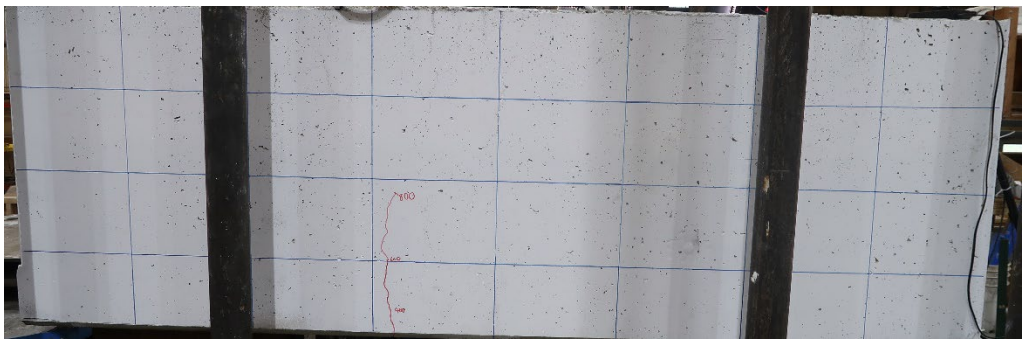

(e) 800 kips

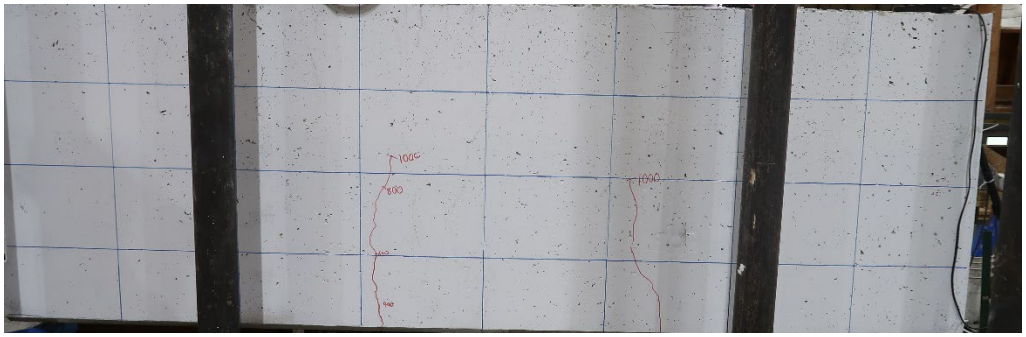

(f) 1000 kips

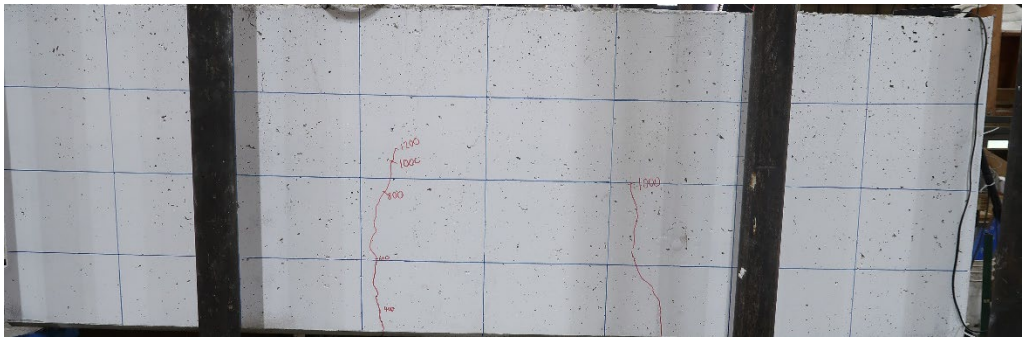

(g) 1200 kips

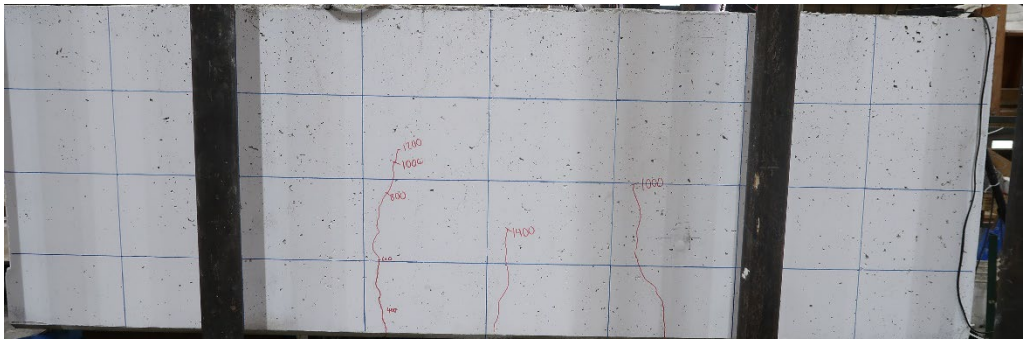

(h) 1400 kips

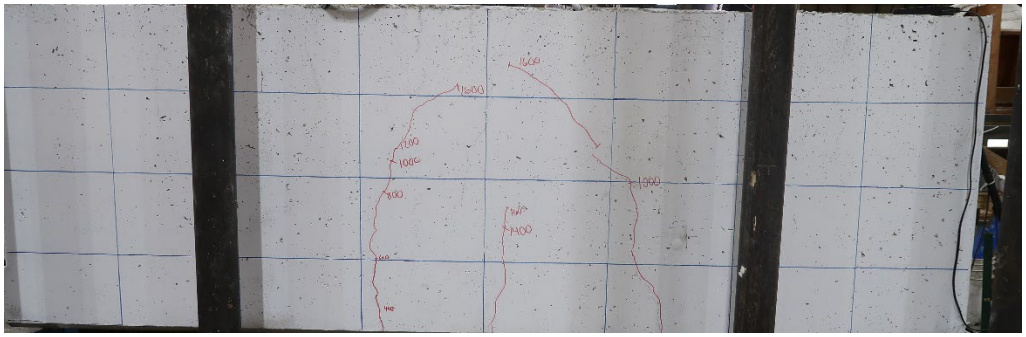

(i) 1600 kips

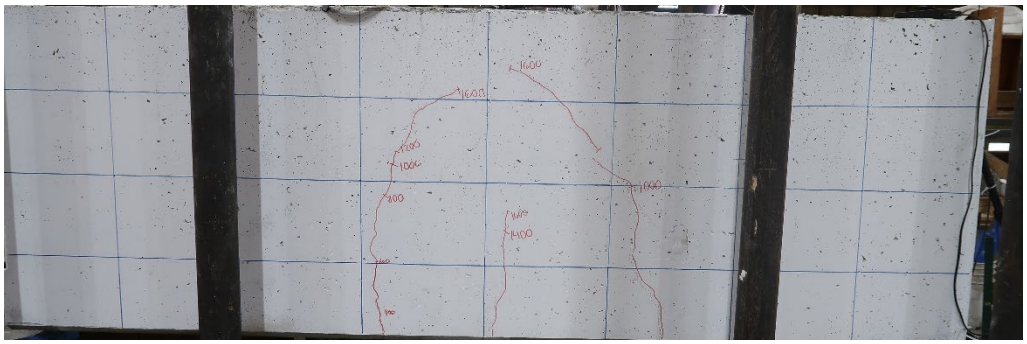

(k) 2000 kips

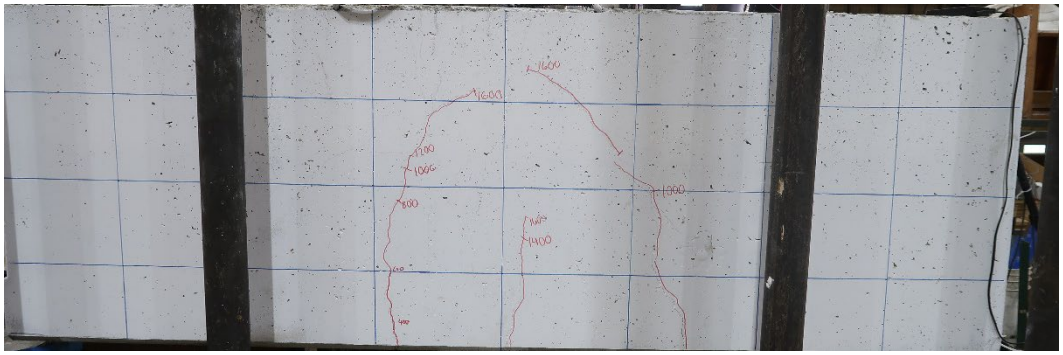

(l) 2200 kips

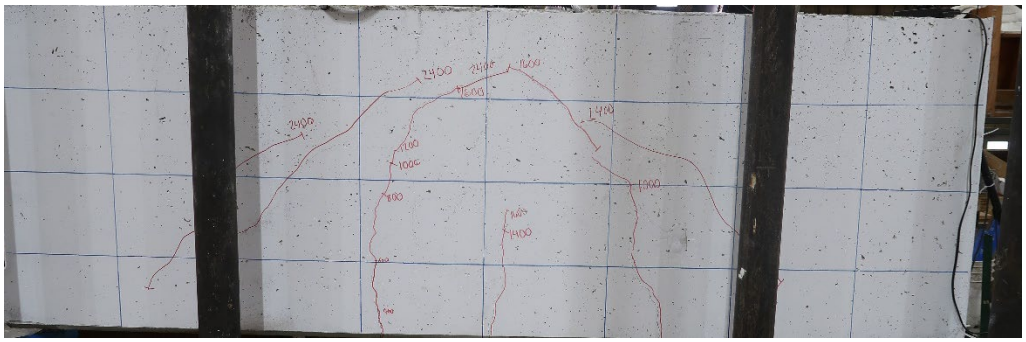

(m) 2400 kips

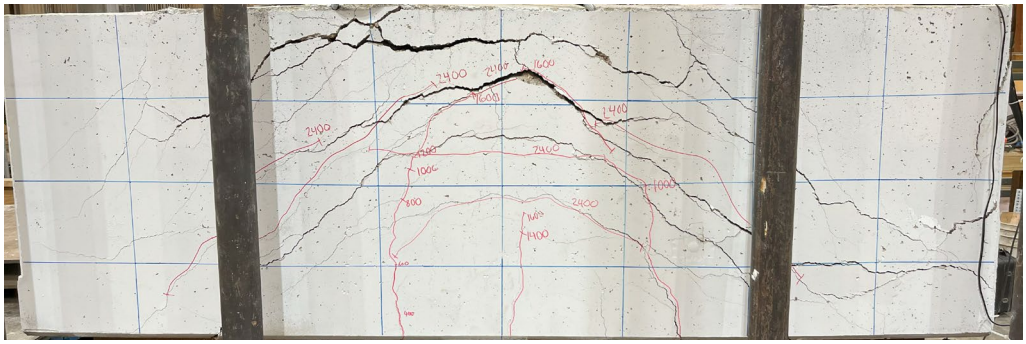

(n) Failure

Figure F.3 West side face of DSF1 at each load step

Appendix G. Design Example

A design example for Specimen III-1.85-00-V from the deep beam experimental program is presented in this appendix. The specimen was designed with an a/d ratio of 1.85 and included 0.3% horizontal and vertical web reinforcement throughout the testing region. A vertical cold joint with no intersecting reinforcement was located at the mid-span of the testing region. The detail design diagram and calculation are presented below.

Deep Beam Design Example

III-1.85-00-V

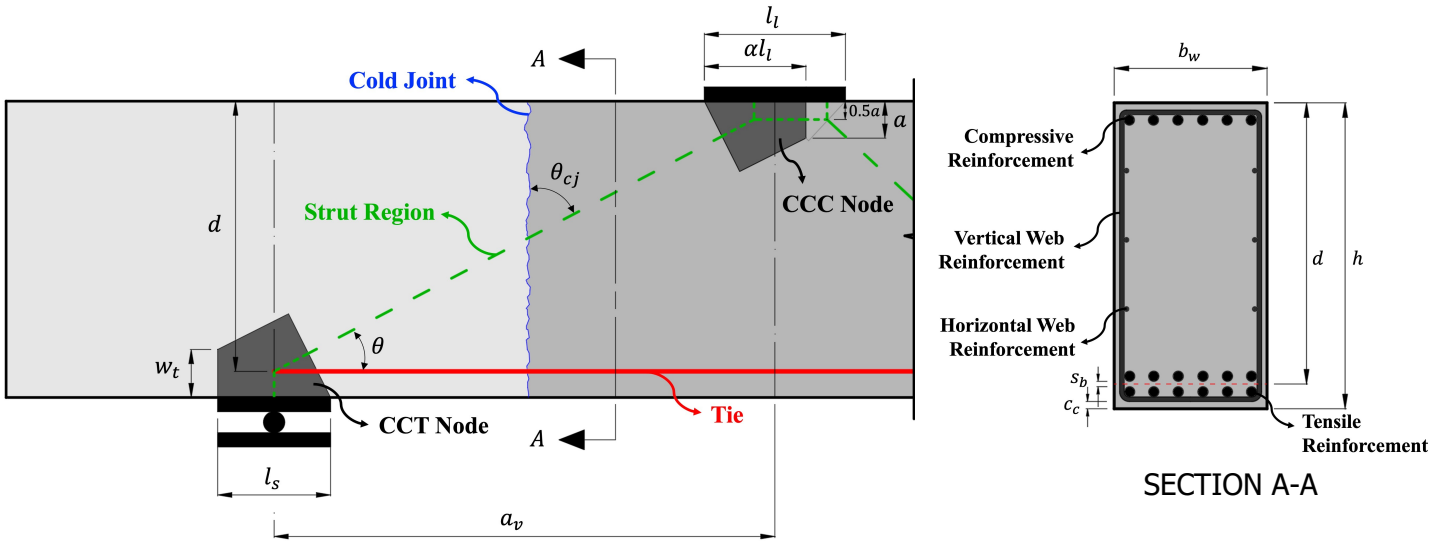

Specimen Dimensions

$b_w := 21\ in$ *Width of the beam*

$h := 42\ in$ *Height of the beam*

$c_c := 1.5\ in$ *Bottom and top clear cover*

$s_b := 1.5\ in$ *Clear spacing between two layers of longitudinal bars*

$d_{bl} := 1.41\ in$ *Diameter of tensile reinforcement*

$d_{bl}' := 1.41\ in$ *Diameter of compressive reinforcement*

$d_{bv} := 0.625\ in$ *Diameter of vertical web reinforcement*

$d_{bh} := 0.625\ in$ *Diameter of horizontal web reinforcement*

$s_v := 9.5\ in$ *Spacing between vertical web reinforcement*

$s_h := 9.5\ in$ *Spacing between horizontal web reinforcement*

$A_s := 18.72\ in^2$ *Area of tensile reinforcement*

$A_s' := 9.36\ in^2$ *Area of compressive reinforcement*

$A_{sv} := 0.31\ in^2$ *Area per vertical web reinforcement*

$A_{sh} := 0.31\ in^2$ *Area per horizontal web reinforcement*

$a_v := 71\ in$ *Shear span of the beam*

$L := 256\ in$ *Distance between supports*

$b_l := 21\ in$ *width of the loading plate*

$b_s := 21\ in$ *width of the supporting plate*

$l_l := 20\ in$ *Length of the loading plate*

$l_s := 16\ in$ *Length of the supporting plate*

$d := h - \left(c_c + d_{bl} + \frac{s_b}{2}\right) = 38.34\ in$ *Effective depth of the beam*

$\frac{a_v}{d} = 1.852$ *Shear-span-to-effective-depth ratio*

Deep Beam Design Example

Material Properties

$f_c' := 4.598\ \textit{ksi}$ — *Compressive strength of concrete*
$f_{yl} := 70.95\ \textit{ksi}$ — *Yielding strength of tensile reinforcement*
$f_{yl}' := 70.95\ \textit{ksi}$ — *Yielding strength of compressive reinforcement*
$f_{yv} := 69.08\ \textit{ksi}$ — *Yielding strength of vertical web reinforcement*
$f_{yh} := 69.08\ \textit{ksi}$ — *Yielding strength of horizontal web reinforcement*

Strut-and-Tie Model

$\alpha := \frac{(L - a_v)}{L} = 0.723$ — *Ratio of near end reaction to applied load*

$a := \frac{(A_s \cdot f_{yl} - A_s' \cdot f_{yl}')}{0.85 \cdot f_c' \cdot b_w} = 8.091\ \textit{in}$ — *Back face length of CCC node*

$\theta := \operatorname{atan}\left(\frac{d - \frac{a}{2}}{a_v}\right) = 25.781\ °$ — *Angle between strut and tie*

$\theta_{cj} := 90\ ° - \theta = 64.219\ °$ — *Angle between strut and cold joint*
$w_t := 2 \cdot (h - d) = 7.32\ \textit{in}$ — *Back face length of CCT node*
$w_{CCC} := \alpha \cdot l_l \cdot \sin(\theta) + a \cdot \cos(\theta) = 13.572\ \textit{in}$ — *Length of strut-to-node interface for CCC node*
$w_{CCT} := l_s \cdot \sin(\theta) + w_t \cdot \cos(\theta) = 13.55\ \textit{in}$ — *Length of strut-to-node interface for CCT node*

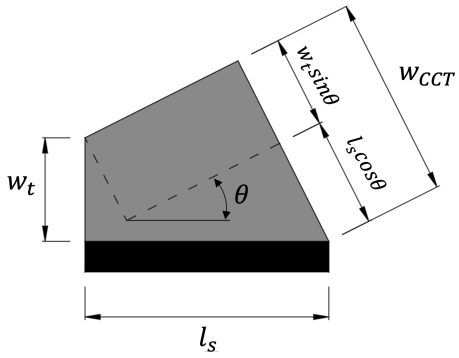

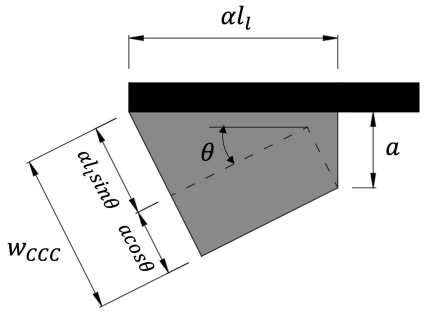

Ultimate Capacity

Ultimate capacity by tie yielding

$T := A_s \cdot f_{yl} = 1328\ \textit{kip}$ — *Tie yielding capacity (AASHTO 5.8.2.4.1-1)*
$R_n := T \cdot \tan(\theta) = 642\ \textit{kip}$ — *Near end reaction at tie yielding*

$P_{tie} := \frac{R_n}{\alpha} = 888\ \textit{kip}$ — *Applied load at tie yielding*

CCC Node

-Bearing face

$m := 1$ *Confinement modificaiton factor (AASHTO Eq. 5.6.5-3)*

$v := 0.85$ *Concrete efficiency factor (AASHTO Table 5.8.2.5.3a-1)*

$f_{cu\_b} := m \cdot v \cdot f_c' = 3.908$ ***ksi*** *Limiting compressive stress (AASHTO Eq. 5.8.2.5.3a-1)*

$F_{cu\_b} := f_{cu\_b} \cdot \alpha \cdot l_l \cdot b_l = 1186$ ***kip*** *Node face capacity (AASHTO Eq. 5.8.2.5.1-1)*

$P_{b\_CCC} := \dfrac{F_{cu\_b}}{\alpha} = 1641$ ***kip*** *Applied load corresponding to node face capacity*

-Back face

$m = 1$ $v = 0.85$

$f_{cu\_bk} := m \cdot v \cdot f_c' = 3.908$ ***ksi***

$F_{cu\_bk} := f_{cu\_bk} \cdot a \cdot b_w + A_s' \cdot f_{yl}' = 1328$ ***kip***

$P_{bk\_CCC} := F_{cu\_bk} \cdot \tan(\theta) = 641.538$ ***kip***

-Strut-to-node interface

$m = 1$

$\rho_v := \dfrac{2 \cdot A_{sv}}{s_v \cdot b_w} = 0.003$ $\rho_h := \dfrac{2 \cdot A_{sh}}{s_h \cdot b_w} = 0.003$

$v := 0.85 - \dfrac{f_c'}{20\ \textbf{ksi}} = 0.62$

$f_{sni} := m \cdot v \cdot f_c' = 2.851$ ***ksi***

$F_{sni} := f_{sni} \cdot w_{CCC} \cdot b_w = 813$ ***kip***

$P_{sni\_CCC} := F_{sni} \cdot \dfrac{\sin(\theta)}{\alpha} = 489$ ***kip***

CCT Node

-Bearing face

$m = 1$ $v := 0.7$

$f_{cu\_b} := m \cdot v \cdot f_c' = 3.219$ ***ksi***

$F_{cu\_b} := f_{cu\_b} \cdot l_s \cdot b_s = 1081$ ***kip***

$P_{b\_CCT} := \dfrac{F_{cu\_b}}{\alpha} = 1496$ ***kip***

-Back face

$m = 1$ $v = 0.7$

$f_{cu\_bk} := m \cdot v \cdot f_c' = 3.219$ ***ksi***

$F_{cu\_bk} := f_{cu\_bk} \cdot w_t \cdot b_w + A_s \cdot f_{yl} = 1823$ ***kip***

$P_{bk\_CCT} := F_{cu\_bk} \cdot \tan(\theta) = 880.517$ ***kip***

-Strut-to-node Interface

$m = 1$ $v := 0.85 - \dfrac{f_c'}{20\ \textbf{ksi}} = 0.62$

$f_{sni} := m \cdot v \cdot f_c' = 2.851$ ***ksi***

$F_{sni} := f_{sni} \cdot w_{CCT} \cdot b_w = 811$ ***kip***

$P_{sni\_CCT} := F_{sni} \cdot \dfrac{\sin(\theta)}{\alpha} = 488$ ***kip***

$P_{STM} := min\left(P_{b\_CCC}, P_{bk\_CCC}, P_{sni\_CCC}, P_{b\_CCT}, P_{bk\_CCT}, P_{sni\_CCT}\right) = 488$ ***kip***

STM capacity governed by strut-to-node interface at CCC node

Deep Beam Design Example

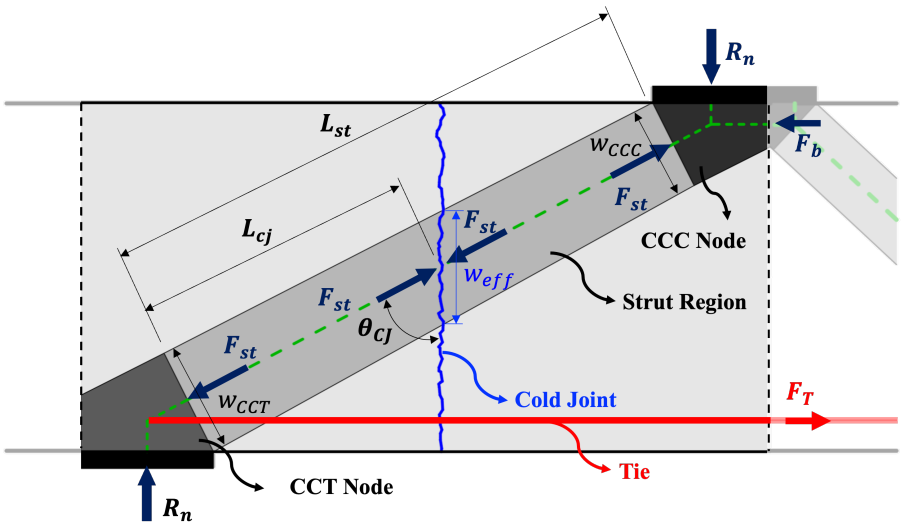

Cold Joint Properties

$R_a := 0\ in$ *Interface roughening amplitude*

$\rho_s := 0$ *Cold joint reinforcement ratio*

$L_{st} := 66\ in$ *Strut length*

$L_{cj} := 35\ in$ *Distance from the cold joint to the CCT node*

$A_{vf} := 0\ in^2$ *Area of reinforcement crossing the effective area*

$f_{vy} := 69.08\ ksi$ *Yielding strength of reinforcement crossing the effective area*

Forces acting on the cold joint

$V_i := F_{st} \cdot \cos(\theta_{cj})$ *Shear force acting on the cold joint*

$N_i := F_{st} \cdot \sin(\theta_{cj})$ *Normal force acting on the cold joint*

Effective Area

$$w_{eff} := \frac{\left(w_{CCT} - (w_{CCT} - w_{CCC}) \cdot \frac{L_{cj}}{L_{st}}\right)}{\sin(\theta_{cj})} = 15.061\ in$$ *Length of the effective area*

$A_{eff} := w_{eff} \cdot b_w = 316\ in^2$ *Effective area*

$c := 0.075\ ksi$ $\mu := 0.6$ *Coefficients for interface shear calculation*

$K_1 := 0.2$ $K_2 := 0.8\ ksi$ *(AASHTO LRFD Article 5.7.4.4)*

$V_{eff} := min\left(c \cdot A_{eff} + \mu \cdot (A_{vf} \cdot f_{vy} + N_i), K_1 \cdot f_c' \cdot A_{eff}, K_2 \cdot A_{eff}\right)$ *Shear resistance of the effective area (AASHTO LRFD Article 5.7.4.3)*

Deep Beam Design Example

Effective Restraint by the Adjacent Regions

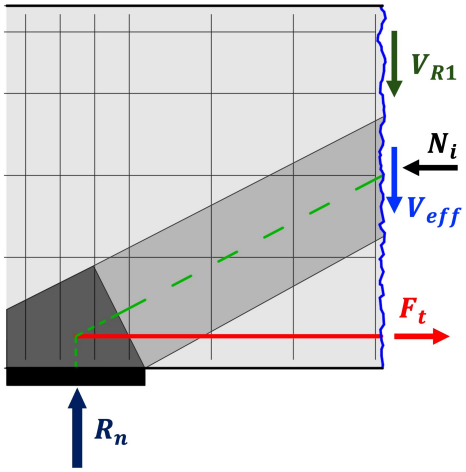

Case 1

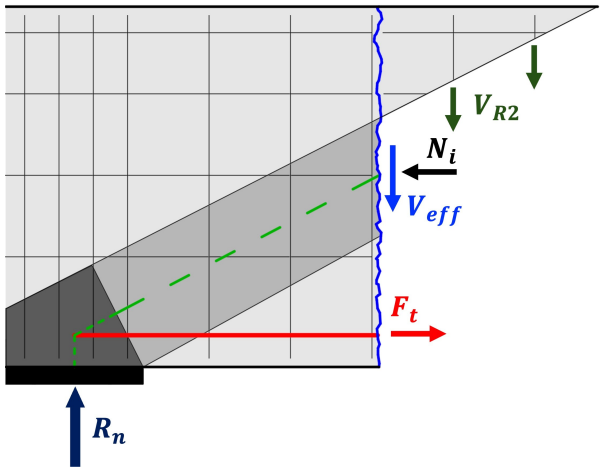

Case 2

- Case 1: shear capacity of cold joint on the compression side

$w_{R1} := 13\ in$ — *Length of the adjacent region*

$A_{R1} := w_{R1} \cdot b_w = 273\ in^2$ — *Area of the adjacent region*

$A_{vR1} := 0\ in^2$ — *Reinforcement area in the adjacent region*

$f_{yR1} := 69.08\ ksi$ — *Yielding strength of reinforcement in the adjacent region*

(No reinforcement intersecting the adjacent region in this case)

$c_R := 0.075\ ksi$ $\quad \mu_R := 0.6$ — *Coefficients for interface shear calulation of the adjacent region*

$K_1 := 0.2$ $\quad K_2 := 0.8\ ksi$

$$V_{R1} := min\left(c_R \cdot A_{R1} + \mu_R \cdot \left(A_{vR1} \cdot f_{yR1}\right), K_1 \cdot f_c' \cdot A_{R1}, K_2 \cdot A_{R1}\right) = 20.475\ kip$$

- Case 2: restraint from the separation of strut

$n_{vR2} := 4$ — *Number of reinforcement intersecting the separated strut*

$A_{vR2} := n_{vR2} \cdot A_{sv} = 1.24\ in^2$ — *Total area of reinforcement intersecting the separated strut*

$V_{R2} := A_{vR2} \cdot f_{yv} = 85.659\ kip$

$V_R := min\left(V_{R1}, V_{R2}\right) = 20.475\ kip$

$V_{ni} := V_{eff} + V_R$

Ultimate capacity by cold joint failure

Iterate P_{cj} until $V_i = V_{ni}$

when $P_{cj} := 379\ kip$

$$F_{st} := \frac{\alpha \cdot P_{cj}}{\sin(\theta)} = 630\ kip$$

$$V_i := F_{st} \cdot \cos(\theta_{cj}) = 274\ kip$$

$$N_i := F_{st} \cdot \sin(\theta_{cj}) = 567\ kip$$

$$V_{eff} := min\left(c \cdot A_{eff} + \mu \cdot \left(A_{vf} \cdot f_{vy} + N_i\right), K_1 \cdot f_c' \cdot A_{eff}, K_2 \cdot A_{eff}\right) = 253.027\ kip$$

$$V_{ni} := V_{eff} + V_R = 274\ kip$$

$$\text{if}\left(V_{ni} \geq V_i, \text{“OK”}, \text{“NG”}\right) = \text{“NG”}$$

$P_{ult} := min\left(P_{cj}, P_{STM}\right) = 379\ kip$ *Failure governed by the cold joint capacity*

$V_{ult} := \alpha \cdot P_{ult} = 274\ kip$ *Shear capacity of the beam*